Metal-Organic-Framework mediated supported-cobalt catalysts in multiphase hydrogenation reactions

Sun, Xiaohui

Important note
To cite this publication, please use the final published version (if applicable).
Please check the document version above.

Metal-Organic-Framework mediated supported-cobalt catalysts in multiphase hydrogenation reactions

XIAOHUI SUN

Metal-Organic-Framework mediated supported-cobalt catalysts in multiphase hydrogenation reactions

Proefschrift

ter verkrijging van de graad van doctor
aan de Technische Universiteit Delft,
op gezag van de Rector Magnificus prof. ir. K.C.A.M. Luyben,
voorzitter van het College voor Promoties,
in het openbaar te verdedigen op
woensdag, 25 oktober, 2017 om 12:30 uur

door

Xiaohui SUN

Master of Engineering in Chemical Engineering and Technology
at China University of Petroleum (East China)
geboren te Zibo, Shandong, China

To my family.

CONTENTS

Metal organic frameworks as precursors for the manufacture of advanced catalytic materials

1

Abstract: Metal-organic-frameworks (MOFs) are crystalline compounds consisting of infinite lattices built up of the inorganic secondary building unit (SBU, metal ions or clusters) and organic linkers, connected by coordination bonds of moderate strength. Owing to their unique structures, MOFs have drawn the attention of the research community in the field of catalysis. MOFs are not only envisioned as catalytic solids themselves, but also as precursors for developing new materials with improved catalytic properties by means of the so-called MOF mediated synthesis (MOFMS), which basically consists of a heat treatment under a certain atmosphere. In this chapter, we highlight the potential of this new synthetic method by selecting recent examples of catalytic processes in which MOFs act as sacrificial templates for the synthesis of improved catalysts.

1.1. INTRODUCTION

Metal-organic frameworks (MOFs) are a class of porous, crystalline materials that consist of inorganic secondary building units connected by multitopic organic ligands. First developed by Hoskins and Robson in 1990 by linking discrete metal clusters[1] and termed MOFs in 1995[2], studies of these materials have entered its third decade by now, and efforts are naturally shifting from fundamental studies to applications, utilizing the unique features of these materials[3]. Prized for their regular and highly tunable pore structures and high surface area, MOF materials are attractive for a range of applications, including heterogeneous catalysis[3], gas storage and separation[4], and drug delivery[5].

Despite advantageous features, their relatively poor stability limits the application in some catalytic reactions, in which harsh conditions (*i.e.* high temperature and pressure), metal (oxide) nanoparticles, and/or mesoporosity are required. In 2008, Xu *et al.* for the first time, demonstrated the application of MOF-5 as a sacrificial template for the synthesis of ZnO@carbon hybrid with hierarchical micro/mesoporous structures[6]. Since then, a variety of MOFs have been carbonized under an inert atmosphere to synthesize metal@carbon catalysts. Bearing in mind the atomic metal dispersion in the framework of MOFs, this novel preparation method allows the formation of metal (oxide or carbide) nanoparticles homogeneously dispersed in the carbon matrix, and the average particle size can be simply tuned by varying the thermal decomposition temperature[7, 8].

Catalytic hydrogenation processes are of great importance in industry. For instance, anilines and, in particular their functionalized derivatives produced through selective hydrogenation of nitroarenes, are key organic

intermediates for manufacturing dyes, pharmaceutics, pigments, and agrochemicals[9, 10]. Carbon monoxide can be hydrogenated into liquid hydrocarbon transportation fuels and various other chemical products through Fischer-Tropsch Synthesis (FTS)[7, 11]. Although a large number of molecular catalysts have been developed for some hydrogenation reactions[12-15], these homogeneous catalysts suffer from difficulties in recycling and separation from products. Therefore, heterogeneous catalysts consisting of supported metal nanoparticles (NPs) are more attractive. In the above-mentioned hydrogenation reactions, supported nanoparticles are widely admitted to be the active components[16-18]. In this regard, a reduction step is required prior to the hydrogenation reaction when catalysts are synthesized using conventional preparation methods (*i.e.* impregnation, drying and calcination)[18], and thus the catalyst handling environment should be rigorously inert in order to prevent the re-oxidation of metallic nanoparticles. Moreover, a huge amount of metal-support species (*i.e.* aluminate, silicate and titanate) are usually produced during the drying and calcination steps[16, 19, 20], that can only be reduced at high temperature and are unable to participate in the reaction. Last but not the least, these supported nanoparticles prepared by using conventional catalyst preparation methods normally display a poor dispersion, and thereby exhibit relatively low hydrogenation activity[20].

Conversely, the homogeneously dispersed metal nanoparticles formed during the pyrolysis of MOFs are well trapped inside the carbon matrix, favorable for their stability[7]. The carbon shells around the metal nanoparticles produced during the pyrolysis and cooling down periods well
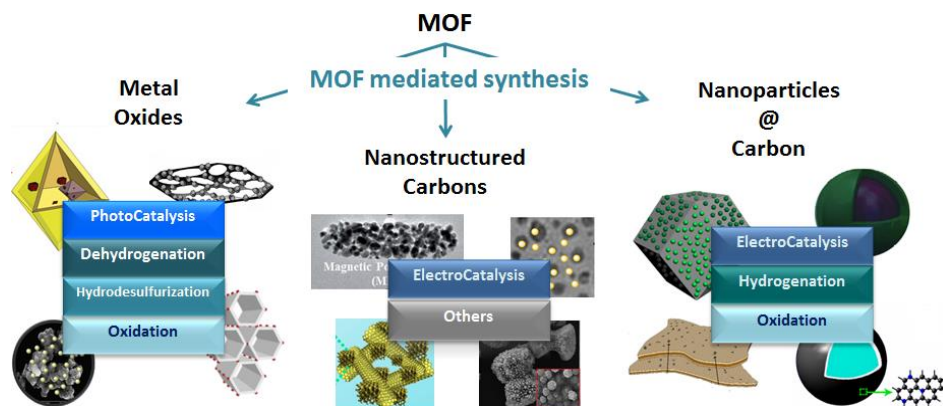
Fig. 1.1. Some nanostructures obtained through the MOF mediated synthesis and their application in catalysis

protect the metallic core from re-oxidation[21]. These advantages of the MOF-mediated synthesis method offer a tremendous potential for application of the metal@carbon hybrids as catalysts or secondary sacrificial templates in heterogeneous catalytic reactions. Hence in this PhD thesis, the MOF-mediated synthesis method is used as a tool to prepare highly loaded, well dispersed supported-metal catalysts in chemoselective hydrogenation of nitroarenes and FTS reactions.

Over the last few years, abundant examples in literature have demonstrated the potential of MOFs in catalysis[22-26]. Thus in this chapter, we highlight the potential of this new synthetic method by selecting recent examples of catalytic processes in which MOFs act as sacrificial templates for the synthesis of improved catalysts. In line with the type of material obtained through the MOFMS, the chapter is divided into three different sections: metals and metal oxides, carbons, and metal nanoparticles in carbon. Likewise, each section is organized according to the catalytic

application of the resulting material, mainly photocatalysis, electrocatalysis, oxidation and hydrogenation reactions.

1.2. METALS AND METAL OXIDES

In recent years, synthesis of nanostructured metal oxides (MOs) has been a topic of intense investigation with special emphasis in controlling the shape, composition and porosity of the resulting MOs. Recently, MOFs have come to light as promising templates for tailoring MOs in a simple manner.

This section gives an account of different nanostructured metal oxides, as well as some metals, using MOFs as sacrificial templates. Depending on the final catalytic application of the metal or metal oxide, different types of MOFs and synthetic methods have been reported in literature. The applications here described range from photodegradation and photocatalytic H_2 production to oxidation, dehydrogenation and hydrodesulfurization processes, with emphasis on high temperature reactions. Despite that most authors point to calcination in air as the typical approach for the preparation of metal oxides from MOFs, acid and other heat treatments are also applied to give place to metals or a combination of both metals and oxides.

1.2.1. Photocatalysis

With the possibility to excite electrons to the conduction band or to generate holes in the valence band, metal oxide nanomaterials can be used to perform photocatalytic reactions, including degradation of organic pollutants or production of solar fuels like hydrogen. On the one hand, large-bandgap metal oxides such as TiO_2 have suitable band positions for photocatalytic solar fuel production, but their main limitation is that they
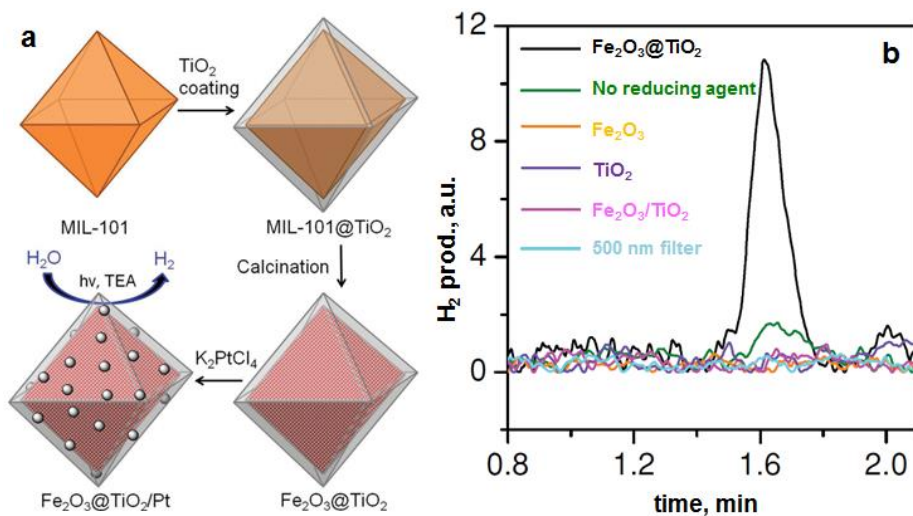
Fig. 1.2. (a) MOF-templated synthesis of $Fe_2O_3@TiO_2$ by coating MIL-101(Fe) with TiO_2 followed by calcination, and its use for photocatalytic hydrogen production after depositing Pt particles; (b) The H_2 peaks in GC analysis of the headspace using 0.5 mg of different catalyst samples[27].

exclusively absorb UV photons, which represent only about 5% of the energy in the solar spectrum. On the other hand, metal oxides with suitable band gaps for efficient absorption in the solar spectrum such as Fe_2O_3 tend to have short carrier diffusion lengths and are ineffective in driving photocatalytic reactions. Recently, De Krafft *et al.* reported a simple MOF-templated strategy for the synthesis of crystalline octahedral nanoshells combining the desired photocatalytic properties from both types of oxides[27]. After coating MIL-101(Fe) particles with an amorphous shell of titania by acid-catalyzed hydrolysis and condensation of titanium(IV) bis (ammonium lactato) dihydroxide (TALH) in H_2O[28], followed by calcination in air at 823 K for 16 h, crystalline $Fe_2O_3@TiO_2$ nanoparticles composed of anatase phase of TiO_2, hematite phase of Fe_2O_3 and pseudobrookite mixed metal oxide phase (Fe_2TiO_5) were formed. This

synthesis method enabled the formation of Fe-doped TiO_2 composite, which exhibited interesting photocatalytic hydrogen production from water using visible light.

In lieu of iron oxide, Li *et al*. described a facile synthetic method for Cu/TiO_2 photocatalysts with hollow structures by treating $Cu_3(BTC)_2$ (BTC = benzene-1,3,5-tricarboxylate) at 413 K in the presence of ascorbic acid (AA) and ethylene glycol (EG) as solvent and TiO_2 hollow particles[29]. The released Cu^{2+} cations were simultaneously reduced by AA to produce Cu nanoparticles when they penetrated through the TiO_2 shells. The AA-reduced Cu/TiO_2 hybrid structures exhibited enhanced charge separation and hydrogen production performance. Likewise, Mondal *et al*. constructed MOF-derived $Cu/CuO@TiO_2$ photocatalysts where the copper species were adsorbed on anatase[30]. Titanium isopropoxide $(Ti(ipro)_4)$ was added to the Cu-BDC (1,4-benzenedicarboxylate) MOF in an ethanol/water mixture and then the amorphous material was calcined at 623 K for 5 h in N_2 atmosphere. The obtained mesoporous $Cu/CuO@TiO_2$ showed a considerable higher rate of H_2 production than conventional CuO loaded TiO_2, attributed to the presence of surface deposited Cu^0 species and the small size of the heterojunction between CuO and TiO_2, which facilitated interfacial charge carrier transfer from the TiO_2 nanoparticles.

Photocatalysis on semiconductors has demonstrated efficiency in degrading a wide range of organic pollutants into biodegradable or less toxic compounds. However, the difficult post-separation, easy agglomeration, and low solar energy conversion efficiency of these inorganic catalysts calls for further research[31]. Recently, Yang *et al*. demonstrated that MOF-derived ZnO nanoparticles, obtained by calcination of MOF-5 $([Zn_4O(bdc)]_3;$

bdc=1,4-benzenedicarboxylate) in air at 873 K, exhibited a much higher photocatalytic degradation of Rhodamine-B (RhB) under ultraviolet (UV) irradiation than the commercial ST01 TiO_2 catalyst[32]. They attributed the high photocatalytic activity of this MOF-derived ZnO nanoparticles to a lower rate of recombination between the photogenerated holes and electrons on the surface of the ZnO crystals than in the ST01 catalyst. Moreover, Cao *et al*. developed a simple method to prepare metal oxide/3D graphene network (3DGN) composites by the use of ZIF-8 as the precursor of the metal oxide and 3DGN as the backbone. After the preparation of the ZIF-8/3DGN composite, the synthesis consisted in a facile two-step annealing process under Ar at 723 K for 1 h, which conferred the ZIF-8/3DGN material with more textured and rougher surface, followed by calcination in air at 653 K for 1 h to give place to the final ZnO/3DGN material[33]. After irradiation of the dye solution with the 3DGN, ZnO, or ZnO/3DGN for 1 h, almost all of the dye was decomposed by ZnO/3DGN, whereas only about 12 and 80% of the dye was decomposed by the 3DGN and ZnO, respectively. The improved performance of ZnO/3DGN composite in the photodegradation of the dye methylene blue (MB) under irradiation with UV light was ascribed to its high specific surface area and the prevention of the recombination of photoinduced holes and electrons due to a good contact and effective interaction between 3DGN and ZnO.

Along with ZnO, mixed metal oxides of the perovskite family also function as good photocatalysts[34]. Mahata *et al*. prepared a nanosized $GdCoO_3$ perovskite oxide by thermal decomposition of a mixed-metal carboxylate framework precursor, $[Gd(H_2O)_3Co_3][35]$. Photocatalytic studies on the decomposition of organic dyes (Remazol Brilliant Blue R)

and phenol as model pollutants, indicated that the photocatalytic degradation rate obtained for 3 nm $GdCoO_3$ was higher than that obtained for Degussa P-25 by 4.2, and 1.3 times, respectively, for the decomposition of Remazol Brilliant Blue R and phenol, besides leading to less intermediates. Likewise, the application of magnetic particles, such as $CoFe_2O_4$ spinel, which allows the quick recovery of the small particles from the reaction medium, has received considerable attention in recent years for addressing environmental problems. Quin *et al*. reported the synthesis of $CoFe_2O_4$ nanocomposites from Fe-containing MOF (MIL-100-Fe) for phenol oxidation in aqueous solution using peroxymonosulfate as oxidant[36]. They immobilized cobalt nitrate hexahydrate into the pores of MIL-100 by incipient wetness impregnation and calcined it at different temperatures (673-873 K). The resulting magnetic nanoparticles reduced phenol concentration more than 95% after 2 h and the regenerated catalysts exhibited good performance and stability in phenol degradation.

Mn_3O_4 has unique properties for photodegradation reactions owing to its mixed-valence state, but the fabrication of mesoporous crystals has been rarely reported due to the lack of a suitable preparation technique. Not long ago, Peng *et al*. proposed a novel methodology for the formation of large-pore mesoporous Mn_3O_4 *via* the conversion of a Mn-MOF fabricated in ionic liquid (IL)-water mixtures, and applied it for the degradation of MB in wastewater treatment[37]. The hydrophobic IL self-assembled to form aggregates in water that worked as templates for the pore formation of the MOF. After IL and water removal, the mesoporous MOF was calcined at 673 K for 2 h to completely decompose the MOF. In the presence of Mn_3O_4,
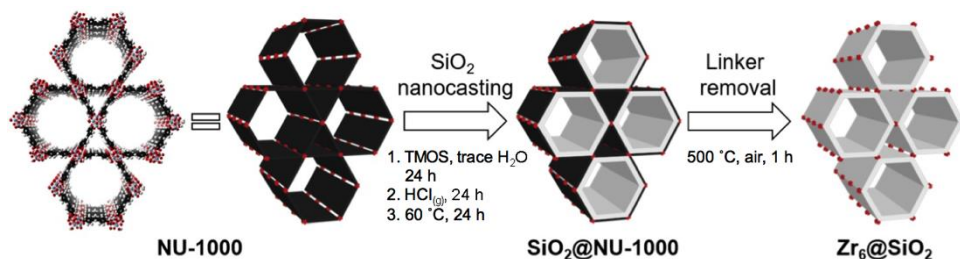
Fig. 1.3. Scheme for the process of stabilizing the oxozirconium clusters in NU-1000 by nanocasting with silica. The left image represents the NU-1000 structure with cluster nodes (*red*) and linkers (*black*). The white layer in the middle image represents silica[39].

more than 99.7% MB degraded after only 1.5 h, while Mn_3O_4 crystals[38], needed 3 h to achieve a MB degradation >99.7% at 353 K.

1.2.2. Lewis acid catalysis

MOF mediated synthesized metal oxides are considered promising as highly stable catalysts for reactions carried out at high temperature. In 2016, Malonzo *et al*. demonstrated the effectiveness of nanocasting for the preparation of highly thermally stable MOF derived single site catalytic clusters for high temperature reactions[39]. They described the nanocasting of NU-1000 (hexanuclear oxozirconium clusters ($[Zr_6(\mu_3\text{-}O)_4(\mu_3\text{-}OH)_4(OH)_4(H_2O)_4]^{8+}$) connected by tetratopic pyrene carboxylate linkers ($TBAPy^{4-}$), with silica. NU-1000 is an excellent Lewis acid catalyst due to the high concentration of the Lewis acidic oxozirconium clusters in its structure, which are easily accessible through its mesoporous channels. By condensing tetramethylorthosilicate within the NU-1000 pores *via* vapor phase HCl treatment, they created silica in the pores of the MOF which was subsequently calcined at 773 K for 1 h yielding the $Zr_6@SiO_2$ composite. The silica layer provided anchoring sites for the oxozirconium clusters in

NU-1000 after the organic linkers were removed at high temperatures while the Lewis acidity was enhanced by dehydration of the clusters during the heat treatment at 773 K[40]. FT-IR spectroscopy of pyridine adsorption showed that $Zr_6@SiO_2$ contains appreciable amounts of Brønsted and Lewis acid sites, and both types of sites remain accessible for pyridine molecules. The catalytic activity of the oxozirconium clusters was tested with the Lewis-acid-catalyzed isomerization of glucose to fructose. Interestingly, the $Zr_6@SiO_2$ composite still showed more than 50% glucose conversion with fructose yield as high as 25% even after it had been heated to 773 K. In contrast, bare NU-1000 heated to the same temperature only had 12% glucose conversion with 6% fructose yield. This showed that site isolation and accessibility of these clusters are necessary to maintain high Lewis acid catalytic activity.

1.2.3. Oxidation of carbon monoxide

Supported metal catalysts, especially for noble metals exhibit good catalytic activities for CO oxidation[41-43]. Investigations have verified that the catalytic activities depend on the size, shape, and chemical nature of supports and the interaction between metals and supports[44]. Liu *et al*. employed MOFs as precursors to prepare Pt-supporting ZnO nanoparticles that exhibited excellent catalytic activities for CO oxidation[45]. Nanocrystalline ZnO-supported platinum nanoparticles were synthesized by introducing inorganic platinum salt into the pores of MOF-5 followed by heating in air at 873 K. This method allowed tuning the platinum nanoparticles size by changing the concentration of platinum precursor. The catalytic activity for CO oxidation of the resultant Pt/ZnO samples is twice as high as a conventional 1 wt.% Pt/ZnO catalyst. Following a similar path,

Bao *et al*. demonstrated a novel 'in-situ self-reduction' route for the fabrication of a nanocomposite consisting of Ag/Co_3O_4 from Prussian blue analogues (PBA) without using any reductant[46]. After calcining the uniform $Ag_3[Co(CN)_6]$ nanocubes at different temperatures in air, porous Ag/Co_3O_4 nanocomposites with abundant well-knit Ag/Co_3O_4 nanojunctions were obtained. The Ag/Co_3O_4 nanocomposite prepared at 473 K, exhibited the smallest particle size of Ag, and displayed the best catalytic activity and excellent stability with a complete CO conversion at 373 K. Frequently, the use of noble metals, which involves higher costs besides limited availability, can be avoided by using copper oxides having similar catalytic performance[47]. Not yet envisioned as a synthesis method, Zamaro *et al*. realized that $Cu_3(BTC)_2(H_2O)_3 \cdot xH_2O$ in CO oxidation was not active by itself, but after 'in-situ' activation in the reaction atmosphere at 513 K for 1.5 h and 573 K for 0.5 h, highly dispersed CuO nanoparticles were produced, which exhibited 50% CO conversion at 448 K[48]. The transformation involved a gradual segregation of CuO nanoparticles from the MOF, simultaneously with a loss of MOF crystallinity. Moreover, the incorporation of a Ce precursor in the network of HKUST-1 with a subsequent activation yielded a highly dispersed mixture of CuO and CeO_2 nanoparticles with a high degree of interaction, which further improved the CO oxidation performance with 50% CO conversion at 384 K. Later, as a proof of concept, Liu *et al*. used the same MOF and TiO_2 whiskers[49] as support to prepare a series of well-dispersed and size-controllable CuO/TiO_2 catalysts derived from the thermolysis of Cu–BTC/TiO_2 composite through calcination in air[50]. The CuO/TiO_2 catalyst with 2.5 wt.% Cu loadings exhibited the best performance among all CuO/TiO_2 catalysts in this work

on the CO oxidation, with a full CO conversion at 448 K, which is 65 K lower than the CuO/TiO_2 catalyst prepared by the conventional deposition precipitation method.

1.2.4. Hydrodesulfurization

Hydrodesulfurization (HDS) is the oil refinery process for removal of sulfur from sulfur-containing organics present in crude oil fractions. The process typically relies on alumina supported heterogeneous catalysts with molybdenum-cobalt or molybdenum-nickel sulfides as active components[51]. Not long ago, Larabi *et al*. reported the application of the well-defined MOF [Ni_2(dhtp)] (H_4dhtp = 2,5-dihydroxyterephthalic acid)[52], as a precursor to bimetallic nickel containing molybdenum sulfide nanoparticles, for HDS reactions[53]. The active material was prepared by subliming $Mo(CO)_6$ on activated [Ni_2(dhtp)], which has the capacity of grafting metal carbonyls on the organic linker. The porous, highly dispersed, bimetallic Ni-Mo material was sulfided for 4 h at 623 K by reaction with H_2S in the presence of 42 bar H_2. The HDS activity of the activated catalyst was measured for the conversion of dibenzothiophene to biphenyl or cyclohexylbenzene at 623 K in the presence of 38 bar H_2. The MOF-derived sulfided material resulted in an active bulk HDS catalyst, stable over several cycles and yielded almost an order of magnitude improvement in the catalytic activity per molybdenum center when compared to the reference unsupported bulk $NiMoO_4$ material. The hydrodenitrogenation (HDN) and hydrogenation activities were also relatively high for this material.

1.2.5. Dehydrogenation of isobutane

Catalytic dehydrogenation of isobutane is an industrially important route for producing isobutene, a vital component for the synthesis of octane number boosters for unleaded gasoline. The supported catalyst Cr_2O_3/Al_2O_3 has been applied on a commercial scale for years in this process[54]. Few years ago, Zhao *et al*. studied the reactivity of isobutane dehydrogenation over a series of non-ordered mesoporous chromia/alumina catalysts promoted with K_2O using MIL-101(Cr) metal-organic-framework as a molecular host and chromium precursor[55]. They impregnated the MIL-101 with aluminium isopropoxide ($Al(i\text{-}OC_3H_7)_3$) and KOH as the aluminium and potassium sources, respectively, and calcined the resulting material in air. The catalyst with 1.5 wt.% K_2O and 10 wt.% Cr_2O_3 loadings calcined at 1073 K was found to have the highest isobutane conversion (60.1%) with the isobutene selectivity up to 93.2% among all the catalysts in this work. More interesting, after ten dehydrogenation-regeneration cycles, the dehydrogenation activity and isobutene selectivity stayed constant, indicative of the high regenerative ability and high stability of the catalyst.

1.3. NANOSTRUCTURED CARBONS

Carbon materials may act as catalysts and catalyst supports. The main hurdle in the case of carbons both as support and as catalyst lies in development of novel methods able to tailor the porosity and morphology of the carbonaceous nanostructures. The intense struggle in the past 20-30 years to control carbon nanostructures has led to the production of various characteristic structures but this field of research is still growing[56, 57].

Recently, metal-organic-frameworks (MOFs) have been demonstrated as interesting precursors to create nanoporous carbon materials, attributed to their unique structure and large carbon contents.

Typically, the procedure for obtaining nanostructured carbons from MOFs implies carbonizing a MOF with metal ions or clusters of relatively low boiling point, such as Zn, at high temperature thus volatilizing the metal phase and leading to well-structured carbon as the final product. Literature reported so far not only addresses their application in electrocatalysis but also aims at the preparation of MOF derived nanostructured carbons as catalyst supports in different types of catalytic processes.

1.3.1. Electrocatalysis

Liu *et al.* employed MOFs as sacrificial templates to synthesize nanoporous carbons (NPCs)[6]. In their work, MOF-5 was heated at 423 K for 48 h under furfuryl alcohol (FA) vapour, so that FA was polymerized in the pores of MOF-5. The carbonization of the PFA/MOF-5 composite was performed at 273 K for 8 h in Ar. Authors found the carbonization temperature to be critical in the structural evolution of the resulting carbon, with its specific surface area increasing from 417 $m^2 \cdot g^{-1}$ at 1073 K to 2870 $m^2 \cdot g^{-1}$ at 1273 K, the macropore/mesopore/micropore volume ratio being 1:15:5 for carbonization at 1273 K. The hydrogen uptake at 1 bar was as high as 2.6 wt.%, which is higher than the H_2 uptake (1.3 wt.%) by MOF-5 under the same condition[58]. The resulting nanoporous carbon displayed a good hydrogen storage capacity as well as excellent electrochemical performance as an electrode material for electrochemical double-layer capacitor due to its well-defined nanostructure. In comparison, carbon materials synthesized using other templates, such as SBA-15[59], show

capacitances much lower than that of NPC from MOF-5 described in their work. With their study, the authors foretold the structural diversity of MOFs would show high potential as templates for synthesizing functional carbon materials.

In order to reduce the cost and encourage wider use, there is a strong research focusing on replacing the expensive Pt-based electrocatalysts in polymer- electrolyte-membrane fuel cells (PEMFC) with a lower-cost alternative. Much of the current research effort is aimed at producing novel catalysts with improved oxygen reduction reaction (ORR) activity[60, 61]. Fe-based cathode catalysts are promising contenders, but their power density has been low compared with Pt-based cathodes, largely due to poor mass-transport properties. Accordingly, Proietti *et al*. used ZIF-8 as a host for Fe and N precursors by means of adding iron acetate and phenantroline to the MOF and mixing them using low-energy ball milling[62]. The mixture was pyrolyzed in Ar at increasing temperatures and optionally in NH_3 at 1223 K, creating highly porous Fe/N/C composites. With an increase in the Ar pyrolysis temperature to 1323 K, Zn could be removed completely to arrive to purely microporous carbons. NH_3 pyrolysis resulted in an additional 17 wt.% loss by hydrogasification, doubling the BET area and introducing substantial mesoporosity besides increasing the nitrogen content in the sample. The introduction of mesopores together with the general increase in the microporous surface area and the nitrogen content resulted in an over four times increased ORR activity compared to the microporous carbon.

Along a similar line, research by Zhang *et al*. showed that the intro-
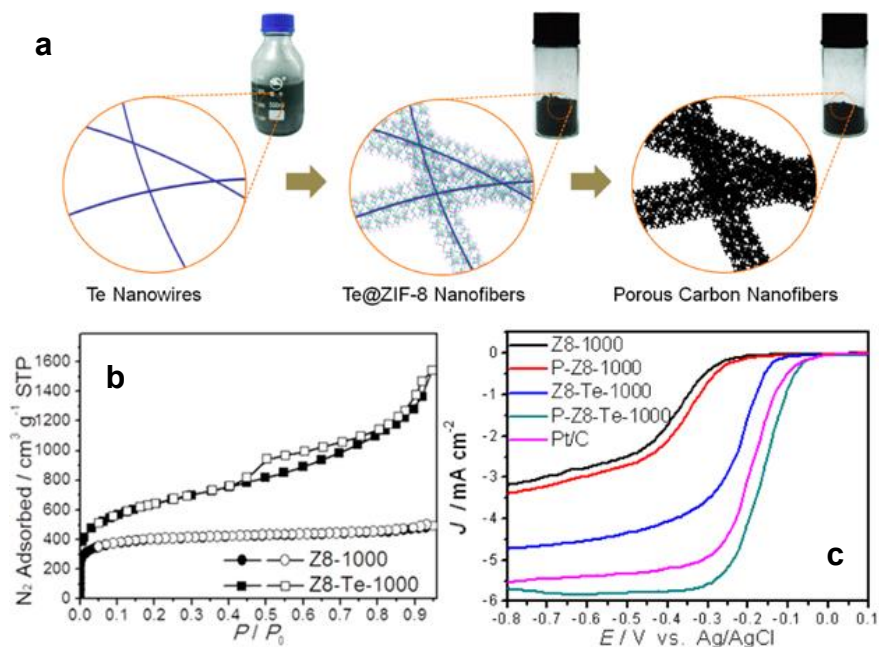
Fig. 1.4. (a) Illustration of the nanowire-directed templating synthesis of ZIF-8 nanofibers and derived porous doped carbon nanofiber; (b) N_2 sorption isotherms (77 K) of Z8-Te-1000 and Z8-1000; (c) Linear sweep voltammetry (LSV) curves of all catalysts in O_2-saturated 0.1 M KOH with a sweep rate of 10 mVs^{-1} and electrode rotation speed of 1600 rpm[63].

duction of ordered mesopores by using Te nanowires (Te-NW) as templating agent dramatically increased performance of cathode ORR [63]. Te-NW was added to the MOF synthesis mixture of ZIF-8, and after crystal growth on the NW surface, the composite was pyrolyzed at high temperatures (1273 K) to vaporize both the Te and the Zn phase. Comparison of the microporous ZIF-8 derived carbon with the Te-NW MOF-templated mesoporous carbon showed large differences in the performance. The ORR activity of the templated carbon was much higher and close to that of the commercial Pt-catalysts. The hollow carbon nanofibers were subsequently phosphorus-doped to create more

ORR active sites. Interestingly, this P-doped catalyst showed a much better catalytic activity than its counterpart without phosphorus dopant, and even outperformed the commercial 20 wt.% Pt/C.Ma *et al*. identified a Co-imidazolate framework $Co(Im)_2$ (Im = imidazolate) described elsewhere[64] as efficient precursor[65]. The sample started to demonstrate ORR activity after heated at 873 K with an onset potential of 0.77 V. An optimal performance was achieved for the sample pyrolyzed at a temperature of 1023 K with an onset potential of 0.83 V, which is comparable to the best cobalt-based non-PGM catalysts[66]. The combined analysis of TEM, XPS and XAFS led the authors to believe that the catalytic sites are constructed by Co-N interactions (Co-N_x) through pyridinic or pyrrolic N species retained in the carbon upon thermal activation, while a higher pyrolysis temperature will destroy these Co-N_x configurations[67]. This model explains the fact why the ORR activity decreases with higher pyrolysis temperatures.

Xia *et al*. obtained similar results in pyrolyzing Co-based ZIF-67 in Ar atmosphere with temperatures ranging from 873-1173 K[68], with the maximum current density of the ORR for the '-1023 K' sample, explained by the maximum of Co-N_x configurations and the optimum in graphitic N atoms witnessed by XPS[67]. In addition, the graphite shells at the surface of cobalt nanoparticles to a large extent protected cobalt from leaching in acidic media. Thus, the electron transfer from the cobalt core to the graphite shells further increased the ORR activity[69]. Interestingly, these MOF-derived samples showed improved stability in acidic media compared to the

Carbon rod

ZIF-9 precursors (Co^{2+} and benzimidazole)

ZIF-9 shell

Core-shell Co@C nanoparticle

Core-bishell Co@Co$_3$O$_4$@C nanoparticle
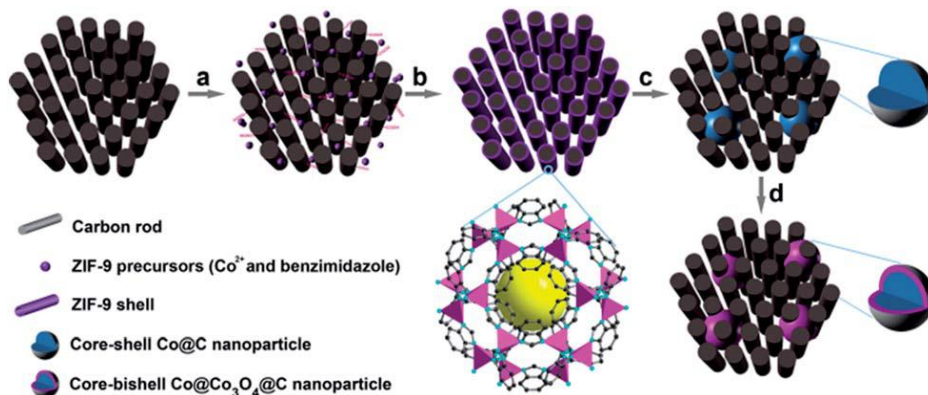
Fig. 1.5. Schematic illustration of the synthesis of the Co@Co$_3$O$_4$@C–CM: (a) functionalization of the CM with carboxylate groups, (b) growth of the MOF on the CM, (c) heat treatment under Ar flow and (d) oxidation in air at 363 K[70].

commercial Pt/C.

The uniform distribution of elements is believed to be an additional advantage that MOFs possess in producing the final highly dispersed systems. Besides the pyrolysis temperature, the effect of MOF crystallite size on the ORR performance was investigated. ZIF-67 nano- and bulk crystallites were produced with sizes ranging from hundreds of nanometers to several hundreds of micrometers. After pyrolysis at 1023 K, the original ZIF-67 crystallite size shrinked, whereas the particle size did not vary much. Interestingly, the catalyst derived from nanocrystallite ZIF-67 exhibited the highest current densities and a dominant four-electron transfer pathway, indicative of a high ORR activity, while the activity decreased with increasing particle size. They attributed this to the fully exposed nano-structure with good mass- and electron-transport properties in the nano-electrocatalyst.

Alternatively, Xia *et al*. proved that MOFs can be coated on highly ordered mesoporous carbon prior to pyrolysis to provide a final catalyst

structure with improved mass and electron transfer characteristics[70]. This procedure comprised the coating of a Co benzimidazole MOF on a CMK-3 mesoporous carbon and subsequently pyrolyzing it at 973 K, followed by partially converting metallic cobalt to Co_3O_4 to form $Co@Co_3O_4@C$-CMK-3 in air at 363 K. The heat treatment resulted in finely dispersed Co agglomerates in the 3D pore structure with sizes around 15-30 nm, without causing pore blockage due to the interconnected carbon matrix. The different heat treatment procedures and additional acid leaching of Co generates a tunable set of ORR catalysts that gives highly relevant insight to the Co core and carbon shell, next to very efficient ORR catalysts in terms of activity and stability.

The oxygen evolution reaction (OER) is also one of the most common and most important anodic processes in electrolysis in various aqueous solutions[71]. Hence to rationally design the reaction interface for OER, an optimal electrode structure involving high-performance catalysts is essential in reducing the overpotential, promoting the reaction kinetics, and enhancing the specific activity for OER, thereby improving the energy efficiency[72]. Substantial research is aimed at increasing electron and mass transfer processes focusing on the structuring of MOF precursors. A lamellar Co MOF was growed by Ma *et al*. on a Cu substrate plate, followed by carbonization at 873 K to prepare Co_3O_4-C porous nanowire arrays (NAs)[73]. Pyrolysis of the layered crystalline MOF structure creates slit-like pores are and the array of ~500 nm thick nanowires provides a large accesible surface area. The anodic current recorded on Co_3O_4-C-NA renders a sharp onset potential

at ~1.47 V with greatly enhanced OER current, indicating that the compositional transformation of the MOF to the Co_3O_4-carbon hybrid can significantly improve the catalytic activity. Noticeably, the OER current of Co_3O_4-C-NA largely exceeds that of a similarly loaded IrO_2/C coated on Cu despite the slightly lower onset potential of IrO_2/C (~1.45 V), featuring a much better catalytic performance of Co_3O_4-C-NA. In terms of durability, the MOF-derived system showed a stable current density of 10.0 mA cm^{-2} at 1.52 V in 0.1 M KOH solution for at least 30 h. Moreover, the carbonized MOF on Cu proved to be a better electrode configuration than calcined MOF on Cu, attributed to both the higher electrical conductivity and a complex synergistic effect between strongly interacting Co_3O_4 and carbon species.

1.3.2. Other catalytic processes

Besides their use in electrocatalysis, nanostructured carbons from MOFs are also advantageous as catalyst supports in different types of catalytic processes. For instance, Feng *et al.* prepared nanoporous carbon materials by carbonization of MOF-5 in N_2 atmosphere at different temperatures, followed by the introduction of silver and palladium precursors by incipient wetness impregnation[74]. Ag_3Pd_{12}/NPCs obtained by pyrolysis at 1173 K exhibited high activity in dehydrogenation of formic acid in sodium formate, with a total turnover frequency (*TOF*$_{total}$, in a yield on theoretical value of 100%) value of 717 h^{-1} at 303 K. The generated gas over the synthesized Ag_3Pd_{12}/NPCs was identified to be H_2 and CO_2 by gas chromatography and no CO can be detected. Authors ascribed the enhanced catalytic performance of

Ag_3Pd_{12}/NPCs to its Pd^0, Ag^0 and AgPd alloy composition as well as to the small particle size and good dispersion of AgPd nanoparticles on the carbon support, thus paving the way to practical application of formic acid as a promising H_2 storage material.

Palladium-catalyzed Suzuki-Miyaura coupling of aryl halides with aryl boronic acids is one of the most powerful methods for constructing biaryl structures[75]. In general, nitrogen dopants can positively modifiy the electron and energy-storage properties of carbon materials. On the other hand, nitrogen atoms in the framework of carbon can also act as anchoring sites to stabilize metals nanoparticles[76]. Therefore, Zhang *et al.* adopted the strategy of pyrolyzing N-containing precursors at high temperature for obtaining N-decorated porous carbons[77]. Nitrogen-doped nanoporous carbon was fabricated by direct carbonization of the nitrogen containing Al-based MOF described elsewhere[78]. They claimed that the presence of aluminum oxide and aluminum in N-doped nanoporous carbon improved the dispersion of the Pd nanoparticles, leading to a high catalytic activity for the Suzuki-Miyaura coupling reaction at room temperature, with biphenyl yield of 97% in 1 h. This is much higher than the commercially available Pd/C catalyst, in which only 78% yield of biphenyl was obtained under the same conditions. Moreover, this catalyst can be recycled and reused in at least 6 consecutive cycles with 10% biphenyl yield loss. Dong *et al.* reported the preparation of magnetic porous carbons (MPCs) as supports for Au and Pd noble metal NPs[79]. They obtained the MPC through carbonization of Fe-MIL-88A, prepared by using $Fe(NO_3)_3$ and fumaric acid as precursors[80], at 973 K under N_2 for 1 h. The reaction rate

constant k was calculated to be 1 x 10^{-2} s^{-1} and 1.2 x 10^{-2} s^{-1} for the reaction catalyzed using Au/MPC[81] and Pd/MPC[82] nanocatalysts, respectively. For a quantitative comparison, the activity parameter $k' = k/C_m$ was introduced, defined as the ratio of the rate constant k to the mass concentration of the active sites (Au or Pd) added. Thus, k' was calculated to be k'_{Au}= 2.54 L s^{-1}g^{-1} and k'_{Pd}= 23.48 L s^{-1} g^{-1} for Au/MPC and Pd/MPC, respectively. The value of activity parameter k' reported for Au NP based catalysts, namely, Au/graphene catalyst, is 0.396 L s^{-1}g^{-1} and the Pd NP based catalyst Pd polypyrrole has an activity parameter k' of about 2.94 L s^{-1}g^{-1}. Accordingly, the smaller k' values in this work indicated that both Au/MPC and Pd/MPC nanocatalysts exhibited an good catalytic activity for the reduction of 4-nitrophenol (4-NP). Moreover, the Pd/MPC catalyst showed a high efficiency toward hydrodechlorination of chlorophenols, with >99% phenol yield obtained in 2 h in water as solvent. In both the synthesized catalysts, the MPC provided a large surface area and mesopores on which the Au and Pd NPs were finely dispersed. The catalysts could be easily recovered from the reaction mixture by using a magnet because of the magnetic NPs encapsulated in the porous carbon, and could be conveniently reused.

1.4. NANOPARTICLES IN CARBON

The major approach to increase the surface/bulk atom ratio in heterogeneous catalysts is by decreasing the size of the metal particles to the nanoscale. However, the smaller the nanoparticle, the more unstable it becomes and higher the danger of aggregation. In order to improve their stability and maintain dispersion, metal nanoparticles are usually stabilized on supports. Inorganic supports, such as SiO_2, Al_2O_3, TiO_2 or zeolites,

however, can easily interact with the metal containing precursors during the catalyst preparation step, and thereby forming irreducible metal-support species. Owing to their chemical inertness, carbon materials are widely used as alternative supports to prevent the formation of these complex compounds[17]. However, the weak interaction between the supported metal and the carbon may increase the agglomeration sensitivity of metal nanoparticles, adverse affecting the catalytic performance. Carbonizing the MOF in an inert atmosphere often leads to a highly dispersed metal phase encapsulated in a porous carbon matrix[7]. This spatial restriction created by encapsulation minimizes the sintering of the metal nanoparticles.

As in the case of nanostructured carbons, the conventional strategy to obtain nanoparticles@carbon (NP@C) from the parental MOF consists of carbonizing the MOF in an inert atmosphere at high temperature. However, contrary to the approach for carbons, in this case the pyrolysis temperature must be lower than the boiling point of the metal in the framework. As a result, during the pyrolysis, a part of the organic ligand decomposes and evaporates to the gas phase, whereas the other part becomes carbonized in the framework. Below, examples of the transformation of MOF to NP@C by different authors are summarized, together with their application mainly in hydrogenation and oxidation reactions.

1.4.1. Catalytic reduction of nitroaromatics

Aromatic nitro compounds, especially nitrophenols, are one of the major pollutants present in industrial and agricultural waste water[83]. An important way to eliminate these compounds is to carry out their catalytic reduction giving place to aminoaromatics[84]. Usually this process takes place on precious metal NPs due to their high catalytic

efficiency. Nevertheless, their scarcity and thus, high-cost of noble metal resources make them unattractive for practical application, thus calling for the development of alternative, economically viable and highly active and selective non precious metal catalysts.

Mesoporous carbon nitrides (m-CN) have pendant amino groups[85] intrinsically present on their mesoporous walls, which can serve as nucleation centers for the grafting of metal NPs, thereby leading to m-CN-material-based catalysts containing well-dispersed catalytically active sites[86]. Very recently, Zuo *et al*. reported the preparation of a N-doped mesoporous carbon supported Ni nanoparticle catalyst (Ni/m-CN) *via* the carbonization of Ni-MOF [Ni(HBTC)(4,4'-bipyridine)] at 973 K[87]. When the resulting Ni/m-CN catalyst was tested in the catalytic reduction of 4-nitrophenol with $NaBH_4$, the reaction rapidly proceeded with the conversion of 4-nitrophenol exceeding 99% at a reaction time of approximately 10 min. Moreover, the catalytic performance was preserved without any loss of efficiency after six cycles, highlighting its excellent activity and stability upon reuse. Besides, this catalyst can be easily recovered due to its superparamagnetism. Compared to other catalysts in literature, the activity of the Ni/m-CN catalyst was approximately the same as that of Ag-doped carbon spheres and $Fe_3O_4@SiO_2$-Ag catalysts[88, 89] and considerably higher than other Ni and Co based catalysts[90, 91].

Following a similar path, Niu *et al*. synthesized a hybrid catalyst for the catalytic reduction of 4-nitrophenol consisting of non-noble Cu/Cu_2O NPs supported on porous carbon using HKUST-1 as sacrificial template[92]. After thoroughly mixing the HKUST-1 with a phenol

formaldehyde resin as an additional carbon source, the resulting solid product was carbonized under N_2 atmosphere at 873 K for 4 h. The $Cu/Cu_2O/C$ composite demonstrated excellent catalytic activity for the reduction of 4-nitrophenol in the presence of $NaBH_4$, comparable with other noble metal or copper based catalysts, such as SiO_2/Fe_3O_4-C/Au[93], Au-Ag/GO[94], and Au/CuO[95]. Moreover, the synthesized catalyst could be reused for at least five cycles due to its good stability. Authors claimed that Cu/Cu_2O NPs were responsible for the rapid reduction of 4-nitrophenol while the carbon matrix could prevent aggregation of Cu/Cu_2O NPs providing high surface-to-volume ratio and chemical stability.

In 2016, Li *et al*. implemented the MOFMS in the hydrogenation of nitro compounds by developing a highly efficient, low-cost, and magnetically recoverable γ-Fe_2O_3@porous carbon catalyst[96]. In their study, Fe-MIL-88A samples were thermally treated at different temperatures and times in N_2 to obtain Fe-based NPs encapsulated inside porous carbon. The reduction of nitrobenzene to aniline in the presence of hydrazine hydrate ($N_2H_4 \cdot H_2O$) was first used to explore the catalytic activity of different catalysts. As a result, the catalyst pyrolyzed at 773 K for 1 h gave the best activity and could be readily recovered with an external magnet and reused at least 10 times without any loss of activity. They concluded that at this temperature the small γ-Fe_2O_3 NPs were uniformly dispersed throughout the porous carbon, which effectively limited the aggregation of the γ-Fe_2O_3 NPs and still facilitated the transportation of substrates, intermediates and products. Remarkably, this nanocomposite also was an efficient and stable catalyst for the

hydrogenation of a variety of substituted aromatic or aliphatic nitro compounds into their corresponding amines.

Before them, Shen *et al*. already proposed a facile and efficient approach to fabricate Co@Pd core-shell catalysts (Co@Pd/CN) by using ZIF-67 and Pd(NO$_3$)$_2$ as a sacrificial template and Pd source, respectively[97]. First, the ZIF-67 was pyrolyzed at 873 K under Ar for 8 h. The obtained Co NPs were coated with an ultrathin Pd shell *via* a galvanic replacement reaction using an aqueous Pd(NO$_3$)$_2$ solution. The highly exposed Pd atoms on Co nanoparticles resulted in a highly active, extremely stable catalyst for nitrobenzene hydrogenation. The Co@Pd/CN showed extremely high activity with a 98% conversion of nitrobenzene within only 45 min of reaction at room temperature, thus opening a new avenue for MOFs-templated non-noble@noble metal core-shell catalysts that could by far surpass the traditional MOFs supporting noble NPs in catalytic properties.

1.4.2. Catalytic hydrogenation reactions

1.4.2.1. Catalytic hydrogenation reactions with H2

Fischer-Tropsch Synthesis (FTS) is a process for flexible production of key chemicals and clean fuels from synthesis gas, the main reaction being the hydrogenation of CO. Recently, MOFs have been used as a precursor to produce high-potential Fe catalysts for the FTS reaction[7]. Interestingly, researchers have employed the commercially available Fe-BTC MOF as precursor in the MOFMS. Heat treatment of Fe-BTC at 773 K in an inert atmosphere resulted in the formation of a Fe@C composite that showed exceptional activity and stability in FTS. The key

factors in the catalytic performance are the high iron loading and maintaining the dispersion of the active phase during reaction. The pyrolysis of the MOF at low heating rates gently carbonized the framework while capturing the Fe in a carbonaceous matrix formed by the linker decomposition, and thereby prevent the agglomeration of iron nanoparticles and produce highly dispersed Fe@C systems. The conversion of the Fe-BTC towards Fe@C was investigated by *in-situ* XAFS and Mössbauer and revealed many intermediate Fe phases [8]. Starting from the Fe(III) oxo-clusters, the pyrolysis formed mixtures of Fe carbides and a Wüstite phase. After reduction of the catalyst, the Wüstite was fully converted to α-Fe and thus, upon syngas exposure creates highly active Hägg carbides. The authors claim the system is stable because of the unique spatial confinement, witnessed with XPS and TEM. The addition of a carbon source allowed for further tuning the porosity and Fe loading of the materials. Moreover, it showed a clear effect on the catalyst performance, increasing the carbon content decreases the rate of carburization during the induction period but increased its activity at steady state conversion. Hence, the spatial confinement created by the porous carbon shell prevents the metal NPs from sintering.

In 2016, Chen *et al*. provided a novel concept for the MOF mediated synthesis by hybridization of clay minerals with metal-organic-frameworks as efficient catalysts for benzene hydrogenation[98]. They grew a ruthenium MOF [$Ru_2^{II,III}(BTC)_2X_xY_{1.5-x}$] (X, Y = Cl^- or OH^-) on montmorillonite (Mt) *via* a solvothermal reaction, fabricating a composite material (Ru-MOF_Mt). In order to obtain stable Ru NCs, the
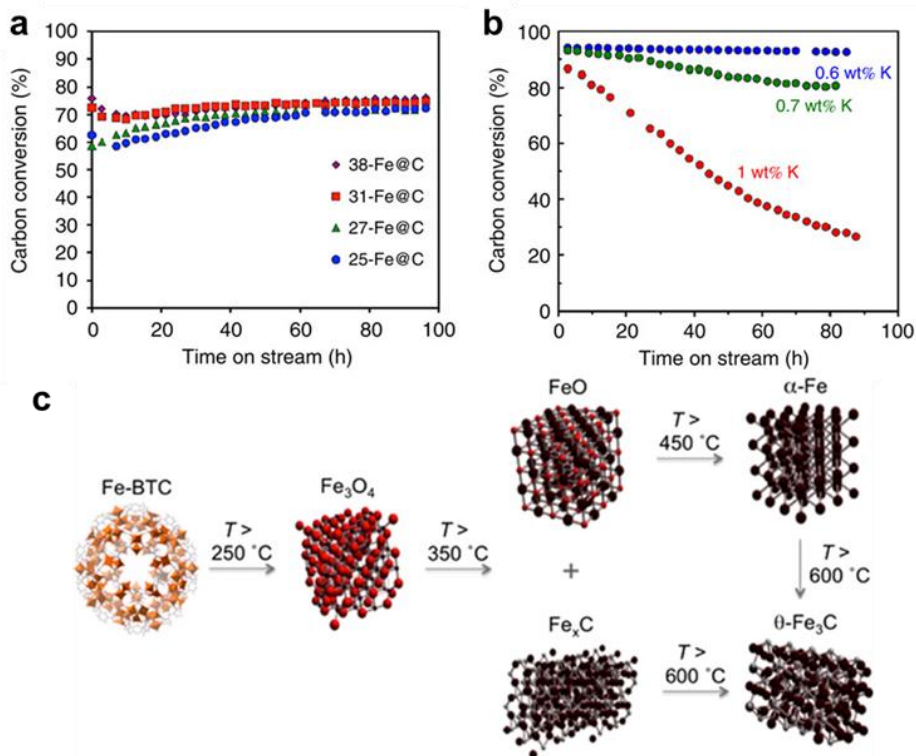
Fig. 1.6. (a) Time-on-stream evolution of CO conversion for the unpromoted Fe@C catalysts with different Fe loadings; (b) Time-on-stream evolution of CO conversion for K-promoted 38-Fe@C catalysts. (c) Fe phase transformation during pyrolysis of Fe-BTC towards Fe@C[7, 8].

prepared hybrids were annealed in H_2 at 573 K, thus partially decomposing the frameworks and producing Ru particles that act as active centers for hydrogenation. In the catalytic tests, benzene was proven to be completely converted into cyclohexane within 2.5 h at 433 K and a H_2 pressure of 60 bar. The turnover frequency (*TOF*) for benzene reached 3478 h^{-1} which is higher than the data reported for Ru/C or other heterogeneous catalysts[99, 100]. Moreover, the Ru-MOF_Mt catalyst was reused 5 times and no obvious deactivation was

detected, which demonstrated the good stability of the Ru particles protected by both the partly decomposed BTC oligomers and the clay layers.

1.4.2.2. Catalytic transfer hydrogenation reactions

Likewise, transition metal-catalyzed transfer hydrogenation protocols are convenient and an alternative method to traditional energy-consuming hydrogenation processes, besides being able to provide high atom efficiency and generating advantageous economics[101, 102]. The use of hydrogen donor reagents such as alcohols in transfer hydrogenation reactions can avoid the use of autoclaves and high-pressure hydrogen, being highly relevant for industrial applications. Not long ago, Long *et al*. hinted at the transfer hydrogenation of unsaturated bonds in the absence of base additives catalyzed by a MOF derived cobalt heterogeneous catalysts[103]. They selected [Co(bdc)(ted)$_{0.5}$] MOF as a template due to the presence of triethylenediamine basic sites which could be favorable for transfer hydrogenation reactions. In the transfer hydrogenation of acetophenone to phenethanol as a model process using isopropanol as both reductant and solvent, the Co@CN materials prepared under longer thermolysis time (15 h) and higher temperatures (1173 K) exhibited higher acetophenone conversion (99%) and phenethanol selectivity of 95%, thus the final selected catalyst was obtained by pyrolysis in argon of the Co MOF at 1123 K for 15 h. Multiple advantages of the proposed catalytic system included a remarkable versatility not only for C=O hydrogenation but also for C=C, C≡N, and N=O bonds, an environmental-benign protocol and the use of a magnetically separable non-noble metal catalyst in a simple and safe

reaction setup. Both mechanisms proposed in literature for the transfer hydrogenation with base additives suggest that the presence of bases facilitates the formation of metal hydrides in the transition metal[104]. As demonstrated in this study by Long *et al*., basic sites were present in as-synthesized Co@CN materials. Therefore, they speculated that the basic sites on Co@CN play a similar role to that of base additives to facilitate the transfer of protons to Co nanoparticles to form Co metal hydride species, thus promoting the production of the desired hydrogenation products. Authors concluded that the combination of high efficiency, versatility and recyclability as well as mild reaction conditions in the absence of bases and gaseous hydrogen makes this system an attractive alternative pathway for various hydrogenation processes.

1.4.3. Oxidation reactions

The direct oxidation of alcohols to esters with molecular oxygen is an attractive and crucial process for the synthesis of fine chemicals. The heterogeneous catalyst used so far are based on noble metals or required the addition of base additives. Therefore, the development of reusable non-noble metal based catalysts for the oxidative direct esterification of alcohols under mild conditions is an attractive and challenging subject in both green chemistry and organic synthesis. To this purpose, Zhong *et al*. developed a simple, cost effective, and environmentally friendly protocol for direct aerobic oxidative esterification of alcohols, using a novel nitrogen doped graphite enclosed cobalt material from a zeolite-type MOF as catalyst[105]. The conversion of ZIF-67 (Co(MeIM)$_2$,

MeIM = 2-methylimidazole) into Co@CN was performed by direct thermal treatment under a flow of argon at 1073 K for 8 h. The strong coordination interaction between Co and N atoms in the parent MOF would allow a stepwise collapse of the MOF structure during slow-heating procedures to prevent a serious aggregation of Co. The MeIM linkers were carbonized gradually and the resulting carbon-nitrogen composite played an important role in isolating the Co nanoparticles, which were surrounded tightly by graphitized carbon. The catalytic system featured a broad substrate scope for aromatic and aliphatic alcohols as well as diols, giving their corresponding esters in good to excellent yields at room temperature and atmospheric conditions without the assistance of any base additives. Moreover, the catalyst was easily recovered due to its magnetic properties and the reactivity could be fully restored for up to five runs when the reused catalyst was treated in H_2 at 673 K for 1 h, to abate the partial oxidization of metallic cobalt during the course of the reaction by oxygen in air. The authors verified that the proposed protocol for ester synthesis from the oxidation of alcohols was scalable under the investigated conditions. In like manner, Zhou *et al*. recently reported a similar route to generate surface-oxidized Co NPs uniformly incorporated in N-doped porous carbon by one-step pyrolysis of ZIF-67, as a hard template[21]. The pyrolysis was carried out at different temperatures and times under N_2 and the MOF pyrolized at 973 K for 3 h showed the best properties. Thus, the resultant Co-CoO@N-doped porous carbon nanocomposite as noble-metal free, stable and magnetically recyclable catalyst exhibited excellent catalytic performance for direct homo- and cross-coupling esterifications of

primary alcohols under mild conditions, at 1 bar of O_2 as an environmentally friendly oxidant. The special structure of the nanocomposite and the synergistic effect between metallic Co core and a thin layer of CoO shell at the surface were proposed to be responsible for the superior activity over other related catalysts. In addition, the N-doped porous carbon scaffold not only stabilized the NPs but also greatly facilitated the accessibility and adsorption of substrates to the active sites and the diffusion of products.

It is well known that the low-temperature oxidation of CO has drawn tremendous interest due to its wide applications such as in air cleaning, lowering automotive emission, and detecting trace amounts of CO. Falling back on ZIF-67 mediated synthesis, Wang *et al*. recently disclosed the preparation of an efficient metallic Co-based catalyst for low-temperature CO oxidation, where the Co was embedded in porous carbon[106]. ZIF-67 was pyrolyzed at 873 K for 10 h in argon atmosphere and the obtained Co@CN-873 catalyst was used for CO oxidation under dry conditions (0.1 vol.% CO, 20% vol.% O_2, and He balanced with a space velocity of 7.5 L h^{-1} g cat^{-1}), 100% CO conversion could be obtained at 273 K. The apparent activation energy of CO oxidation over the Co@CN-873 catalyst was comparable to those of the Co_3O_4[107], Pd[108] and Au[109] catalysts and when comparing the activity of Co@CN-873 to other Co supported catalysts it was found that the light off temperature decreased by 78 K for Co@CN-873. The catalytic activity over the Co@CN-873 catalyst remained unchanged after 24 h time on stream at room temperature, thus indicating the Co@CN-873 was stable over this period. Furthermore, catalytic stability

tests under wet gas conditions demonstrated that the catalyst showed improved moisture tolerance as compared to other Co-based materials.

The ability to transport electrons has been identified as a key property of the resultant catalyst to remove organic contaminants in wastewater. Therefore, besides their use in electrocatalysis, Andrew *et al*. have also adopted the MOFMS, and combined the MOF with graphene oxide (GO), in order to enhance electron transport and use GO as a co-catalyst to activate the peroxymonosulfate (PMS)[110]. Through Co leaching experiments it was confirmed that the main process of PMS activation is heterogenous on the Co_2O_3@GO material. The carbonization temperature showed insignificant effect on the oxidation performance. Facile catalyst recovery without regeneration showed that 97.6% of the initial activity was preserved even after 50 cycles. In another work, the same authors identified Fe-based MOFMS systems as promising heterogeneous catalysts in liquid phase reactions because of their ease of separation[111]. The magnetic nature of the carbonized Fe-MOF allows for facile recovery of the dispersed catalyst in the liquid phase that creates a highly regenerative system. Researchers carbonized MIL-88A nanorods and found that the resulting Fe@C exhibited superparamagnetic characteristics with insignificant hysteresis and low coercivity of around 50 Oe. The mixture of ferric and ferrous phases can activate oxidants like peroxide and persulfate through a Fenton-like reaction, that in turn causes decoloration of dyes in water. After magnetic recovery of the catalyst, direct use without regeneration in subsequent decolorization experiments showed virtually no loss of activity after 4 cycles.

1.5. PERSPECTIVE

Apart from their direct use in catalysis[112], metal organic frameworks (MOFs) have emerged as ideal hard templates and precursors for the synthesis of highly dispersed, catalytically active materials. As highlighted by the examples above, when obtained through the MOF mediated synthesis (MOFMS), metal oxides, carbons and nanoparticles encapsulated in carbon have unique structural properties that result in improved catalytic performance.

The type of MOF and the conditions employed in the MOFMS play an essential role in determining the size, morphology and, therefore, catalytic activity of the resulting material. From basic to advanced catalytic design, the MOFMS embraces a wide range of synthetic techniques. In this process, besides the general synthesis parameters widely applied during the conventional catalyst preparation, including the activation atmosphere, and heat treatment conditions such as temperature, time and heating rate, which can be used during the MOFMS process, the uniform metal distribution in the original MOF allows for an exquisite control in the final size of supported or encapsulated nanoparticles. Moreover, further development and modification of the technique has led to sophisticated catalytic systems through 'nanoengineering' at the molecular level giving place to well defined catalysts. This approach does not only lead to improved catalytic systems but is an excellent tool for the design of model systems that help generating knowledge through understanding.

One last point that seems to raise some concern regarding the MOFMS approach is the fact that highly engineered, beautiful, very

often expensive, materials are simply destroyed, and this may look like something unaffordable from an industrial-ecomomical point of view. This may indeed be somehow controversial, but one should keep first a certain level of pragmatism in mind, the main target of catalyst synthesis is the design and preparation of outstanding catalysts and the MOFMS is an excellent tool to this end. Indeed, some of the state of the art catalysts are synthesized through similar protocols using naturally abundant minerals, commercial MeOH synthesis catalysts (formed through controlled decomposition of hydroxycarbonate minerals such as zincian malachite, aurichalcite or rosasite)[113] are an outstanding example. On the other hand, one should also consider that a large part of the final price of a MOF comes from the solvent used during the synthesis and washing steps needed to purify the as synthesized materials. Obviously, the nature and depth of these steps required for MOFMS may be far milder and this should moderate the price of the hard template. For instance, by simply mixing copper acetate salt and a bridging organic ligand, isonicotinic acid, grinding together wholly in the absence of solvent, followed by thermal treatment at 473 K for 3 h, multi-dimensional microporous Cu-BTC was successfully synthesized[114]. Moreover, if the stability of the resulting catalysts is increased by orders of magnitude, the impact in terms of catalyst makeup and less process operation interruptions has the potential of bringing additional economic attractiveness.

Overall, we are certain that over the next few years this approach will be adopted by more research groups and that new methodologies will be developed. For instance the addition of further components to the

MOF synthesis, i.e. by impregnation and/or the use of more sophisticated atmospheres during activation will lead to a whole new family of catalysts with unprecedented performance. At this stage we can just say that our imagination is the only limit when it comes to design possibilities in MOF mediated synthesis.

1.6. OUTLINE OF THE THESIS

This thesis consists of three main parts. Part I (**Chapter 1**) gives an introduction to the developments and progress made in the application of MOF-mediated synthesized materials in catalysis in recent years. MOFs have become promising precursors for the synthesis of nanomaterials and exhibit interesting catalytic performances in various reactions because of their unique structure, atomic metal dispersion and textural properties.

In the following parts of this thesis, a cobalt-contaning zeolitic imidazolate framework (Co-ZIF) has been chosen as a template to further extend the investigation of MOF-mediated synthesized catalysts for multiphase hydrogenation reactions.

Part II (**Chapter 2 and 3**) focuses on the selective hydrogenation of nitroarenes. A cobalt-containing ZIF (Co-ZIF) is used as a sacrificial template to prepare a cobalt@N-doped carbon hybrid (Co@NC) under N_2 atmosphere. **Chapter 2** investigates the pyrolysis temperature effect on the structure and cobalt composition in Co@NC prepared by one-step pyrolysis of ZIF-67, the different cobalt species formed and their role in the catalysis. Three types of cobalt species, comprising partially and fully encapsulated cobalt nanoparticles by graphitic shells, and highly

dispersed cobalt species in strong interaction with nitrogen-doped graphene (Co-N$_x$), are formed during pyrolysis, whereas only those accessible cobalt nanoparticles and the highly dispersed Co-N$_x$ catalyze the hydrogenation reaction. After removing those accessible cobalt nanoparticles by acid leaching, a further increase in hydrogenation activity is observed, indicating that the highly dispersed Co-N$_x$ species have a much larger activity contribution in this reaction.

In **Chapter 3**, we extend this study to preferably generate those Co-N$_x$ sites by employing a bimetallic ZIF (Co/Zn-ZIF) as the precursor. The catalyst synthesis consists of hydrolysis of tetramethyl orthosilicate (TMOS) in the pores of a BIMZIF(Co,Zn), high-temperature pyrolysis under N$_2$ atmosphere, and silica etching. Theoretically, a high Zn/Co ratio in the parent BIMZIF is proved essential to extend the spatial interval between two Co atoms in the framework, which to a large extent, prevents the agglomeration of cobalt atoms to nanoparticles. Besides, during the pyrolysis step, the evaporation of zinc at high temperature (900 ^{o}C) generates free N sites, that are capable of stabilizing Co single atoms as well. Interstingly, in this work, SiO$_2$ in the porosity of BIMZIF seems crucial to further mitigate the sintering of cobalt atoms, and thereby favorable for the formation of stable single cobalt atoms in the carbon matrix. The SiO$_2$-templated stratergy at the same time largely increases the specfic surface area and creates mesoporosity in the N-doped carbon matrix. Importantly, the presence of mesoporosity in the carbon support significantly improve the hydrogenation activity and stability of these Co-N$_x$ acitve sites compared to its microporous counterpart prepared by direct pyrolysis of BIMZIF.

Part III (**Chapter 4 and 5**) focuses on the Fischer-Tropsch Synthesis (FTS).

In **Chapter 4**, a cobalt-ZIF (ZIF-67) impregnated with trimethyl orthosilicate (TMOS) is used as raw material to synthesize highly loaded Co@SiO$_2$ catalyst (~50 wt.%), together with high cobalt reducibility and good dispersion. A pyrolysis step prior to calcination is essential to narrow the cobalt particle size distribution and to avoid the formation of irreducible cobalt silicate species. This MOF-mediated Co@SiO$_2$ catalyst shows a cobalt-time-yield (*CTY*) almost twice as high as the conventional Co/SiO$_2$ catalyst, together with an excellent stability and high C5+ selectivity under low-temperature FTS conditions.

Chapter 5 switches the focus from MOF to zeolite-supported cobalt catalyst and investigates the effect of pretreatment atmosphere on the structure and activity of Co/*meso*ZSM-5 catalysts in FTS process. It reveals that the pretreatment atmosphere affects the cobalt particle size distribution and cobalt reducibility, which directly influence the FTS performance (*i.e.* activity and product selectivity). The catalyst prepared under air condition displays a much broader cobalt particle size distribution compared to the catalysts prepared under N$_2$ and NO atmospheres. The '-NO' sample shows the lowest cobalt reducibility in comparison with the other catalysts, *albeit* with the highest cobalt dispersion, because of the strongest Co-support interaction. The inferior cobalt reducibility and small cobalt particle size in the '-NO' catalyst leads to the worst FTS activity and highest methane selectivity.

Overall, this PhD Thesis highlights the potential of new synthetic protocols for the preparation of metal nanoparticle based heterogeneous

catalysts. More specifically, the so called MOF mediated synthesis (MOFMS) is shown to address long standing issues in the preparation of this class of catalysts: namely the production of highly loaded samples with almost full control over particle size and speciation, in combination with a stable catalytic performance.

The chapters in the thesis are written as independent papers and that some introductory overlap may exist.

REFERENCES

[1] B.F. Hoskins, R. Robson, Design and construction of a new class of scaffolding-like materials comprising infinite polymeric frameworks of 3D-linked molecular rods. A reappraisal of the zinc cyanide and cadmium cyanide structures and the synthesis and structure of the diamond-related frameworks [N(CH3)4] [CuIZnII(CN)$_4$] and CuI[4,4',4'',4'''-tetracyanotetraphenylmethane] BF$_4$.xC$_6$H$_5$NO$_2$, Journal of the American Chemical Society, 112 (1990) 1546-1554.

[2] O.M. Yaghi, H. Li, Hydrothermal Synthesis of a Metal-Organic Framework Containing Large Rectangular Channels, Journal of the American Chemical Society, 117 (1995) 10401-10402.

[3] M.S. Denny, J.C. Moreton, L. Benz, S.M. Cohen, Metal–organic frameworks for membrane-based separations, Nature Reviews Materials, 1 (2016) 16078.

[4] H. Furukawa, K.E. Cordova, M. O'Keeffe, O.M. Yaghi, The Chemistry and Applications of Metal-Organic Frameworks, Science, 341 (2013).

[5] P. Horcajada, R. Gref, T. Baati, P.K. Allan, G. Maurin, P. Couvreur, G. Férey, R.E. Morris, C. Serre, Metal–Organic Frameworks in Biomedicine, Chemical Reviews, 112 (2012) 1232-1268.

[6] B. Liu, H. Shioyama, T. Akita, Q. Xu, Metal-Organic Framework as a Template for Porous Carbon Synthesis, Journal of the American Chemical Society, 130 (2008) 5390-5391.

[7] V.P. Santos, T.A. Wezendonk, J.J.D. Jaén, A.I. Dugulan, M.A. Nasalevich, H.-U. Islam, A. Chojecki, S. Sartipi, X. Sun, A.A. Hakeem, A.C.J. Koeken, M. Ruitenbeek, T. Davidian, G.R. Meima, G. Sankar, F. Kapteijn, M. Makkee, J. Gascon, Metal organic framework-mediated synthesis of highly active and stable Fischer-Tropsch catalysts, Nature Communications, 6 (2015) 6451.

[8] T.A. Wezendonk, V.P. Santos, M.A. Nasalevich, Q.S.E. Warringa, A.I. Dugulan, A. Chojecki, A.C.J. Koeken, M. Ruitenbeek, G. Meima, H.-U. Islam, G. Sankar, M. Makkee, F. Kapteijn, J. Gascon, Elucidating the Nature of Fe Species during Pyrolysis of the Fe-BTC MOF into Highly Active and Stable Fischer–Tropsch Catalysts, ACS Catalysis, 6 (2016) 3236-3247.

[9] A. Corma, P. Serna, Chemoselective Hydrogenation of Nitro Compounds with Supported Gold Catalysts, Science, 313 (2006) 332-334.

[10] F.A. Westerhaus, R.V. Jagadeesh, G. Wienhöfer, M.-M. Pohl, J. Radnik, A.-E. Surkus, J. Rabeah, K. Junge, H. Junge, M. Nielsen, A. Brückner, M. Beller, Heterogenized cobalt oxide catalysts for nitroarene reduction by pyrolysis of molecularly defined complexes, Nat Chem, 5 (2013) 537-543.

[11] H.M. Torres Galvis, J.H. Bitter, C.B. Khare, M. Ruitenbeek, A.I. Dugulan, K.P. de Jong, Supported Iron Nanoparticles as Catalysts for Sustainable Production of Lower Olefins, Science, 335 (2012) 835-838.

[12] F. L'Eplattenier, P. Matthys, F. Calderazzo, Homogeneous ruthenium-catalyzed reduction of nitrobenzene, Inorganic Chemistry, 9 (1970) 342-345.

[13] A. Corma, C. González-Arellano, M. Iglesias, F. Sánchez, Gold complexes as catalysts: Chemoselective hydrogenation of nitroarenes, Applied Catalysis A: General, 356 (2009) 99-102.

[14] H.-U. Blaser, H. Steiner, M. Studer, Selective Catalytic Hydrogenation of Functionalized Nitroarenes: An Update, ChemCatChem, 1 (2009) 210-221.

[15] K. Junge, K. Schroder, M. Beller, Homogeneous catalysis using iron complexes: recent developments in selective reductions, Chemical Communications, 47 (2011) 4849-4859.

[16] D. Schanke, S. Vada, E.A. Blekkan, A.M. Hilmen, A. Hoff, A. Holmen, Study of Pt-Promoted Cobalt CO Hydrogenation Catalysts, Journal of Catalysis, 156 (1995) 85-95.

[17] G.L. Bezemer, J.H. Bitter, H.P.C.E. Kuipers, H. Oosterbeek, J.E. Holewijn, X. Xu, F. Kapteijn, A.J. van Dillen, K.P. de Jong, Cobalt Particle Size Effects in the Fischer−Tropsch Reaction Studied with Carbon Nanofiber Supported Catalysts, Journal of the American Chemical Society, 128 (2006) 3956-3964.

[18] A. Corma, P. Serna, P. Concepción, J.J. Calvino, Transforming Nonselective into Chemoselective Metal Catalysts for the Hydrogenation of Substituted Nitroaromatics, Journal of the American Chemical Society, 130 (2008) 8748-8753.

[19] I. Puskas, T.H. Fleisch, J.B. Hall, B.L. Meyers, R.T. Roginski, Metal-support interactions in precipitated, magnesium-promoted cobaltsilica catalysts, Journal of Catalysis, 134 (1992) 615-628.

[20] S. Sartipi, K. Parashar, M.J. Valero-Romero, V.P. Santos, B. van der Linden, M. Makkee, F. Kapteijn, J. Gascon, Hierarchical H-ZSM-5-supported cobalt for the direct synthesis of gasoline-range hydrocarbons from syngas: Advantages, limitations, and mechanistic insight, Journal of Catalysis, 305 (2013) 179-190.

[21] Y.-X. Zhou, Y.-Z. Chen, L. Cao, J. Lu, H.-L. Jiang, Conversion of a metal-organic framework to N-doped porous carbon incorporating Co and CoO nanoparticles: direct oxidation of alcohols to esters, Chemical Communications, 51 (2015) 8292-8295.

[22] D. Farrusseng, S. Aguado, C. Pinel, Metal-organic frameworks: opportunities for catalysis, Angewandte Chemie (International ed. in English), 48 (2009) 7502-7513.

[23] A. Corma, H. García, F.X. Llabrés i Xamena, Engineering Metal Organic Frameworks for Heterogeneous Catalysis, Chemical Reviews, 110 (2010) 4606-4655.

[24] J. Lee, O.K. Farha, J. Roberts, K.A. Scheidt, S.T. Nguyen, J.T. Hupp, Metal-organic framework materials as catalysts, Chemical Society Reviews, 38 (2009) 1450-1459.

[25] B. Li, K. Leng, Y. Zhang, J.J. Dynes, J. Wang, Y. Hu, D. Ma, Z. Shi, L. Zhu, D. Zhang, Y. Sun, M. Chrzanowski, S. Ma, Metal–Organic Framework Based upon the Synergy of a Brønsted Acid Framework and Lewis Acid Centers as a Highly Efficient Heterogeneous Catalyst for Fixed-Bed Reactions, Journal of the American Chemical Society, 137 (2015) 4243-4248.

[26] F.X. Llabres i Xamena, J. Gascon, CHAPTER 14 Towards Future MOF Catalytic Applications, in: Metal Organic Frameworks as Heterogeneous Catalysts, The Royal Society of Chemistry, 2013, pp. 406-424.

[27] K.E. deKrafft, C. Wang, W. Lin, Metal-Organic Framework Templated Synthesis of Fe2O3/TiO2 Nanocomposite for Hydrogen Production, Advanced Materials, 24 (2012) 2014-2018.

[28] S.-w. Lee, J. Drwiega, C.-Y. Wu, D. Mazyck, W.M. Sigmund, Anatase TiO2 Nanoparticle Coating on Barium Ferrite Using Titanium Bis-Ammonium Lactato Dihydroxide and Its Use as a Magnetic Photocatalyst, Chemistry of Materials, 16 (2004) 1160-1164.

[29] X. Kang, H. Liu, M. Hou, X. Sun, H. Han, T. Jiang, Z. Zhang, B. Han, Synthesis of Supported Ultrafine Non-noble Subnanometer-Scale Metal Particles Derived from Metal–Organic Frameworks as Highly Efficient Heterogeneous Catalysts, Angewandte Chemie, 128 (2016) 1092-1096.

[30] I. Mondal, U. Pal, Synthesis of MOF templated Cu/CuO@TiO2 nanocomposites for synergistic hydrogen production, Physical Chemistry Chemical Physics, 18 (2016) 4780-4788.

[31] C.-C. Wang, J.-R. Li, X.-L. Lv, Y.-Q. Zhang, G. Guo, Photocatalytic organic pollutants degradation in metal-organic frameworks, Energy & Environmental Science, 7 (2014) 2831-2867.

[32] S.J. Yang, J.H. Im, T. Kim, K. Lee, C.R. Park, MOF-derived ZnO and ZnO@C composites with high photocatalytic activity and adsorption capacity, Journal of Hazardous Materials, 186 (2011) 376-382.

[33] X. Cao, B. Zheng, X. Rui, W. Shi, Q. Yan, H. Zhang, Metal Oxide-Coated Three-Dimensional Graphene Prepared by the Use of Metal–Organic Frameworks as Precursors, Angewandte Chemie International Edition, 53 (2014) 1404-1409.

[34] X. Niu, H. Li, G. Liu, Preparation, characterization and photocatalytic properties of REFeO3 (RE = Sm, Eu, Gd), Journal of Molecular Catalysis A: Chemical, 232 (2005) 89-93.

[35] P. Mahata, T. Aarthi, G. Madras, S. Natarajan, Photocatalytic Degradation of Dyes and Organics with Nanosized GdCoO3, The Journal of Physical Chemistry C, 111 (2007) 1665-1674.

[36] F.-X. Qin, S.-Y. Jia, Y. Liu, X. Han, H.-T. Ren, W.-W. Zhang, J.-W. Hou, S.-H. Wu, Metal-organic framework as a template for synthesis of magnetic CoFe2O4 nanocomposites for phenol degradation, Materials Letters, 101 (2013) 93-95.

[37] L. Peng, J. Zhang, Z. Xue, B. Han, J. Li, G. Yang, Large-pore mesoporous Mn3O4 crystals derived from metal-organic frameworks, Chemical Communications, 49 (2013) 11695-11697.

[38] P. Zhang, Y. Zhan, B. Cai, C. Hao, J. Wang, C. Liu, Z. Meng, Z. Yin, Q. Chen, Shape-controlled synthesis of Mn3O4 nanocrystals and their catalysis of the degradation of methylene blue, Nano Research, 3 (2010) 235-243.

[39] C.D. Malonzo, S.M. Shaker, L. Ren, S.D. Prinslow, A.E. Platero-Prats, L.C. Gallington, J. Borycz, A.B. Thompson, T.C. Wang, O.K. Farha, J.T. Hupp, C.C. Lu, K.W. Chapman, J.C. Myers, R.L. Penn, L. Gagliardi, M. Tsapatsis, A. Stein, Thermal Stabilization of Metal–Organic Framework-Derived Single-Site Catalytic Clusters Through Nanocasting, Journal of the American Chemical Society, (2016).

[40] J.E. Mondloch, M.J. Katz, W.C. Isley Iii, P. Ghosh, P. Liao, W. Bury, G.W. Wagner, M.G. Hall, J.B. DeCoste, G.W. Peterson, R.Q. Snurr, C.J. Cramer, J.T. Hupp, O.K. Farha, Destruction of chemical warfare agents using metal–organic frameworks, Nat Mater, 14 (2015) 512-516.

[41] A. Fukuoka, J.-i. Kimura, T. Oshio, Y. Sakamoto, M. Ichikawa, Preferential Oxidation of Carbon Monoxide Catalyzed by Platinum Nanoparticles in Mesoporous Silica, Journal of the American Chemical Society, 129 (2007) 10120-10125.

[42] M. Haruta, Catalysis: Gold rush, Nature, 437 (2005) 1098-1099.

[43] O. Pozdnyakova, D. Teschner, A. Wootsch, J. Kröhnert, B. Steinhauer, H. Sauer, L. Toth, F.C. Jentoft, A. Knop-Gericke, Z. Paál, R. Schlögl, Preferential CO

oxidation in hydrogen (PROX) on ceria-supported catalysts, part I: Oxidation state and surface species on Pt/CeO2 under reaction conditions, Journal of Catalysis, 237 (2006) 1-16.

[44] J. Chen, J. Li, H. Li, X. Huang, W. Shen, Facile synthesis of Ag−OMS-2 nanorods and their catalytic applications in CO oxidation, Microporous and Mesoporous Materials, 116 (2008) 586-592.

[45] B. Liu, S. Han, K. Tanaka, H. Shioyama, Q. Xu, Metal–Organic Framework (MOF) as a Precursor for Synthesis of Platinum Supporting Zinc Oxide Nanoparticles, Bulletin of the Chemical Society of Japan, 82 (2009) 1052-1054.

[46] S. Bao, N. Yan, X. Shi, R. Li, Q. Chen, High and stable catalytic activity of porous Ag/Co3O4 nanocomposites derived from MOFs for CO oxidation, Applied Catalysis A: General, 487 (2014) 189-194.

[47] A. Razeghi, A. Khodadadi, H. Ziaei-Azad, Y. Mortazavi, Activity enhancement of Cu-doped ceria by reductive regeneration of CuO−CeO2 catalyst for preferential oxidation of CO in H2-rich streams, Chemical Engineering Journal, 164 (2010) 214-220.

[48] J.M. Zamaro, N.C. Pérez, E.E. Miró, C. Casado, B. Seoane, C. Téllez, J. Coronas, HKUST-1 MOF: A matrix to synthesize CuO and CuO−CeO2 nanoparticle catalysts for CO oxidation, Chemical Engineering Journal, 195−196 (2012) 180-187.

[49] S. Qian, C. Wang, W. Liu, Y. Zhu, W. Yao, X. Lu, An enhanced CdS/TiO2 photocatalyst with high stability and activity: Effect of mesoporous substrate and bifunctional linking molecule, Journal of Materials Chemistry, 21 (2011) 4945-4952.

[50] H. Liu, S. Zhang, Y. Liu, Z. Yang, X. Feng, X. Lu, F. Huo, Well-Dispersed and Size-Controlled Supported Metal Oxide Nanoparticles Derived from MOF Composites and Further Application in Catalysis, Small, 11 (2015) 3130-3134.

[51] H. Topsøe, B.S. Clausen, F.E. Massoth, Hydrotreating Catalysis, in: J.R. Anderson, M. Boudart (Eds.) Catalysis: Science and Technology, Springer Berlin Heidelberg, Berlin, Heidelberg, 1996, pp. 1-269.

[52] P.D.C. Dietzel, B. Panella, M. Hirscher, R. Blom, H. Fjellvag, Hydrogen adsorption in a nickel based coordination polymer with open metal sites in the cylindrical cavities of the desolvated framework, Chemical Communications, (2006) 959-961.

[53] C. Larabi, P.K. Nielsen, S. Helveg, C. Thieuleux, F.B. Johansson, M. Brorson, E.A. Quadrelli, Bulk Hydrodesulfurization Catalyst Obtained by Mo(CO)6 Grafting on the Metal−Organic Framework Ni2(2,5-dihydroxoterephthalate), ACS Catalysis, 2 (2012) 695-700.

[54] G. Wang, C. Li, H. Shan, Highly Efficient Metal Sulfide Catalysts for Selective Dehydrogenation of Isobutane to Isobutene, ACS Catalysis, 4 (2014) 1139-1143.

[55] H. Zhao, H. Song, L. Xu, L. Chou, Isobutane dehydrogenation over the mesoporous Cr2O3/Al2O3 catalysts synthesized from a metal-organic framework MIL-101, Applied Catalysis A: General, 456 (2013) 188-196.

[56] W. Xia, A. Mahmood, R. Zou, Q. Xu, Metal-organic frameworks and their derived nanostructures for electrochemical energy storage and conversion, Energy & Environmental Science, 8 (2015) 1837-1866.

[57] W. Feng, M. Qin, Y. Feng, Toward highly thermally conductive all-carbon composites: Structure control, Carbon, 109 (2016) 575-597.

[58] B. Panella, M. Hirscher, Hydrogen Physisorption in Metal–Organic Porous Crystals, Advanced Materials, 17 (2005) 538-541.

[59] D.-w. Wang, F. Li, M. Liu, H.-m. Cheng, Improved capacitance of SBA-15 templated mesoporous carbons after modification with nitric acid oxidation, New Carbon Materials, 22 (2007) 307-314.

[60] H.A. Gasteiger, N.M. Marković, Just a Dream—or Future Reality?, Science, 324 (2009) 48-49.

[61] P. Strasser, S. Koh, T. Anniyev, J. Greeley, K. More, C. Yu, Z. Liu, S. Kaya, D. Nordlund, H. Ogasawara, M.F. Toney, A. Nilsson, Lattice-strain control of the activity in dealloyed core–shell fuel cell catalysts, Nat Chem, 2 (2010) 454-460.

[62] E. Proietti, F. Jaouen, M. Lefèvre, N. Larouche, J. Tian, J. Herranz, J.-P. Dodelet, Iron-based cathode catalyst with enhanced power density in polymer electrolyte membrane fuel cells, Nat Commun, 2 (2011) 416.

[63] W. Zhang, Z.-Y. Wu, H.-L. Jiang, S.-H. Yu, Nanowire-Directed Templating Synthesis of Metal–Organic Framework Nanofibers and Their Derived Porous Doped Carbon Nanofibers for Enhanced Electrocatalysis, Journal of the American Chemical Society, 136 (2014) 14385-14388.

[64] Y.-Q. Tian, Z.-X. Chen, L.-H. Weng, H.-B. Guo, S. Gao, D.Y. Zhao, Two Polymorphs of Cobalt(II) Imidazolate Polymers Synthesized Solvothermally by Using One Organic Template N,N-Dimethylacetamide, Inorganic Chemistry, 43 (2004) 4631-4635.

[65] S. Ma, G.A. Goenaga, A.V. Call, D.-J. Liu, Cobalt Imidazolate Framework as Precursor for Oxygen Reduction Reaction Electrocatalysts, Chemistry – A European Journal, 17 (2011) 2063-2067.

[66] F. Jaouen, J. Herranz, M. Lefèvre, J.-P. Dodelet, U.I. Kramm, I. Herrmann, P. Bogdanoff, J. Maruyama, T. Nagaoka, A. Garsuch, J.R. Dahn, T. Olson, S. Pylypenko, P. Atanassov, E.A. Ustinov, Cross-Laboratory Experimental Study of Non-Noble-Metal Electrocatalysts for the Oxygen Reduction Reaction, ACS Applied Materials & Interfaces, 1 (2009) 1623-1639.

[67] J.R. Pels, F. Kapteijn, J.A. Moulijn, Q. Zhu, K.M. Thomas, Evolution of nitrogen functionalities in carbonaceous materials during pyrolysis, Carbon, 33 (1995) 1641-1653.

[68] W. Xia, J. Zhu, W. Guo, L. An, D. Xia, R. Zou, Well-defined carbon polyhedrons prepared from nano metal-organic frameworks for oxygen reduction, Journal of Materials Chemistry A, 2 (2014) 11606-11613.

[69] J. Deng, P. Ren, D. Deng, X. Bao, Enhanced Electron Penetration through an Ultrathin Graphene Layer for Highly Efficient Catalysis of the Hydrogen Evolution Reaction, Angewandte Chemie International Edition, 54 (2015) 2100-2104.

[70] W. Xia, R. Zou, L. An, D. Xia, S. Guo, A metal-organic framework route to in situ encapsulation of $Co@Co_3O_4@C$ core@bishell nanoparticles into a highly ordered porous carbon matrix for oxygen reduction, Energy & Environmental Science, 8 (2015) 568-576.

[71] Y. Matsumoto, E. Sato, Electrocatalytic properties of transition metal oxides for oxygen evolution reaction, Materials Chemistry and Physics, 14 (1986) 397-426.

[72] S.H. Oh, R. Black, E. Pomerantseva, J.-H. Lee, L.F. Nazar, Synthesis of a metallic mesoporous pyrochlore as a catalyst for lithium–O2 batteries, Nat Chem, 4 (2012) 1004-1010.

[73] T.Y. Ma, S. Dai, M. Jaroniec, S.Z. Qiao, Metal–Organic Framework Derived Hybrid Co3O4-Carbon Porous Nanowire Arrays as Reversible Oxygen Evolution Electrodes, Journal of the American Chemical Society, 136 (2014) 13925-13931.

[74] C. Feng, Y. Wang, S. Gao, N. Shang, C. Wang, Hydrogen generation at ambient conditions: AgPd bimetal supported on metal–organic framework derived porous carbon as an efficient synergistic catalyst, Catalysis Communications, 78 (2016) 17-21.

[75] S.S. Shendage, A.S. Singh, J.M. Nagarkar, Facile approach to the electrochemical synthesis of palladium-reduced graphene oxide and its application for Suzuki coupling reaction, Tetrahedron Letters, 55 (2014) 857-860.

[76] H.-L. Jiang, B. Liu, Y.-Q. Lan, K. Kuratani, T. Akita, H. Shioyama, F. Zong, Q. Xu, From Metal–Organic Framework to Nanoporous Carbon: Toward a Very High Surface Area and Hydrogen Uptake, Journal of the American Chemical Society, 133 (2011) 11854-11857.

[77] L. Zhang, C. Feng, S. Gao, Z. Wang, C. Wang, Palladium nanoparticle supported on metal–organic framework derived N-decorated nanoporous carbon as an efficient catalyst for the Suzuki coupling reaction, Catalysis Communications, 61 (2015) 21-25.

[78] T. Ahnfeldt, N. Guillou, D. Gunzelmann, I. Margiolaki, T. Loiseau, G. Férey, J. Senker, N. Stock, [Al4(OH)2(OCH3)4(H2N-bdc)3]· x H2O: A 12-Connected Porous Metal–Organic Framework with an Unprecedented Aluminum-Containing Brick, Angewandte Chemie International Edition, 48 (2009) 5163-5166.

[79] Z. Dong, X. Le, Y. Liu, C. Dong, J. Ma, Metal organic framework derived magnetic porous carbon composite supported gold and palladium nanoparticles as highly efficient and recyclable catalysts for reduction of 4-nitrophenol and hydrodechlorination of 4-chlorophenol, Journal of Materials Chemistry A, 2 (2014) 18775-18785.

[80] C. Serre, F. Millange, S. Surblé, G. Férey, A Route to the Synthesis of Trivalent Transition-Metal Porous Carboxylates with Trimeric Secondary Building Units, Angewandte Chemie International Edition, 43 (2004) 6285-6289.

[81] J. Li, C.-y. Liu, Y. Liu, Au/graphene hydrogel: synthesis, characterization and its use for catalytic reduction of 4-nitrophenol, Journal of Materials Chemistry, 22 (2012) 8426-8430.

[82] Y. Xue, X. Lu, X. Bian, J. Lei, C. Wang, Facile synthesis of highly dispersed palladium/polypyrrole nanocapsules for catalytic reduction of p-nitrophenol, Journal of Colloid and Interface Science, 379 (2012) 89-93.

[83] I. Ibrahim, I.O. Ali, T.M. Salama, A.A. Bahgat, M.M. Mohamed, Synthesis of magnetically recyclable spinel ferrite (MFe2O4, M = Zn, Co, Mn) nanocrystals engineered by sol gel-hydrothermal technology: High catalytic performances for nitroarenes reduction, Applied Catalysis B: Environmental, 181 (2016) 389-402.

[84] Y. Du, H. Chen, R. Chen, N. Xu, Synthesis of p-aminophenol from p-nitrophenol over nano-sized nickel catalysts, Applied Catalysis A: General, 277 (2004) 259-264.

[85] A. Thomas, A. Fischer, F. Goettmann, M. Antonietti, J.-O. Muller, R. Schlogl, J.M. Carlsson, Graphitic carbon nitride materials: variation of structure and morphology and their use as metal-free catalysts, Journal of Materials Chemistry, 18 (2008) 4893-4908.

[86] Z. Dong, C. Dong, Y. Liu, X. Le, Z. Jin, J. Ma, Hydrodechlorination and further hydrogenation of 4-chlorophenol to cyclohexanone in water over Pd nanoparticles modified N-doped mesoporous carbon microspheres, Chemical Engineering Journal, 270 (2015) 215-222.

[87] W. Zuo, G. Yu, Z. Dong, A MOF-derived nickel based N-doped mesoporous carbon catalyst with high catalytic activity for the reduction of nitroarenes, RSC Advances, 6 (2016) 11749-11753.

[88] S. Tang, S. Vongehr, X. Meng, Carbon Spheres with Controllable Silver Nanoparticle Doping, The Journal of Physical Chemistry C, 114 (2010) 977-982.

[89] Y. Chi, Q. Yuan, Y. Li, J. Tu, L. Zhao, N. Li, X. Li, Synthesis of Fe3O4@SiO2–Ag magnetic nanocomposite based on small-sized and highly dispersed silver nanoparticles for catalytic reduction of 4-nitrophenol, Journal of Colloid and Interface Science, 383 (2012) 96-102.

[90] N. Sahiner, H. Ozay, O. Ozay, N. Aktas, New catalytic route: Hydrogels as templates and reactors for in situ Ni nanoparticle synthesis and usage in the reduction of 2- and 4-nitrophenols, Applied Catalysis A: General, 385 (2010) 201-207.

[91] N. Sahiner, H. Ozay, O. Ozay, N. Aktas, A soft hydrogel reactor for cobalt nanoparticle preparation and use in the reduction of nitrophenols, Applied Catalysis B: Environmental, 101 (2010) 137-143.

[92] H. Niu, S. Liu, Y. Cai, F. Wu, X. Zhao, MOF derived porous carbon supported Cu/Cu2O composite as high performance non-noble catalyst, Microporous and Mesoporous Materials, 219 (2016) 48-53.

[93] T. Zeng, X. Zhang, S. Wang, Y. Ma, H. Niu, Y. Cai, A double-shelled yolk-like structure as an ideal magnetic support of tiny gold nanoparticles for nitrophenol reduction, Journal of Materials Chemistry A, 1 (2013) 11641-11647.

[94] T. Wu, L. Zhang, J. Gao, Y. Liu, C. Gao, J. Yan, Fabrication of graphene oxide decorated with Au-Ag alloy nanoparticles and its superior catalytic performance for the reduction of 4-nitrophenol, Journal of Materials Chemistry A, 1 (2013) 7384-7390.

[95] S. Gao, X. Jia, Z. Li, Y. Chen, Hierarchical plasmonic-metal/semiconductor micro/nanostructures: green synthesis and application in catalytic reduction of p-nitrophenol, Journal of Nanoparticle Research, 14 (2012) 1-11.

[96] Y. Li, Y.-X. Zhou, X. Ma, H.-L. Jiang, A metal-organic framework-templated synthesis of [gamma]-Fe2O3 nanoparticles encapsulated in porous carbon for efficient and chemoselective hydrogenation of nitro compounds, Chemical Communications, 52 (2016) 4199-4202.

[97] K. Shen, L. Chen, J. Long, W. Zhong, Y. Li, MOFs-Templated Co@Pd Core–Shell NPs Embedded in N-Doped Carbon Matrix with Superior Hydrogenation Activities, ACS Catalysis, 5 (2015) 5264-5271.

[98] D. Chen, M. Huang, S. He, S. He, L. Ding, Q. Wang, S. Yu, S. Miao, Ru-MOF enwrapped by montmorillonite for catalyzing benzene hydrogenation, Applied Clay Science, 119, Part 1 (2016) 109-115.

[99] S. Miao, Z. Liu, B. Han, J. Huang, Z. Sun, J. Zhang, T. Jiang, Ru Nanoparticles Immobilized on Montmorillonite by Ionic Liquids: A Highly Efficient Heterogeneous Catalyst for the Hydrogenation of Benzene, Angewandte Chemie International Edition, 45 (2006) 266-269.

[100] D. Banerjee, R.V. Jagadeesh, K. Junge, M.-M. Pohl, J. Radnik, A. Brückner, M. Beller, Convenient and Mild Epoxidation of Alkenes Using Heterogeneous Cobalt Oxide Catalysts, Angewandte Chemie International Edition, 53 (2014) 4359-4363.

[101] S. Enthaler, D. Addis, K. Junge, G. Erre, M. Beller, A General and Environmentally Benign Catalytic Reduction of Nitriles to Primary Amines, Chemistry – A European Journal, 14 (2008) 9491-9494.

[102] D. Pingen, C. Müller, D. Vogt, Direct Amination of Secondary Alcohols Using Ammonia, Angewandte Chemie International Edition, 49 (2010) 8130-8133.

[103] J. Long, Y. Zhou, Y. Li, Transfer hydrogenation of unsaturated bonds in the absence of base additives catalyzed by a cobalt-based heterogeneous catalyst, Chemical Communications, 51 (2015) 2331-2334.

[104] Z.-R. Dong, Y.-Y. Li, J.-S. Chen, B.-Z. Li, Y. Xing, J.-X. Gao, Highly Efficient Iridium Catalyst for Asymmetric Transfer Hydrogenation of Aromatic Ketones under Base-Free Conditions, Organic Letters, 7 (2005) 1043-1045.

[105] W. Zhong, H. Liu, C. Bai, S. Liao, Y. Li, Base-Free Oxidation of Alcohols to Esters at Room Temperature and Atmospheric Conditions using Nanoscale Co-Based Catalysts, ACS Catalysis, 5 (2015) 1850-1856.

[106] X. Wang, W. Zhong, Y. Li, Nanoscale Co-based catalysts for low-temperature CO oxidation, Catalysis Science & Technology, 5 (2015) 1014-1020.

[107] X. Xie, Y. Li, Z.-Q. Liu, M. Haruta, W. Shen, Low-temperature oxidation of CO catalysed by Co3O4 nanorods, Nature, 458 (2009) 746-749.

[108] I. Stará, V. Nehasil, V. Matolín, The influence of particle size on CO oxidation on Pdalumina model catalyst, Surface Science, 331–333, Part A (1995) 173-177.

[109] M. Haruta, S. Tsubota, T. Kobayashi, H. Kageyama, M.J. Genet, B. Delmon, Low-Temperature Oxidation of CO over Gold Supported on TiO2, α-Fe2O3, and Co3O4, Journal of Catalysis, 144 (1993) 175-192.

[110] K.-Y. Andrew Lin, F.-K. Hsu, W.-D. Lee, Magnetic cobalt-graphene nanocomposite derived from self-assembly of MOFs with graphene oxide as an activator for peroxymonosulfate, Journal of Materials Chemistry A, 3 (2015) 9480-9490.

[111] K.-Y. Andrew Lin, F.-K. Hsu, Magnetic iron/carbon nanorods derived from a metal organic framework as an efficient heterogeneous catalyst for the chemical oxidation process in water, RSC Advances, 5 (2015) 50790-50800.

[112] J. Gascon, A. Corma, F. Kapteijn, F.X. Llabrés i Xamena, Metal Organic Framework Catalysis: Quo vadis?, ACS Catalysis, 4 (2014) 361-378.

[113] S.A. Kondrat, P.J. Smith, P.P. Wells, P.A. Chater, J.H. Carter, D.J. Morgan, E.M. Fiordaliso, J.B. Wagner, T.E. Davies, L. Lu, J.K. Bartley, S.H. Taylor, M.S. Spencer, C.J. Kiely, G.J. Kelly, C.W. Park, M.J. Rosseinsky, G.J. Hutchings, Stable amorphous georgeite as a precursor to a high-activity catalyst, Nature, advance online publication (2016).

[114] D. MATOGA, New MOF-type layered coordination polymers of manganese, method of their preparation, modification and use thereof, in, Google Patents, 2015.

Metal organic framework mediated Co/N-doped carbon hybrids as efficient and chemoselective catalysts for the hydrogenation of nitroarenes

2

Abstract: A Co@N-doped carbon (Co@NC) hybrid was synthesised *via* thermal decomposition of the metal organic framework (MOF) ZIF-67 under N_2 atmosphere. These hybrid materials exhibit outstanding catalytic activity and chemoselectivity for the hydrogenation of a wide range of substituted nitroarenes to their corresponding anilines under relatively mild reaction conditions. The high catalytic performance is attributed to the formation of cobalt nanoparticles and to the presence of atomically dispersed Co species in close interaction with nitrogen doped graphene. Both active species are formed *in situ* during the pyrolytic transformation of ZIF-67. The catalysts could be reused in consecutive runs, exhibiting a slightly lower activity ascribed to blockage of the active sites by strongly adsorbed reaction species. These results open up a pathway for the design of noble metal-free solid catalysts for industrial applications.

2.1. INTRODUCTION

Anilines and, in particular their functionalised derivatives, are key organic intermediates for manufacturing dyes, pharmaceuticals, pigments, and agrochemicals obtained *via* reduction of their corresponding nitroarenes.[1-3] Conventional Béchamp (using Fe/HCl) or sulfide reduction (with H_2S or NaSH as reducing agents) processes are widely applied to produce functionalised anilines in industry.[4] However, these non-catalytic processes generate large amounts of undesirable waste, resulting in severe environmental problems. Because of these reasons, the direct catalytic hydrogenation of nitroarenes has been extensively studied over the last few years.[5-7]

In this spirit, a large number of molecular catalysts have been developed.[8-11] However, these homogeneous catalysts suffer from difficulties in recycling and separation from products. Therefore, heterogeneous catalysts consisting of supported metal nanoparticles (NPs) are more attractive. Supported Pt catalysts have been proposed as alternative and are used in the direct hydrogenation of nitroarenes.[12-14] However, despite very efficient for the activation of nitro groups, Pt is also an excellent catalyst for the reduction of carbonyl groups and double bonds, which usually leads to unselective hydrogenations.[15, 16] An alternative to improve the chemoselectivity of supported Pt catalysts is to introduce additives, such as PdO or H_3PO_2, *albeit* in most cases at the expense of activity.[15-17] Lack of selective hydrogenation is not the only associated problem. Side products such as phenylhydroxylamine derivatives, one type of byproduct formed with Pt-PbO or Pt-H_3PO_2 catalysts during the hydrogenation process, can be explosive even at low concentrations.[15]

Recently, Corma *et al.* investigated this reaction using gold instead of platinum. This less active hydrogenation metal surprisingly exhibited high activity and chemoselectivity to the corresponding substituted anilines.[6, 18, 19] Along with the use of Au, recent efforts have led to the development of cheaper first-row transition metal-based hydrogenation catalysts (*e.g.* Fe, Co and Ni).[1, 20-22] However, most of these supported noble metal-free catalysts are not yet ideal because of lack of stability, activity and in some cases reusability. Major problems are aggregation, metal leaching and/or metal surface modification under reaction conditions.[20-24]

Different strategies have been proposed to improve the stability of metal nanoparticles, including coating with organic molecules, polymers or oxides.[25-29] For instance, cobalt NPs were reported to be protected against agglomeration and air oxidation by capping with organic ligands. In general, these coatings possess poor electron conductivity and can effectively block charge transfer between catalytic site and reagents, thereby negatively influencing the catalytic activity. In contrast, graphite-like carbon coatings with unique chemical, electrical, and functional properties are capable of protecting transition metal (*e.g.* Co, Fe) NPs from agglomeration and re-oxidation by air,[30-32] while preserving high activities in a variety of catalytic reactions.[30-34] Recently, the group of Beller developed a novel heterogeneous catalyst in which cobalt nanoparticles are embedded in a N-doped carbon matrix *via* direct carbonization of non-volatile Co-amine coordination complexes.[5] This cobalt/N-doped carbon hybrid shows outstanding activity in the hydrogenation of different nitroarenes along with chemoselectivity to their substituted anilines. Although cobalt is claimed to play a crucial role, the reasons behind such high activity still remain elusive, largely because of the complexity of the system. Cheng *et al.* suggested that

those exposed cobalt nanoparticles do not play any role in the hydrogenation activity, and proposed that the real active sites are highly dispersed Co-N$_x$ species located at the carbon matrix.[35] However, Liu *et al.* indicated no detectable hydrogenation activity after acid leaching in a Co@C catalyst, and concluded that the hydrogenation activity is to be attributed to those accessible metallic cobalt NPs.[36] Similarly, Wang *et al.* neither detected any hydrogenation activity after leaching Co with aqua regia from a Co@NC catalyst using ZIF-67 as template.[37] On the other hand, along the already mentioned issues in the identification of the active sites in Co-based catalysts, recycling is also confronted with great challenges. Indeed, most of these cobalt-based catalysts deactivate in a couple of runs. Chen *et al.* observed the gradual oxidation of cobalt in Co@C during the hydrogenation process.[38] However, Wei and Liu both claimed that oxidized cobalt can be *in situ* reduced to its metallic phase by H$_2$ under hydrogenation conditions.[20, 36]

In order to further contribute to this discussion, we prepared N-doped Co@NC composites *via* one-step pyrolysis of ZIF-67 in a N$_2$ atmosphere along with an in-depth investigation on the nature of the active sites and the reasons behind deactivation during the hydrogenation of different nitroarenes. We demonstrate that the pyrolysis temperature and heterogeneity of the metal species play a major role in the challenging hydrogenation of nitroarenes over Co based catalysts.

2.2. EXPERIMENTAL

2.2.1. Materials

2-Methylimidazole (MeIm, purity 99%), cobalt nitrate hexahydrate ($Co(NO_3)_2 \cdot 6H_2O$, >99%), zinc nitrate hexahydrate ($Zn(NO_3)_2 \cdot 6H_2O$, 98%), hydrochloric acid (37%), and methanol (>99.8%) were purchased from Sigma-Aldrich Chemical Co. All chemicals were used without further purification.

2.2.2 Catalyst synthesis

ZIF-67 precursors were synthesized according to a previous report with some modification.[39] Typically, 2.933 g $Co(NO_3)_2 \cdot 6H_2O$ and 6.489 g MeIm were separately dissolved in 200 mL methanol. The clear linker solution was rapidly poured into the metal solution under magnetic stirring and kept at room temperature for 24 h. Afterwards, the bright purple product was collected by filtration, washed 3 times with methanol, and dried at 353 K under vacuum. For the synthesis of ZIF-8, having the same structure, all the steps are the same except substituting $Co(NO_3)_2 \cdot 6H_2O$ with $Zn(NO_3)_2 \cdot 6H_2O$. The Co@NC catalysts were prepared independently but in an almost similar manner as recently reported by Wang and Li.[37] Typically, carbonization of 1 g ZIF-67 was performed in a ceramic crucible inside a quartz tubular reactor (approx. L = 1.0 m x ID = 5.0 cm) horizontally situated in a ceramic fiber oven (Carbolite, Sheffield). The reactor was flushed with nitrogen (150 ml min^{-1}) at 303 K for 0.5 h, followed by further carbonization at different temperatures for 8 h under N_2 (150 ml min^{-1}) at a ramp of 2 K min^{-1}. Before exposure to ambient conditions, these catalysts were passivated for 2 h at room temperature in a

stream of 5 vol% O_2 in N_2 and denoted herein as Co@NC-*T* (*T* = 873, 973, 1073, 1173 K), where *T* refers as the pyrolysis temperature. 0.5 g of the ground Co@NC-*T* samples were further immersed in 200 mL 0.5 M hydrochloric acid solution for 24 h at ambient temperature to dissolve the exposed cobalt nanoparticles. The leaching process was repeated 3 additional times, followed by washing with deionized water until the pH reached ~7. After drying at 323 K for 24 h under vacuum, these samples are defined as Co@NC-*T(al)* (*T* = 873, 973, 1073, 1173 K). For the preparation of NC sample, 1 g ZIF-8 was pyrolyzed at 1073 K followed by a complete acid leaching step with 0.5 M HCl solution, using the same procedures as Co@NC-*1073(al)* sample.

2.2.3. Characterization

The amount of Co and N in the samples was measured by atomic adsorption spectroscopy (AAS) (AAnalyst 200, Perkin Elmer, USA) and elemental analysis (Vario EL, Elementar, Germany), respectively.

The Brunauer-Emmett-Teller (BET) areas and porosity parameters of the samples were determined using a Micromeritics Tristar 3020 apparatus after degassing under vacuum overnight at 423 K in Micromeritics Vacprep 061 apparatus[40].

Thermogravimetric (TG) analysis was carried out using a Mettler Toledo TGA/SDTA851e instrument. The experiments were performed from room temperature to 1073 K with a heating rate of 5 K min^{-1} under continuous flow of N_2 or air (100 ml min^{-1}).

Raman spectra were obtained with a commercial Renishaw inVia reflex confocal microscope using a 532 nm laser. Measurements were carried out in samples without any pre-treatment and exposed to normal conditions of

air and humidity at room temperature. Spectra analysis was carried with WIRE4.1 software after subtracting the baseline.

X-ray diffraction (XRD) patterns were recorded in Bragg-Brentano geometry in Bruker D8 Advance X-ray diffractometer equipped with a Vantec position sensitive detector and graphite monochromator. Measurements were performed at room temperature with monochromatic Co $K\alpha$ radiation ($\lambda = 0.179026$ nm) in the 2θ range (10°-90°).

Transmission electron microscopy (TEM) and high resolution TEM (HR-TEM) images were obtained by using a Talos F200X microscope (FEI, Hillsboro, OR, USA) at 200 kV.

XPS measurements were performed on a *K*-alpha Thermo Fisher Scientific spectrometer using monochromated Al $K\alpha$ X-ray source at ambient temperature and chamber pressure of about 10^{-8} mbar. The spot size was 400 μm. A flood gun was always used for charge compensation. All the spectra measured were corrected by setting the reference binding energy of carbon (*1s*) at 284.8 eV. The spectra were analyzed and processed using Thermo Avantage v5.903 software (Thermo Fisher Scientific). The peaks were fitted using Lorentzian–Gaussian product function. Smart background (derived from the Shirley background) was used over the peak width. The binding energy reported is within ± 0.2 eV.

H_2 chemisorption was carried out with a Micromeritics ASAP 2020 C instrument using the method reported by Bartholomew and co-workers.[41, 42] Typically, the Co@NC-*1073(al)* sample was first reduced for 3 h in H_2 gas flow at 623 K, followed by evacuating at that temperature for 30 min. Then, the temperature was cooled down to 423 K, at which temperature the H_2 adsorption isotherms were measured. The total H_2 uptake at zero

pressure was obtained by extrapolating the linear part of the isotherm. The amount of chemisorbed hydrogen is negligible on Co@NC-*1073(al)* sample.

2.2.4. Catalyst performance

The hydrogenation reactions were performed in a Parr 5000 Multi Reactor Stirrer System.[43] The reaction vessels have a volume of 45 cm^3 with stirring and an internal temperature controller. In a typical experiment, hydrogenation reactions are carried out in batch mode, for which autoclaves are filled with nitrobenzene (1 mmol), an amount of catalyst (Co@NC-*T* or Co@NC-*T(al)*) corresponding to a substrate to cobalt molar ratio of 37 (unless otherwise stated), internal standard (*n*-hexadecane, 0.34 mmol), and 5 ml ethanol as solvent. Before starting the reaction, the autoclaves are purged 3 times with He to remove air, and pressurized to 3 MPa H$_2$, followed by heating to 383 K under stirring at 500 rpm. After a fixed reaction time, the autoclaves are cooled down to room temperature and the hydrogen pressure is carefully released. The resulting reaction mixture is filtered and liquids are analyzed by GC (Agilent Technologies, GC 6890N). For recycling studies, 6.5 mg Co@NC-*1073* was added into the reactant mixtures (3 mmol nitrobenzene, substrate to cobalt molar ratio of 73, 0.34 mmol *n*-hexadecane, and 5 ml ethanol) under the same conditions as mentioned above except using the recovered catalyst. The catalyst was recovered by filtration, washed three times with ethanol, dried under vacuum at 323 K for 2 h and then used for the next run without any reactivation or purification.

2.3. RESULTS AND DISCUSSION

2.3.1. Catalyst Characterization Results

ZIF-67 was synthesized by mixing a cobalt nitrate methanolic solution and MeIm at room temperature. The relative intensity and peak positions of the powder X-ray diffraction (PXRD) pattern confirm the formation of pure crystalline ZIF-67 (Fig. A1a/Appendix A)[44]. Thermogravimetric (TG) analysis of the synthesized ZIF-67 under N_2 atmosphere suggests that ZIF-67 crystals are thermally stable up to 753 K (Fig. A1b/Appendix A). The sample mass then decreases sharply with increasing temperature until 873 K, which can be ascribed to the decomposition of the organic linker (MeIm)[45, 46]. After that, the sample mass decline slows down steadily up to 1073 K, implying that most organic fraction has decomposed below 873 K.

The specific BET area (S_{BET}) and pore volume (V_{pore}) of ZIF-67 and Co@NC-*T* samples were determined by N_2 adsorption-desorption isotherms (Table A1/Appendix A and Fig. A2/Appendix A). ZIF-67 with a high S_{BET} of 1930 m^2 g^{-1}, displays a type I isotherm with steep N_2 uptakes at low relative pressures, typically associated with microporosity[47]. After pyrolysis at 873 K, the S_{BET} of Co@NC-*873* drastically decreases to ~400 m^2 g^{-1}, due to the collapse of the well-defined microporous structure of ZIF-67 during the carbonization process (note that this area is referred to the support, as explained above)[45, 48]. A hysteresis loop also appears with gradual N_2 uptake at a relative pressure from 0.45 to 1.0, caused by the capillary condensation of N_2 in mesopores with a wide size distribution. The microporous volume of Co@NC-*873* is considerably smaller (0.1 cm^3 g^{-1}) compared to the parent ZIF-67 (0.68 cm^3 g^{-1}). In contrast, an increase in mesoporous volume for the pyrolyzed sample from 0.03 cm^3 g^{-1} to 0.14 cm^3
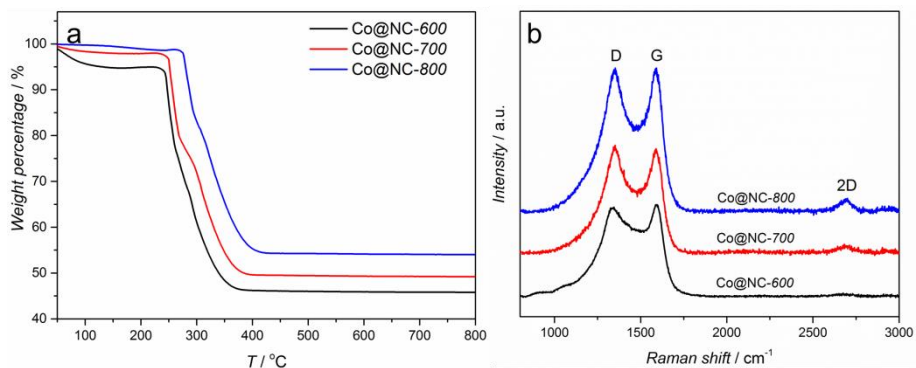
Fig. 2.1. (a) TGA profile of Co@NC-*T* under air flow (100 ml min^{-1} STP, heating rate 5 K min^{-1}), (b) Raman spectra of Co@NC-*T*

g[-1] is also observed. The change in pore structure proves that the original microporosity of ZIF-67 was transformed into a hierarchically interconnected micro/mesoporous structure during the pyrolysis process. Interestingly, further rising of the pyrolysis temperature does not significantly influence the S_{BET} and V_{pore} of Co@NC. Although the overall S_{BET} and V_{pore} do decrease due to the lower amount of support after different pyrolysis temperatures, the structure of the support does not change, as inferred by the similar S_{BET} and V_{pore} values obtained per gram of support.Fig. 2.1a shows the thermogravimetric (TG) analyses under air atmosphere of the Co@NC-*T* samples. All samples present approximately the same oxidation profile. There are two major mass losses directly attributed to two carbonaceous species bearing different thermal stabilities[49]. Despite these similar profiles, the final residual mass, attributed to Co_3O_4, increases with pyrolysis temperature, related to the fact that carbon content decreases with pyrolysis temperature. According to AAS (atomic adsorption spectroscopy) analysis, the Co contents in Co@NC-*T* catalysts are 31.0 *wt*.% 32.9 *wt*.% and 37.4 *wt*.% for Co@NC-
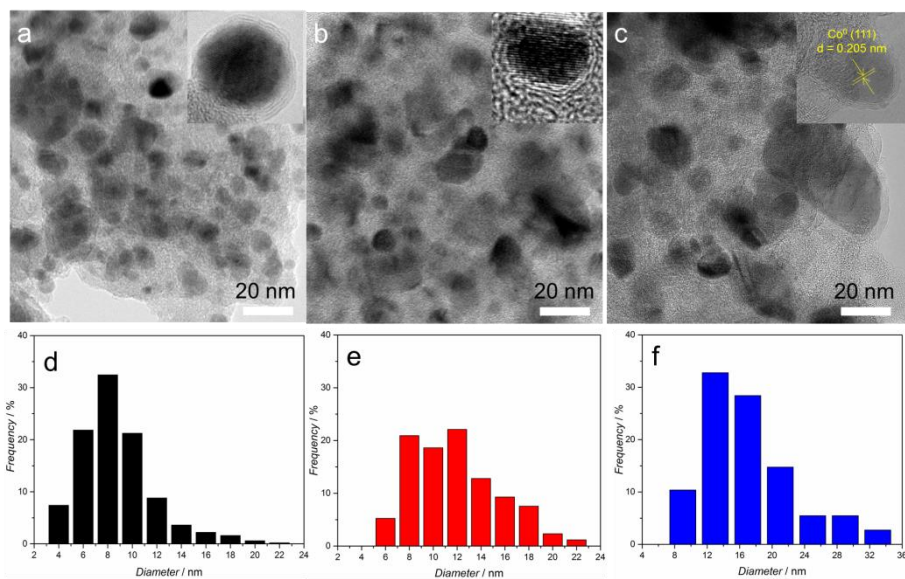
Fig. 2.2. TEM images and corresponding size distribution of Co NPs in Co@NC-*T*: (a, d) 873 K, (b, e) 973 K, (c, f) 1073 K.

873, *-973*, and *-1073*, respectively (Table A2/Appendix A). More importantly, the pyrolysis temperature also impacts the initial oxidation temperature of the carbon matrix in Co@NC-*T* samples. The higher the pyrolysis temperature used, the higher the temperature for carbon oxidation, pointing out to a higher graphitization degree of the carbon structure. This can be also inferred from the Raman spectra in Fig. 2.1b. All the Raman spectra of Co@NC-*T* reveal the characteristic G and D bands of carbon at 1580 cm^{-1} and 1350 cm^{-1}, which are correlated to graphitic *sp*^{2}-carbon and disordered or defect carbon, respectively[50]. When a higher pyrolysis temperature is employed (*i.e.* 973 K), a new band around 2700 cm^{-1} appears and sharpens with further increasing pyrolysis temperature to 1073 K. This signal can be assigned to the 2D band of graphitic carbon[45, 51].

The TEM images of Co@NC-*T* in Fig. 2.2a-c indicate that cobalt NPs are uniformly dispersed in the N-doped carbon matrix. The average particle

size of Co NPs in Co@NC-*T* is dependent on the pyrolysis temperature (K), increasing from 8 nm in '-*873*' to 12 nm and 18 nm for '-*973*' and '-*1073*', respectively (Figure 2.2d-f). Clearly, higher pyrolysis temperatures induce aggregation of Co to larger NPs[45]. The high-resolution (HR) TEM image of Co@NC-*1073* (see insert in Fig. 2.2c) reveals a lattice fringe of 2.05 Å attributed to the (111) plane of Co^0, and confirms that the Co^0 NP is embedded in N-doped carbon matrix and encapsulated by a few graphitic-like carbon layers, inferring a highly stable catalytic system[31]. In view of these results, it can be proposed that Co^{2+} in the structure of ZIF-67 is reduced during the pyrolysis process to Co^0, and that the final size of the formed Co nanoparticles can be controlled by varying the pyrolysis temperature. At the same time, these NPs facilitate the formation of graphitic carbon layers surrounding the nanocrystals during the pyrolysis and cooling down period[52, 53].

The presence of Co^0 and crystalline carbon is also observed in the XRD patterns shown in Fig. 2.3a. All Co@NC samples exhibit a diffraction peak at 30.6^o, indexed to the (002) planes of graphitic carbon (JCPDS No. 75-1621)[54]. In addition, the two peaks at 51.8^o and 60.6^o indicate the diffraction of (111) and (200) planes of metallic cobalt, respectively (JCPDS No. 15-0806)[55]. The diffraction peaks of both graphite and Co^0 become narrower and sharper as the pyrolysis temperature increases, pointing to a higher graphitization degree of the carbon matrix and to the formation of larger cobalt NPs. Importantly, no cobalt oxide and/or cobalt carbide reflections are found.
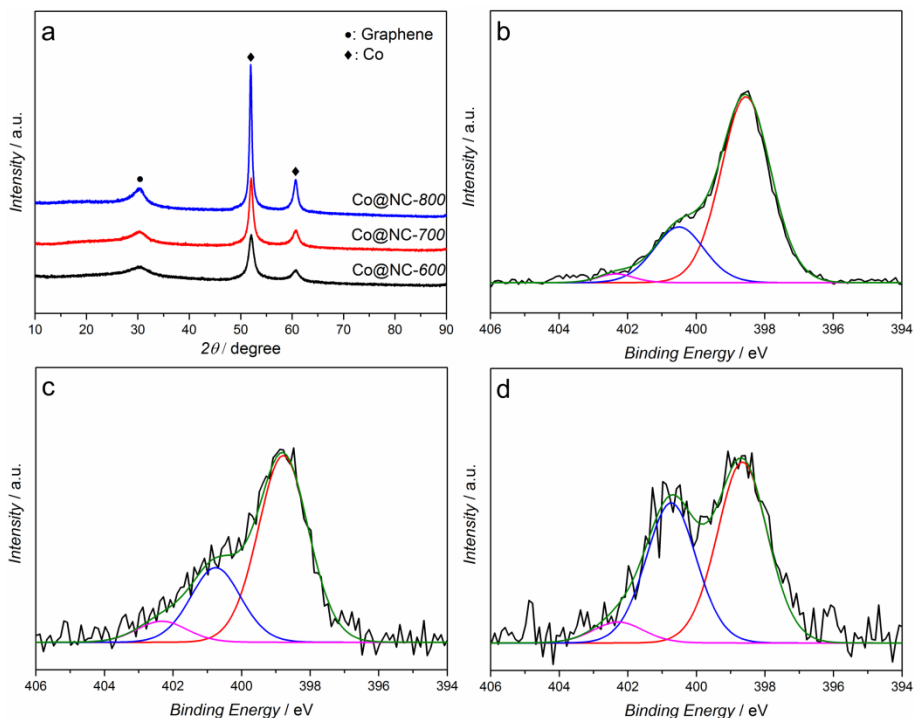
Fig. 2.3. (a) XRD patterns of Co@NC-*T*, N *1s* XPS region of (b) Co@NC-*873*, (c) Co@NC-*973*, (d) Co@NC-*1073*.

X-ray photoelectron spectroscopy (XPS) was further employed for all Co@NC-*T* samples to analyze the state of nitrogen, as stated in Fig. 2.3b-d. N *1s* signals of Co@NC-*T* were deconvoluted into three types of nitrogen species with binding energies around 398.8 eV, 400.8 eV, and 402.3 eV, which can be attributed to pyridinic-N, graphitic-N (pyrrolic and quaternary–N) and oxidized-N[23, 56], respectively. The peak at a binding energy of 398.8 eV could also be partially due to a contribution from nitrogen coordinated to the metal (Me-N), due to the small difference between binding energies of N-Me and pyridinic N[57-59]. Evidently, the N atoms in the pentagonal ring of the original imidazole units were mostly

converted into two types of N moieties (pyridinic- and graphitic-N) during the carbonization process. The pyridinic-N to graphitic-N atomic ratio (Table A3/Appendix A) decreases from 3.3 for '-873' to 2.4 for '-973' and 1.3 for '-1073', demonstrating that relatively more nitrogen atoms incorporate into the graphitic carbon layers at higher pyrolysis temperatures. According to elemental analysis, the N contents in the three catalysts are 7.8 *wt*.% for Co@NC-*873*, 3.7 *wt*.% for Co@NC-*973*, and 2.4 *wt*.% for Co@NC-*1073* (Table A2/Appendix A), indicating a loss of nitrogen with increasing thermal decomposition temperature[7, 56].

2.3.2. Catalytic Performance in Nitrobenzene Hydrogenation.

The catalytic activity of the Co@NC-*T* materials was assessed in the hydrogenation of nitrobenzene (Table 2.1). To clearly understand the catalytic activity of the Co@NC-*T* materials, a series of control experiments were performed. Neither in blank runs (without catalyst) nor with the parent ZIF-67 (Table 2.1, entries 1, 2) any conversion was observed, indicating that the active species are formed during the pyrolysis process. Furthermore, the comparable NC sample synthesised using ZIF-8(Zn) as precursor (Figure S1c) exhibited no activity (Table 2.1, entry 13),[60] whereas the as-synthesized Co@NC-*T* catalysts exhibit good hydrogenation activity together with a >99% selectivity to aniline, suggesting that cobalt-containing species are responsible for the catalytic action in this reaction. More interestingly, the hydrogenation activity of these Co@NC-*T* catalysts (Table 2.1, entries 3-5) correlates with the pyrolysis temperature, with conversions after 3 h reaction ranging from 48% to 69% as the pyrolysis temperature increases from 873 to 1073 K (note that the amount of Co used in all cases was similar). Given that the S_{BET} and V_{pore} of Co@NC do not

vary with pyrolysis temperature (Table A1/Appendix A), the different hydrogenation activity for these Co@NC has to be attributed to: (i) the different feature of the N-doped carbon matrix, such as the graphitization degree, that might have an impact on hydrogen dissociation;[61] and/or (ii) the cobalt phases or particle size. The impact of reaction temperature on the catalytic activity for Co@NC-*1073* further shows that the conversion of nitrobenzene is below 15% for a reaction temperature below 343 K (Table A4/Appendix A). However, the activity sharply rises with the reaction temperature, and reaches 99% conversion after 3 h at a reaction temperature of 383 K. Moreover, similar turnover numbers (*TON*s) are obtained for experiments performed with different initial concentrations of nitrobenzene on Co@NC-*1073* (Table A5/Appendix A)*,* indicating an apparent zeroth order reaction with respect to this reactant, attributed to a strong adsorption of nitrobenzene on the catalyst in these experiments.

The Co@NC-*T* catalysts were further post-treated in a 0.5 M HCl solution to remove those accessible cobalt NPs (hence, acid leached samples are denoted as Co@NC-*T (al)*). AAS analysis indicates that cobalt content in the acid leached samples is 27.1 *wt.*% for Co@NC-*873(al)*, 19.4 *wt.*% for Co@NC-*973(al)*, and 13.6 *wt.*% for Co@NC-*1073(al)* (Table A2/Appendix A). Apparently, a larger fraction of cobalt can be leached out by acid when ZIF-67 is carbonized at a higher temperature. At the same time, XRD analysis (Fig. A3/Appendix A and Table A6/Appendix A) clearly demonstrates that these Co@NC-*T(al)* samples still contain metallic cobalt nanoparticles with a similar average Co particle size. These Co nanoparticles exhibit high resistance toward acid leaching, owing to a well encapsulation by graphitic carbon layers on the surface.[62] As it is well known, acid leaching under mild conditions only removes those Co

nanoparticles that are not fully encapsulated by the graphite shells.[63, 64] Hydrogenation experiments were further performed with these leached samples using a similar total amount of catalyst (5.1 mg) of Co@NC-*T(al)* and Co@NC-*T* (Table 2.1, entry 3, 7-11, 14). Obviously, the Co@NC-*T(al)* samples exhibit a lower nitrobenzene conversion compared to their counterparts, *albeit* with similar aniline selectivity, suggesting that those leached cobalt nanoparticles did participate in the hydrogenation reaction. Interestingly, the Co@NC-*T(al)* samples (*T* = 873, 973, 1073 K) still retain a considerable activity and Co@NC-*1073(al)* exhibits the highest nitrobenzene conversion (62%) among the three Co@NC-*T(al)* samples, indicating that acid-leaching resistant cobalt species are able to perform the hydrogenation as well.

Recently, Wang *et al.*, reported a similar strategy to prepare Co@NC catalyst by pyrolysis of ZIF-67, and claimed that no hydrogenation activity was observed after acid leaching in aqua regia.[37] Bearing in mind the superior oxidation power of aqua regia, this is not surprising. Indeed, it has been reported by other authors that N-doped graphene can be easily destroyed by acid treatment in concentrated HNO_3, one of the main components of aqua regia.[35] In order to gain more insight into the nature of the active sites in our Co@NC-*1073(al)*, additional characterization was performed. The Raman and C *1s* XPS spectra of Co@NC-*1073(al)* (Figure A4/Appendix A and Figure A5a,b/Appendix A) are similar to those of the non-acid leached sample, suggesting that a possible carbon surface modification is not responsible for a change in activity. Besides, a relatively higher graphitic-N content of Co@NC-*1073(al)* (Figure A5d/Appendix A) than of Co@NC-*1073* (Figure 3d) is also observed. Taking into consideration that XPS is a surface analysis technique, this is presumably

due to more detectable graphitic-N atoms after removal of some cobalt NPs. TEM analysis of acid leached samples reveals that some cobalt NPs together with some hollow carbon shells (Figure 4a) are present in these samples. HR-TEM (Figure A6a/Appendix A) along with H_2 chemisorption results (see experimental section for detail) both demonstrate that the remaining cobalt NPs are tightly encapsulated by multiple graphitic carbon shells which render them inaccessible, even to H_2. Figure 4b shows a high-angle annular dark-field (HAADF) image of the Co@NC-*1073(al)* sample, in which cobalt nanoparticles can be easily distinguished. At the same time, a cloud-like structure dispersed along the carbon support is also noticeable. Although no cobalt nanoparticles can be observed in these regions, cobalt (Figure A6c/Appendix A) is still detected by energy-dispersive X-ray spectroscopy (EDXS) analysis (area 2 in Figure 4b). It has been reported that metal atoms (*e.g.* Co, Fe) released during high-temperature pyrolysis are extremely reactive towards other heteroatoms such as nitrogen to form atomically dispersed metal-N_x species embedded in the carbon matrix.[65] These species, once formed, can be very resistant towards acid leaching. To further demonstrate this claim, we performed additional hydrogenation experiments in the presence of thiocyanate ions (SCN⁻), a well-known inhibitor for metal centres in homogeneous catalysts.[66] After the addition of SCN⁻, the hydrogenation activity of Co@NC-*1073(al)* decreases from 62% to 39% (Table 1, entry 12). Taking into account that no accessible cobalt NPs are present in the acid leached Co@NC-*1073(al)*, it is proposed that the highly dispersed Co-N_x sites do participate in the hydrogenation process.

Table 2.1. Results of the catalytic hydrogenation of nitrobenzene over Co@NC-*T* and Co@NC-*T(al)*.[a]

Entry	Catalyst	Co content (*wt.* %)	Substrate to cobalt molar ratio	X (%)[b]	TON[c]
1	Blank	-	-	< 1	-
2	ZIF-67	26.0	37	< 1	-
3	Co@NC-*873*	31.0	37	48	18
4	Co@NC-*973*	32.9	37	57	21
5	Co@NC-*1073*	37.4	37	69	24
6	Co@NC-*1073*	37.4	24	99	24
7	Co@NC-*973*	32.9	35	59	21
8	Co@NC-*1073*	37.4	31	79	24
9	Co@NC-*873(al)*	27.1	43	43	18
10	Co@NC-*973(al)*	19.4	60	38	22
11	Co@NC-*1073(al)*	13.6	85	62	53
12[d]	Co@NC-*1073(al)*	13.6	85	39	33
13	NC-*1073(al)*	-	-	< 1	-
14	Co@NC-*1173(al)*	4.1	282	36	101

a: Reaction conditions: 1 mmol nitrobenzene, 5 mL ethanol, 383 K, 3 MPa H_2, 3 h, aniline selectivity in all cases > 99% (no byproducts were detected by GC analysis, carbon balance nears 100% in all cases). b: Determined by GC (internal standard: *n*-hexadecane), X = mol nitrobenzene consumed divided by total mol nitrobenzene. c: TON = mol nitrobenzene consumed divided by total mol cobalt. d: 0.02 M NaSCN as catalyst inhibitor with SCN- to cobalt molar ratio of 8.5.

The reduced activity can be attributed to a competitive adsorption on Co-N_x sites between SCN⁻ ions and -NO_2 group in nitrobenzene molecules, as it was reported that the thiocyanate does not permanently bind to or alter the metal-centred site but rather interacts competitively.[67] In summary, the superior catalytic activity of Co@NC-*1073* can be attributed to the presence of accessible cobalt nanoparticles and atomically dispersed Co in close interaction with the nitrogen doped graphene. Both active species are
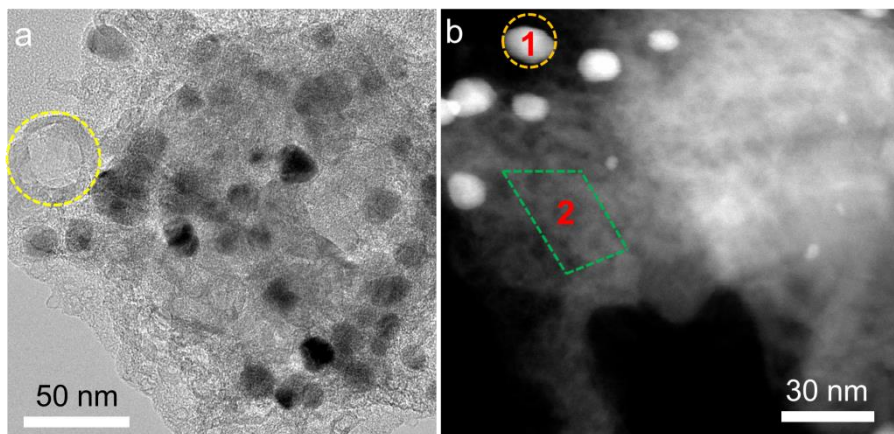
Fig. 2.4. (a) TEM pictures of Co@NC-*1073 (al)*, (b) HAADF image of Co@NC-*1073 (al)*.

formed *in situ* during the pyrolytic transformation of ZIF-67.

A comparison (Table A8/Appendix A) between the *TONs* achieved by the catalysts here reported and literature data reveals that the *TON* value of Co@NC-*1173(al)* obtained for a single run is comparable (*TON* = 101) with the best catalysts reported to date by Beller *et al*. (*TON* = 97)[5], and larger than those for other Co based catalysts. For repeated runs with Co@NC-*1073 and 1173 (al)* a total *TON* of 118 and 393 is reached (Table A8/Appendix A), respectively (*vide infra*). Furthermore, when productivity is calculated per gram of solid instead of per amount of Co all our catalysts stand out. In view of the characterization performed and the fact that the *TON* doubles already after leaching (Table 2.1), it is reasonable to argue that the presence of inaccessible cobalt NPs which are fully encapsulated by the graphene layers, result in lower *TON* values than actually should apply.
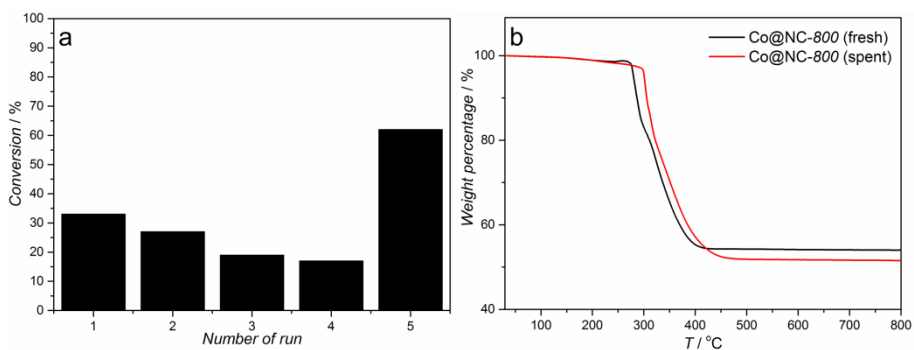
Fig. 2.5. Nitrobenzene conversion upon reuse of Co@NC-*1073* (a). Reaction conditions: 3 mmol nitrobenzene, substrate to cobalt molar ratio of 73, 5 mL ethanol, 383 K, 3 MPa H_2, 3 h for 1st - 4th run and 12 h for the 5th run. (b) TGA curve of Co@NC-*1073* (fresh) and Co@NC-*1073* (spent) under air flow (100 ml min^{-1} STP, heating rate 5 K min^{-1}).
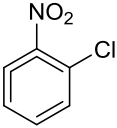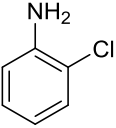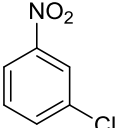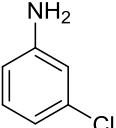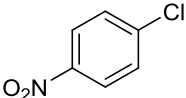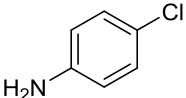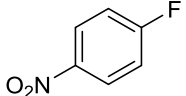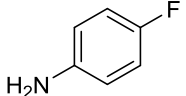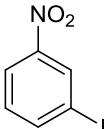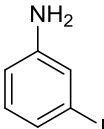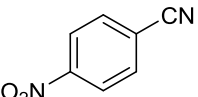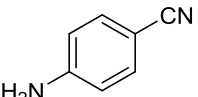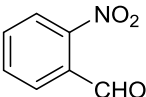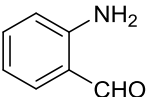
2.3.3. Reusability and Catalyst Deactivation
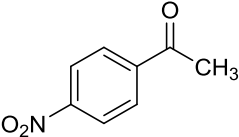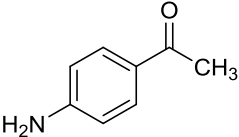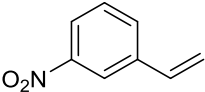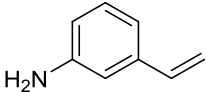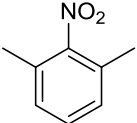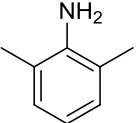
Catalyst stability and reusability is a key factor to evaluate heterogeneous catalysts. In this sense, the most active catalyst, Co@NC-*1073* and *1173(al)*, were tested in successive runs. The yield of aniline decreases gradually after each run (Fig. 2.5a and A10/Appendix A), but the aniline selectivity is well preserved in four consecutive runs (> 99%). In spite of this activity decline, after 4 cycles Co@NC-*1073* has still half of its activity: extending the reaction time to 12 h leads to an aniline yield as high as 65%. Overall a *TON* of 118 is attained with this catalyst. Loss of the active component is one of causes of catalyst deactivation and usually results from leaching in liquid phase reactions. Wang *et al.* observed that 40 *wt.*% of cobalt was lost by the CoO_x@NCNT hybrid after 11 runs in nitrobenzene hydrogenation, and attributed the deactivation to this loss of cobalt.[20] However, in our case the negligible amount of cobalt found in the solution (< 3 ppm, below the ICP detection limit, Table A7/Appendix A) after each run suggests that the graphite shells prevent leaching of the cobalt

NPs under reaction conditions, implying that the observed deactivation cannot be attributed to a loss of cobalt during the hydrogenation. At the same time, both the XRD pattern and C *1s* XPS spectrum of the spent Co@NC-*1073* catalyst exhibit the same features as the fresh Co@NC-*1073* (Fig. A7/Appendix A and Fig. A8/Appendix A), indicative of a well-preserved structure after recycling.

TG analysis in air (Fig. 2.5b) indicated a 323 K lower initial oxidation temperature of the carbon matrix in *fresh* than in *spent* Co@NC-*1073*. Bearing in mind that the carbon structure in the fresh and spent Co@NC-*1073* is the same, the temperature deviation is ascribed to the number of exposed cobalt sites, considering that oxidized cobalt species can catalyze carbon oxidation at low temperature[68]. For the spent Co@NC-*1073* catalyst, a more intense Co *2p* XPS signal from CoO_x is detected compared to the fresh sample (Fig. A9/Appendix A). Oxidized cobalt can be *in situ* reduced to its metallic phase by H_2 under similar hydrogenation conditions[20, 36]; therefore the increase of the CoO_x signal in our case might be attributed to the re-oxidation of cobalt in air after the recycling. A ~3 *wt.*% lower residual mass in the spent Co@NC-*1073* than in the fresh catalyst is also observed. As no mass decrease due to possible adsorbed water release is observed below 573 K, and the delay in the weight loss, the extra ~3 *wt.*% mass loss in Co@NC-*1073*(spent) is ascribed to the removal of some strongly adsorbed reaction species (of unknown nature) on the catalyst. Indeed, the presence of strongly adsorbed species would explain the delay in oxidation of carbon support observed in the TGA analysis. Co@NC-*1173(al)* exhibits the highest activity and stability of all samples

Table 2.2. Results of the chemoselective hydrogenation of substituted nitroarenes over Co@NC-*1073* [a]

Entry	Substrate	Product	t (h)	Y (%)[b]
1			4	98
2			6	98
3			6	97
4			6	97
5			6	97
6			4	96
7[c]			6	96

8			6	98
9[c]			1	47[d]
10			12	99

a: Reaction conditions: 1 mmol nitroarene, substrate to cobalt molar ratio of 24, 5 mL ethanol, 383 K, 3 MPa H_2, > 99% conversion observed in all cases. b: Determined by GC (internal standard: *n*-hexadecane). c: substrate to cobalt molar ratio of 12. d: 1 h reaction with 53% conversion.

(Figure A10/Appendix A). The lower content of cobalt, and the smaller fraction of encapsulated cobalt nanoparticles suggest that the highly dispersed Co is associated with the activity in this catalyst system.

2.3.4. Hydrogenation of Substituted Nitroarenes

To investigate the general applicability of Co@NC-*1073*, various substituted nitroarenes were explored under standard conditions. A variety of industrially relevant anilines such as chloro- and fluoroanilines were produced in excellent yields (Table 2.2, entries 1-4). The most challenging substrates bearing other easily reducible groups such as iodine, nitrile, aldehyde, ketone and alkene (Table 2.2, entries 5-9) could be converted easily and selectively into the corresponding anilines. Even a sterically hindered nitroarene (Table 2.2, entry 10) was hydrogenated to the

substituted aniline with outstanding yield. These results demonstrate again that this Co@NC-*1073* catalyst displays an intriguing activity and chemoselectivity in the hydrogenation of substituted aromatic compounds in general.

2.4. CONCLUSIONS

The one-step thermal decomposition of ZIF-67 under a N_2 atmosphere is a straightforward and scalable approach to synthesize recyclable and active heterogeneous catalysts for the hydrogenation of nitroarenes. The resulting cobalt containing carbon composites exhibit an excellent catalytic performance in the hydrogenation of a wide range of nitroarenes to their substituted anilines under relatively mild conditions. By controlling the pyrolysis temperature and with a subsequent acid leaching treatment, it is possible to control the total metal loading, resulting in high performance catalysts. The high activity of the Co-N-C system is attributed to cobalt nanoparticles and the presence of highly dispersed Co in close interaction with nitrogen-doped graphene, both of which are formed *in situ* during the pyrolytic transformation of ZIF-67. Furthermore, these atomically dispersed Co-N$_x$ species exhibit a much higher turnover number (*TON*) than cobalt nanoparticles, probably due to its higher cobalt atom utilization in the hydrogenation reaction. Unfortunately, with this MOF-mediated synthesis method, it is impossible to investigate the differences in N-doped carbon structure and cobalt particle size individually on the hydrogenation performance, and a more in-depth work on these two factors is under investigation. Furthermore, the mild deactivation observed in these Co-N-C catalysts can be attributed to the partial blockage of active sites by strongly adsorbed reaction species.

The presented synthetic approach opens up an avenue to develop and improve powerful non-noble metal catalysts for industrial applications.

REFERENCES

[1] D. Cantillo, M. Baghbanzadeh, C.O. Kappe, In Situ Generated Iron Oxide Nanocrystals as Efficient and Selective Catalysts for the Reduction of Nitroarenes using a Continuous Flow Method, Angewandte Chemie International Edition, 51 (2012) 10190-10193.

[2] R.S. Downing, P.J. Kunkeler, H. van Bekkum, Catalytic syntheses of aromatic amines, Catalysis Today, 37 (1997) 121-136.

[3] N. Ono, The Nitro Group in Organic Synthesis, Wiley-VCH, New York, 2001.

[4] S. Nishimura, Handbook of Heterogeneous Catalytic Hydro-genation for Organic Synthesis, Wiley-Interscience, New York, 2001.

[5] F.A. Westerhaus, R.V. Jagadeesh, G. Wienhöfer, M.-M. Pohl, J. Radnik, A.-E. Surkus, J. Rabeah, K. Junge, H. Junge, M. Nielsen, A. Brückner, M. Beller, Heterogenized cobalt oxide catalysts for nitroarene reduction by pyrolysis of molecularly defined complexes, Nat Chem, 5 (2013) 537-543.

[6] A. Corma, P. Serna, Chemoselective Hydrogenation of Nitro Compounds with Supported Gold Catalysts, Science, 313 (2006) 332-334.

[7] R.V. Jagadeesh, A.-E. Surkus, H. Junge, M.-M. Pohl, J. Radnik, J. Rabeah, H. Huan, V. Schünemann, A. Brückner, M. Beller, Nanoscale Fe2O3-Based Catalysts for Selective Hydrogenation of Nitroarenes to Anilines, Science, 342 (2013) 1073-1076.

[8] F. L'Eplattenier, P. Matthys, F. Calderazzo, Homogeneous ruthenium-catalyzed reduction of nitrobenzene, Inorganic Chemistry, 9 (1970) 342-345.

[9] A. Corma, C. González-Arellano, M. Iglesias, F. Sánchez, Gold complexes as catalysts: Chemoselective hydrogenation of nitroarenes, Applied Catalysis A: General, 356 (2009) 99-102.

[10] H.-U. Blaser, H. Steiner, M. Studer, Selective Catalytic Hydrogenation of Functionalized Nitroarenes: An Update, ChemCatChem, 1 (2009) 210-221.

[11] K. Junge, K. Schroder, M. Beller, Homogeneous catalysis using iron complexes: recent developments in selective reductions, Chemical Communications, 47 (2011) 4849-4859.

[12] G. Vilé, N. Almora-Barrios, N. López, J. Pérez-Ramírez, Structure and Reactivity of Supported Hybrid Platinum Nanoparticles for the Flow Hydrogenation of Functionalized Nitroaromatics, ACS Catalysis, 5 (2015) 3767-3778.

[13] A. Yarulin, C. Berguerand, I. Yuranov, F. Cárdenas-Lizana, I. Prokopyeva, L. Kiwi-Minsker, Pt–Zn nanoparticles supported on porous polymeric matrix for selective 3-nitrostyrene hydrogenation, Journal of Catalysis, 321 (2015) 7-12.

[14] M. Carrus, M. Fantauzzi, F. Riboni, M. Makosch, A. Rossi, E. Selli, J.A. van Bokhoven, Increased conversion and selectivity of 4-nitrostyrene hydrogenation to 4-aminostyrene on Pt nanoparticles supported on titanium-tungsten mixed oxides, Applied Catalysis A: General, 519 (2016) 130-138.

[15] A. Corma, P. Serna, P. Concepción, J.J. Calvino, Transforming Nonselective into Chemoselective Metal Catalysts for the Hydrogenation of Substituted Nitroaromatics, Journal of the American Chemical Society, 130 (2008) 8748-8753.

[16] G.C. Bond, Supported metal catalysts: some unsolved problems, Chemical Society Reviews, 20 (1991) 441-475.

[17] A.M. Tafesh, J. Weiguny, A Review of the Selective Catalytic Reduction of Aromatic Nitro Compounds into Aromatic Amines, Isocyanates, Carbamates, and Ureas Using CO, Chemical Reviews, 96 (1996) 2035-2052.

[18] A. Grirrane, A. Corma, H. García, Gold-Catalyzed Synthesis of Aromatic Azo Compounds from Anilines and Nitroaromatics, Science, 322 (2008) 1661-1664.

[19] M. Boronat, P. Concepción, A. Corma, S. González, F. Illas, P. Serna, A Molecular Mechanism for the Chemoselective Hydrogenation of Substituted Nitroaromatics with Nanoparticles of Gold on TiO2 Catalysts: A Cooperative Effect between Gold and the Support, Journal of the American Chemical Society, 129 (2007) 16230-16237.

[20] Z. Wei, J. Wang, S. Mao, D. Su, H. Jin, Y. Wang, F. Xu, H. Li, Y. Wang, In Situ-Generated Co0-Co3O4/N-Doped Carbon Nanotubes Hybrids as Efficient and Chemoselective Catalysts for Hydrogenation of Nitroarenes, ACS Catalysis, 5 (2015) 4783-4789.

[21] O. Beswick, I. Yuranov, D.T.L. Alexander, L. Kiwi-Minsker, Iron oxide nanoparticles supported on activated carbon fibers catalyze chemoselective reduction of nitroarenes under mild conditions, Catalysis Today, 249 (2015) 45-51.

[22] R.K. Rai, A. Mahata, S. Mukhopadhyay, S. Gupta, P.-Z. Li, K.T. Nguyen, Y. Zhao, B. Pathak, S.K. Singh, Room-Temperature Chemoselective Reduction of Nitro Groups Using Non-noble Metal Nanocatalysts in Water, Inorganic Chemistry, 53 (2014) 2904-2909.

[23] L. Zhao, J. Chen, J. Zhang, Deactivation of Ni/K2O-La2O3-SiO2 catalyst in hydrogenation of m-dinitrobenzene to m-phenylenediamine, Journal of Molecular Catalysis A: Chemical, 246 (2006) 140-145.

[24] W. Lin, H. Cheng, J. Ming, Y. Yu, F. Zhao, Deactivation of Ni/TiO2 catalyst in the hydrogenation of nitrobenzene in water and improvement in its stability by coating a layer of hydrophobic carbon, Journal of Catalysis, 291 (2012) 149-154.

[25] J. Lee, O.K. Farha, J. Roberts, K.A. Scheidt, S.T. Nguyen, J.T. Hupp, Metal-organic framework materials as catalysts, Chemical Society Reviews, 38 (2009) 1450-1459.

[26] V.K. Mittal, S. Bera, T. Saravanan, S. Sumathi, R. Krishnan, S. Rangarajan, S. Velmurugan, S.V. Narasimhan, Formation and characterization of bi-layer oxide coating on carbon-steel for improving corrosion resistance, Thin Solid Films, 517 (2009) 1672-1676.

[27] B.V. Appa Rao, M. Yakub Iqbal, B. Sreedhar, Self-assembled monolayer of 2-(octadecylthio)benzothiazole for corrosion protection of copper, Corrosion Science, 51 (2009) 1441-1452.

[28] J. Lee, D.H.K. Jackson, T. Li, R.E. Winans, J.A. Dumesic, T.F. Kuech, G.W. Huber, Enhanced stability of cobalt catalysts by atomic layer deposition for aqueous-phase reactions, Energy & Environmental Science, 7 (2014) 1657-1660.

[29] Y.-Z. Chen, C. Wang, Z.-Y. Wu, Y. Xiong, Q. Xu, S.-H. Yu, H.-L. Jiang, From Bimetallic Metal-Organic Framework to Porous Carbon: High Surface Area and Multicomponent Active Dopants for Excellent Electrocatalysis, Advanced Materials, 27 (2015) 5010-5016.

[30] D. Deng, L. Yu, X. Chen, G. Wang, L. Jin, X. Pan, J. Deng, G. Sun, X. Bao, Iron Encapsulated within Pod-like Carbon Nanotubes for Oxygen Reduction Reaction, Angewandte Chemie International Edition, 52 (2013) 371-375.

[31] J. Deng, P. Ren, D. Deng, L. Yu, F. Yang, X. Bao, Highly active and durable non-precious-metal catalysts encapsulated in carbon nanotubes for hydrogen evolution reaction, Energy & Environmental Science, 7 (2014) 1919-1923.

[32] X. Zheng, J. Deng, N. Wang, D. Deng, W.-H. Zhang, X. Bao, C. Li, Podlike N-Doped Carbon Nanotubes Encapsulating FeNi Alloy Nanoparticles: High-Performance Counter Electrode Materials for Dye-Sensitized Solar Cells, Angewandte Chemie International Edition, 53 (2014) 7023-7027.

[33] L. Zhang, A. Wang, W. Wang, Y. Huang, X. Liu, S. Miao, J. Liu, T. Zhang, Co–N–C Catalyst for C–C Coupling Reactions: On the Catalytic Performance and Active Sites, ACS Catalysis, 5 (2015) 6563-6572.

[34] Y. Hou, Z. Wen, S. Cui, S. Ci, S. Mao, J. Chen, An Advanced Nitrogen-Doped Graphene/Cobalt-Embedded Porous Carbon Polyhedron Hybrid for Efficient Catalysis of Oxygen Reduction and Water Splitting, Advanced Functional Materials, 25 (2015) 872-882.

[35] T. Cheng, H. Yu, F. Peng, H. Wang, B. Zhang, D. Su, Identifying active sites of CoNC/CNT from pyrolysis of molecularly defined complexes for oxidative esterification and hydrogenation reactions, Catalysis Science & Technology, 6 (2016) 1007-1015.

[36] L. Liu, P. Concepción, A. Corma, Non-noble metal catalysts for hydrogenation: A facile method for preparing Co nanoparticles covered with thin layered carbon, Journal of Catalysis, 340 (2016) 1-9.

[37] X. Wang, Y. Li, Chemoselective hydrogenation of functionalized nitroarenes using MOF-derived co-based catalysts, Journal of Molecular Catalysis A: Chemical, 420 (2016) 56-65.

[38] B. Chen, F. Li, Z. Huang, G. Yuan, Recyclable and Selective Nitroarene Hydrogenation Catalysts Based on Carbon-Coated Cobalt Oxide Nanoparticles, ChemCatChem, 8 (2016) 1132-1138.

[39] Z. Jiang, Z. Li, Z. Qin, H. Sun, X. Jiao, D. Chen, LDH nanocages synthesized with MOF templates and their high performance as supercapacitors, Nanoscale, 5 (2013) 11770-11775.

[40] M.F. De Lange, T.J.H. Vlugt, J. Gascon, F. Kapteijn, Adsorptive characterization of porous solids: Error analysis guides the way, Microporous and Mesoporous Materials, 200 (2014) 199-215.

[41] R.C. Reuel, C.H. Bartholomew, The stoichiometries of H2 and CO adsorptions on cobalt: Effects of support and preparation, Journal of Catalysis, 85 (1984) 63-77.

[42] J.M. Zowtiak, C.H. Bartholomew, The kinetics of H2 adsorption on and desorption from cobalt and the effects of support thereon, Journal of Catalysis, 83 (1983) 107-120.

[43] S. Sartipi, M.J. Valero Romero, E. Rozhko, Z. Que, H.A. Stil, J. de With, F. Kapteijn, J. Gascon, Dynamic Release–Immobilization of a Homogeneous Rhodium Hydroformylation Catalyst by a Polyoxometalate Metal–Organic Framework Composite, ChemCatChem, 7 (2015) 3243-3247.

[44] R. Banerjee, A. Phan, B. Wang, C. Knobler, H. Furukawa, M. O'Keeffe, O.M. Yaghi, High-Throughput Synthesis of Zeolitic Imidazolate Frameworks and Application to CO2 Capture, Science, 319 (2008) 939-943.

[45] N.L. Torad, M. Hu, S. Ishihara, H. Sukegawa, A.A. Belik, M. Imura, K. Ariga, Y. Sakka, Y. Yamauchi, Direct Synthesis of MOF-Derived Nanoporous Carbon with

Magnetic Co Nanoparticles toward Efficient Water Treatment, Small, 10 (2014) 2096-2107.

[46] S.J. Yang, T. Kim, J.H. Im, Y.S. Kim, K. Lee, H. Jung, C.R. Park, MOF-Derived Hierarchically Porous Carbon with Exceptional Porosity and Hydrogen Storage Capacity, Chemistry of Materials, 24 (2012) 464-470.

[47] J. Tang, R.R. Salunkhe, J. Liu, N.L. Torad, M. Imura, S. Furukawa, Y. Yamauchi, Thermal Conversion of Core–Shell Metal–Organic Frameworks: A New Method for Selectively Functionalized Nanoporous Hybrid Carbon, Journal of the American Chemical Society, 137 (2015) 1572-1580.

[48] N.L. Torad, R.R. Salunkhe, Y. Li, H. Hamoudi, M. Imura, Y. Sakka, C.-C. Hu, Y. Yamauchi, Electric Double-Layer Capacitors Based on Highly Graphitized Nanoporous Carbons Derived from ZIF-67, Chemistry – A European Journal, 20 (2014) 7895-7900.

[49] S. Gadipelli, T. Zhao, S.A. Shevlin, Z. Guo, Switching effective oxygen reduction and evolution performance by controlled graphitization of a cobalt-nitrogen-carbon framework system, Energy & Environmental Science, (2016).

[50] B.Y. Xia, Y. Yan, N. Li, H.B. Wu, X.W. Lou, X. Wang, A metal–organic framework-derived bifunctional oxygen electrocatalyst, Nature Energy, 1 (2016) 15006.

[51] D. Yang, A. Velamakanni, G. Bozoklu, S. Park, M. Stoller, R.D. Piner, S. Stankovich, I. Jung, D.A. Field, C.A. Ventrice Jr, R.S. Ruoff, Chemical analysis of graphene oxide films after heat and chemical treatments by X-ray photoelectron and Micro-Raman spectroscopy, Carbon, 47 (2009) 145-152.

[52] J. Tang, T. Wang, X. Pan, X. Sun, X. Fan, Y. Guo, H. Xue, J. He, Synthesis and Electrochemical Characterization of N-Doped Partially Graphitized Ordered Mesoporous Carbon–Co Composite, The Journal of Physical Chemistry C, 117 (2013) 16896-16906.

[53] N.A.M. Barakat, B. Kim, S.J. Park, Y. Jo, M.-H. Jung, H.Y. Kim, Cobalt nanofibers encapsulated in a graphite shell by an electrospinning process, Journal of Materials Chemistry, 19 (2009) 7371-7378.

[54] Z. Zhuang, S.A. Giles, J. Zheng, G.R. Jenness, S. Caratzoulas, D.G. Vlachos, Y. Yan, Nickel supported on nitrogen-doped carbon nanotubes as hydrogen oxidation reaction catalyst in alkaline electrolyte, Nature Communications, 7 (2016) 10141.

[55] W. Zhou, J. Zhou, Y. Zhou, J. Lu, K. Zhou, L. Yang, Z. Tang, L. Li, S. Chen, N-Doped Carbon-Wrapped Cobalt Nanoparticles on N-Doped Graphene Nanosheets for High-Efficiency Hydrogen Production, Chemistry of Materials, 27 (2015) 2026-2032.

[56] J.R. Pels, F. Kapteijn, J.A. Moulijn, Q. Zhu, K.M. Thomas, Evolution of nitrogen functionalities in carbonaceous materials during pyrolysis, Carbon, 33 (1995) 1641-1653.

[57] J. Casanovas, J.M. Ricart, J. Rubio, F. Illas, J.M. Jiménez-Mateos, Origin of the Large N 1s Binding Energy in X-ray Photoelectron Spectra of Calcined Carbonaceous Materials, Journal of the American Chemical Society, 118 (1996) 8071-8076.

[58] H.-W. Liang, W. Wei, Z.-S. Wu, X. Feng, K. Müllen, Mesoporous Metal–Nitrogen-Doped Carbon Electrocatalysts for Highly Efficient Oxygen Reduction Reaction, Journal of the American Chemical Society, 135 (2013) 16002-16005.

[59] G. Wu, C.M. Johnston, N.H. Mack, K. Artyushkova, M. Ferrandon, M. Nelson, J.S. Lezama-Pacheco, S.D. Conradson, K.L. More, D.J. Myers, P. Zelenay, Synthesis-structure-performance correlation for polyaniline-Me-C non-precious metal cathode catalysts for oxygen reduction in fuel cells, Journal of Materials Chemistry, 21 (2011) 11392-11405.

[60] L. Zhang, Z. Su, F. Jiang, L. Yang, J. Qian, Y. Zhou, W. Li, M. Hong, Highly graphitized nitrogen-doped porous carbon nanopolyhedra derived from ZIF-8 nanocrystals as efficient electrocatalysts for oxygen reduction reactions, Nanoscale, 6 (2014) 6590-6602.

[61] R.W. Coughlin, Carbon as Adsorbent and Catalyst, Product R&D, 8 (1969) 12-23.

[62] J. Deng, P. Ren, D. Deng, X. Bao, Enhanced Electron Penetration through an Ultrathin Graphene Layer for Highly Efficient Catalysis of the Hydrogen Evolution Reaction, Angewandte Chemie International Edition, 54 (2015) 2100-2104.

[63] X. Zou, X. Huang, A. Goswami, R. Silva, B.R. Sathe, E. Mikmeková, T. Asefa, Cobalt-Embedded Nitrogen-Rich Carbon Nanotubes Efficiently Catalyze Hydrogen Evolution Reaction at All pH Values, Angewandte Chemie, 126 (2014) 4461-4465.

[64] L.-B. Lv, T.-N. Ye, L.-H. Gong, K.-X. Wang, J. Su, X.-H. Li, J.-S. Chen, Anchoring Cobalt Nanocrystals through the Plane of Graphene: Highly Integrated Electrocatalyst for Oxygen Reduction Reaction, Chemistry of Materials, 27 (2015) 544-549.

[65] W.-J. Jiang, L. Gu, L. Li, Y. Zhang, X. Zhang, L.-J. Zhang, J.-Q. Wang, J.-S. Hu, Z. Wei, L.-J. Wan, Understanding the High Activity of Fe–N–C Electrocatalysts in Oxygen Reduction: Fe/Fe3C Nanoparticles Boost the Activity of Fe–Nx, Journal of the American Chemical Society, 138 (2016) 3570-3578.

[66] H.-W. Liang, S. Bruller, R. Dong, J. Zhang, X. Feng, K. Mullen, Molecular metal-Nx centres in porous carbon for electrocatalytic hydrogen evolution, Nat Commun, 6 (2015).

[67] M.S. Thorum, J.M. Hankett, A.A. Gewirth, Poisoning the Oxygen Reduction Reaction on Carbon-Supported Fe and Cu Electrocatalysts: Evidence for Metal-Centered Activity, The Journal of Physical Chemistry Letters, 2 (2011) 295-298.

[68] J. van Doorn, M.A. Vuurman, P.J.J. Tromp, D.J. Stufkens, J.A. Moulijn, Coal Characterisation for Conversion Processes II Correlation between Raman spectroscopic data and the temperature-programmed oxidation reactivity of coals and carbons, Fuel Processing Technology, 24 (1990) 407-413.

Atomically Dispersed Cobalt Sites in Mesoporous N-Doped Carbon Matrix for Selective Catalytic hydrogenation of Nitroarenes

3

Abstract: A supported cobalt catalyst with atomically dispersed Co-N$_x$ sites (3.5 wt.% Co) in a mesoporous N-doped carbon matrix (named Co@mesoNC) is synthesized by hydrolysis of tetramethyl orthosilicate (TMOS) in a Zn/Co bimetallic zeolitic imidazolate framework (BIMZIF(Co,Zn)), followed by high-temperature pyrolysis and SiO$_2$ leaching. TEM, XRD XPS and X-ray absorption spectroscopy analysis techniques confirm the absence of cobalt nanoparticles, and indicate that these highly dispersed cobalt species are present in the form of Co-N$_x$. The outstanding stability of these Co-N$_x$ sites in the carbon matrix can be attributed to the presence of a large amount of Zn and N in the BIMZIF precursor, and SiO$_2$ in the pore space of BIMZIF(Co,Zn), extending the spatial distance between cobalt atoms and thereby impeding their agglomeration. The presence of SiO$_2$ during high-temperature pyrolysis proved crucial to create mesoporosity and maintain a high BET area and pore volume of the N-doped carbon support (1780 m^2/g, 1.54 cm^3/g). This heterogeneous Co@mesoNC catalyst has a high activity and selectivity >99% for the selective hydrogenation of nitrobenzene to aniline at mild conditions (0.5-3 MPa, 343-383 K). This reaction is nearly zero order in nitrobenzene, 0.78 order in hydrogen and an apparent activation energy of ~43 kJ/mol. Also in the hydrogenation of a wide range of functionalized nitroarenes the catalyst exhibits an outstanding activity and chemoselectivity to the corresponding substituted anilines. The presence of mesoporosity improves the mass transport of reactants and/or products and the accessibility of the active Co-N$_x$ sites, and reduces the fouling as main cause for some deactivation in subsequents runs

3.1. INTRODUCTION

Reduction of nitroarenes to their substituted anilines is of great importance in organic synthesis and applied on large scale for the production of dyes, pharmaceuticals, pigments, and agrochemicals [1-4]. In this context, hydrogen represents the most clean reductant [5-7]. Despite the development of a large number of molecular catalysts [8-12], in general these homogeneous catalysts suffer from difficulties in recycling and separation from products. Hence, heterogeneous catalysts containing supported metal nanoparticles (NPs) are more attractive [13-18]. Platinum-group metals and nickel have been proposed as alternative and are used in the direct hydrogenation of nitroarenes [19-23]. Although they are highly efficient in the activation of nitro groups, these catalysts are also highly active for hydrogenolysis of the carbon-halogen bond (*i.e.* –F, -Cl *etc.*) and hydrogenation of other reducible groups (*i.e.* C=O and C=C *etc.*), which usually leads to poor chemoselectivity [24-28]. Thus, the exploration for advanced materials that catalyse the hydrogenation of nitroarenes with outstanding activity and without compromising chemoselectivity remains challenging.

Recently, tremendous efforts have led to the development of cheaper first-row transition-metal-based hydrogenation catalysts (*i.e.* Fe, Co, and Ni) [15, 29-41], among which N-doped carbon supported cobalt materials prepared by carbonization of metal-organic-frameworks (MOFs) or a mixture of cobalt salts and organic complex exhibited good activity and chemoselectivity in the hydrogenation of nitroarenes [29-32, 39-46]. There is a general agreement that cobalt plays an indispensable role in enhancing the hydrogenation activity of the catalysts. Yet, the heterogeneity of the

cobalt species (*i.e.* accessible and inaccessible cobalt nanoparticles encapsulated by graphite shells, single cobalt atoms coordinated with nitrogen (Co-N$_x$) *etc.*) raises debate on what is the real active site in the hydrogenation process, and therefore greatly hinders the rational design and development of highly active and durable catalysts. Very recently, by one-step pyrolysis of a cobalt-containing MOF (ZIF-67) under N$_2$ atmosphere followed by a subsequent acid treatment, we proved that the accessible cobalt nanoparticles in that system exhibit a high activity for this reaction [36]. Surprisingly, after acid leaching the sample still shows outstanding hydrogenation activity. Although highly dispersed cobalt species (*i.e.* Co-N$_x$) are considered to exist in the acid-leached sample, the presence of those acid-resistant cobalt nanoparticles, fully encapsulated by multilayer graphitic carbon shells largely impedes further exploration of the structure-activity relation in this reaction. Hence, a rational design strategy that can preferentially produce active Co-N$_x$ sites should be explored.

In view of the same coordination of Co^{2+} and Zn^{2+} with 2-methylimidazole in ZIF-67 and ZIF-8 [47-49], a series of Zn/Co bimetallic zeolitic imidazolate framework (BIMZIF(Co,Zn)) have been recently reported, where the spatial distribution of Co and Zn in the framework is largely dependent on sequential addition of the metal precursors during synthesis [50-54]. Remarkably, when the precursors are added together, a homogeneous distribution of Zn and Co in the BIMZIF(Co,Zn) can be obtained. The presence of Zn^{2+} extends the adjacent distance of Co atoms in the framework, and to some extent precludes their agglomeration to cobalt NPs during the high-temperature pyrolysis [52, 53]. The carbon matrix generated using this strategy exhibits high surface area but normally

microporosity [52, 53], which can lead to significant internal mass transport limitations during the catalytic process, and therefore the catalytic activity and stability can be severely inhibited [55, 56].

Herein, we report a facile and easily scalable method to construct an atomically dispersed cobalt catalyst with 3.5 wt.% content in a mesoporous N-doped carbon for chemoselective hydrogenation of nitroarene to their substituted anilines under mild conditions. The catalyst synthesis consists of hydrolysis of tetramethyl orthosilicate (TMOS) in the pores of a BIMZIF(Co,Zn), followed by high-temperature pyrolysis and silica leaching. We demonstrate that the high Zn/Co molar ratio in the parent BIMZIF together with the SiO_2-protection strategy is crucial to impede the formation of cobalt nanoparticles and preferentially generate atomically dispersed Co-N_x sites. At the same time, the SiO_2-templated approach maintains the high specific surface area and generates mesoporosity in the N-doped carbon matrix. These Co-N_x sites in the mesoporous N-doped carbon matrix exhibit superior hydrogenation activity and chemoselectivity, and good catalytic stability. This finding opens a path for rationally designing highly active non-noble catalyst for hydrogenation reactions.

3.2. EXPERIMENTAL

3.2.1. Materials

2-Methylimidazole (MeIm, purity 99%), zinc nitrate hexahydrate ($Zn(NO_3)_2 \cdot 6H_2O$, >98%), cobalt nitrate hexahydrate ($Co(NO_3)_2 \cdot 6H_2O$, >99%), tetramethyl orthosilicate (TMOS ≥99%), and methanol (>99.8%) were purchased from Sigma-Aldrich Chemical Co. All the chemicals were used without further purification.

3.2.2 Catalyst synthesis

For the synthesis of BIMZIF(Co,Zn), a mixture of $Zn(NO_3)_2 \cdot 6H_2O$ and $Co(NO_3)_2 \cdot 6H_2O$ with Zn^{2+}/Co^{2+} molar ratio of 25 was dissolved in 200 mL methanol. A mixture of MeIm (6.489 g) in 200 mL methanol was rapidly poured into the above solution with vigorous stirring for 24 h at room temperature [52]. The total molar amount of $(Co^{2+} + Zn^{2+})$ was fixed to be 10 mmol. Afterwards, the products were collected by filtration, washed thoroughly with methanol, and dried overnight at 353 K under vacuum. For the synthesis of ZIF-8, all the steps were the same except only $Zn(NO_3)_2 \cdot 6H_2O$ and MeIm were used.

1 g of the synthesized BIMZIF(Co,Zn) was immersed in 5 mL TMOS in an autoclave, which was further transferred into a rotation oven and heated up to 333 K overnight. After the oven was cool down to room temperature, the mixture was carefully washed with 0.5 mL ethanol by filtration. Then the obtained BIMZIF@TMOS material was placed in a cotton thimble of 22 mm diameter in a glass tube of 25 mm diameter. The glass tube was fitted to a round bottom flask containing 500 ml of water. A needle to bubble the water with 10 ml min^{-1} of N_2 flux was also fitted. The temperature was raised to 323 K to create a wet N_2 stream to directly hydrolyze the TMOS molecules for 24 h, followed by drying in an oven at 333 K overnight. The obtained sample was denoted as BIMZIF@SiO_2.

Co@NC-SiO_2 was prepared by pyrolysis of 1 g BIMZIF@SiO_2 at 1173 K for 4 h under N_2 at a ramp of 2 K min^{-1}. The obtained Co@NC-SiO_2 was further leached in 1 M NaOH solution for 24 h to remove the SiO_2 template, followed by washing with deionized water until the pH reached neutral, and dried at 323 K overnight under vacuum to afford Co@mesoNC sample.

For comparison, Co@NC and NC were prepared by pyrolysis of 1 g BIMZIF(Co,Zn) and ZIF-8 at 1173 K for 4 h under N_2 at a ramp of 2 K min^{-1}, respectively.

3.2.3. Characterization

X-ray diffraction (XRD) patterns were recorded on a Bruker D8 Advance X-ray diffractometer equipped with a Co *Kα* radiation (λ = 0.179026 nm). Transmission electron microscopy (TEM) and high-resolution TEM (HR-TEM) characterization were performed by using a Talos F200X microscope (FEI, Hillsboro, OR, USA) at an acceleration voltage of 200 kV. Raman spectra were obtained with a commercial Renishaw in Via Reflex confocal microscope using a 532 nm laser. Measurements were carried out in samples without any pre-treatment at ambient conditions. The N_2 adsorption-desorption measurements were performed by using Micromeritics Tristar 3020 apparatus at 77 K [57]. Prior to measurement, samples were degassed under vacuum at 383 K overnight. The Co and N contents in the samples were measured by atomic adsorption spectroscopy (AAS) (AAnalyst 200, Perkin Elmer, USA) and elemental analysis (Vario EL, Elementar, Germany), respectively.

XPS measurements were performed on a *K*-alpha Thermo Fisher Scientific spectrometer using monochromatic Al-*Kα* radiation at ambient temperature and chamber pressure of about 10^{-8} mbar. All the spectra measured were corrected by setting the reference binding energy of carbon (*1s*) at 284.8 eV.

X-ray absorption experiments were performed at DUBBLE beam line BM26A in ESRF, Grenoble. The materials were studied using Co K-edge.

Energy calibration was achieved using metal foil as reference and the first peak in the first derivative of the metal foil XAS spectrum was calibrated to 7709 eV. Calibration and data alignment was performed using Athena and obtaining values for reference compounds from Hephaestus. After averaging, the spectra of the studied samples were normalized to a total absorption of unity and processed using the Athena data normalization and analysis package. For normalization, the spline *r*-background parameter was set to 1.0. The background subtraction was carried using a pre-edge range of -200 to -50 eV and a post-edge linear range of 60 to 830 eV. A spline range of $k = 0$ to $k = 14.8$ A^{-1} and *k*-weight of 3 was used to isolate the EXAFS (chi)function. The Co *K*-edge EXAFS spectra were Fourier transformed over a *k*-range of $k = 3$ to $k = 11$ Å^{-1}.

3.2.4. Catalyst performance

In a typical experiment, hydrogenation reactions are carried out in a batch mode, for which autoclave is filled with nitrobenzene (1 mmol), the internal standard (dodecane, 0.65 mmol), Co@mesoNC catalyst with a substrate/cobalt molar ratio of 150, and ethanol (5 ml) as solvent. Before starting the reaction, the autoclaves are purged 3 times with He to remove air, and pressurized to 3 MPa H_2, followed by heating to 383 K. After a fixed reaction time, the autoclaves are cooled down to room temperature and the hydrogen pressure is carefully released. The stirring speed is kept at 800 rpm to avoid mass transfer limitations. For recycling studies, the reaction was performed under the same conditions as mentioned above except using the recovered catalyst. The used catalyst was washed thoroughly with ethanol, dried under vacuum at 313 K overnight and then used for the next

run without any reactivation or purification. Conversions of all substrates were determined by gas chromatography (GC) analysis.

3.3. RESULTS AND DISCUSSION

3.3.1. Preparation and Characterization of the Co@mesoNC catalysts

Figure 3.1 illustrates the preparation process for the Co@mesoNC catalyst. In the first step, the BIMZIF(Co,Zn) was synthesized by reacting Co^{2+} and Zn^{2+} ions with 2-methylimidazolate (MeIm) in methanolic solution. Then tetramethyl orthosilicate (TMOS) was introduced into the pores of BIMZIF followed by hydrolysis to obtain BIMZIF@SiO_2 material. Finally, the BIMZIF@SiO_2 sample was pyrolyzed at 1173 K, and the SiO_2 template was subsequently leached with NaOH solution to generate the Co@mesoNC catalyst (see Experiment Section for the details).

The powder X-ray diffraction (XRD) pattern (Fig. B1/Appendix B) of the bimetallic ZIF matches well with ZIF-8 (Zn), confirming the structure [42, 48]. High-angle annular dark-field scanning transmission electron microscopy (HAADF-STEM) (Fig. B2a/Appendix B) and energy-dispersive X-ray spectroscopy (EDX) (Fig. B2b-e/Appendix B) images of the prepared BIMZIF crystals with size of 30-50 nm clearly exhibit a typical rhombic dodecahedral shape with homogeneously dispersed cobalt, zinc, carbon and nitrogen throughout the crystals. The tracking of each synthetic step for Co@mesoNC by TEM combined with elemental mapping analysis confirms the uniform distribution of Si and Co in both BIMZIF@SiO_2 (Fig. B3a-c/Appendix B) and Co@NC-SiO_2 materials (Fig. B3d-f/Appendix B), without cobalt nanoparticles present in Co@NC-SiO_2 (Fig. B4/Appendix B). After removal of the SiO_2 template, the absence of cobalt nanoparticles
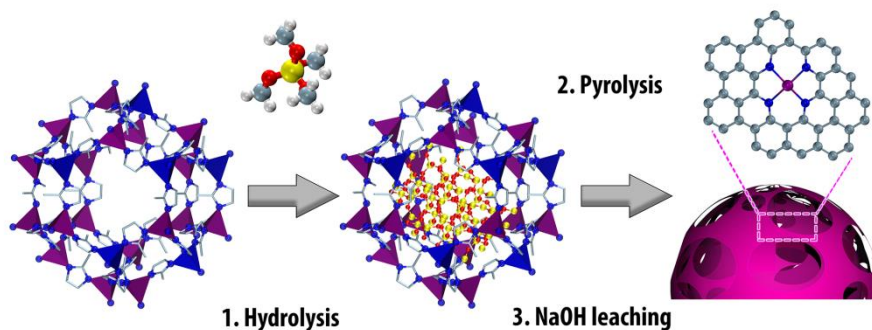
Figure 3.1: Schematic illustration of the synthesis of the Co@mesoNC catalyst. (1) Impregnation and hydrolysis of TMOS molecules in the porosity of BIMZIF. (2) Pyrolysis of the mixture of BIMZIF@SiO$_2$ in N$_2$ to decompose BIMZIF and form Co@NC-SiO$_2$. (3) NaOH leaching to remove SiO$_2$ to generate Co@mesoNC catalyst.

in the Co@mesoNC catalyst is further confirmed in Figure 3.2a,b, and uniformly dispersed Co and N EDX-signals can be clearly detected throughout the catalyst (Figure 3.2c,d). However, increasing the initial Co-loading by using an initial Zn^{2+}/Co^{2+} molar ratio of 20 in the BIMZIF(Co,Zn), some cobalt nanoparticles can be observed in the Co@NC-SiO$_2$ sample (data not shown), indicating that the current approach to avoid cobalt particle formation has limitations regarding the cobalt content. The high-resolution TEM (HR-TEM) image of Co@mesoNC in the insert of Figure 3.2a clearly demonstrates the presence of layered graphitic carbon structure with a typical interplanar distance of 0.34 nm. The absence of cobalt nanoparticles is further confirmed by the powder XRD analysis, as shown in Figure 3.3a. No cobalt (oxide) peaks can be identified, and only two diffractions at 2Θ = 30 ° and 50.5 ° can be observed, which can be attributed to the (002) and (100) planes of the graphitic carbon, respectively
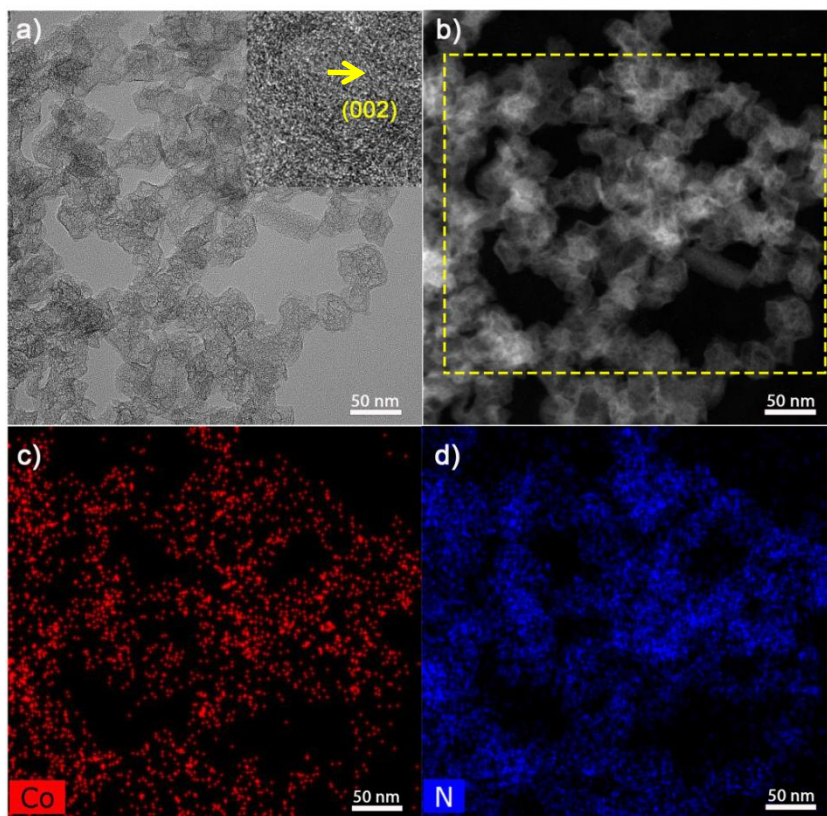
Figure 3.2: Bright field (a) and dark field (b) TEM image of Co@mesoNC catalyst; element mapping image of Co (c) and N (d) for Co@mesoNC catalyst.

[58]. The graphitization degree of the carbon matrix in the Co@mesoNC sample was further analysed by Raman spectroscopy (Fig. B5/Appendix B). The characteristic D and G bands of carbon at 1350 cm^{-1} and 1580 cm^{-1} can be clearly observed, correlated to graphitic disordered or defect carbon and sp^2-bonded graphitic carbon sheets, respectively [59]. The BET area (S_{BET}) and pore volume (V_{pore}) of the BIMZIF and Co@mesoNC were determined by N$_2$ adsorption-desorption isotherms, as shown in Figure 3.3b and Table B1/Appendix B. BIMZIF with a high S_{BET} of 1780 m^2 g^{-1} and V_{pore} of 1.44 cm^3 g^{-1}, displays a steep N$_2$ uptake at low relative pressures, typically
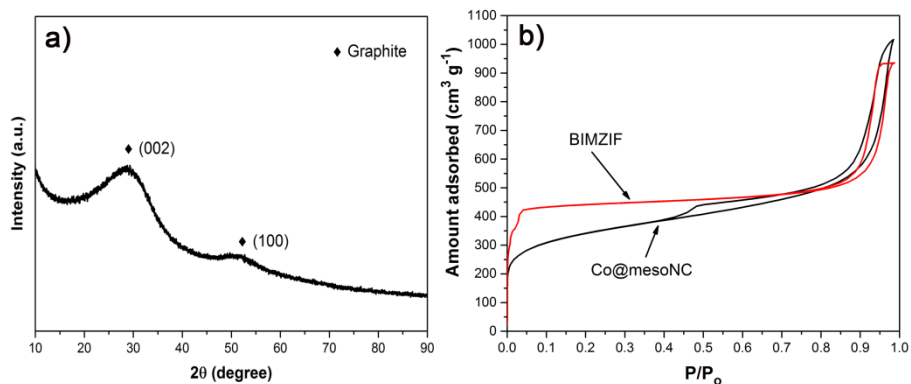
Figure 3.3: (a) XRD pattern of Co@mesoNC catalyst; (b) N_2-adsorption-desorption isotherms of BIMZIF and Co@mesoNC materials.

associated with microporosity [50]. A hysteresis loop above $P/P_0 \approx 0.8$ can also be observed for BIMZIF, suggesting the presence of intergranular mesoporosity between the crystals. After high-temperature pyrolysis and SiO_2 leaching, Co@mesoNC exhibits a S_{BET} of 1230 m^2 g^{-1} and V_{pore} of 1.54 cm^3 g^{-1}. At the same time, the N_2 adsorption-desorption isotherms of Co-@mesoNC change to type IV with type H_3 hysteresis that closes at $P/P_0 \approx$ 0.4, suggesting the presence of mesoporous structure inside the nanoparticles. The Co and N contents in the Co@mesoNC catalyst is 3.5 wt.% and 15.0 wt.%, according to atomic adsorption spectroscopy (AAS) and elemental analysis, respectively.

X-ray photoelectron spectroscopy (XPS) was further employed for Co@mesoNC catalyst to analyze the bonding state of cobalt and nitrogen. As shown in Figure 3.4a, N*1s* signals of Co@mesoNC were deconvoluted into four types of nitrogen species with binding energy around 398.5 eV, 399.8 eV, 400.8 eV, and 402.3 eV, which can be attributed to pyridinic-N (53.4 at.%), pyrrolic-N (25.5 at.%), quaternary-N (17.0 at.%) and oxidized-

N (4.1 at.%), respectively [60, 61]. A contribution from nitrogen bound to metal (Co-N) to the pyridinic-N peak at binding energy of 398.5 eV can be expected, since there is a negligible difference between binding energies of N-Co and pyridinic N species [61-63]. It is revealed that the N atoms in the pentagonal ring of the original imidazole units were mostly converted into three types of N states (pyridinic-, pyrrolic-, and quaternary-N) during the high-temperature pyrolysis process. The Co*2p* XPS spectra of Co@mesoNC is present in Figure 3.4b. No metallic Co signal (778.5 eV) can be found and the peak at 780.5 eV can be ascribed to Co-N_x configuration [53, 58, 64].

X-ray absorption spectroscopy at Co *K*-edge was conducted in an attempt to further explore the state of cobalt in the Co@mesoNC sample. As shown in the X-ray absorption near-edge structure (XANES) spectra (Figure 3.4c), a well-developed peak at 7709 eV in the pre-edge region can be observed in BIMZIF, ascribed to the electronic transition from the core *1s* to the unoccupied *3d* orbitals. This intense pre-edge peak clearly reveals that the local symmetry around cobalt ions is not centrosymmetric, confirming the tetrahedral symmetry around central cobalt atoms. The main edge absorption is due to the electronic transition from *1s* to *4p* orbitals. The threshold energy of 7725 eV in the white line, determined from the first derivative of the XANES spectra, represents a divalent state of cobalt ions in the framework. After pyrolysis and SiO_2 removal, the edge for Co@mesoNC is situated at higher energy than that of Co foil, indicating that no metallic cobalt phase is present in Co@mesoNC. In addition, a lower intensity of the pre-edge feature in Co@mesoNC can be observed compared to the original BIMZIF, suggesting that the tetrahedral coordination environment of cobalt in the framework changed during the pyrolysis [65].
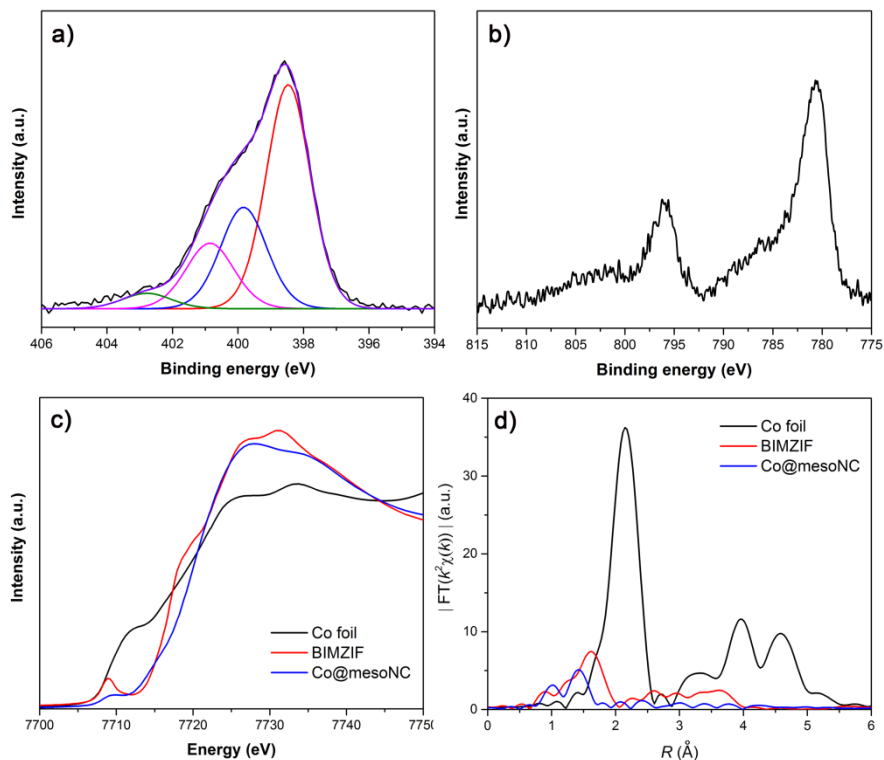
Figure 3.4: N*1s* (a) and Co*2p* (b) XPS regions of Co@mesoNC catalyst; (c) Co *K*-edge XANES spectra and (d) the k^2-weighted $\chi(k)$-function of the EXAFS spectra of Co@mesoNC catalyst.

Further local structural information about Co atoms can be obtained from the extended X-ray absorption fine structure (EXAFS), as shown in Figure 3.4d. The Fourier transformed curve for BIMZIF exhibits a peak at 1.60 Å, which can be attributed to the Co-N bond in the sodalite crystal structure [53, 65]. After pyrolysis, the Co-N coordination peak shifts to a lower R-position for Co@mesoNC at 1.41 Å, demonstrating that the main coordination mode of Co varies slightly. Indeed, a similar shift was also observed by Yin *et al.*, who attributed it to the breakage of part of Co-N bonds from Co-N_4 to Co-N_2 during high-temperature pyrolysis [53].

Importantly, compared to the Co foil, the Fourier transform for Co@mesoNC clearly shows the absence of Co-Co path at 2.16 Å, further confirming that Co is atomically dispersed.

To clarify the role of SiO_2 during the synthesis, Co@NC prepared by direct pyrolysis of BIMZIF under the same conditions was also investigated. In the absence of SiO_2 during pyrolysis, both cobalt nanoparticles and highly dispersed $Co-N_x$ species can be observed in the TEM image of this sample (Fig. B6a-d/Appendix B), although it exhibits a comparable graphitization degree as the Co@mesoNC sample, as concluded from a similar I_D/I_G ratio in the Raman spectra (Fig. B5/Appendix B). In addition, N_2 adsorption-desorption isotherms indicate that Co@NC exhibits a typical microporous structure with some intergranular mesoporosity, as concluded from the presence of hysteresis loop above $P/P_0 \approx 0.8$ (Fig. B7/Appendix B). The Brunauer-Emmett-Teller area (S_{BET}) and pore volume (V_{pore}) of Co@NC are 680 m^2 g^{-1} and 0.98 m^3 g^{-1}, much lower than that of Co-@mesoNC (1230 m^2 g^{-1} and 1.54 m^3 g^{-1}) (Table B1/Appendix B), attributed to the collapse of the well-defined microporous structure of BIMZIF during the pyrolysis process [36, 66].

The preferred formation of $Co-N_x$ sites and the absence of cobalt nanoparticles in the Co@mesoNC catalyst can be attributed to the following: (1) When a large amount of Zn is present in the original BIMZIF material, the spatial distance between two Co atoms can be finely controlled by Zn atoms acting as a spacer, thereby precluding the agglomeration of cobalt atoms to nanoparticles during the high-temperature pyrolysis. (2) During the pyrolysis process, the low boiling point Zn atoms can evaporate [67], and free N-coordination sites can be generated in the carbon matrix, which aid to

stabilize the Co atoms [52, 53]. (3) The presence of SiO_2 nanoparticles in the well-developed porosity of BIMZIF further mitigates the sintering of Co atoms under high-temperature pyrolysis condition [68]. Thus, the SiO_2-templated strategy in this work impedes the formation of cobalt nanoparticles, creates mesoporosity and maintains the high specific surface area in the N-doped carbon matrix.

3.3.2. Catalytic Hydrogenation of Nitrobenzene to Aniline over the Co-@mesoNC catalyst

Direct hydrogenation of nitrobenzene with H_2 requires an efficient catalyst to simultaneously promote the activation of hydrogen molecules and nitro groups in the substrates. In order to clearly understand the catalytic activity of the Co@mesoNC catalyst in this process, a series of control experiments were firstly performed. As shown in Table 3.1, hydrogenation of nitrobenzene to aniline did not proceed in the absence of catalyst (Entry 1, Table 3.1) or H_2 (Entry 2, Table 3.1). Similarly, no aniline was detected over the original BIMZIF (Entry 3, Table 3.1) and the 'NC' sample prepared by pyrolysis of ZIF-8 crystals (Entry 4, Table 3.1) under the same conditions. However, the Co@mesoNC sample catalysed effciently the hydrogenation of nitrobenzene to aniline without any other detectable products (Entry 5, Table 3.1) under the identical conditions. These results reveal that the highly dispersed Co-N_x species generated during high temperature pyrolysis are the active sites for the chemoselective hydrogenation of nitro groups. In addition, the hydrogenation activity of the Co@mesoNC catalyst is dependent on H_2 pressure (Entries 5-8, Table 3.1) and reaction temperature (Entry 5, Entries 9-10, Table 3.1) as well, with

Table 3.1: Results of the catalytic hydrogenation of nitrobenzene over the prepared catalysts [a].

Entry	Sample	T (K)	P (MPa)	X_{Nitro} (%)	$S_{Aniline}$ (%)	Catalyst productivity ($mmol_{NB}$ h^{-1} mg_{Co}^{-1})[b]
1	No catalyst	383	3	-	-	-
2[c]	Co@mesoNC	383	3	-	-	-
3	BIMZIF	383	3	-	-	-
4[d]	NC	383	3	-	-	-
5	Co@mesoNC	383	3	55	>99	0.72
6	Co@mesoNC	383	0.5	14	>99	0.18
7	Co@mesoNC	383	1	25	>99	0.32
8	Co@mesoNC	383	2	43	>99	0.55
9	Co@mesoNC	343	3	12	>99	0.15
10	Co@mesoNC	363	3	27	>99	0.34

[a]: Reaction conditions: 1 mmol nitrobenzene, substrate to cobalt molar ratio of 150, 0.65 mmol dodecane as internal standard, 5 mL ethanol, 383 K, 3MPa H_2, 2 h. [b]: calculated by moles of nitrobenzene consumed divided by total weight of cobalt per hour. [c]: reaction was performed in He atmosphere. d: prepared by pyrolysis of ZIF-8 crystals under N_2 flow.

reaction order in hydrogen of ~0.78 and an apparent activation energy of ~43 kJ/mol. Obviously, a higher H_2 pressure and a high reaction temperature promote the hydrogenation; hence in all subsequent experiments the reaction conditions were fixed at 3 MPa H_2 and 383 K. Importantly, the kinetic profile of the reaction in Figure 3.5a indicates that nitrobenzene could be converted smoothly into aniline with initially a nearly zero order in concentration, and no intermediates could be detected by gas chromatography during the entire reaction process. Interestingly, the catalytic activity of Co@mesoNC is superior to the behavior of other recently reported supported cobalt catalysts (Table B2/Appendix B), such as Co@N-doped Carbon [29], CoO_x@NCNTs [30], Co-SiCN [31], and Co-Co_3O_4/NGr@C [43].
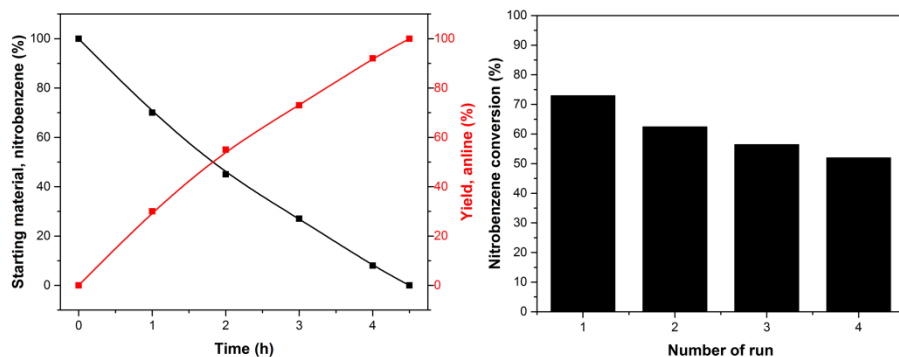
Figure 3.5: (a) Kinetic data of hydrogenation of nitrobenzene with Co@mesoNC catalyst (*left*); (b) Recycling experiments of hydrogenation of nitrobenzene with Co@mesoNC catalyst (*right*). Reaction conditions: 1 mmol nitrobenzene, substrate to cobalt molar ratio of 150, 0.65 mmol dodecane as internal standard, 5 mL ethanol, 383 K, 3 MPa H_2, 3 h for recycling experiments. Aniline selectivity >99%.

The stability and reusability of the Co@mesoNC catalyst was also investigated. As presented in Figure 3.5b, the Co@mesoNC catalyst exhibits an initial nitrobenzene conversion as high as 73% (2 h), and can be reused at least four times with a nitrobenzene conversion still >51% after the fourth run. The TEM image of the Co@mesoNC after the fourth run shows that the Co atoms in the N-doped carbon matrix are still well dispersed and no cobalt nanoparticles can be detected (Fig. B8/Appendix B), excluding the agglomeration of cobalt as a major cause of deactivation during hydrogenation. The carbon structure (i.e. graphitization degree) in the spent Co@mesoNC catalyst is still well preserved as revealed by the Raman spectra analysis in Fig. B9/Appendix B, suggesting that the deactivation cannot be attributed to the modification of carbon structure during the hydrogenation process. ICP analysis indicates that a small amount of cobalt (~ 2 wt.% of the total cobalt content) could be detected in the reaction medium after each run (Table B3/Appendix B). At the same time, after each
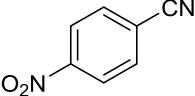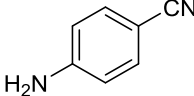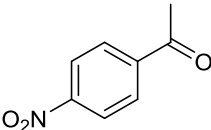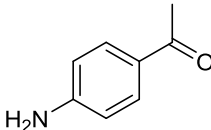
run, a slight increase of catalyst mass (~2%) was observed even after a thorough washing with ethanol and vacuum drying, indicative of some residual deposit in the pores of the catalysts, which cannot be easily removed. Hence, the deactivation of Co@mesoNC catalyst is ascribed mainly to fouling by unidentified deposits during reaction, although some minute loss of cobalt cannot be excluded. This fouling is stronger for the microporous Co@NC sample prepared by direct pyrolysis of BIMZIF(Co,Zn). After an initial nitrobenzene conversion of only 34%, this decreases sharply to 6% after 4 consecutive runs (Fig. B10/Appendix B). The inferior hydrogenation performance of Co@NC further demonstrates the high activity of these highly dispersed Co-N$_x$ sites in the mesoporous carbon matrix, which contributes to the accessibility of the active Co-N$_x$ sites and improved mass transport of substrate molecules during the hydrogenation process.

3.3.3. Co@mesoNC Catalyzed Hydrogenation of Nitroarenes to Substituted Anilines

To explore the general applicability of Co@mesoNC, a variety of substituted nitroarenes containing electron-donating and electron-withdrawing groups at different positions were investigated under the standard test conditions. As shown in Table 3.2, the Co@mesoNC catalyst exhibits a high activity for the hydrogenation of industrially relevant nitroarenes such as fluoro- and chloro-nitrobenzenes toward their corresponding anilines in high selectivities (Table 3.2, entries 1-4). Even a sterically hindered nitroarene was hydrogenated to the substituted aniline with outstanding activity and chemoselectivity (Table 3.2, entry 5). As it is

Table 3.2: Results of the chemoselective hydrogenation of substituted nitroarenes over Co@mesoNC [a].

Entry	Substrate	Product	S (%)[b]	Catalyst productivity (mmol$_{Nitro}$ h^{-1} mg$_{Co}$$^{-1}$)[c]
1			>98	0.70
2			>99	0.79
3			>99	0.79
4			>98	0.75
5			>99	0.40
6			>97	0.46
7			>97	0.22
8			>98	0.53

Entry	Substrate	Product	Selectivity	Activity
9[d]	O₂N–C₆H₄–CN	H₂N–C₆H₄–CN	>93	0.51
10[d]	O₂N–C₆H₄–C(=O)CH₃	H₂N–C₆H₄–C(=O)CH₃	>96	0.48

a: Reaction conditions: 1 mmol nitrobenzene, substrate to cobalt molar ratio of 150, 0.65 mmol dodecane as internal standard, 5 mL ethanol, 383 K, 3MPa H_2, 2 h; b: selectivity to the substituted anilines; c: calculated by moles of nitroarenes consumed divided by total mass of cobalt per hour; d: reaction time 3 h.

well known, the most-challenging substrates are those that bear other easily reducible groups (Table 3.2, entries 6-11). Surprisingly, the Co@mesoNC catalyst is able to chemoselectively reduce nitro groups in the presence of C=C bonds with high activity (Table 3.2, entry 6) (Table B4/Appendix B), which is hardly achieved by Pt-group and Ni catalysts [39, 43]. Furthermore, substrates containing sensitive groups, such as –I, -OCH$_3$, and -CN can be as well smoothly and chemoselectively hydrogenated into the corresponding anilines without dehalogenation and/or competitive hydrogenation on these substituted moieties (Table 3.2, entries 7-11). All these results demonstrate again that the atomically dispersed Co-N$_x$ sites in the mesoporous N-doped carbon matrix displays excellent catalytic activity and chemoselectivity for hydrogenation of nitroarenes using molecular hydrogen.

3.4. CONCLUSIONS

In this work a strategy is presented to synthesize a supported cobalt catalyst with atomically dispersed Co-N$_x$ sites (3.5 wt.% Co) in a mesoporous N-doped carbon matrix. The synthesis process consists of hydrolysis of TMOS molecules in BIMZIF(Co,Zn), high-temperature

pyrolysis and removal of the SiO_2 template. The preferential formation and high stability of these $Co-N_x$ sites in the carbon support are attributed to the presence of a large amount of Zn and N in the structure of the BIMZIF precursor and the presence of SiO_2 in the porosity of BIMZIF, which to a large extent extend the spatial distance between the cobalt atoms, thereby impeding their agglomeration to nanoparticles. The SiO_2-templated approach is proven essential to generate mesoporosity in the N-doped carbon support and to maintain a high specific surface area in the carbon support during high-temperature pyrolysis as well. These $Co-N_x$ sites in the mesoporous N-doped carbon matrix exhibit an outstanding activity and selectivity for the chemoselective hydrogenation of nitroarenes for a wide range of substrates under mild reaction conditions. The mesoporosity of this catalyst probably guaranteed a good mass transport of reactants and/or products and the accessibility of the active $Co-N_x$ sites, thereby also reducing the deactivation of the catalyst by fouling.

REFERENCES

[1] R.S. Downing, P.J. Kunkeler, H. van Bekkum, Catalytic Amination Reactions - Catalytic syntheses of aromatic amines, Catalysis Today, 37 (1997) 121-136.

[2] N. Ono, The Nitro Group in Organic Synthesis, Wiley-VCH, New York, 2001.

[3] H.-U. Blaser, H. Steiner, M. Studer, Selective Catalytic Hydrogenation of Functionalized Nitroarenes: An Update, ChemCatChem, 1 (2009) 210-221.

[4] H.-U. Blaser, C. Malan, B. Pugin, F. Spindler, H. Steiner, M. Studer, Selective Hydrogenation for Fine Chemicals: Recent Trends and New Developments, Advanced Synthesis & Catalysis, 345 (2003) 103-151.

[5] P.N. Rylander, Catalytic Hydrogenation in Organic Syntheses: Paul Rylander, Academic Press Incorporated, 1979.

[6] J.G. de Vries, C.J. Elsevier, The handbook of homogeneous hydrogenation, Wiley-VCH, 2007.

[7] P.G. Andersson, I.J. Munslow, Modern Reduction Methods, Wiley, 2008.

[8] F. L'Eplattenier, P. Matthys, F. Calderazzo, Homogeneous ruthenium-catalyzed reduction of nitrobenzene, Inorganic Chemistry, 9 (1970) 342-345.

[9] A. Corma, C. González-Arellano, M. Iglesias, F. Sánchez, Gold complexes as catalysts: Chemoselective hydrogenation of nitroarenes, Applied Catalysis A: General, 356 (2009) 99-102.

[10] K. Junge, K. Schroder, M. Beller, Homogeneous catalysis using iron complexes: recent developments in selective reductions, Chemical Communications, 47 (2011) 4849-4859.

[11] R.J. Rahaim, R.E. Maleczka, Pd-Catalyzed Silicon Hydride Reductions of Aromatic and Aliphatic Nitro Groups, Organic Letters, 7 (2005) 5087-5090.

[12] P.M. Reis, B. Royo, Chemoselective hydrogenation of nitroarenes and deoxygenation of pyridine N-oxides with H2 catalyzed by MoO2Cl2, Tetrahedron Letters, 50 (2009) 949-952.

[13] S. Nishimura, Handbook of Heterogeneous Catalytic Hydrogenation for Organic Synthesis, Wiley, 2001.

[14] R.A. Sheldon, H. Bekkum, Fine Chemicals Through Heterogenous Catalysis, Wiley-VCH, 2001.

[15] R.V. Jagadeesh, A.-E. Surkus, H. Junge, M.-M. Pohl, J. Radnik, J. Rabeah, H. Huan, V. Schünemann, A. Brückner, M. Beller, Nanoscale Fe2O3-Based Catalysts for Selective Hydrogenation of Nitroarenes to Anilines, Science, 342 (2013) 1073-1076.

[16] A. Corma, P. Serna, Chemoselective Hydrogenation of Nitro Compounds with Supported Gold Catalysts, Science, 313 (2006) 332-334.

[17] Y. Chen, C. Wang, H. Liu, J. Qiu, X. Bao, Ag/SiO2: a novel catalyst with high activity and selectivity for hydrogenation of chloronitrobenzenes, Chemical Communications, (2005) 5298-5300.

[18] A. Onopchenko, E.T. Sabourin, C.M. Selwitz, Selective catalytic hydrogenation of aromatic nitro groups in the presence of acetylenes. Synthesis of (3-aminophenyl)acetylene via hydrogenation of dimethylcarbinol substituted (3-nitrophenyl)acetylene over heterogeneous metallic ruthenium catalyst, The Journal of Organic Chemistry, 44 (1979) 1233-1236.

[19] G. Vilé, N. Almora-Barrios, N. López, J. Pérez-Ramírez, Structure and Reactivity of Supported Hybrid Platinum Nanoparticles for the Flow Hydrogenation of Functionalized Nitroaromatics, ACS Catalysis, 5 (2015) 3767-3778.

[20] A. Yarulin, C. Berguerand, I. Yuranov, F. Cárdenas-Lizana, I. Prokopyeva, L. Kiwi-Minsker, Pt–Zn nanoparticles supported on porous polymeric matrix for selective 3-nitrostyrene hydrogenation, Journal of Catalysis, 321 (2015) 7-12.

[21] M. Carrus, M. Fantauzzi, F. Riboni, M. Makosch, A. Rossi, E. Selli, J.A. van Bokhoven, Increased conversion and selectivity of 4-nitrostyrene hydrogenation to 4-aminostyrene on Pt nanoparticles supported on titanium-tungsten mixed oxides, Applied Catalysis A: General, 519 (2016) 130-138.

[22] J. Gu, Z. Zhang, P. Hu, L. Ding, N. Xue, L. Peng, X. Guo, M. Lin, W. Ding, Platinum Nanoparticles Encapsulated in MFI Zeolite Crystals by a Two-Step Dry Gel Conversion Method as a Highly Selective Hydrogenation Catalyst, ACS Catalysis, 5 (2015) 6893-6901.

[23] S. Zhang, C.-R. Chang, Z.-Q. Huang, J. Li, Z. Wu, Y. Ma, Z. Zhang, Y. Wang, Y. Qu, High Catalytic Activity and Chemoselectivity of Sub-nanometric Pd Clusters on Porous Nanorods of CeO_2 for Hydrogenation of Nitroarenes, Journal of the American Chemical Society, 138 (2016) 2629-2637.

[24] A. Corma, P. Serna, P. Concepción, J.J. Calvino, Transforming Nonselective into Chemoselective Metal Catalysts for the Hydrogenation of Substituted Nitroaromatics, Journal of the American Chemical Society, 130 (2008) 8748-8753.

[25] G.C. Bond, Supported metal catalysts: some unsolved problems, Chemical Society Reviews, 20 (1991) 441-475.

[26] B. Coq, A. Tijani, R. Dutartre, F. Figuéras, Influence of support and metallic precursor on the hydrogenation of p-chloronitrobenzene over supported platinum catalysts, Journal of Molecular Catalysis, 79 (1993) 253-264.

[27] X. Han, R. Zhou, G. Lai, X. Zheng, Influence of support and transition metal (Cr, Mn, Fe, Co, Ni and Cu) on the hydrogenation of p-chloronitrobenzene over supported platinum catalysts, Catalysis Today, 93–95 (2004) 433-437.

[28] S. Kataoka, Y. Takeuchi, A. Harada, T. Takagi, Y. Takenaka, N. Fukaya, H. Yasuda, T. Ohmori, A. Endo, Microreactor containing platinum nanoparticles for nitrobenzene hydrogenation, Applied Catalysis A: General, 427–428 (2012) 119-124.

[29] D. Formenti, F. Ferretti, C. Topf, A.-E. Surkus, M.-M. Pohl, J. Radnik, M. Schneider, K. Junge, M. Beller, F. Ragaini, Co-based heterogeneous catalysts from well-defined α-diimine complexes: Discussing the role of nitrogen, Journal of Catalysis, 351 (2017) 79-89.

[30] Z. Wei, J. Wang, S. Mao, D. Su, H. Jin, Y. Wang, F. Xu, H. Li, Y. Wang, In Situ-Generated Co0-Co3O4/N-Doped Carbon Nanotubes Hybrids as Efficient and Chemoselective Catalysts for Hydrogenation of Nitroarenes, ACS Catalysis, 5 (2015) 4783-4789.

[31] T. Schwob, R. Kempe, A Reusable Co Catalyst for the Selective Hydrogenation of Functionalized Nitroarenes and the Direct Synthesis of Imines and Benzimidazoles from Nitroarenes and Aldehydes, Angewandte Chemie International Edition, 55 (2016) 15175-15179.

[32] T. Cheng, H. Yu, F. Peng, H. Wang, B. Zhang, D. Su, Identifying active sites of CoNC/CNT from pyrolysis of molecularly defined complexes for oxidative

esterification and hydrogenation reactions, Catalysis Science & Technology, 6 (2016) 1007-1015.

[33] B. Chen, F. Li, Z. Huang, G. Yuan, Recyclable and Selective Nitroarene Hydrogenation Catalysts Based on Carbon-Coated Cobalt Oxide Nanoparticles, ChemCatChem, 8 (2016) 1132-1138.

[34] G. Hahn, J.-K. Ewert, C. Denner, D. Tilgner, R. Kempe, A Reusable Mesoporous Nickel Nanocomposite Catalyst for the Selective Hydrogenation of Nitroarenes in the Presence of Sensitive Functional Groups, ChemCatChem, 8 (2016) 2461-2465.

[35] S. Pisiewicz, D. Formenti , A.-E. Surkus, M.-M. Pohl, J. Radnik, K. Junge, C. Topf, S. Bachmann, M. Scalone, M. Beller, Synthesis of Nickel Nanoparticles with N-Doped Graphene Shells for Catalytic Reduction Reactions, ChemCatChem, 8 (2016) 129-134.

[36] X. Sun, A.I. Olivos-Suarez, L. Oar-Arteta, E. Rozhko, D. Osadchii, A. Bavykina, F. Kapteijn, J. Gascon, Metal–Organic Framework Mediated Cobalt/Nitrogen-Doped Carbon Hybrids as Efficient and Chemoselective Catalysts for the Hydrogenation of Nitroarenes, ChemCatChem, 9 (2017) 1854-1862.

[37] W.-J. Liu, K. Tian, H. Jiang, One-pot synthesis of Ni-NiFe2O4/carbon nanofiber composites from biomass for selective hydrogenation of aromatic nitro compounds, Green Chemistry, 17 (2015) 821-826.

[38] L. Liu, P. Concepción, A. Corma, Non-noble metal catalysts for hydrogenation: A facile method for preparing Co nanoparticles covered with thin layered carbon, Journal of Catalysis, 340 (2016) 1-9.

[39] L. Liu, F. Gao, P. Concepción, A. Corma, A new strategy to transform mono and bimetallic non-noble metal nanoparticles into highly active and chemoselective hydrogenation catalysts, Journal of Catalysis, 350 (2017) 218-225.

[40] F. Zhang, C. Zhao, S. Chen, H. Li, H. Yang, X.-M. Zhang, In situ mosaic strategy generated Co-based N-doped mesoporous carbon for highly selective hydrogenation of nitroaromatics, Journal of Catalysis, 348 (2017) 212-222.

[41] X. Wang, Y. Li, Chemoselective hydrogenation of functionalized nitroarenes using MOF-derived co-based catalysts, Journal of Molecular Catalysis A: Chemical, 420 (2016) 56-65.

[42] X. Sun, A.I. Olivos Suarez, L. Oar Arteta, E. Rozhko, D. Osadchii, A. Bavykina, F. Kapteijn, J. Gascon, Metal-Organic-Framework Mediated Cobalt/N-Doped Carbon Hybrids as Efficient and Chemoselective Catalysts for the Hydrogenation of Nitroarenes, ChemCatChem, (2017) n/a-n/a.

[43] F.A. Westerhaus, R.V. Jagadeesh, G. Wienhöfer, M.-M. Pohl, J. Radnik, A.-E. Surkus, J. Rabeah, K. Junge, H. Junge, M. Nielsen, A. Brückner, M. Beller, Heterogenized cobalt oxide catalysts for nitroarene reduction by pyrolysis of molecularly defined complexes, Nat Chem, 5 (2013) 537-543.

[44] R.V. Jagadeesh, D. Banerjee, P.B. Arockiam, H. Junge, K. Junge, M.-M. Pohl, J. Radnik, A. Bruckner, M. Beller, Highly selective transfer hydrogenation of functionalised nitroarenes using cobalt-based nanocatalysts, Green Chemistry, 17 (2015) 898-902.

[45] D. Formenti, C. Topf, K. Junge, F. Ragaini, M. Beller, Fe2O3/NGr@C- and Co-Co3O4/NGr@C-catalysed hydrogenation of nitroarenes under mild conditions, Catalysis Science & Technology, 6 (2016) 4473-4477.

[46] K. Shen, L. Chen, J. Long, W. Zhong, Y. Li, MOFs-Templated Co@Pd Core–Shell NPs Embedded in N-Doped Carbon Matrix with Superior Hydrogenation Activities, ACS Catalysis, 5 (2015) 5264-5271.

[47] X.-C. Huang, Y.-Y. Lin, J.-P. Zhang, X.-M. Chen, Ligand-Directed Strategy for Zeolite-Type Metal–Organic Frameworks: Zinc(II) Imidazolates with Unusual Zeolitic Topologies, Angewandte Chemie International Edition, 45 (2006) 1557-1559.

[48] K.S. Park, Z. Ni, A.P. Côté, J.Y. Choi, R. Huang, F.J. Uribe-Romo, H.K. Chae, M. O'Keeffe, O.M. Yaghi, Exceptional chemical and thermal stability of zeolitic imidazolate frameworks, Proceedings of the National Academy of Sciences, 103 (2006) 10186-10191.

[49] R. Banerjee, A. Phan, B. Wang, C. Knobler, H. Furukawa, M. O'Keeffe, O.M. Yaghi, High-Throughput Synthesis of Zeolitic Imidazolate Frameworks and Application to CO_2 Capture, Science, 319 (2008) 939-943.

[50] J. Tang, R.R. Salunkhe, J. Liu, N.L. Torad, M. Imura, S. Furukawa, Y. Yamauchi, Thermal Conversion of Core–Shell Metal–Organic Frameworks: A New Method for Selectively Functionalized Nanoporous Hybrid Carbon, Journal of the American Chemical Society, 137 (2015) 1572-1580.

[51] J. Yang, F. Zhang, H. Lu, X. Hong, H. Jiang, Y. Wu, Y. Li, Hollow Zn/Co ZIF Particles Derived from Core–Shell ZIF-67@ZIF-8 as Selective Catalyst for the Semi-Hydrogenation of Acetylene, Angewandte Chemie International Edition, 54 (2015) 10889-10893.

[52] Y.-Z. Chen, C. Wang, Z.-Y. Wu, Y. Xiong, Q. Xu, S.-H. Yu, H.-L. Jiang, From Bimetallic Metal-Organic Framework to Porous Carbon: High Surface Area and Multicomponent Active Dopants for Excellent Electrocatalysis, Advanced Materials, 27 (2015) 5010-5016.

[53] P. Yin, T. Yao, Y. Wu, L. Zheng, Y. Lin, W. Liu, H. Ju, J. Zhu, X. Hong, Z. Deng, G. Zhou, S. Wei, Y. Li, Single Cobalt Atoms with Precise N-Coordination as Superior Oxygen Reduction Reaction Catalysts, Angewandte Chemie International Edition, 55 (2016) 10800-10805.

[54] J. Tang, R.R. Salunkhe, H. Zhang, V. Malgras, T. Ahamad, S.M. Alshehri, N. Kobayashi, S. Tominaka, Y. Ide, J.H. Kim, Y. Yamauchi, Bimetallic Metal-Organic Frameworks for Controlled Catalytic Graphitization of Nanoporous Carbons, Scientific Reports, 6 (2016) 30295.

[55] X. Kang, H. Liu, M. Hou, X. Sun, H. Han, T. Jiang, Z. Zhang, B. Han, Synthesis of Supported Ultrafine Non-noble Subnanometer-Scale Metal Particles Derived from Metal–Organic Frameworks as Highly Efficient Heterogeneous Catalysts, Angewandte Chemie, 128 (2016) 1092-1096.

[56] H. Li, H. Yang, H. Li, Highly active mesoporous Co–B amorphous alloy catalyst for cinnamaldehyde hydrogenation to cinnamyl alcohol, Journal of Catalysis, 251 (2007) 233-238.

[57] M.F. De Lange, T.J.H. Vlugt, J. Gascon, F. Kapteijn, Adsorptive characterization of porous solids: Error analysis guides the way, Microporous and Mesoporous Materials, 200 (2014) 199-215.

[58] H. Fei, J. Dong, M.J. Arellano-Jiménez, G. Ye, N. Dong Kim, E.L.G. Samuel, Z. Peng, Z. Zhu, F. Qin, J. Bao, M.J. Yacaman, P.M. Ajayan, D. Chen, J.M. Tour,

Atomic cobalt on nitrogen-doped graphene for hydrogen generation, Nature Communications, 6 (2015) 8668.

[59] B.Y. Xia, Y. Yan, N. Li, H.B. Wu, X.W. Lou, X. Wang, A metal–organic framework-derived bifunctional oxygen electrocatalyst, Nature Energy, 1 (2016) 15006.

[60] J.R. Pels, F. Kapteijn, J.A. Moulijn, Q. Zhu, K.M. Thomas, Evolution of nitrogen functionalities in carbonaceous materials during pyrolysis, Carbon, 33 (1995) 1641-1653.

[61] J. Casanovas, J.M. Ricart, J. Rubio, F. Illas, J.M. Jiménez-Mateos, Origin of the Large N 1s Binding Energy in X-ray Photoelectron Spectra of Calcined Carbonaceous Materials, Journal of the American Chemical Society, 118 (1996) 8071-8076.

[62] H.-W. Liang, W. Wei, Z.-S. Wu, X. Feng, K. Müllen, Mesoporous Metal–Nitrogen-Doped Carbon Electrocatalysts for Highly Efficient Oxygen Reduction Reaction, Journal of the American Chemical Society, 135 (2013) 16002-16005.

[63] G. Wu, C.M. Johnston, N.H. Mack, K. Artyushkova, M. Ferrandon, M. Nelson, J.S. Lezama-Pacheco, S.D. Conradson, K.L. More, D.J. Myers, P. Zelenay, Synthesis-structure-performance correlation for polyaniline-Me-C non-precious metal cathode catalysts for oxygen reduction in fuel cells, Journal of Materials Chemistry, 21 (2011) 11392-11405.

[64] L. Shang, H. Yu, X. Huang, T. Bian, R. Shi, Y. Zhao, G.I.N. Waterhouse, L.-Z. Wu, C.-H. Tung, T. Zhang, Well-Dispersed ZIF-Derived Co,N-Co-doped Carbon Nanoframes through Mesoporous-Silica-Protected Calcination as Efficient Oxygen Reduction Electrocatalysts, Advanced Materials, 28 (2016) 1668-1674.

[65] F. Hillman, J.M. Zimmerman, S.-M. Paek, M.R.A. Hamid, W.T. Lim, H.-K. Jeong, Rapid microwave-assisted synthesis of hybrid zeolitic-imidazolate frameworks with mixed metals and mixed linkers, Journal of Materials Chemistry A, 5 (2017) 6090-6099.

[66] N.L. Torad, M. Hu, S. Ishihara, H. Sukegawa, A.A. Belik, M. Imura, K. Ariga, Y. Sakka, Y. Yamauchi, Direct Synthesis of MOF-Derived Nanoporous Carbon with Magnetic Co Nanoparticles toward Efficient Water Treatment, Small, 10 (2014) 2096-2107.

[67] B. Liu, H. Shioyama, T. Akita, Q. Xu, Metal-Organic Framework as a Template for Porous Carbon Synthesis, Journal of the American Chemical Society, 130 (2008) 5390-5391.

[68] Y.J. Sa, D.-J. Seo, J. Woo, J.T. Lim, J.Y. Cheon, S.Y. Yang, J.M. Lee, D. Kang, T.J. Shin, H.S. Shin, H.Y. Jeong, C.S. Kim, M.G. Kim, T.-Y. Kim, S.H. Joo, A General Approach to Preferential Formation of Active Fe–Nx Sites in Fe–N/C Electrocatalysts for Efficient Oxygen Reduction Reaction, Journal of the American Chemical Society, 138 (2016) 15046-15056.

Stepwise synthesis of highly loaded and active Silica supported Cobalt Fischer-Tropsch catalysts using Metal Organic Frameworks as sacrificial templates

4

Abstract: The development of synthetic protocols for the preparation of highly loaded metal nanoparticle supported catalysts has received a great deal of attention over the last few decades. Independently controlling metal loading, nanoparticle size, distribution and accessibility has proven challenging because of the clear interdependence between these crucial performance parameters. Here we present a stepwise methodology that, making use of a cobalt-containing Metal Organic Framework as hard template (ZIF-67), allows addressing this long-standing challenge. Condensation of silica in the Co-MOF pore space followed by pyrolysis and subsequent calcination of these composites renders highly loaded cobalt nanocomposites (~50 wt.% Co), with cobalt oxide reducibility in the order of 80% and a good particle dispersion, that exhibit high activity, C5+ selectivity, and excellent stability in Fischer-Tropsch synthesis.

4.1. INTRODUCTION

Metal (oxide) nanoparticles are instrumental in the development of new applications: from the production of fuels and chemicals through catalytic processes,[1] to nanoelectronics,[2] and energy conversion and storage.[3] Because most chemical and electronic phenomena occur at the surface, the intrinsic properties of nanoparticles depend strongly on their size, spatial distribution and even on their shape.[4, 5] In general, small nanoparticles show high surface energies and are thermally unstable and prone to aggregate into larger clusters.[6] To tackle this issue, a general strategy consists of the use of supports with high surface area and well-developed porosity (e.g. SiO_2 and Al_2O_3) that stabilize and prevent nanoparticle aggregation.[5, 7, 8]

Ion-adsorption,[9, 10] impregnation and subsequent drying,[7] or deposition-precipitation[11, 12] are among the most commonly used methods for the preparation of supported nanoparticles. Metal loading, nanoparticle size and distribution are the three most important parameters that define performance of supported nanoparticles. While it would be ideal to control independently each one of these parameters, in reality a strong interdependence exists. For example, for the methods described above, metal loading and particle size usually go hand in hand as a result of the fact that bigger nanoparticles and/or clusters are formed when high metal loadings are used. This interdependence is a clear drawback for the development of more efficient nanoparticle based composites for application in i.e. heterogeneous catalysis. Structure sensitive reactions such as Fischer-Tropsch synthesis (FTS) are an outstanding example. For this specific process, when Co is used as the active metal, catalytic activity and

selectivity to long chain hydrocarbons are maximized when nanoparticles in the order of 8-30 nm are used.[13, 14] Because of this reason, impregnation is the most widely used method for the preparation of industrial FTS catalysts.[15, 16] However, using this method the maximum metal loading usually achieved is not higher than a 20 wt.%.[7, 17, 18] As an alternative, deposition-precipitation methods have been developed to achieve higher metal loadings.[19, 20] Yet, a large fraction of irreducible species (i.e. metal silicates and/or aluminates) is formed, resulting in non-optimal utilization of the active phase (that requires to be in the metallic form under reaction conditions).[20, 21] In this respect, it is not surprising that the development of alternative methods for the preparation of these composites is gaining a tremendous attention in both the open and patent literature.

Among the different strategies suggested in literature, the use of metal-organic-frameworks (MOFs) as precursors for the synthesis of nanomaterials such as metal (oxide) nanoparticles,[22-25] porous silica,[26, 27] or nanoporous carbons[28] offers unrivalled design possibilities, as we also demonstrate in this work. Herein we report a multi-step approach for the preparation of highly loaded Co on silica FTS catalysts that circumvents the interdependence between metal loading, active site dispersion and accessibility. By using this approach, highly loaded cobalt nanocomposites (~50 wt.% Co) with cobalt oxide reducibility in the order of 80% and good particle dispersion were synthesized and tested in FTS. These catalysts exhibit high activity, C5+ selectivity, and excellent stability.

4.2. EXPERIMENTAL

4.2.1. Materials

2-Methylimidazole (MeIm, purity 99%), cobalt nitrate hexahydrate ($Co(NO_3)_2 \cdot 6H_2O$, >99%), Tetramethyl orthosilicate (TMOS 99%), and methanol (>99.8%) were purchased from Sigma-Aldrich Chemical Co. All chemicals were used without further purification.

4.2.2 Catalyst synthesis

In the synthesis of ZIF-67, 2.933 g of $Co(NO_3)_2 \cdot 6H_2O$ and 6.489 g of 2-methylimidazole (MeIm) were separately dissolved in 200 mL methanol. The latter clear solution was rapidly poured into the former pink solution with vigorous stirring for 24 h at room temperature. Afterwards, the bright purple products were collected by filtration, washed with methanol, and dried at 353 K for 10 h under vacuum.

0.8 g of the synthesized ZIF-67 was immersed in 5 mL TMOS in an autoclave, which was further transferred into a rotation oven and heated up to 333 K overnight. After the oven was cooled down to room temperature, the mixture was carefully washed with 1 mL ethanol to remove the excess TMOS on the external surface of ZIF-67 by filtration. Then the purple material was placed in a cotton thimble of 22 mm diameter and placed in a glass tube of 25 mm diameter. The glass tube was fitted to a round bottom flask containing 500 ml of water. A needle to bubble the water with 10 ml min^{-1} of N_2 flux was also fitted. The temperature was raised to 323 K to create a wet N_2 stream to directly hydrolyze the TMOS molecules for 30 h, followed by air drying at 333 K and vacuum drying at 373 K for 10 h, successively. The obtained sample was denoted as ZIF-67@SiO_2.

0.8 g of ZIF-67@SiO$_2$ were transferred into a quartz tubular reactor (approx. L = 1.0 m x ID = 5.0 cm) horizontally situated in a ceramic fiber oven (Carbolite, Sheffield). The reactor was flushed with N$_2$ at 303 K for 0.5 h, followed by direct carbonization at different temperature for 4 h under N$_2$ (150 mL min^{-1}) at a ramp of 2 K min^{-1}. The obtained sample was denoted as Co@C-SiO$_2$-T, where T (T = 773, 873, 973 K) refers to the pyrolysis temperature. After the temperature was decreased to room temperature, the carbonized samples were further calcined at 673 K in air (150 mL min^{-1}) for 2 h at a ramp of 1 K min^{-1}. The obtained sample was denoted as Co@SiO$_2$-T, where T (T = 773, 873, 973 K) refers to the pyrolysis temperature. For comparison, 0.8 g of ZIF-67@SiO$_2$ was directly calcined at 673 K in air (150 mL min^{-1}) for 2 h at a ramp of 1 K min^{-1}, and this sample was denoted as Co@SiO$_2$-*cal*. Co@C-*873* was prepared by pyrolysis of 0.8 g ZIF-67 at 873 K for 4 h under 150 ml min^{-1} N$_2$ flow at a ramp of 2 K min^{-1}.

For the melt infiltration (MI) samples, 2.9 g Co(NO$_3$)$_2$·6H$_2$O and 0.6 g of degassed SiO$_2$ support (Aerosil-200 or CARiACT Q-10) were physically mixed in a mortar with a pestle under ambient conditions until the powder was homogeneously pink. Then the samples were transferred into a Teflon-lined steel autoclave and kept at 333 K for 24 h, followed by calcination by heating to 673 K (1 K min^{-1}, 2 h) in a flow of air (150 mL min^{-1} for 0.8 g precursor loaded catalyst) in the same setup as mentioned above. The obtained samples were denoted as Co/SiO$_2$-*A*-*MI* (Aerosil-200) and Co/SiO$_2$-*F*-*MI* (CARiACT Q-10), respectively. For the incipient wetness impregnation (IWI) sample, 1 g of degassed SiO$_2$ support (CARiACT Q-10) was impregnated with 1 mL of aqueous cobalt nitrate solution. The catalyst precursor was dried overnight under vacuum at 373 K followed by

calcination by heating to 673 K (1 K min^{-1}, 2 h) in a flow of air (150 mL min^{-1} for 0.8 g precursor loaded catalyst) in the same setup as mentioned above. The obtained sample was denoted as Co/SiO₂-*F-IWI*.

4.2.3. Characterization

The Co contents in the samples were measured by atomic adsorption spectroscopy (AAS) (AAnalyst 200, Perkin Elmer, USA). Powder X-ray diffraction (PXRD) patterns were measured by a Bruker D8 Advance X-ray diffractometer using monochromatic Co *Kα* radiation ($\lambda = 0.179026$ nm). N₂ adsorption-desorption isotherms were obtained using a Micromeritics Tristar 3020 at 77 K, and samples were outgassed under vacuum at 423 K overnight prior to the analysis. For the analysis, the BET area was determined as outlined in Lange et al.[29] The mesopore surface area was obtained from the *t*-plot applied to the N₂ isotherm. Thermogravimetric (TG) analysis was carried out using a Mettler Toledo TGA/SDTA851e instrument by heating samples in N₂ (100 mL min^{-1}) from room temperature to 1073 K at a ramp rate of 5 K min^{-1}. Transmission electron microscopy (TEM) imaging and elemental energy dispersive X-ray (EDX) mapping were performed on a JEM-2100 (JEOL) and a Talos F200X (FEI) microscopes operated at 200 kV. Tilt series of bright-field TEM images for electron tomography were taken with a Talos F200X (FEI) microscope, over the angle range of ± 76° with a tilt increment of 2°. Tilt series were aligned and reconstructed using IMOD software package.[30] Cobalt particle diameter (d_{TEM}) was calculated based on a minimum of 200 nanoparticles using the equation of $d_{TEM} = \dfrac{\Sigma_i\, n_i d_i^3}{\Sigma_i\, n_i d_i^2}$, where n_i is the number of particles with diameter of d_i. Temperature-programmed reduction in hydrogen

(TPR(H_2)) was performed in a flow of 10 vol.% H_2/Ar (30 ml min^{-1}) at a heating rate of 5 K min^{-1} from ambient temperature to 1223 K. The degree of reduction (*DOR*) was measured using TGA (Mettler Toledo TGA/SDTA851e) in a flow of 10% H_2/He. The samples were heated to 673 K and held there for 8 h (No weight loss was obtained after this time). After that the temperature was further increased to 1273 K (5 K min^{-1}). The *DOR* of cobalt was calculated using the equation of $\left(n_{Co}^{total} - n_{Co}^{>673}\right)\Big/ n_{Co}^{total}$. H_2-chemisorption measurements were performed on a Micromeritics ASAP 2020 instrument. Samples were dried at 100 °C for 1 h in dynamic vacuum followed by a reduction in H_2 at 673 K (10 h, 5 K min^{-1}) and evacuation at that temperature. Isotherms were measured at 423 K. Apparent cobalt surface areas were calculated assuming H:Co = 1 and a Co-atomic cross section of 0.0662 nm^2. The corrected particle sizes were deduced from the cobalt surface areas using the amount cobalt per gram of catalysts multiplied by the degree of reduction.

4.2.4. Catalyst performance

The FTS was carried out in a parallel 6-flow fixed-bed microreactor (FBM) setup as previously described.[31] Certain amount of catalyst was mixed with SiC of similar size and loaded into a stainless steel tube lined with a quartz layer. Catalysts were reduced in situ in pure H_2 at 673 K for 10 h at 2 K min^{-1}. Afterwards, the reactors were cooled to 453 K at which the pressure was increased to 20 bar under H_2. Then, a CO flow was gradually introduced into the system, and finally reached an H_2/CO ratio of 1 with syngas flow of 40 ml min^{-1}. Next, the temperature was increased to the reaction temperature of 483 K at 2 K min^{-1}. The C5+ selectivity was

calculated from the CO conversion by subtracting the fraction of CO used for the formation of C_1 to C_4 products, as determined *via* online GC (Hewlett Packard 5890, Series II) using N_2 as an internal standard, from the total amount of CO converted.

4.3. RESULTS AND DISCUSSION

4.3.1. Catalyst Characterization Results

Figure 4.1 illustrates the followed synthetic procedure. We used the zeolitic-imidazolate-framework ZIF-67, containing a 30 wt.% Co $(Co(MeIm)_2,\ MeIm = 2\text{-methylimidazolate})$ and tetramethyl orthosilicate (TMOS) as starting materials for the synthesis of cobalt catalysts. In this approach, a TMOS impregnated ZIF-67 was first subjected to a wet N_2 flow under ambient conditions to facilitate TMOS hydrolysis inside the pores of the MOF. The obtained ZIF-67@SiO₂ sample was then pyrolyzed at different temperatures in the range of 773-973 K under N_2 for 4 h, followed by calcination in air at 673 K for 2 h. The catalysts after pyrolysis and calcination are denoted as Co@C-SiO₂-*T* and Co@SiO₂-*T*, respectively, with *T* representing the pyrolysis temperature. For comparison, a 'Co@SiO₂-*cal.*' sample was also prepared by direct calcination (skipping the intermediate pyrolysis step) of ZIF-67@SiO₂ in air (details of the preparation process for all materials are shown in the Methods section). The Co loadings of the Co@SiO₂ catalysts are around 50 wt.% (Table 4.1).

The XRD pattern of the original ZIF-67 (Fig. C1/Appendix C), confirms the structure of the MOF precursor.[32] TG analysis in N_2 atmosphere of the hydrolyzed ZIF-67@SiO₂ indicates that the complete pyrolytic decomposition of the crystalline ZIF-67 occurs in the range of 800-850 K
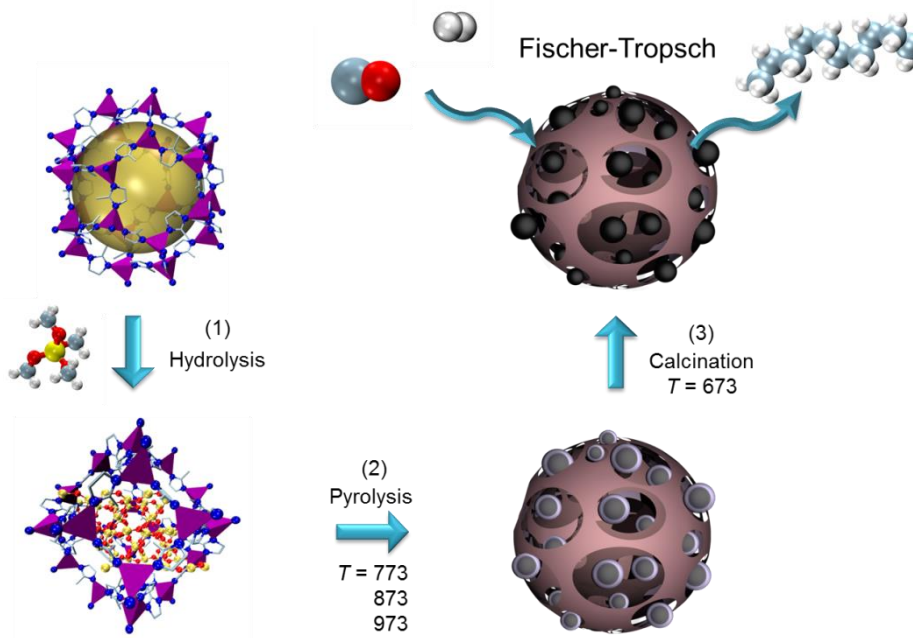
Fig. 4.1. (1) Impregnation and hydrolysis of TMOS molecules in the porosity of ZIF-67. (2) Pyrolysis of the mixture of ZIF-67@SiO$_2$ in N$_2$ to decompose ZIF-67 and form Co@C-SiO$_2$. (3) Calcination of the Co@C-SiO$_2$ in air leads to carbon removal and oxidation of Co. The resulting composite is an excellent catalyst for the low temperature Fischer-Tropsch synthesis.

(Fig. C2/Appendix C), further confirmed by XRD (Fig. C3a/Appendix C). After the pyrolysis step, graphite ($2\Theta = 30.6^{\circ}$) and metallic cobalt ($2\Theta = 51.8^{\circ}$, 60.6°) phases are formed. Notably, when a higher pyrolysis temperature is used, these peaks become much narrower and sharper, indicating a higher graphitization degree and a larger crystallite size of cobalt nanoparticles.[33] After the additional calcination step, the characteristic peaks corresponding to ZIF-67, graphite and metallic cobalt phases have disappeared and only the Co$_3$O$_4$ phase is observed (Fig. C3b/Appendix C). Both ZIF-67 and ZIF-67@SiO$_2$ display type-I N$_2$ sorp-

Table 4.1: Textural properties of Co-based catalysts obtained from N_2 adsorption isotherms at 77 K, and cobalt loading of Co containing catalysts.

Catalyst	S / (m^2/g)			V_p / (cm^3/g)			Co loading (wt.%)
	Total	Micro	Meso[c]	Total	Micro	Meso	
ZIF-67	1930	1910	20	0.71	0.68	0.03	30[d]
ZIF-67@SiO₂	1430	1400	30	0.56	0.04	0.52	26[d]
Co@SiO₂-*773*	260	35	225	0.46	0.02	0.44	49[e]
Co@SiO₂-*873*	285	80	205	0.50	0.03	0.46	51[e]
Co@SiO₂-*973*	305	70	235	0.51	0.03	0.48	50[e]
Co@SiO₂-*cal.*	250	55	200	0.46	0.02	0.44	46[e]

a: Data obtained based on ZIF-67 support mass. b: Data obtained based on SiO₂ support mass. c: Mesopore surface area obtained from the *t*-plot applied to the N_2 isotherm. d: 10 mg samples were calcined in air (100 ml min⁻¹, STP) from 303 K to 1073 K at a heating rate of 5 K min⁻¹, and after 700 K no weight change was observed. Then Co loading was obtained based on Thermogravimetric (TG) analysis assuming that cobalt was fully converted to Co_3O_4. e: Data obtained based on atomic adsorption spectroscopy (AAS) analysis.

tion isotherm (Fig. C4a/Appendix C) typically associated with microporosity.[34] The Brunauer-Emmett-Teller area (S_{BET}) and pore volume (V_p) decreases from 1930 m² g⁻¹ and 0.71 cm³ g⁻¹ to 1430 m² g⁻¹ and 0.56 cm³ g⁻¹ after incorporation of SiO₂ (Table 4.1).[29] In contrast with the original ZIF-67@SiO₂, the S_{BET} and V_p of all Co@SiO₂ catalysts decreases drastically and exhibit type IV isotherms with type H_3 hysteresis that closes at $P/P_0 \approx 0.4$, suggesting the presence of a predominantly mesoporous structure which is the result of the agglomeration of small SiO₂ particles (Fig. C4b/Appendix C).

Transmission electron microscopy (TEM) and high-resolution transmission electron microscopy (HR-TEM) analysis in combination with elemental mapping (STEM/EDX) give further information on the textural properties of the composites at different synthesis stages. High-angle annular dark-field scanning TEM (HAADF-STEM, Figure 4.2a) analysis

shows a well-defined rhombic dodecahedral morphology (~250 nm) of the ZIF-67@SiO$_2$ catalysts similar to that of the original ZIF-67,[32] while elemental mapping demonstrates an homogeneous dispersion of Si, Co and C (Figure 4.2b-d). After pyrolysis under N$_2$ atmosphere, well dispersed cobalt nanoparticles in the carbon matrix can be observed in Co@C-SiO$_2$-*T* (Fig. C5a-c/Appendix C), with average particle size increasing from 5.4 nm in Co@C-SiO$_2$-*773* to 11.0 nm in Co@C-SiO$_2$-*873*, and 13.3 nm in Co@C-SiO$_2$-*973* (Fig. C5d-f/Appendix C). According to HR-TEM, during pyrolysis, cobalt nanoparticles are encapsulated by multilayers of graphitic-carbon shells (Fig. C5g-i/Appendix C) that seem to render them inaccessible and to avoid their oxidation upon exposure to air, as suggested by XRD (*vide supra*). The subsequent calcination removes the graphite shells and oxidizes metallic cobalt to Co$_3$O$_4$ (Figure 4.3f-h, and Fig. C6b-d/Appendix C), but hardly affects Co particle size (Figure 4.3j-l, and Table 4.2). No large cobalt clusters can be found in the Co@SiO$_2$-*873* even after H$_2$ reduction (Fig. C7a-d/Appendix C). Co@SiO$_2$-*cal.* (Figure 4.2e,m and Fig. C8a/Appendix C) and Co@SiO$_2$-*773* (the inset of Figure 4.2f) show the presence of needle-like structures absent in samples pyrolyzed at higher temperatures. Additional analysis by combining TEM and EDX (Fig. C8b,c/Appendix C) reveals the presence of both Si and Co in needle-rich areas and made us tentatively attribute this phase to the formation of cobalt phyllosilicates.
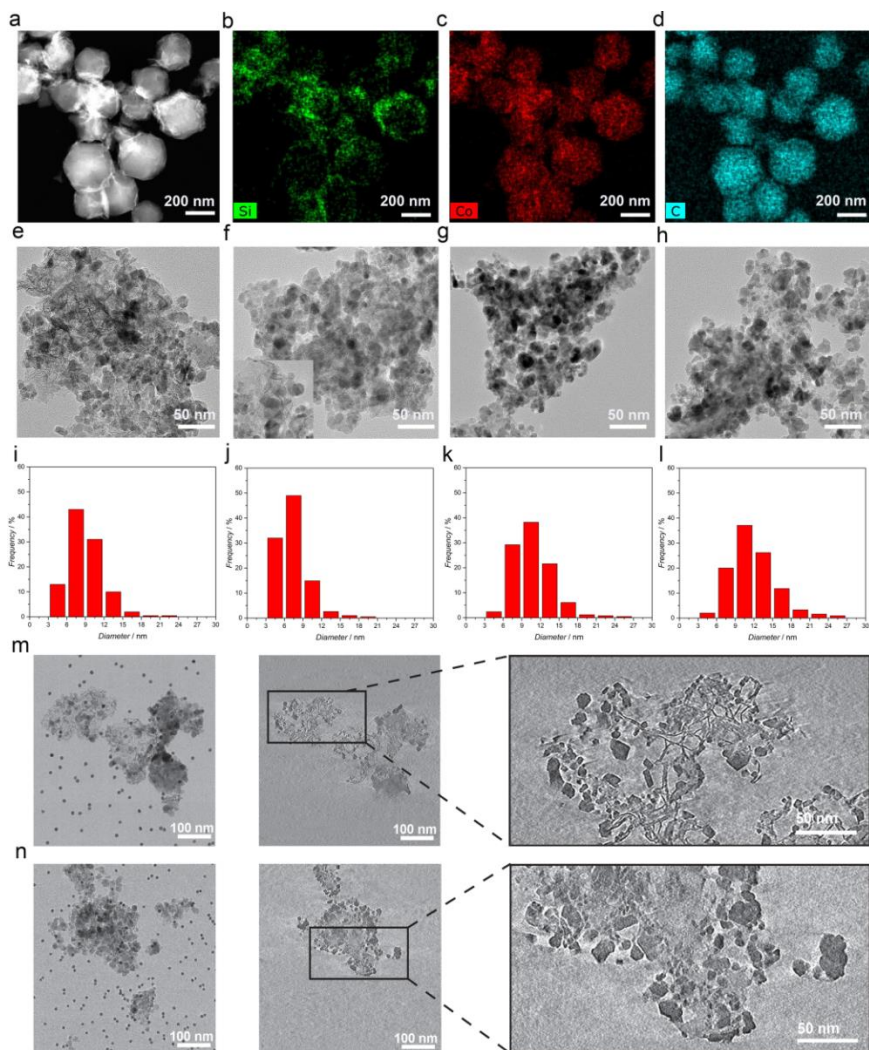
Fig. 4.2. (a) High-angle annular dark-field scanning electron (HAADF-STEM) micrograph of ZIF-67@SiO$_2$. (b) Elemental mapping of Si, (c) of Co, and (d) of C in ZIF-67@SiO$_2$ sample. (e) TEM micrograph of Co@SiO$_2$-*cal.*. (f) TEM micrograph of Co@SiO$_2$-*773*, with inset of the observable needle-like structure. (g) TEM micrograph of Co@SiO$_2$-*873,* and (h) of Co@SiO$_2$-*973*. Particle size histograms obtained from TEM analysis for (i) Co@SiO$_2$-*cal.,* (j) Co@SiO$_2$-*773*, (k) Co@SiO$_2$-*873,* and (l) Co@SiO$_2$-*973*. Electron tomography results for (m) Co@SiO$_2$-*cal*., and (n) Co@SiO$_2$-*873*.

Table 4.2. Average cobalt particle size and degree of reduction (*DOR*) of Co@SiO$_2$ catalysts.

Catalyst	d_{Co}*	d_{Co}#	*DOR (%)*
Co@SiO$_2$-*773*	8.6	7.6	66
Co@SiO$_2$-*873*	12.3	11.8	78
Co@SiO$_2$-*973*	14.3	13.5	79
Co@SiO$_2$-*cal.*	10.7	9.5	52

* Cobalt particle size is obtained from TEM analysis using at least 200 Co$_3$O$_4$ nanoparticles and calculated from Co$_3$O$_4$ particle size using Co and Co$_3$O$_4$ densities. # Cobalt particle size is calculated from H$_2$-chemisorption assuming the surface stoichiometry H/Co = 1 and an atomic cross-sectional area of 0.0662 nm^2. Cobalt oxide degree of reduction (*DOR*).
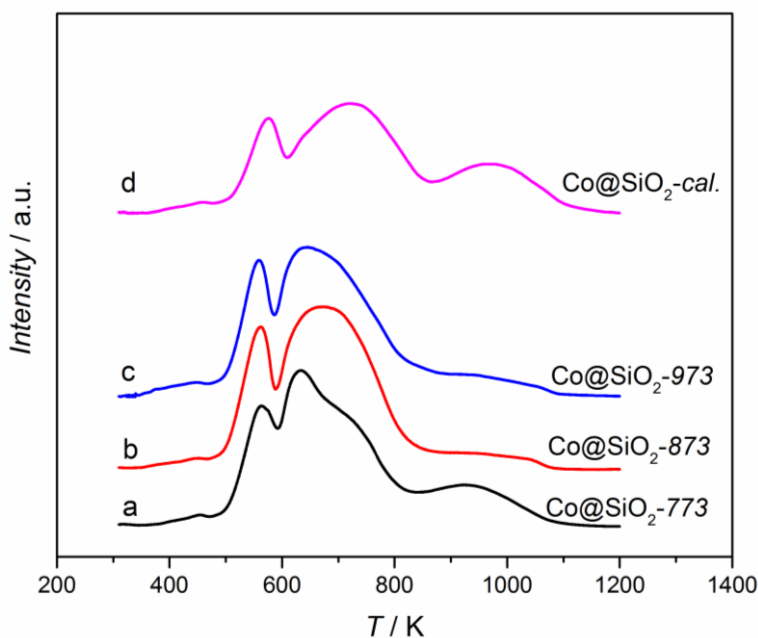
Fig. 4.3. TPR(H$_2$) profiles of Co@SiO$_2$ catalysts. (a) Co@SiO$_2$-*773*, (b) Co@SiO$_2$-*873*, (c) Co@SiO$_2$-*973*, and (d) Co@SiO$_2$-*cal.* The TPR(H$_2$) experiments were performed from 303 to 1223 K at a ramp of 5 K min^{-1} in 10 vol.% H$_2$/Ar.

The reducibility of the metallic species in all calcined samples was studied by temperature programmed reduction in H$_2$ (TPR(H$_2$)). All of the

Co@SiO$_2$ samples exhibit two overlapping reduction peaks centered at ~570 K and 700 K, and a broad reduction band between 850 and 1150 K, as shown in Figure 4.3. The first two peaks can be ascribed to the two-step reduction of Co$_3$O$_4$ via CoO to metallic Co,[35] along with gasification of the residual carbon in the samples (Fig. C9/Appendix C), while the broad feature illustrates the reduction of highly dispersed cobalt species in strong interaction with the SiO$_2$ support (*e.g.* cobalt phyllosilicate).[36] In the case of Co@SiO$_2$-*cal.*, the second reduction occurs at a slightly higher temperature, indicative of a stronger interaction between cobalt nanoparticles and support, most likely due to the presence of very small cobalt particles, as proven from the electron tomography results in Figure 4.2m. Moreover, the broad high temperature band in Co@SiO$_2$-*cal.* and Co@SiO$_2$-*773* implies the presence of a large fraction of irreducible cobalt silicates, in agreement with the TEM analysis above. This is further confirmed by the lower degree of reduction (*DOR*) of cobalt oxide in Co@SiO$_2$-*cal.* (52%) and Co@SiO$_2$-*773* (66%) than in Co@SiO$_2$-*873* (78%) and Co@SiO$_2$-*973* (79%), see Table 4.2. These results highlight the importance of the intermediate pyrolysisstep at a sufficiently high temperature as to achieve full destruction of the ZIF-67 sample to prevent the formation of irreducible cobalt silicate and therefore ensure an almost full utilization of the catalyst's cobalt loading.

4.3.2. Catalytic Performance in Fischer Tropsch synthesis.

The Co@SiO$_2$ catalysts were tested in the Fischer-Tropsch synthesis at 483 K, 20 bar, H$_2$/CO = 1, and a space velocity (*SV*) of 0.5 mol$_{CO}$ g$^{-1}_{cat.}$ h^{-1}.
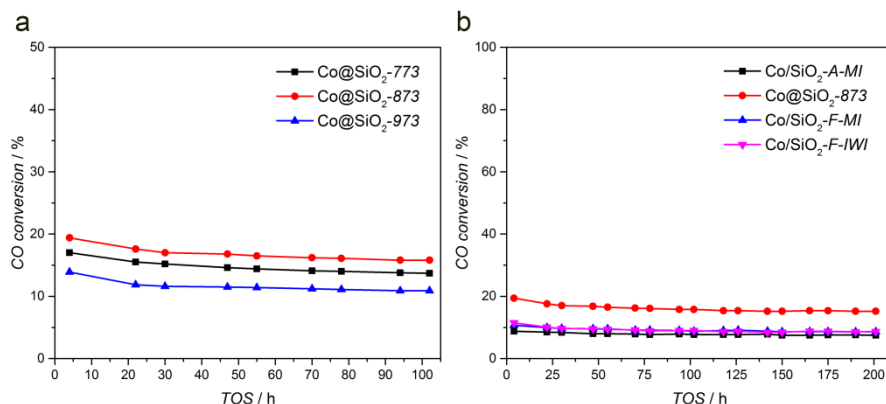
Fig. 4.4. Catalytic performance. (a) Time-on-stream evolution of CO conversion for the Co@SiO$_2$ catalysts. (b) Time-on-stream evolution of CO conversion for the Co@SiO$_2$-*873* and Co/SiO$_2$ catalysts prepared using conventional methods. '-*MI*' refers to melt infiltration. '-*IWI*' refers to incipient wetness impregnation. '-*A*' refers to Aerosil-200 support and '-*F*' refers to CARiACT Q-10 support. Reaction conditions: 483 K, 20 bar, H$_2$/CO=1, and syngas flow of 40 ml min^{-1}.

Fig. 4.4a shows time-on-stream (*TOS*) evolution of CO conversion. All catalysts exhibit a good stability, and differences observed in activity are in line with the observed textural properties. Co@SiO$_2$-*873* displays the highest CO conversion, followed by Co@SiO$_2$-*773* and Co@SiO$_2$-*973*. Table 4.3 summarizes cobalt-time-yield (*CTY*), apparent turnover frequencies (*TOF*) and products selectivities for these catalysts after 102 h on stream. When *CTY* is plotted as a function of the pyrolysis temperature, a volcano-like curve is obtained, with an optimum for the sample pyrolyzed at 873 K. The *TOF* values calculated for samples pyrolyzed at 873 and 973 K are similar and higher than that of the Co@SiO$_2$-*773* sample. The FTS process occurs on the surface of metallic cobalt nanoparticles with an optimal particle size around 10 nm. On one hand, small cobalt nanoparticles

Table 4.3. Catalytic performance of Co@SiO$_2$ catalysts after 102 h *TOS*.

Catalyst	Catalyst weight (mg)	Cobalt loadings (wt.%)	X_{CO} (%)	CTY (10^{-5} mol$_{CO}$g$^{-1}_{Co}$s^{-1})	TOF (10^{-2} s^{-1})	S [%]		
						C1	C2-4	C5+
Co@SiO$_2$-*773*	100	49	13.7	4.0	1.9	6.5	6.3	87.2
Co@SiO$_2$-*873*	100	51	15.8	4.4	3.1	5.3	4.2	90.5
Co@SiO$_2$-*973*	100	50	10.9	3.3	2.8	5.8	4.7	89.5
Co@SiO$_2$-*cal.*	100	46	10.6	3.3	1.9	7.5	6.8	85.7

Carbon conversion (*X*, %), activity per gram of Co (*CTY*), apparent turnover frequency (*TOF*, mol CO converted per mol Co surface atoms per second), hydrocarbon selectivity (*S*, %). FTS experiments were carried out at 483 K, 20 bar, and H$_2$/CO=1, and syngas flow of 40 ml min^{-1}.
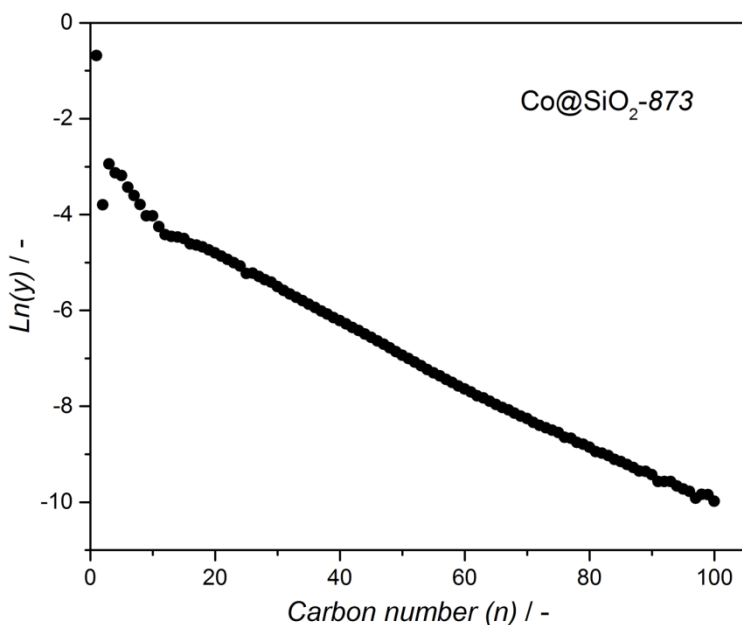
Fig. 4.5. Molar fraction distribution of FTS products from Co@SiO$_2$-*873* after 201 h on stream at 483 K, 20 bar, and H$_2$/CO=1, and syngas flow of 40 ml min^{-1}. Chain growth probability (α = 0.94) obtained from the ASF plot in the C15-C100 hydrocarbon range.

Table 4.4. Catalytic performance of Co@SiO$_2$-*873*, Co@C-*873*, and Co@C-SiO$_2$-*873* catalysts after 102 h *TOS*.

Catalyst	Catalyst weight (mg)	Cobalt loadings (wt.%)	X_{CO} (%)	CTY (10^{-5} mol$_{CO}$g$^{-1}_{Co}$s^{-1})	S [%]		
					C1	C2-4	C5+
Co@SiO$_2$-*873*	100	51	15.8	4.4	5.3	4.2	90.5
Co@C-*873*	150	32	4.9	1.5	13.1	7.5	79.4
Co@C-SiO$_2$-*873*	150	28	5.8	2.1	17.1	11.1	71.7

Carbon conversion (X_{CO}, %), activity per gram of Co (*CTY*), hydrocarbon selectivity (*S*, %). Prior to FTS reaction, catalysts were reduced in H$_2$ at 623 K for 2 h. FTS experiments were carried out at 483 K, 20 bar, and H$_2$/CO=1, and syngas flow of 40 ml min^{-1}.

Table 4.5. Catalytic performance of Co@SiO$_2$-*873* and Co/SiO$_2$ catalysts prepared using conventional methods after 201 h *TOS*.

Catalyst	Catalyst weight (mg)	Cobalt loadings (wt.%)	X_{CO} (%)	CTY (10^{-5} mol$_{CO}$g$^{-1}_{Co}$s^{-1})	S [%]		
					C1	C2-4	C5+
Co@SiO$_2$-*873*	100	51	15.2	4.2	5.2	3.8	91.0
Co/SiO$_2$-*A-MI*	100	42	7.5	2.6	4.5	4.1	91.5
Co/SiO$_2$-*F-MI*	100	42	8.6	3.0	4.8	4.3	90.9
Co/SiO$_2$-*F*-IWI	250	16.5	8.7	3.1	4.7	4.9	90.4

Carbon conversion (*X*, %), activity per gram of Co (*CTY*), hydrocarbon selectivity (*S*, %). FTS experiments were carried out at 483 K, 20 bar, and H$_2$/CO=1, and syngas flow of 40 ml min^{-1}.

normally possess a large fraction of low-coordinated surface sites (i.e. corner, kink, edge etc.), which to a large extent hamper CO dissociation and/or CH$_x$ hydrogenation.[13, 37] Hence, we attribute the superior activity of Co@SiO$_2$-*873* to the high Co reducibility and the optimal Co particle size (Table 4.2).[13-15, 38, 39] On the other hand, small cobalt nanoparticles have only few step sites, known for C-C formation towards long chain hydrocarbons, therefore resulting in a high methane selectivity.[40, 41] Thus, the larger Co-particle size in the Co@SiO$_2$-*873* and Co@SiO$_2$-*973* samples when compared to Co@SiO$_2$-*773* results in a lower CH$_4$ and a

higher C5+ selectivity for these catalysts (Table 4.3), in excellent agreement with literature.[13] Interestingly, theCo@SiO$_2$-*873* exhibits a chain growth probability (α) as high as 0.94, without any deliberate addition of a promotor (i.e. Mn, Zr etc.), further confirming the high C5+ selectivity in this work, as shown in Figure 4.5.

The performance of the Co@SiO$_2$-*cal.* sample further emphasizes the key role of the intermediate pyrolysis step (Table 4.3). A high initial CO conversion over this sample along with a clear deactivation during the first 50 h on stream (Fig. C10/Appendix C) is observed. We attribute the severe deactivation at the initial stage to the presence of a substantial amount of small cobalt nanoparticles (< 4 nm), that are more susceptible to aggregation and/or oxidation than larger particles during high-pressure FTS and which also more selective for the formation of CH$_4$.[42, 43] In addition, although pyrolysis of Co based MOFs under an inert atmosphere has recently been demonstrated as a promising route to prepare highly loaded Co@C hybrids with controllable cobalt particle size and distribution,[24, 44-48] these directly pyrolyzed samples such as Co@C-*873* and Co@C-SiO$_2$-*873* synthesized in this work show a poor activity and low C5+ selectivity along with an unacceptable CH$_4$ selectivity in the FTS process under the same conditions as Co@SiO$_2$ catalysts (Fig. C11/Appendix C and Table C1/Appendix C). The inferior performance of these pyrolyzed samples can be ascribed to the inaccessibility of most cobalt nanoparticles, which are completely encapsulated by graphitic shells (Fig. C12/Appendix C and Table C2/Appendix C).[49, 50] Comparison of our results demonstrates the importance of the synthetic protocol here presented.

4.3.3. Discussion

The results here presented demonstrate that the stepwise hydrolysis-pyrolysis-calcination methodology is a promising route to synthesize highly loaded Co@SiO$_2$ catalysts using ZIF-67 as a sacrificial template and TMOS as silicon source. During the high-temperature pyrolysis, the ZIF-67 structure decomposes, generating cobalt nanoparticles encapsulated by graphitic carbon shells, which prevent the formation of large agglomerates, controlling in this way cobalt particle dispersity, while optimization of the pyrolysis temperature improves cobalt reducibility.

To further demonstrate the advantages of this synthetic methodology, we prepared additional highly loaded Co catalysts, with Co supported on commercially available Aerosil-200 (denoted as "A") or CARiACT Q-10 (denoted as "F") silica, by using melt infiltration (MI). Also a benchmark 16 wt.% Co/SiO$_2$ catalyst was prepared by means of incipient wetness impregnation (IWI). The Co/SiO$_2$ catalyst with a comparable Co loading as those synthesized using ZIF-67 as template consists mostly of large aggregates (>100 nm, Fig. C13a-c/Appendix C) as a result of the lower versatility of the MI method. The comparison between the FTS performance of these catalysts and Co@SiO$_2$-*873* is shown in Figure 4.4b and Table 4.5. Our Co@SiO$_2$-*873* catalyst displays excellent stability even after 200 h on stream. Under the studied conditions, the Co@SiO$_2$-*873* displays a *CTY* at least 1.5 times higher than the other samples (in spite of the higher Co loading) and a comparable C5+ selectivity.

Overall, our results further highlight the potential and versatility of the use of MOFs as catalyst templates and opens the door to the controlled fabrication of highly loaded, accessible, active and stable metal supported

catalysts thus coping with a major challenge in materials science and industrial catalysis.

4.4. CONCLUSIONS

In this work, we present a stepwise 'hydrolysis-pyrolysis-calcination' methodology that, making use of a cobalt-containing Metal Organic Framework as hard template (ZIF-67) to prepare highly loaded Co@SiO$_2$ catalyst (~ 50 wt.%). This strategy consists of condensation of silica in the Co-MOF pore space followed by pyrolysis and subsequent calcination of these composites. We prove that the intermediate pyrolysis between hydrolysis and calcination steps is essential to improve cobalt oxide reducibility in the order of 80% and maintain a good particle dispersion. The synthesized Co@SiO$_2$ catalyst is further applied in low-temperature Fischer-Tropsch synthesis, and exhibits high activity, C5+ selectivity, and excellent stability.

REFERENCES

[1] H.M. Torres Galvis, J.H. Bitter, C.B. Khare, M. Ruitenbeek, A.I. Dugulan, K.P. de Jong, Supported Iron Nanoparticles as Catalysts for Sustainable Production of Lower Olefins, Science, 335 (2012) 835-838.

[2] P. Poizot, S. Laruelle, S. Grugeon, L. Dupont, J.M. Tarascon, Nano-sized transition-metal oxides as negative-electrode materials for lithium-ion batteries, Nature, 407 (2000) 496-499.

[3] B. O'Regan, M. Gratzel, A low-cost, high-efficiency solar cell based on dye-sensitized colloidal TiO2 films, Nature, 353 (1991) 737-740.

[4] A.T. Bell, The Impact of Nanoscience on Heterogeneous Catalysis, Science, 299 (2003) 1688-1691.

[5] T.M. Eggenhuisen, J.P.d. Breejen, D. Verdoes, P.E.d. Jongh, K.P.d. Jong, Fundamentals of Melt Infiltration for the Preparation of Supported Metal Catalysts. The Case of Co/SiO2 for Fischer−Tropsch Synthesis, Journal of the American Chemical Society, 132 (2010) 18318-18325.

[6] C. Petit, A. Taleb, M.-P. Pileni, Self-Organization of Magnetic Nanosized Cobalt Particles, Advanced Materials, 10 (1998) 259-261.

[7] P. Munnik, P.E. de Jongh, K.P. de Jong, Control and Impact of the Nanoscale Distribution of Supported Cobalt Particles Used in Fischer–Tropsch Catalysis, Journal of the American Chemical Society, 136 (2014) 7333-7340.

[8] L. Espinosa-Alonso, M.G. O'Brien, S.D.M. Jacques, A.M. Beale, K.P.d. Jong, P. Barnes, B.M. Weckhuysen, Tomographic Energy Dispersive Diffraction Imaging To Study the Genesis of Ni Nanoparticles in 3D within γ-Al2O3 Catalyst Bodies, Journal of the American Chemical Society, 131 (2009) 16932-16938.

[9] M. Schreier, J.R. Regalbuto, A fundamental study of Pt tetraammine impregnation of silica: 1. The electrostatic nature of platinum adsorption, Journal of Catalysis, 225 (2004) 190-202.

[10] J.R. Regalbuto, A. Navada, S. Shadid, M.L. Bricker, Q. Chen, An Experimental Verification of the Physical Nature of Pt Adsorption onto Alumina, Journal of Catalysis, 184 (1999) 335-348.

[11] M. Che, Z.X. Cheng, C. Louis, Nucleation and Particle Growth Processes Involved in the Preparation of Silica-Supported Nickel Materials by a Two-Step Procedure, Journal of the American Chemical Society, 117 (1995) 2008-2018.

[12] P. Serp, P. Kalck, R. Feurer, Chemical Vapor Deposition Methods for the Controlled Preparation of Supported Catalytic Materials, Chemical Reviews, 102 (2002) 3085-3128.

[13] G.L. Bezemer, J.H. Bitter, H.P.C.E. Kuipers, H. Oosterbeek, J.E. Holewijn, X. Xu, F. Kapteijn, A.J. van Dillen, K.P. de Jong, Cobalt Particle Size Effects in the Fischer−Tropsch Reaction Studied with Carbon Nanofiber Supported Catalysts, Journal of the American Chemical Society, 128 (2006) 3956-3964.

[14] G. Prieto, A. Martínez, P. Concepción, R. Moreno-Tost, Cobalt particle size effects in Fischer–Tropsch synthesis: structural and in situ spectroscopic characterisation on reverse micelle-synthesised Co/ITQ-2 model catalysts, Journal of Catalysis, 266 (2009) 129-144.

[15] J.-S. Girardon, A.S. Lermontov, L. Gengembre, P.A. Chernavskii, A. Griboval-Constant, A.Y. Khodakov, Effect of cobalt precursor and pretreatment conditions

on the structure and catalytic performance of cobalt silica-supported Fischer–Tropsch catalysts, Journal of Catalysis, 230 (2005) 339-352.

[16] B. Mile, D. Stirling, M.A. Zammitt, A. Lovell, M. Webb, The location of nickel oxide and nickel in silica-supported catalysts: Two forms of "NiO" and the assignment of temperature-programmed reduction profiles, Journal of Catalysis, 114 (1988) 217-229.

[17] P. Munnik, M.E.Z. Velthoen, P.E. de Jongh, K.P. de Jong, C.J. Gommes, Nanoparticle Growth in Supported Nickel Catalysts during Methanation Reaction—Larger is Better, Angewandte Chemie International Edition, 53 (2014) 9493-9497.

[18] P. Munnik, N.A. Krans, P.E. de Jongh, K.P. de Jong, Effects of Drying Conditions on the Synthesis of Co/SiO2 and Co/Al2O3 Fischer–Tropsch Catalysts, ACS Catalysis, 4 (2014) 3219-3226.

[19] M. Nele, A. Vidal, D.L. Bhering, J. Carlos Pinto, V.M.M. Salim, Preparation of high loading silica supported nickel catalyst: simultaneous analysis of the precipitation and aging steps, Applied Catalysis A: General, 178 (1999) 177-189.

[20] J.H. Bitter, M.K. van der Lee, A.G.T. Slotboom, A.J. van Dillen, K.P. de Jong, Synthesis of Highly Loaded Highly Dispersed Nickel on Carbon Nanofibers by Homogeneous Deposition–Precipitation, Catalysis Letters, 89 (2003) 139-142.

[21] G.L. Bezemer, P.B. Radstake, V. Koot, A.J. van Dillen, J.W. Geus, K.P. de Jong, Preparation of Fischer–Tropsch cobalt catalysts supported on carbon nanofibers and silica using homogeneous deposition-precipitation, Journal of Catalysis, 237 (2006) 291-302.

[22] A.S. Hall, A. Kondo, K. Maeda, T.E. Mallouk, Microporous Brookite-Phase Titania Made by Replication of a Metal–Organic Framework, Journal of the American Chemical Society, 135 (2013) 16276-16279.

[23] K.E. deKrafft, C. Wang, W. Lin, Metal-Organic Framework Templated Synthesis of Fe2O3/TiO2 Nanocomposite for Hydrogen Production, Advanced Materials, 24 (2012) 2014-2018.

[24] V.P. Santos, T.A. Wezendonk, J.J.D. Jaén, A.I. Dugulan, M.A. Nasalevich, H.-U. Islam, A. Chojecki, S. Sartipi, X. Sun, A.A. Hakeem, A.C.J. Koeken, M. Ruitenbeek, T. Davidian, G.R. Meima, G. Sankar, F. Kapteijn, M. Makkee, J. Gascon, Metal organic framework-mediated synthesis of highly active and stable Fischer-Tropsch catalysts, Nature Communications, 6 (2015) 6451.

[25] T.B. Čelič, M. Grilc, B. Likozar, N.N. Tušar, In situ Generation of Ni Nanoparticles from Metal–Organic Framework Precursors and Their Use for Biomass Hydrodeoxygenation, ChemSusChem, 8 (2015) 1703-1710.

[26] A. Kondo, A.S. Hall, T.E. Mallouk, K. Maeda, A New Synthetic Route to Microporous Silica with Well-Defined Pores by Replication of a Metal–Organic Framework, Chemistry – A European Journal, 21 (2015) 12148-12152.

[27] W.J. Rieter, K.M.L. Taylor, W. Lin, Surface Modification and Functionalization of Nanoscale Metal-Organic Frameworks for Controlled Release and Luminescence Sensing, Journal of the American Chemical Society, 129 (2007) 9852-9853.

[28] B. Liu, H. Shioyama, T. Akita, Q. Xu, Metal-Organic Framework as a Template for Porous Carbon Synthesis, Journal of the American Chemical Society, 130 (2008) 5390-5391.

[29] M.F. De Lange, T.J.H. Vlugt, J. Gascon, F. Kapteijn, Adsorptive characterization of porous solids: Error analysis guides the way, Microporous and Mesoporous Materials, 200 (2014) 199-215.

[30] J.R. Kremer, D.N. Mastronarde, J.R. McIntosh, Computer Visualization of Three-Dimensional Image Data Using IMOD, Journal of Structural Biology, 116 (1996) 71-76.

[31] S. Sartipi, H. Jansma, D. Bosma, B. Boshuizen, M. Makkee, J. Gascon, F. Kapteijn, Six-flow operations for catalyst development in Fischer-Tropsch synthesis: Bridging the gap between high-throughput experimentation and extensive product evaluation, Review of Scientific Instruments, 84 (2013) 124101.

[32] R. Banerjee, A. Phan, B. Wang, C. Knobler, H. Furukawa, M. O'Keeffe, O.M. Yaghi, High-Throughput Synthesis of Zeolitic Imidazolate Frameworks and Application to CO_2 Capture, Science, 319 (2008) 939-943.

[33] N.L. Torad, M. Hu, S. Ishihara, H. Sukegawa, A.A. Belik, M. Imura, K. Ariga, Y. Sakka, Y. Yamauchi, Direct Synthesis of MOF-Derived Nanoporous Carbon with Magnetic Co Nanoparticles toward Efficient Water Treatment, Small, 10 (2014) 2096-2107.

[34] J. Tang, R.R. Salunkhe, J. Liu, N.L. Torad, M. Imura, S. Furukawa, Y. Yamauchi, Thermal Conversion of Core–Shell Metal–Organic Frameworks: A New Method for Selectively Functionalized Nanoporous Hybrid Carbon, Journal of the American Chemical Society, 137 (2015) 1572-1580.

[35] S. Sartipi, K. Parashar, M.J. Valero-Romero, V.P. Santos, B. van der Linden, M. Makkee, F. Kapteijn, J. Gascon, Hierarchical H-ZSM-5-supported cobalt for the direct synthesis of gasoline-range hydrocarbons from syngas: Advantages, limitations, and mechanistic insight, Journal of Catalysis, 305 (2013) 179-190.

[36] I. Puskas, T.H. Fleisch, J.B. Hall, B.L. Meyers, R.T. Roginski, Metal-support interactions in precipitated, magnesium-promoted cobaltsilica catalysts, Journal of Catalysis, 134 (1992) 615-628.

[37] J.P. den Breejen, P.B. Radstake, G.L. Bezemer, J.H. Bitter, V. Frøseth, A. Holmen, K.P.d. Jong, On the Origin of the Cobalt Particle Size Effects in Fischer−Tropsch Catalysis, Journal of the American Chemical Society, 131 (2009) 7197-7203.

[38] N. Tsubaki, S. Sun, K. Fujimoto, Different Functions of the Noble Metals Added to Cobalt Catalysts for Fischer–Tropsch Synthesis, Journal of Catalysis, 199 (2001) 236-246.

[39] A.Y. Khodakov, A. Griboval-Constant, R. Bechara, V.L. Zholobenko, Pore Size Effects in Fischer Tropsch Synthesis over Cobalt-Supported Mesoporous Silicas, Journal of Catalysis, 206 (2002) 230-241.

[40] R.A. Van Santen, Complementary Structure Sensitive and Insensitive Catalytic Relationships, Accounts of Chemical Research, 42 (2009) 57-66.

[41] W.T. Ralston, G. Melaet, T. Saephan, G.A. Somorjai, Evidence of Structure Sensitivity in the Fischer–Tropsch Reaction on Model Cobalt Nanoparticles by Time-Resolved Chemical Transient Kinetics, Angewandte Chemie International Edition, 56 (2017) 7415-7419.

[42] E. van Steen, M. Claeys, M.E. Dry, J. van de Loosdrecht, E.L. Viljoen, J.L. Visagie, Stability of Nanocrystals: Thermodynamic Analysis of Oxidation and Re-

reduction of Cobalt in Water/Hydrogen Mixtures, The Journal of Physical Chemistry B, 109 (2005) 3575-3577.

[43] N.E. Tsakoumis, J.C. Walmsley, M. Rønning, W. van Beek, E. Rytter, A. Holmen, Evaluation of Reoxidation Thresholds for γ-Al2O3-Supported Cobalt Catalysts under Fischer–Tropsch Synthesis Conditions, Journal of the American Chemical Society, 139 (2017) 3706-3715.

[44] S. You, X. Gong, W. Wang, D. Qi, X. Wang, X. Chen, N. Ren, Enhanced Cathodic Oxygen Reduction and Power Production of Microbial Fuel Cell Based on Noble-Metal-Free Electrocatalyst Derived from Metal-Organic Frameworks, Advanced Energy Materials, 6 (2016) n/a-n/a.

[45] X. Wang, J. Zhou, H. Fu, W. Li, X. Fan, G. Xin, J. Zheng, X. Li, MOF derived catalysts for electrochemical oxygen reduction, Journal of Materials Chemistry A, 2 (2014) 14064-14070.

[46] Y.-X. Zhou, Y.-Z. Chen, L. Cao, J. Lu, H.-L. Jiang, Conversion of a metal-organic framework to N-doped porous carbon incorporating Co and CoO nanoparticles: direct oxidation of alcohols to esters, Chemical Communications, 51 (2015) 8292-8295.

[47] B. Qiu, C. Yang, W. Guo, Y. Xu, Z. Liang, D. Ma, R. Zou, Highly dispersed Co-based Fischer-Tropsch synthesis catalysts from metal-organic frameworks, Journal of Materials Chemistry A, 5 (2017) 8081-8086.

[48] Y. Pei, Z. Li, Y. Li, Highly active and selective Co-based Fischer–Tropsch catalysts derived from metal–organic frameworks, AIChE Journal, 63 (2017) 2935-2944.

[49] L. Zhang, A. Wang, W. Wang, Y. Huang, X. Liu, S. Miao, J. Liu, T. Zhang, Co–N–C Catalyst for C–C Coupling Reactions: On the Catalytic Performance and Active Sites, ACS Catalysis, 5 (2015) 6563-6572.

[50] X. Sun, A.I. Olivos-Suarez, L. Oar-Arteta, E. Rozhko, D. Osadchii, A. Bavykina, F. Kapteijn, J. Gascon, Metal–Organic Framework Mediated Cobalt/Nitrogen-Doped Carbon Hybrids as Efficient and Chemoselective Catalysts for the Hydrogenation of Nitroarenes, ChemCatChem, 9 (2017) 1854-1862.

Effect of pretreatment atmosphere on the activity and selectivity of Co/*meso*HZSM-5 for Fischer-Tropsch Synthesis

5

Abstract: The structure and catalytic performance of bifunctional 10 wt.% Co/*meso*HZSM-5 catalysts pretreated under different conditions, *i.e.* in stagnant air, or in a flow of air, N_2, or 1 vol.% NO/Ar, were investigated for the Fischer-Tropsch Synthesis (FTS) under fixed operating conditions of $T = 513$ K, $P = 15$ bar, $H_2/CO = 1$. The combination of acid sites and FTS functionality leads to the direct formation of gasoline range hydrocarbons and suppresses the formation of C20+ products. The highest activity, C5-C11 selectivity and lowest CH_4 selectivity were obtained for Co/*meso*HZSM-5 catalysts pretreated in stagnant air. Pretreatment in gas flow resulted in a lower activity and C5-C11 selectivity, and in a higher CH_4 selectivity, in particular for samples pretreated with NO. In depth characterization of the different catalysts suggests that changes in the Co_3O_4 particle size distribution and cobalt reducibility upon treatment in different atmospheres determine catalytic performance. Pretreatment in air or N_2 flow increased the number of small Co_3O_4 particles and cobalt reducibility by suppressing the formation of highly dispersed cobalt, *e.g.* cobalt silicates, in strong interaction with *meso*HZSM-5. Pretreatment in a 1 vol.% NO/Ar flow significantly increased cobalt dispersion further, decreasing the cobalt reducibility due to the strong interaction between the metal and *meso*HZSM-5. Based on both TEM and *in-situ* DRIFTS studies, the optimum performance of Co/*meso*HZSM-5 pretreated in stagnant air could be attributed to a lower fraction of small cobalt particles, known to promote the formation of CH_4 *via* hydrogenolysis or direct methanation. Additionally, small cobalt particles are more susceptible to be oxidized under FT conditions, thereby decreasing FT activity and indirectly increasing CH_4 selectivity by increasing the H_2/CO ratio through the water gas shift reaction.

5.1. INTRODUCTION

The gradual depletion of crude oil has resulted in the resurrection of Fischer-Tropsch synthesis (FTS) in both industrial and academic research. Fischer-Tropsch synthesis is a feasible route to produce clean liquid fuels such as gasoline and diesel oil free of sulphur and aromatic compounds from syngas (mixture of H_2 and CO obtained from natural gas, coal or biomass)[1]. In spite of recent promising results with iron based catalysts[2], supported cobalt is the preferred catalyst for FTS because of its low water-gas-shift (WGS) activity, relatively low price compared to ruthenium, and high activity and selectivity towards long chain hydrocarbons[3, 4]. In this sense, the traditional Fischer-Tropsch Synthesis is always followed by product upgrading units in which hydrocracking and/or isomerization of FTS products is carried out. One way to achieve the intensification of the abovementioned process is by combining the FTS functionality with the acidity of zeolites[5-9].

The combination of an FTS active phase with zeolites which could "break" the classical Anderson-Schulz-Flory (ASF) product distribution can be traced back to 1980s[10]. However, methane selectivity in these bifunctional FT catalysts reached as high as 20%, in spite of a higher selectivity towards hydrocarbons in the C5-C11 fraction and lower C12+ selectivity compared to the conventional Co-based catalysts[5, 11-13]. Recently, the introduction of mesoporous structures in Co/HZSM-5 has been proven to effectively decrease methane selectivity and further increase C5-C11 selectivity in comparison with Co/HZSM-5, attributable to both the reduced diffusion path-length and resistance for reactants and/or products[14] and the decrease of acidity in the mesopores[5, 11-14].

However, CH_4 selectivity is still twice as high as that in Co/SiO_2 with the same Co content[5, 11-13]. By transmission electron microscopy, Sartipi *et al.*[12] showed that Co particles are inhomogeneously distributed over Co/*meso*HZSM-5, with a large percentage of these particles being smaller than 6 nm, even at moderately high 20 wt.% cobalt loadings.

Generally speaking, FT reaction is structure sensitive, with methane selectivity increasing as cobalt particle size decreases below 8-10 nm[15-19]. Small cobalt particles with a large fraction of edge/corner sites participate in the direct hydrogenation of CH_x species to methane, thereby giving rise to high CH_4 selectivity[15, 16]. At the same time, the FTS activity of Co-based catalysts, expressed by the cobalt-time yield (*CTY*), is related to the number of cobalt atoms on the surface, therefore depends on the cobalt particle size and exhibits a volcano-like curve with the optimum cobalt particle size at around 6-10 nm[15, 17-19]. Thus, the search for methods to optimize the cobalt particle size and dispersion has triggered intense investigations by a number of research groups[20-23].

Martínez *et. al.*[21] showed that cobalt dispersion over SBA-15 was improved by changing cobalt precursors from nitrate to acetate and acetylacetonate. Such an improved dispersion resulted in a lower reducibility and activity and in higher CH_4 selectivity. Addition of rhenium[4, 24] promoted the activity of 20 wt.% Co/SBA-15 and decreased CH_4 selectivity, which was assigned to the higher reducibility and to the more uniform dispersion of cobalt species in this sample[21]. However, the introduction of 0.3 wt.% ruthenium in 20 wt.% Co/*meso*HZSM-5 neither changed methane selectivity nor catalytic activity[12].

Recent research[25-32] by De Jong and co-workers showed that the activity of supported metal nanoparticles could be remarkably influenced by

various factors during catalyst pretreatment, including temperature[25, 29], atmosphere[26-28, 31, 32], and gas-hourly-space-velocity (*GHSV*)[29, 30]. Co-based FT catalysts (-SiO_2, -Al_2O_3) had a maximum cobalt-time yield (*CTY*) activity, in spite of a slightly increased CH_4 selectivity, after fluid-bed drying at 373 K in an appropriate N_2 flow. This was attributed to the improved cobalt dispersion by preventing formation of large cobalt aggregates, thereby enlarging the spacing between cobalt crystallites[25, 29]. When the gas atmosphere was changed from inert to air, large particles were observed[29]. In contrast, highly dispersed Co_3O_4 particles with dimensions around 4-5 nm were formed in 18 wt.% Co/SiO_2 catalysts by using a 1 vol.% NO/He flow[17, 28]. These highly dispersed cobalt nanoparticles exhibited excellent *CTY* activities in FTS, although no methane selectivities were presented. Similar results were also published by Wang *et al.*[7] by changing Co/SiO_2 to Co/HZSM-5. They showed that using a gas flow during catalyst pretreatment improved the FT activity, and 8 wt.% Co/HZSM-5 pretreated in a 5 vol.% NO/Ar flow exhibited much higher CO conversion than after calcination in air.

Recent studies[5, 11] in our group have shown that formation of mesopores in the zeolite support resulted in an improved activity and stability, and in a lower CH_4 selectivity than for Co/HZSM-5 catalysts. In this work, we further extend our study by focusing on fine-tuning Co dispersion by varying catalyst pretreatment conditions. Structural properties and catalytic performance of the resulting catalysts is evaluated by combining detailed characterization and catalytic testing.

5.2. EXPERIMENTAL

5.2.1. Materials

ZSM-5 zeolite (Si/Al = 40) in ammonium form was purchased from Zeolyst (CBV 8014). TPAOH (1 M), HNO_3 (70 wt.%), $Co(NO_3)_2 \cdot 6H_2O$ (> 99%) were purchased from Sigma-Aldrich. All chemicals were used without any further purification.

5.2.2 Support preparation and catalyst synthesis

ZSM-5 in ammonium form was calcined at 823 K for 5 h to obtain HZSM-5. Mesoporous HZSM-5 was synthesized by base and acid treatment, as reported previously[12]. Desilication was carried out in 1 M TPAOH aqueous solution (volume$_{base\ solution}$/weight$_{zeolite}$ = 8.0 cm^3/g) in a capped bottle with continuous stirring at 343 K for 1 h in an oil bath. This bottle was then immediately cooled in ice to terminate the reaction. After desilication the zeolite powders were centrifuged and washed to neutral pH with deionized water, followed by drying at 393 K for 12 h and calcined at 823 K for 5 h. The obtained samples were then treated in 1 M HNO_3 aqueous solution (volume$_{acid\ solution}$/weight$_{zeolite}$ = 28.6 cm^3/g) at 343 K for 2 h under stirring in the same oil bath. Then the samples were quenched, washed, dried, and calcined the same as for desilication. The acid treated zeolite is denoted as *meso*HZSM-5.

Catalysts were prepared by incipient wetness impregnation (IWI) of *meso*HZSM-5 (38-75 μm) with an aqueous solution of $Co(NO_3)_2 \cdot 6H_2O$ to reach a nominal 10 wt.% Co loading. The impregnated samples were kept in a desiccator at room temperature

overnight, followed by drying in a reactor (ID = 2 cm) in upflow mode with air, N_2 or 1 vol.% NO/Ar at a *GHSV* of 4500 h^{-1} at 373 K for 12 h (2 K/min) and then further heating to 623 K for 1 h (1 K/min) in the same atmosphere. Another impregnated sample was dried in an oven in a crucible (ID = 7.5 cm) at 373 K for 12 h (2 K/min) and then further heated to 623 K for 1 h (1 K/min) in stagnant air. The amount of the impregnated samples used during the pretreatment step is based on 0.5 g *meso*HZSM-5 support. Notation of the catalysts corresponds with the pretreatment atmosphere used (-stag, -air, -N_2, or -NO).

5.2.3. Characterization

N_2 physisorption was measured using a Micromeritics Tristar 3020 apparatus at liquid nitrogen temperature (77 K) after degassing under vacuum overnight at 623 K in a Micromeritics Vacprep 061 apparatus. In each adsorption experiment 100 mg sample was used.

Chemical analysis was performed by inductively coupled plasma optical emission spectrometry (ICP-OES) in Perkin-Elmer Optima instruments. Appropriately 25 mg of each sample was dissolved in a mixture of 4 ml 30% HCl, 1 ml 65% HNO_3 and 1 ml 40% HF using a microwave oven (900 W; hold for 15 min). The solutions were diluted in a ratio of 1:10 in milli-Q water and then the analysis was performed.

X-ray diffraction (XRD) patterns were recorded in Bragg-Brentano geometry in a Bruker D8 Advance X-ray diffractometer equipped with a Vantec position sensitive detector and graphite monochromator. Measurements were performed at room temperature with monochromatic Co *Kα* radiation ($\lambda = 0.179026$ nm) in the 2Θ range between 5° and 90°. The samples were placed on a Si (5 1 0) substrate

and rotated during measurements. The average particle sizes of Co_3O_4 in these catalysts were calculated from Scherrer equation using the most intense reflexion at $2\Theta = 43.07^o$, and the average cobalt particle size was calculated with the following relation[33]:

$$d(Co^0) = 0.75 \times d(Co_3O_4) \tag{1}$$

Transmission electron microscopy (TEM) analysis was performed by using a JEOL JEM-2010 operated at a voltage of 200 kV. The freshly prepared sample powder was ultrasonically dispersed in ethanol and deposited on a copper grid prior to the measurement.

Temperature-programmed reduction in hydrogen (TPR(H_2)) was performed in a homemade equipment with a packed bed of 100 mg of fresh catalyst (100-212 μm) in a flow of 10 vol.% H_2/Ar (30 ml/min) at a heating rate of 5 K/min. The reactor temperature was increased from ambient temperature to 1273 K and after water removal, the H_2 consumption ($n(H_2)_{total}$) was monitored by a TCD calibrated with CuO.

The reactor temperature was ramped from room temperature to 673 K (5 K/min) and stayed there for 5 h in a flow of 10 vol.% H_2/Ar (30 ml/min), followed by cooling down to 473 K. After the signal had become stable, the reactor temperature was heated to 1273 K (5 K/min) and H_2 consumption ($n(H_2)_{>673K}$) was measured. The consumption of H_2 below 673 K is calculated as follows,

$$n(H_2)_{<673K} = n(H_2)_{total} - n(H_2)_{>673K} \tag{2}$$

Then the extent of Co reduction was calculated from the amount of H_2 consumed below 673 K needed for a complete reduction of a fraction of the assumed Co_3O_4 starting compound to Co^0 during the in-situ reduction treatment at 673 K.

In situ DRIFTS of CO adsorption was performed in a Nicolet 6700 FT-IR (Thermo Scientific) equipped with a MCD/A detector in order to characterize the cobalt species in Co/*meso*HZSM-5 catalysts[11]. Samples were reduced by pure H_2 flow (20 cm^3_{STP}/min) at 673 K for 4 h (5 K/min). Afterwards, the cell was evacuated with He at 673 K for 0.5 h to remove the adsorbed H_2 molecules on the cobalt surface, followed by cooling down to 303 K under He flow (20 cm^3_{STP}/min). Then 1.5 vol.% CO/He (30 cm^3_{STP}/min) was fed to the cell for 0.5 h at 303 K. Subsequently, the catalysts were flushed in He (20 cm^3_{STP}/min) for 1 h. Then the IR spectra were consecutively collected at 473 K and 513 K. Spectra of KBr at 303 K were recorded as background, and sample spectra collected at 573 K after total CO desorption under He flow (20 cm^3_{STP}/min) were used as reference.

5.2.4. Catalyst performance

FTS experiments were performed in a six-flow fixed-bed microreactor setup as previously described[34, 35]. 0.5 g fresh catalysts (100-212 μm) was mixed with SiC of similar size to keep a constant fixed bed volume of 1.3 cm^3. Prior to the FTS operation, catalysts were activated *in-situ* by H_2 (80 cm^3_{STP}/min) at 673 K for 10 h at atmospheric pressure, followed by cooling to 453 K. As the pressure was increased to 15 bar (FT operation), CO was gradually introduced in the feed stream at 453 K until reaching a final H_2/CO ratio of 1. Then the reactor was heated to the reaction temperature of 513 K to reach the used standard operating conditions with a gas-

hourly space velocity (*GHSV*) of 6 m$^3_{STP}$ kg$^{-1}_{cat}$ h^{-1}. All the heating and cooling steps were performed at 2 K/min.

Waxes were collected in gas/liquid separators at 448 K and 15 bar during FTS experiments. Liquid hydrocarbons and water were collected in cold traps at 278 K at atmospheric pressure. These liquid hydrocarbons and waxes were weighed and dissolved in CS_2 separately. Then these samples were analysed offline by a simulated distillation (SimDis) GC (Hewlett Packard 5890, Series II) equipped with an FID and HP-1 column (7.5 m × 0.53 mm, film thickness 2.65 µm), with a carrier gas of He. The oven temperature in the analysis was programmed from 308 K to 623 K (14 K/min) and kept at the final temperature for 5 min.

Permanent gases as well as light hydrocarbons in the gas phase were analyzed online by a Compact GC (Interscience) equipped with three columns and detectors in parallel using He as carrier gas. In the first column (Carboxen 1010, 10 m × 0.32 mm) N_2, CO, CH_4 and CO_2 were separated at 333 K and analyzed by TCD. In the second column (Al_2O_3/KCl, 10 m × 0.32 mm) and FID detection, separation between all C1–C4 components was achieved at 434 K. In the third column (RTx-1 0.5µm, 15 m × 0.32 mm) C5–C10 hydrocarbons were separated at 353 K and analyzed by FID.

The selectivity was determined after 92.5 h when a pseudo-steady-state was reached. CO conversion and carbon selectivity were defined as follows,

$$X_{CO} = \left. (F_{in,CO} - F_{out,CO}) \middle/ F_{in,CO} \right. \times 100\% \tag{3}$$

$$S_{C_n} = \frac{nF_{C_n}}{(F_{CO_2} + \sum_{n=1}^{N} nF_{C_n})} \times 100\% \qquad (4)$$

where X_{CO} stands for CO conversion, F indicates the molar flow rate, S_{Cn} is the carbon selectivity towards a product with n carbon atoms.

5.3. RESULTS

Bifunctional Co/*meso*HZMS-5 catalysts were prepared using incipient wetness impregnation (IWI), followed by pretreatment under different gas conditions. The structural and catalytic properties of these Co/*meso*HZSM-5 catalysts will be discussed below in detail.

### 5.3.1. Structural characterization

The textural properties of all Co/*meso*HZSM-5 catalysts are shown in Table 5.1. As a consequence of cobalt loading, the specific surface area and mesopore volume (based on support mass) of *meso*HZSM-5 in Co/*meso*HZSM-5 catalysts are lower than the initial *meso*HZSM-5 (717 m^2/g and 0.62 cm^3/g) support. The mesopore volumes were different after each pretreatment atmosphere, being smaller when either N$_2$ or 1 vol.% NO/Ar flows were used. ICP analysis demonstrates that cobalt loadings in all catalysts are close to 10 wt.%, consistent with the targeted value.

The XRD patterns of all freshly prepared Co/*meso*HZSM-5 catalysts are shown in Fig. 5.1. The reflections characteristic for the MFI structure of HZSM-5 can be observed, indicating the crystalline structure present after the consecutive base and acid treatment[36].

Table 5.1. Textual properties obtained from N_2 adsorption isotherms at 77 K and cobalt loading of *meso*HZSM-5 supported Co catalysts.

Samples	S / (m^2/g)		V / $(cm^3/g)^c$			Co
	Total[a]	Meso[b]	Total[d]	Micro[e]	Meso[f]	wt.%[g]
*meso*HZSM-5	717	491	0.62	0.1	0.52	-
Co/*meso*HZSM-5 -						
stag	591	374	0.57	0.1	0.46	10.5
-air	596	379	0.58	0.1	0.47	10.5
-N_2	544	345	0.52	0.1	0.41	9.3
-NO	560	349	0.53	0.1	0.42	8.9

a: BET area based per gram *meso*ZSM-5. b: Mesopore surface area obtained from the *t*-plot applied to the N_2 isotherm. c: Pore volume based per gram *meso*ZSM-5. d: Total pore volume. e: Micropore volume obtained from the *t*-plot. f: Mesopore volume calculated as $V_{meso} = V_{total} - V_{micro}$. g: Obtained from ICP-OES.
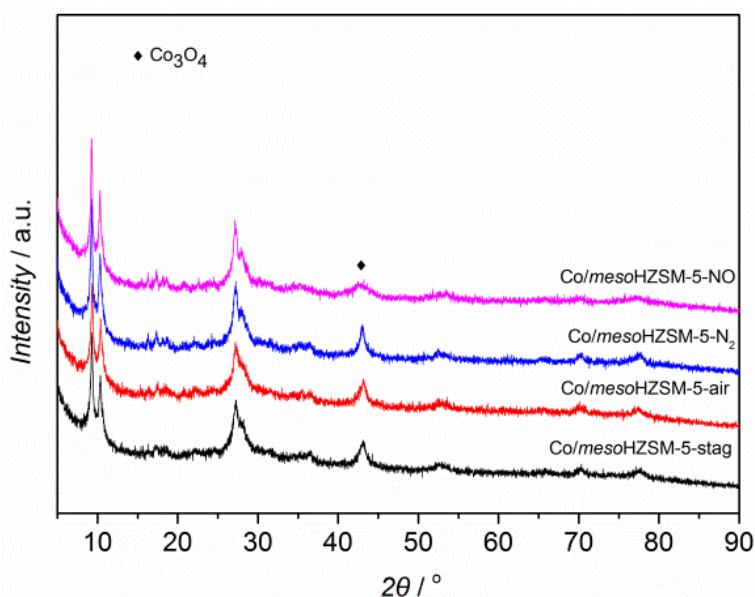
Fig. 5.1. X-ray diffraction patterns of Co/*meso*HZSM-5 catalysts with different pretreatment conditions

Further, only Co_3O_4 reflections can be identified[5, 11, 12], indicative of the decomposition of cobalt nitrate after the pretreatment. Line-

broadening analysis (Table 5.2) shows that Co/*meso*HZSM-5 catalysts pretreated in stagnant air or air flow result in Co_3O_4 crystallites of 12 nm on average, while the average Co_3O_4 crystal size increases to 17 nm after treatment in a pure N_2 flow as shown by the narrower and more intense diffraction peak in Fig. 5.1. Adding 1 vol.% NO to Ar flow results in the formation of Co_3O_4 crystallites of 9 nm on average, characterized by the low and broad reflection (Fig. 5.1). The observed differences indicate that the pretreatment atmosphere has an impact on the size and distribution of cobalt species, in agreement with other reports[30, 32].

Freshly prepared Co/*meso*HZSM-5 samples were studied by TEM (see Fig. 5.2.). All catalysts exhibit a spongy morphology, representative of the mesoporous support[11]. Large Co_3O_4 aggregates can be observed in Co/*meso*HZSM-5-stag sample (Fig. 5.2a, e), which are composed of small Co_3O_4 crystals smaller than 15 nm, consistent with the mean particle size (12 nm) estimated by XRD. Co_3O_4 particles could hardly be detected on the outside of the support, indicating that most Co species are inside the mesopores[12]. Pretreatment in a gas flow does not only impact the Co_3O_4 particle size but also the particle size distribution. An almost bimodal particle size distribution is found in the air-flow pretreated sample, with smaller Co_3O_4 particles (Fig. 5.2b) than for the '-stag' one, and some larger ones at the external part of the support. This scenario is more pronounced in the '-N_2' sample where a few Co_3O_4 particles larger ones at the external part of the support. This scenario is more pronounced in the '-N_2' sample where a few Co_3O_4 particles larger than 30 nm (not shown) together with a highly dispersed Co_3O_4 phase
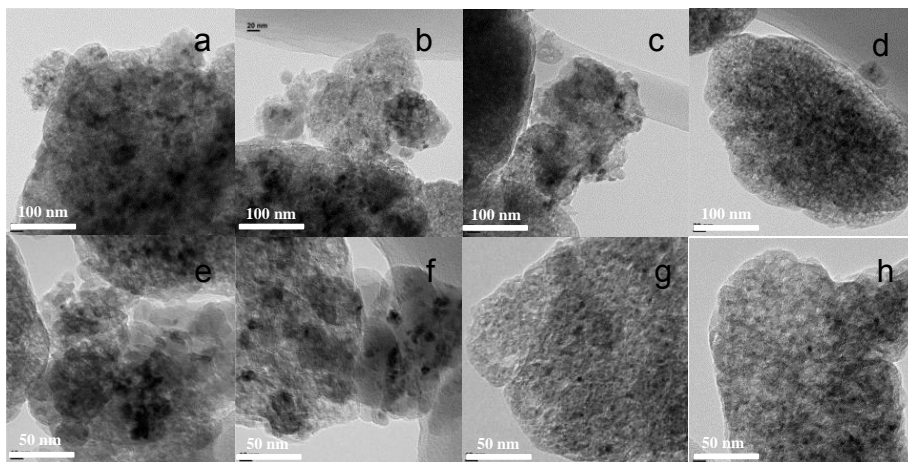
Fig. 5.2. TEM images for Co/*meso*HZSM-5 with different pretreatments: (a, e) Co/*meso*HZSM-5-stag, (b, f) Co/*meso*HZSM-5-air, (c, g) Co/*meso*HZSM-5-N_2, (d, h) Co/*meso*HZSM-5-NO.

(Fig. 5.2g) are observed, in agreement with the more intense XRD diffraction lines, dominated by the large particles. Large nanoparticles (CuO or NiO) were also observed on the external surface of the support (SiO_2[30] or SBA-15[32]) when catalysts were prepared at a low space velocity. Finally, in the Co/*meso*HZSM-5-NO sample, a large number of well-distributed Co_3O_4 nanoparticles is found with crystallite sizes not larger than 8 nm (Fig. 5.2d, h).

Fig. 5.3 shows the TPR(H_2) profiles for all Co/*meso*HZSM-5 catalysts. The TPR profiles have been normalized per mass of cobalt in the catalysts. The multiple reduction peaks in Co/*meso*HZSM-5 stand for heterogeneity of reducible cobalt species and several cobalt reduction steps[37, 38]. In agreement with previous study[12],
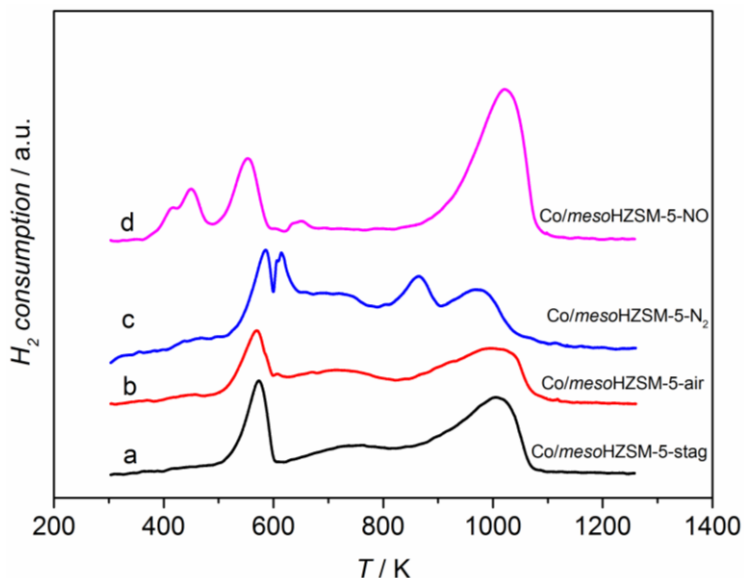
Fig. 5.3. TPR(H_2) profiles (5 K/min) of Co/*meso*HZSM-5 catalysts prepared under different gas conditions. H_2 consumption normalized for the Co content of the samples
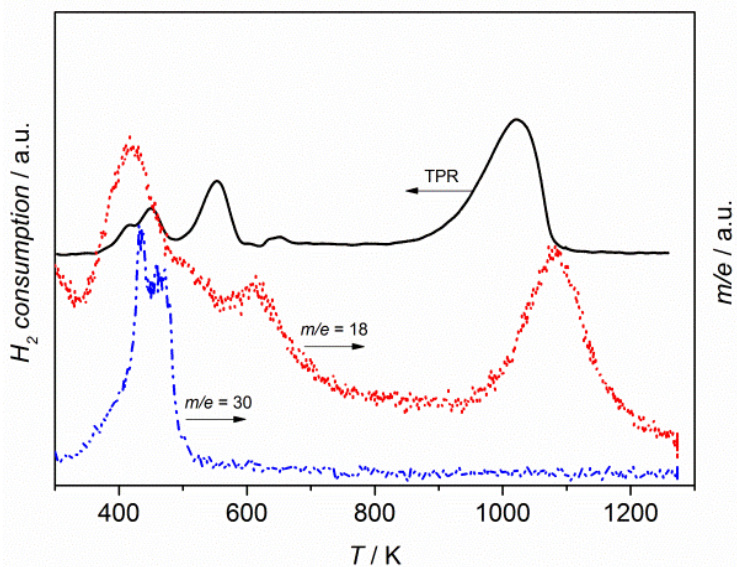

Fig. 5.4. Products analysis of Co/*meso*HZSM-5-NO catalyst in TPR(H_2) profile.
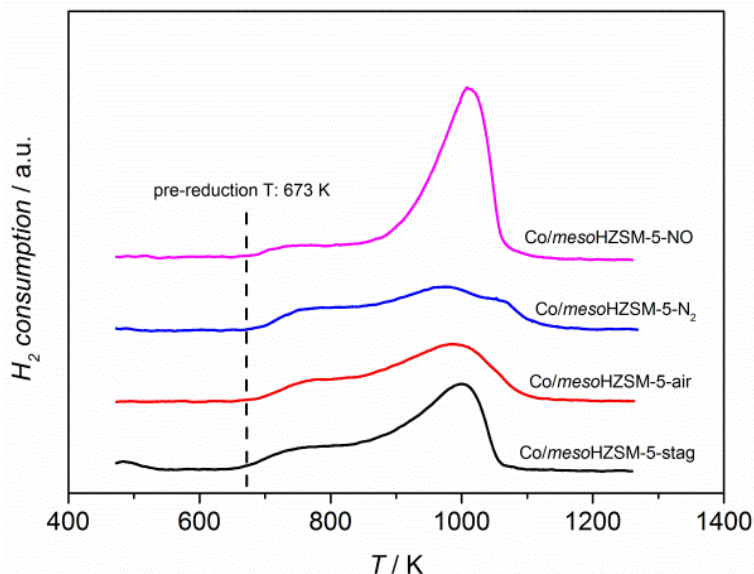
Fig. 5.5. TPR(H$_2$) profiles (5 K/min) of pre-reduced Co/*meso*HZSM-5 catalysts at 673 K for 5 h. H$_2$ consumption normalized for the Co content of the samples.

Table 5.2. Physico-chemical properties of cobalt phases in Co/*meso*HZSM-5 catalysts as determined from XRD and TPR(H$_2$) characterization.

Sample	XRD		Extent of Co reduction (%)
	Co$_3$O$_4$ diameter (nm)	Co diameter (nm)	
Co/*meso*HZSM-5			
-stag	12	9	28
-air	12	9	34
-N$_2$	17	13	45
-NO	9	7	-

Co/*meso*HZSM-5-stag exhibits a sharp reduction peak at ~575 K, followed by a broad reduction band ranging from 600 K to 900 K, and a peak above 900 K. The '575 K' peak can be assigned to the reduction of Co^{3+} to Co^{2+} and some Co^{2+} to Co^0[11, 20, 39], which weakly interacts with *meso*HZSM-5. Note that the reduction

temperature of CoO particles is related to the interaction between cobalt species and the support[21], the broad feature thus illustrates the stabilisation of CoO in different interaction with *meso*HZSM-5, representative of the heterogeneous distribution in particle sizes[37, 40]. The peak above 900 K has been ascribed to the reduction of highly dispersed cobalt oxide in strong interaction with *meso*HZSM-5[20, 37]. TPR profiles of Co/*meso*HZSM-5 depend on the pretreatment atmosphere. The peak area above 900 K, corresponding to hardly reducible Co species decreases, and the broad feature increases for the '-air' and '-N_2' sample, particularly for the latter. Besides, a doublet below 600 K can also be observed in Co/*meso*HZSM-5-N_2 sample, indicative of big Co_3O_4 particles[38], as confirmed by XRD and TEM results.

The TPR profile of Co/*meso*HZSM-5-NO contains a doublet below 500 K. The reduction products were analysed using a mass spectrometer, and the results are shown in Fig. 5.4. A signal at *m/e* = 30 accompanied by the formation of water is observed at around the temperature of the low-temperature reduction peak, confirming a reduction process. The *m/e* = 30 value stems from the NO^+ ion, which is the most intense fragment contribution of both NO and NO_2[40].Accordingly, the low-temperature peak can be assigned to the reduction of residual cobalt nitrate present after the thermal treatment. Additionally, the sharp reduction peak appears 25 K below the temperature observed for the other catalysts, tentatively attributed to the reduction promoted by hydrogen spillover from the Co reduced
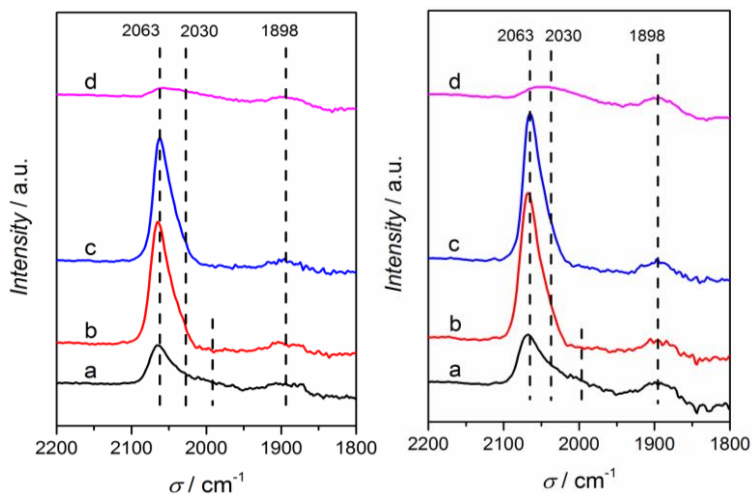
Fig. 5.6. DRIFT spectra of CO adsorbed on Co/*meso*HZSM-5 (*left*: 473 K, *right*: 513 K) with different pretreatment conditions: (a) Co/*meso*HZSM-5-stag, (b) Co/*meso*HZSM-5-air, (c) Co/*meso*HZSM-5-N$_2$, (d) Co/*meso*HZSM-5-NO.

below 500 K. The broad feature disappears while the peak area above 900 K significantly increases, indicating the existence of a large fraction of hardly reducible cobalt species.

In order to determine the cobalt reducibility, all catalysts were pre-reduced at 673 K for 5 h, corresponding to the pretreatment before the FTS operation, and a TPR profile was recorded afterwards (Fig. 5.5). The appearance of multiple reduction peaks above 673 K after 'pre-reduction' proves the presence of poorly reducible Co species under the applied FTS activation temperature, as shown in Table 5.2.

5.3.2. In situ CO-FTIR characterization of Co/mesoHZSM-5 catalysts

FTIR spectroscopy of adsorbed CO has been widely employed to investigate the nature of surface sites in most transition metal catalysts,

due to the sensitivity of the CO stretching frequency to the electronic state of the adsorption sites [39, 41].

Figure 5.6 shows the results obtained applying this technique on the different Co/*meso*HZSM-5 at 473 K and 513 K. Earlier research from our group confirmed that CO desorbed completely at 473 K from the zeolite surface[11], eliminating the interference from adsorption on acid sites in the spectra. Two regions, 2100-2000 cm^{-1} and 1850-1950 cm^{-1} are observed in the spectra of pre-adsorbed CO over all these Co-based catalysts, ascribable to linear and bridged adsorption of CO, respectively, on metallic cobalt sites[41, 42]. The exact identification of the 2063 cm^{-1} band is still controversial in the literature, where this band has been often ascribed to different species: (i) $Co(CO)_n$ ($n>1$) species attached to cobalt defect sites[43, 44], (ii) a blue shift of the intensity maximum at high coverage of linearly adsorbed CO due to long range dipole-dipole interactions[43], (iii) a structure of hydrocarbonyl[45] and (iv) CO adsorbing on $Co^{\delta+}$ sites[44-46]. The assignment to $Co(CO)_n$ ($n>1$) and the dipole-dipole interactions can be excluded in our results as this band does not shift to lower wavenumber after increasing temperature to 513 K, although the band intensity decreases due to some CO desorption from cobalt sites at higher temperature. Additionally, the attribution of the 2063 cm^{-1} band to hydrocarbonyl species is neither appropriate because hydrocarbonyl is unstable and would only be present in the presence of coadsorbed hydrogen[47], which is not the case in the experiments here reported (samples were flushed in He at 673 K prior to CO adsorption). Thus the 2063 cm^{-1} band can be ascribed to CO species adsorbed on Co^0 sites with weak electron-donor properties (with partial positive charge

$Co^{\delta+}$)[46, 48] in close contact with *meso*HZSM-5 or unreducible cobalt oxides, since these partially oxidized species result in a certain electropositive character of the Co ($Co^{\delta+}$)[41]. The amount of these cobalt sites ($Co^{\delta+}$) significantly increases when comparing samples pretreated in stagnant air and samples activated in air- and N_2 flow, with a much larger contribution of these sites in the latter cases. In contrast, the relative intensity of this band in Co/*meso*HZSM-5-NO decreases strongly.

The 2063 cm^{-1} band with a contribution at a lower wavenumber (ca. 2030 cm^{-1}), especially for '-stag' sample, has been attributed to CO molecules linearly bonded on surface cobalt atoms of relatively large metal particles[45, 48]. Furthermore, the '-stag' sample also contains a tail ranging from 2010 cm^{-1} to 1995 cm^{-1}, indicating the heterogeneity of cobalt adsorption sites [49], in good agreement with the inhomogeneous particle-size distribution observed by TEM. The intensity of the band around 1898 cm^{-1} which is ascribed to bridged adsorbed CO on relatively large cobalt particles [41] also decreases after changing pretreatment atmosphere from stagnant air to gas flows, indicating a decrease in the amount of large cobalt particles in the latter cases.

5.3.3. Catalytic performance in FTS

Time-on-stream (*TOS*) evolution of CO conversion over all these Co/*meso*HZSM-5 samples is presented in Fig. 5.7. As a function of *TOS*, all tested catalysts display similar behaviour, with a gradual deactivation before reaching 'steady state' after approximately 50 h on stream. Co/*meso*HZSM-5 catalysts pretreated under different

atmospheres exhibit different CO conversion levels, which is consistent with the general belief that Co-based FT catalysts are structure sensitive[15-17]. The '-stag' sample shows the highest CO conversion (36%) and cobalt-time yield (*CTY*) (13 mol_{CO} g^{-1}_{Co} s^{-1}) in comparison with samples pretreated in gas flows (Table 5.3) after 92.5 h. This is different from Co/SiO_2[17, 28] and Co/HZSM-5[7] systems, in which the *CTY* activity for the sample pretreated under NO flow was twice as high as that calcined in air.

The hydrocarbon product distributions for all Co/*meso*HZSM-5 catalysts after 92.5 h are included in both Fig. 5.8 and Table 5.3. Carbon balances for these experiments are in every case above 95%. Carbon selectivity to CH_4 and hydrocarbons in C5-C11 fraction is much higher than for Co/SiO_2 catalysts [5, 11, 12], while that of C12-C20 decreases considerably and no hydrocarbons with carbon chain number larger than 20 were detected. Molar product distributions over these Co/*meso*HZSM-5 after 92.5 h on stream are presented in Fig. 5.9. Unlike Co/SiO_2 FT catalysts, for which the molar product distributions *versus* their carbon number follows a linear trend[11], Co/*meso*HZSM-5 catalysts prepared in our experiments exhibit a break in the ASF distribution at around C12 and molar fractions of hydrocarbons drop remarkably as their carbon number exceeds the upper limit of gasoline range, due to the hydrocracking over the acid sites[5, 11-13]. The trend in CH_4 selectivity for different catalysts follows the order of Co/*meso*HZSM-5-stag < Co/*meso*HZSM-5-air < Co/*meso*HZSM-5-N_2 < Co/*meso*HZSM-5-NO, while selectivities to the C5-C11 and C12-C20 product ranges decrease in this order (Fig. 8). The increased selectivity to longer-chain hydrocarbons concurs with
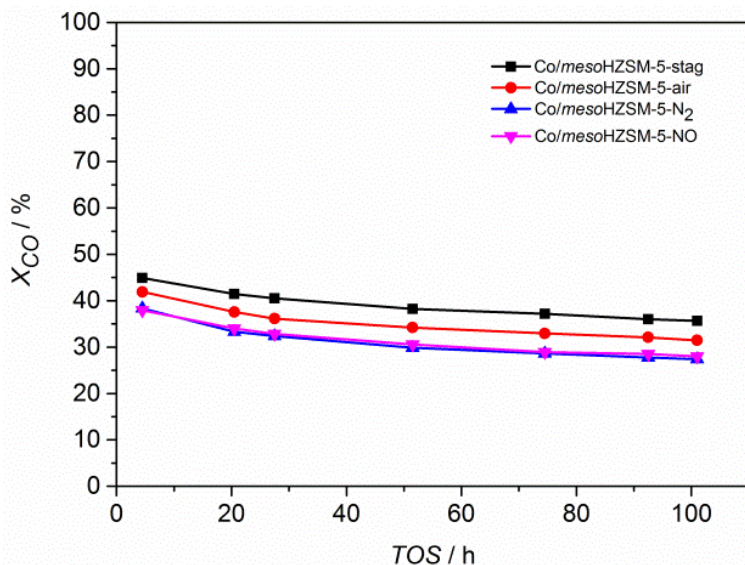
Fig. 5.7. Time-on-stream (*TOS*) evolution of CO conversion for Co/*meso*HZSM-5 prepared in different ways during FTS at 513 K, 15 bar total pressure, feed composition $H_2/CO = 1$, and $GHSV = 6 \text{ m}^3_{\text{STP}} \text{ kg}^{-1}_{\text{cat}} \text{ h}^{-1}$.

the increase in cobalt particle and aggregate size (Fig. 5.2), in agreement with earlier reports where C5+ selectivity relates to sizes of cobalt particles above 8 nm [15]. Also, large aggregates were reported to increase selectivity to long chain alkanes, probably due to the re adsorption and secondary chain growth of olefins[25, 29], by which the chain growth probability factor (α) may be larger. For all samples the CO_2 selectivity is below 2%, revealing a relatively low water-gas-shift (WGS) activity for Co-based catalysts under this reaction condition.

Finally, in order to check how CH_4 selectivity behaves in the initial reaction period, CH_4 selectivity *versus TOS* is displayed in Fig. 5.10. Note that to arrive to these plots a constant production of liquid
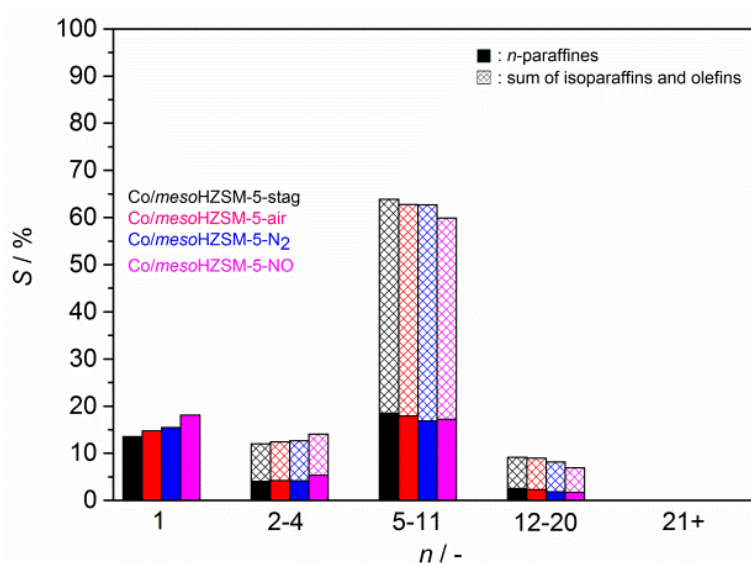
Fig. 5.8. Carbon selectivity toward products of FTS after 92.5 h on stream. In each group from left to right: Co/*meso*HZSM-5-stag, Co/*meso*HZSM-5-air, Co/*meso*HZSM-5-N$_2$, and Co/*meso*HZSM-5-NO. Experiments were performed at 513 K, 15 bar total pressure, feed composition H$_2$/CO = 1, and $GHSV$ = 6 m$^3_{STP}$ kg $^{-1}_{cat}$ h^{-1}. Key: solid fill *n*-paraffins, hatched fill olefins and isoparaffins.

hydrocarbons over *TOS* was assumed, since only gas products can be analyzed online. The CH$_4$ selectivity increases with *TOS*, in agreement with previous results [12], attributed to a combination of the partial oxidation of small Co aggregates with *TOS*, and the higher hydrogen partial pressure level due to the lower CO conversion.
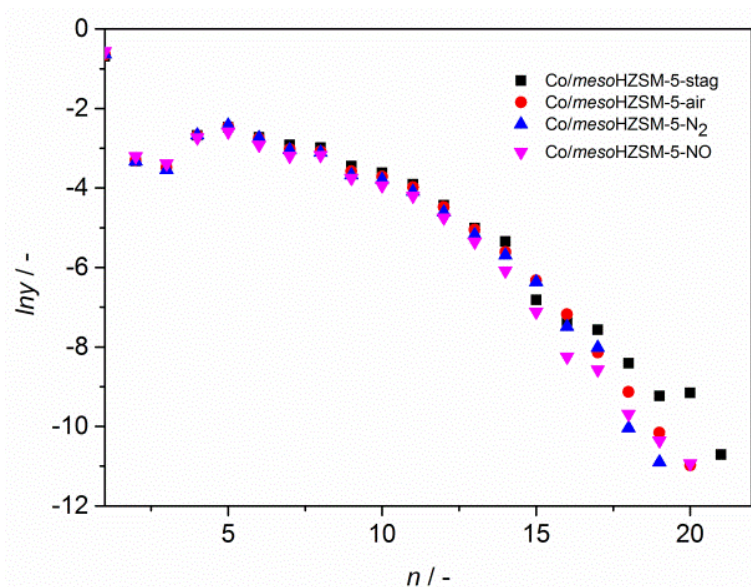
Fig. 5.9. ASF plot after 92.5 h on-stream at 513 K, 15 bar total pressure, $H_2/CO = 1$, and *GHSV* = 6 m^3_{STP} kg $^{-1}_{cat}$ h^{-1}.

Table 5.3. CO conversion, chain growth probability factor (☐), C1, C5-C11, C5+, and CO_2 carbon selectivities of FTS products after 92.5 h for Co/*meso*HZSM-5 synthesized in different ways.

Sample	Co loading (wt.%)	X_{CO} (%)	*CTY* (10^{-5} mol$_{CO}$ g$^{-1}_{Co}$ s^{-1})	C1	C5-C11	C12+	CO2	α^a
Co/*meso*HZSM-5 -stag	10.5	36.0	13	13.5	63.8	10.2	1.4	0.79
-air	10.5	32.1	11	14.8	62.7	9.0	1.1	0.78
-N$_2$	9.3	27.8	11	15.5	62.7	8.1	1.0	0.76
-NO	8.9	28.5	12	18.1	59.9	6.9	1.0	0.76

Reaction conditions: T = 513 K, P = 15 bar, $H_2/CO = 1$, *GHSV* = 6 m^3_{STP} kg^{-1} $_{cat}$ h^{-1}.
a: chain growth probability (α) obtained from the ASF plot in the C5–C11 hydrocarbon range.
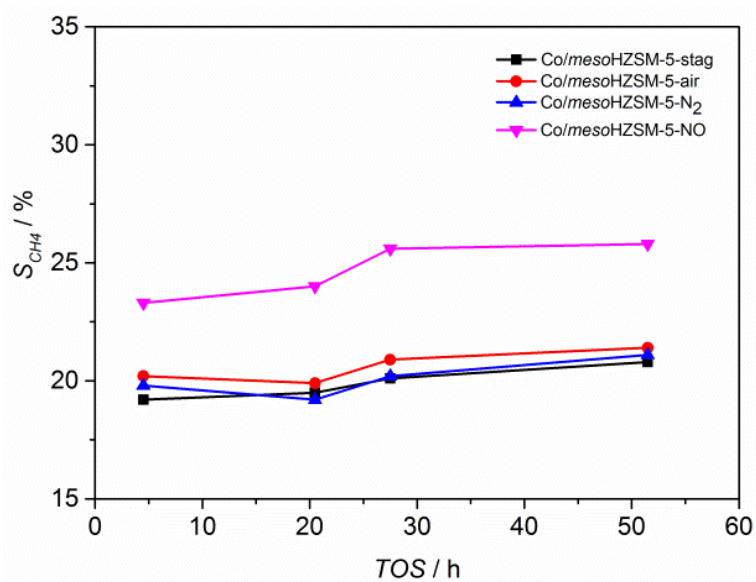
Fig. 5.10. Time-on-stream (*TOS*) evolution of CH$_4$ selectivity obtained from online GC product for Co/*meso*HZSM-5 prepared in different ways during FTS at 513 K, 15 bar total pressure, feed composition H$_2$/CO = 1, and *GHSV* = 6 m^3$_{STP}$ kg $^{-1}$$_{cat}$ h^{-1}.

5.4. DISCUSSION

The above results show that catalytic performance of Co/*meso*HZSM-5 catalysts strongly depends on the pretreatment atmosphere after impregnation. Introducing a gas flow during the pre- treatment step changes the Co$_3$O$_4$ particle size distribution and cobalt reducibility compared to Co/*meso*HZSM-5 prepared in stagnant air, in which Co$_3$O$_4$ particles distribute inhomogeneously, with scattered large aggregates.

Previous research[25, 29] has shown that the size and distribution of supported nanoparticles are influenced by both the support and the pretreatment conditions. Munnik *et al.*[25] investigated extensively the difference in cobalt dispersion with γ-Al$_2$O$_3$ and SiO$_2$ supported cobalt

catalysts. Higher cobalt dispersion was obtained on γ-Al_2O_3 support, and this was attributed to the increased precursor-support interactions in comparison with silica. Note that *meso*HZSM-5 prepared under consecutive base and acid treatment exposes a large number of silanol groups[11, 36] on the surface. These silanol groups can act as anchoring sites for Co^{2+} cations of the precursor, increasing the interaction between cobalt species and the surface of the support. The strong interaction between cobalt and *meso*HZSM-5 improves the dispersion of cobalt species on the support and results in many cobalt oxide particles of small size as shown in Fig. 5.2.

Aggregation of cobalt oxide can be controlled by changing the humidity during the pretreatment, and hence the decomposition of metal hydroxynitrate during the drying and calcination steps[28, 31, 32]. The drying temperature employed in our study (373 K) has been proven to balance the removal rate of water and the precipitation rate of nitrate during the drying step[25, 29].

Oxygen, a decomposition product of metal hydroxynitrate during calcination (stagnant air and air flow), has been reported to promote the sintering or redistribution of metal oxides (NiO or Co_3O_4)[28, 31, 32] and may be the cause of the formation of larger Co_3O_4 aggregates in Co/*meso*HZSM-5-stag catalyst. Using an air flow during the pretreatment step leads to the formation of more homogeneously distributed small cobalt oxide particles in Co/*meso*HZSM-5, consistent with the results from De Jong and co-workers[29, 31]. When an inert flow of N_2 is employed, the oxidizing power of the gas is further reduced and results in highly dispersed small Co_3O_4 particles, although some aggregates and large Co_3O_4 particles can be observed in the

Co/*meso*HZSM-5-N_2 sample. At a similar *GSHV* as the one here reported, a bimodal distribution of metal oxides with large particles on the external surface of the supports were also obtained by Munnik *et al.*[30] and Sietsma *et al.*[32]. Finally, a highly dispersed Co_3O_4 phase with a narrow size distribution (< 8 nm) can be found in NO-pretreated Co/*meso*HZSM-5, which is in agreement with earlier reports[28, 32]. NO moderates the decomposition rate of metal hydroxynitrate and lowers the heat of this reaction by NO_2 formation, thereby making the decomposition thermodynamically feasible at lower temperatures than without NO. Furthermore, NO acts as an oxygen scavenger, inhibiting the formation of O_2 during the decomposition of hydroxynitrate and therefore prevents sintering and redistribution of the active phase. The presence of a highly dispersed Co_3O_4 phase in N_2- and NO-pretreated samples can be also confirmed from N_2 physisorption results, in which pore volumes of *meso*HZSM-5 for these two samples further decrease probably due to the presence of these smaller and highly dispersed particles inside the mesopores[32]. In contrast to our results, Wang *et al.*[7] reported that an optimal cobalt particle size (around 7.7-10.5 nm) in 8 wt.% Co/*meso*HZSM-5 was obtained after pretreatment in a 5 vol.% NO/Ar flow, and the cobalt particle size decreased from 10.5 nm to 7.7 nm when increasing the mesopore surface area in *meso*HZSM-5. Comparing the mesopore areas in the samples used in this work with that in the samples used by Wang *et al.*, shows that in our work it is at least twice as large. Therefore, it is concluded that the dispersion of Co under similar pretreatment conditions is related to the mesopore surface area available for deposition[50] and the targetted

cobalt loading. So, depending on the mesopore surface area an optimal pretreatment atmosphere should be selected for a certain Co-loading.

TPR shows that cobalt reducibility (673 K for 5 h) increases after pretreatment from 28% in stagnant air to 34% in airflow and 45% in N_2 flow. TEM results show that more small cobalt oxide particles are present in air- and N_2-pretreated samples (Fig. 5.2b, g) compared to the '-stag' sample. As mentioned above, the strong interaction between cobalt species and *meso*HZSM-5 leads to the formation of highly dispersed cobalt oxides or even cobalt silicates, which can only be reduced at extremely high temperature (>900 K Fig. 5.3a). The gas flow (air and/or N_2) inhibits the redistribution of cobalt species and makes the deposition of cobalt hydroxynitrate more homogeneous[28, 29], resulting in well distributed small cobalt species. These small cobalt oxide particles become easier to be reduced, due to a weaker interaction with the support and a lower surface energy[15, 16, 51], as confirmed by the decreasing reduction peak area above 900 K in Fig. 3b and c. The higher cobalt reducibility of the N_2-pretreated sample compared to '-air' sample can be ascribed to the presence of large Co_3O_4 particles, as confirmed by TEM. However, Co/*meso*HZSM-5 pretreated in 1 vol.% NO/Ar flow shows a significantly large reduction peak area above 900 K. Indeed, as discussed above, the introduction of NO flow during catalysts pretreatment suppresses the sintering and redistribution of cobalt species (cobalt oxides and hydroxynitrate), causing the formation of a highly dispersed cobalt oxide. These highly dispersed cobalt oxides display a very strong interaction with the surface of *meso*HZSM-5. Because the Co/*meso*HZSM-5-NO sample still contains some cobalt nitrate, the

cobalt reducibility of this sample would be overestimated from the TPR results (Fig. 5.3). However, if the cobalt loading and the reduction peaks above 673 K of all catalysts are considered, the NO-pretreated sample shows the largest degree of reduction (Fig. 5.5). Therefore it is concluded that NO pretreatment decreases the reducibility of cobalt species under the applied FT activation conditions (673 K).

FT synthesis occurs on the surface of metallic cobalt particles[15, 16]. The number of active sites is a function of the cobalt particle size, determined by cobalt dispersion and reducibility. Further, the FT reaction is structure sensitive: cobalt particles below 8-10 nm[15-19, 52] are hardly active in FT and produce mostly methane. This is attributed to three effects. Firstly, as cobalt particle size decreases, the amount of coordinatively unsaturated cobalt sites increases, on which CO molecules bind strongly and irreversibly. Such strong adsorption[16] prevents the insertion of additional CO molecules, promoting the direct hydrogenation of CO to CH_4[15, 16]. Secondly, small cobalt particles (< 4 nm) are more susceptible to get oxidized at a high p_{H2O}/p_{H2} ratios than larger particles, as proven by both high pressure FT testing[3] and thermodynamic calculations[51]. It goes without saying that oxidized cobalt is not active in FTS. Nevertheless, these oxidized cobalt oxides catalyse the water-gas-shift (WGS) reaction[6, 53-55], which contributes to a higher H_2 to CO ratio. This additional hydrogen promotes the termination step in FTS, decreasing chain growth probability and indirectly increasing overall CH_4 selectivity. Finally, hydrogenolysis[6, 12, 56] is known to occur during FT reaction by which extra CH_4 can be produced.

Mesoporous zeolite based FT catalysts[5, 7-9, 11-14] are very interesting systems because of their high activity, C5-C11 selectivity and lower C20+ selectivity compared to conventional Co based FT catalysts. Several similar catalysts have been recently reported: a 3 wt.% Ru/*meso*HZSM-5 exhibited a selectivity of C5-C11 above 70%, together with CH_4 selectivity as low as 7% after 12 h on stream[9, 14]. Exchanging Ru by Co resulted in slightly higher CH_4 and lower C5-C11 selectivities for 8 wt.% Co/*meso*HZSM-5[7]. Although the performance of the catalysts here presented is somewhat poorer than those systems, it must be stressed that experimental conditions in those works[7, 9, 14] differ from ours: specially the operating pressure (20 bar *versus* 15 bar), time on stream (12 h *versus* 92.5 h), *GHSV* (2.4 m^3_{STP} kg^{-1}_{cat} h^{-1} *versus* 6 m^3_{STP} kg^{-1}_{cat} h^{-1}), and reactor diameter (7.0 mm *versus* 3.9 mm). Earlier studies have shown that higher operating pressures[15] and lower *GHSV*[12] normally result in higher chain growth probabilities. At the same time, as the reaction time increases, CH_4 selectivity increases (Fig. 5.10) for Co/*meso*HZSM-5 catalysts[12]. Indeed, CO conversion and C5-C11 selectivity decreased from 45% and 75% to 36% and 65%, respectively. Unfortunately, for their 8 wt.% Co/*meso*HZSM-5 catalysts no CH_4 selectivity was reported after 107 h on stream[7].

Furthermore, the different preparation method for *meso*HZSM-5 support may also cause a different catalytic performance for Co/*meso*HZSM-5 FT catalysts. After changing the desilication agent from NaOH to TPAOH[5], the surface area of *meso*HZSM-5 increased by 35% and CO conversion increased by 15% while keeping a similar CH_4 selectivity. The higher FT activity in the latter case could be due

to a higher cobalt dispersion and the absence of Na species, a well-known poison for Co-based FT catalysts[57]. When a successive acid washing (1 M HNO_3 solution) was performed after the desilication step (1 M TPAOH solution), both the surface area of *meso*HZSM-5 and CH_4 selectivity at iso-conversion conditions increased (from 18.5% to 20%)[12]. This may be ascribed to a higher cobalt dispersion caused by the removal of extra-framework aluminium and the exposure of more hydroxyl groups on the surface of *meso*HZSM-5. The higher CH_4 selectivity reported by Sartipi *et al.*[12] can be attributed to the higher H_2/CO ratio ($H_2/CO = 2$) used in that study. As it is well known, a higher H_2/CO ratio favours FT reaction towards chain termination[58]. Hence, a larger mesopore surface area in our case compared to that from Wang *et al.*[7] may also lead to a better accessibility of the micropores of the zeolite for cobalt, causing a higher cobalt dispersion and poorer cobalt reducibility, thereby increasing CH_4 formation[6, 15, 53-55].

Co/*meso*HZSM-5 catalysts prepared under stagnant air conditions exhibit higher C5-C11 selectivity (63.8%) than samples pretreated in a gas flow in our experiments. Obviously, the N_2- and NO-pretreated catalysts contain smaller cobalt particles than the samples calcined in air (Fig. 5.2). This is also confirmed by N_2 adsorption and CO-FTIR results. Considering the presence of the 2063 cm^{-1} band (assigned to CO adsorbed on cobalt in strong interaction with the support[46, 47]), the difference in the intensity of this band for '-stag', '-air' and '-N_2' samples can only be explained by the larger number of small cobalt particles in the latter cases. Despite the fact that air- and N_2-flow pretreatments increase the cobalt reducibility at FT conditions,

resulting in more cobalt sites being exposed to the syngas environment, as shown by the much higher intensity of the 2063 cm^{-1} absorbance in Fig. 5.6b and c, these small reduced cobalt particles can only take part in direct CO hydrogenation and are more easily oxidized in the initial operation period of FT synthesis[12]. Interestingly, compared to the results from Sartipi *et al.*[12], Co/*meso*HZSM-5-stag in our case also shows a higher C5-C11 selectivity (63.8% *versus* 53.5%) and lower C12+ selectivity (10.2% *versus* 18%). Note that these data were collected at a similar CO conversion and the same operating conditions (513 K, 15 bar and H$_2$/CO = 1), and that the difference between our two catalysts is only the cobalt loading (10.5 wt.% *versus* 23.8 wt.%). Clearly, a good balance between the number of cobalt and acid sites seems to play a key role in the final product distribution for these catalysts. Indeed, the smaller surface area and pore volume in *meso*HZSM-5 for 23.8 wt.% Co/*meso*HZSM-5 than 10.5 wt.% Co/*meso*HZSM-5-stag in the current experiment indicates a more severe pore blocking for the former case, which prevents the contact between the acid sites and hydrocarbons formed from cobalt sites, thereby lowering the hydrocracking ability.

Thus, the Co particle size distribution and FT activity for Co/*meso*HZSM-5 catalysts are dependent on pretreatment conditions. Co/*meso*HZSM-5 pretreated in gas flows contain more small Co$_3$O$_4$ particles than for Co/*meso*HZSM-5 calcined in stagnant air, although large Co$_3$O$_4$ particles can also be observed in the air- and N$_2$-pretreated samples. Unlike results reported for Co/SiO$_2$[17, 28] and Co/HZSM-5[25], a dedicated gas pretreatment resulted for the samples in this study in a decreased FT activity, C5+ selectivity and an

increased CH_4 selectivity in comparison with calcination in stagnant air. This lower FT activity and higher CH_4 selectivity are attributed to the lower chain growth probability, a higher hydrogenolysis activity and/or easier oxidation of the present small cobalt particles in these samples.

From the above discussion it has become clear that the choice for the optimal preparation method of bifunctional Co/*meso*HZSM-5 FTS catalysts is strongly dependent on the targeted cobalt loading and mesoporosity of the used support in order to obtain the optimal cobalt particle size for FTS and avoid highly dispersed cobalt. Further for an optimal bifunctionality a fine balance between the number of FTS sites and acid cracking sites is needed together with their accessibility.

5.5. CONCLUSIONS

In this study, the effect of the pretreatment atmosphere on the structure and catalytic performance of bifunctional Co/*meso*HZSM-5 catalysts in the direct formation of gasoline range hydrocarbons during Fischer-Tropsch Synthesis has been investigated. TEM and TPR results showed that the pretreatment atmosphere influences Co_3O_4 particle size and cobalt reducibility. Pretreatment in a flow of air or N_2 leads to a larger number of small Co_3O_4 particles and a higher cobalt reducibility compared with calcination in stagnant air. This can be explained when taking into account that treatment under gas flow suppresses the redistribution of cobalt oxides. NO pretreatment significantly improved cobalt dispersion, while it decreased cobalt reducibility due to the strong interaction between the highly dispersed cobalt oxides or cobalt silicates and *meso*HZSM-5. Given the structure

sensitive character of the FTS process, excellent metal dispersion in this case does not lead to a better catalytic performance. Indeed, Co/*meso*HZSM-5-stag exhibited the highest FT activity and C5-C11 selectivity, and the lowest CH_4 selectivity, which is ascribed to the lowest fraction of small cobalt particles. The optimal catalyst preparation method of this bifunctional FTS catalyst depends on the mesoporosity of the zeolite support and the targeted cobalt loading.

REFERENCES

[1] E. Iglesia, S.L. Soled, R.A. Fiato, Fischer-Tropsch synthesis on cobalt and ruthenium. Metal dispersion and support effects on reaction rate and selectivity, Journal of Catalysis, 137 (1992) 212-224.

[2] V.P. Santos, T.A. Wezendonk, J.J.D. Jaén, A.I. Dugulan, M.A. Nasalevich, H.-U. Islam, A. Chojecki, S. Sartipi, X. Sun, A.A. Hakeem, A.C.J. Koeken, M. Ruitenbeek, T. Davidian, G.R. Meima, G. Sankar, F. Kapteijn, M. Makkee, J. Gascon, Metal organic framework-mediated synthesis of highly active and stable Fischer-Tropsch catalysts, Nat Commun, 6 (2015).

[3] E. Iglesia, Design, synthesis, and use of cobalt-based Fischer-Tropsch synthesis catalysts, Applied Catalysis A: General, 161 (1997) 59-78.

[4] S. Storsæter, Ø. Borg, E.A. Blekkan, A. Holmen, Study of the effect of water on Fischer–Tropsch synthesis over supported cobalt catalysts, Journal of Catalysis, 231 (2005) 405-419.

[5] S. Sartipi, K. Parashar, M. Makkee, J. Gascon, F. Kapteijn, Breaking the Fischer-Tropsch synthesis selectivity: direct conversion of syngas to gasoline over hierarchical Co/H-ZSM-5 catalysts, Catalysis Science & Technology, 3 (2013) 572-575.

[6] X. Peng, K. Cheng, J. Kang, B. Gu, X. Yu, Q. Zhang, Y. Wang, Impact of Hydrogenolysis on the Selectivity of the Fischer–Tropsch Synthesis: Diesel Fuel Production over Mesoporous Zeolite Y-Supported Cobalt Nanoparticles, Angewandte Chemie International Edition, (2015) n/a-n/a.

[7] K. Cheng, L. Zhang, J. Kang, X. Peng, Q. Zhang, Y. Wang, Selective Transformation of Syngas into Gasoline-Range Hydrocarbons over Mesoporous H-ZSM-5-Supported Cobalt Nanoparticles, Chemistry – A European Journal, 21 (2015) 1928-1937.

[8] Q. Zhang, K. Cheng, J. Kang, W. Deng, Y. Wang, Fischer–Tropsch Catalysts for the Production of Hydrocarbon Fuels with High Selectivity, ChemSusChem, 7 (2014) 1251-1264.

[9] K. Cheng, J. Kang, S. Huang, Z. You, Q. Zhang, J. Ding, W. Hua, Y. Lou, W. Deng, Y. Wang, Mesoporous Beta Zeolite-Supported Ruthenium Nanoparticles for Selective Conversion of Synthesis Gas to C5–C11 Isoparaffins, ACS Catalysis, 2 (2012) 441-449.

[10] V. Udaya, S. Rao, R.J. Gormley, Bifunctional catalysis in syngas conversions, Catalysis Today, 6 (1990) 207-234.

[11] S. Sartipi, K. Parashar, M.J. Valero-Romero, V.P. Santos, B. van der Linden, M. Makkee, F. Kapteijn, J. Gascon, Hierarchical H-ZSM-5-supported cobalt for the direct synthesis of gasoline-range hydrocarbons from syngas: Advantages, limitations, and mechanistic insight, Journal of Catalysis, 305 (2013) 179-190.

[12] S. Sartipi, M. Alberts, V.P. Santos, M. Nasalevich, J. Gascon, F. Kapteijn, Insights into the Catalytic Performance of Mesoporous H-ZSM-5-Supported Cobalt in Fischer–Tropsch Synthesis, ChemCatChem, 6 (2014) 142-151.

[13] S. Sartipi, M. Alberts, M.J. Meijerink, T.C. Keller, J. Pérez-Ramírez, J. Gascon, F. Kapteijn, Towards Liquid Fuels from Biosyngas: Effect of Zeolite Structure in Hierarchical-Zeolite-Supported Cobalt Catalysts, ChemSusChem, 6 (2013) 1646-1650.

[14] J. Kang, K. Cheng, L. Zhang, Q. Zhang, J. Ding, W. Hua, Y. Lou, Q. Zhai, Y. Wang, Mesoporous Zeolite-Supported Ruthenium Nanoparticles as Highly Selective Fischer–Tropsch Catalysts for the Production of C5–C11 Isoparaffins, Angewandte Chemie International Edition, 50 (2011) 5200-5203.

[15] G.L. Bezemer, J.H. Bitter, H.P.C.E. Kuipers, H. Oosterbeek, J.E. Holewijn, X. Xu, F. Kapteijn, A.J. van Dillen, K.P. de Jong, Cobalt Particle Size Effects in the Fischer−Tropsch Reaction Studied with Carbon Nanofiber Supported Catalysts, Journal of the American Chemical Society, 128 (2006) 3956-3964.

[16] J.P. den Breejen, P.B. Radstake, G.L. Bezemer, J.H. Bitter, V. Frøseth, A. Holmen, K.P.d. Jong, On the Origin of the Cobalt Particle Size Effects in Fischer−Tropsch Catalysis, Journal of the American Chemical Society, 131 (2009) 7197-7203.

[17] J.P. den Breejen, J.R.A. Sietsma, H. Friedrich, J.H. Bitter, K.P. de Jong, Design of supported cobalt catalysts with maximum activity for the Fischer–Tropsch synthesis, Journal of Catalysis, 270 (2010) 146-152.

[18] Ø. Borg, P.D.C. Dietzel, A.I. Spjelkavik, E.Z. Tveten, J.C. Walmsley, S. Diplas, S. Eri, A. Holmen, E. Rytter, Fischer–Tropsch synthesis: Cobalt particle size and support effects on intrinsic activity and product distribution, Journal of Catalysis, 259 (2008) 161-164.

[19] N. Fischer, E. van Steen, M. Claeys, Structure sensitivity of the Fischer–Tropsch activity and selectivity on alumina supported cobalt catalysts, Journal of Catalysis, 299 (2013) 67-80.

[20] A. Martínez, G. Prieto, Breaking the dispersion-reducibility dependence in oxide-supported cobalt nanoparticles, Journal of Catalysis, 245 (2007) 470-476.

[21] A.n. Martínez, C. López, F. Márquez, I. Díaz, Fischer–Tropsch synthesis of hydrocarbons over mesoporous Co/SBA-15 catalysts: the influence of metal loading, cobalt precursor, and promoters, Journal of Catalysis, 220 (2003) 486-499.

[22] A. Jean-Marie, A. Griboval-Constant, A.Y. Khodakov, E. Monflier, F. Diehl, [small beta]-Cyclodextrin for design of alumina supported cobalt catalysts efficient in Fischer-Tropsch synthesis, Chemical Communications, 47 (2011) 10767-10769.

[23] J.-S. Girardon, A.S. Lermontov, L. Gengembre, P.A. Chernavskii, A. Griboval-Constant, A.Y. Khodakov, Effect of cobalt precursor and pretreatment conditions on the structure and catalytic performance of cobalt silica-supported Fischer–Tropsch catalysts, Journal of Catalysis, 230 (2005) 339-352.

[24] N.E. Tsakoumis, A. Voronov, M. Rønning, W.v. Beek, Ø. Borg, E. Rytter, A. Holmen, Fischer–Tropsch synthesis: An XAS/XRPD combined in situ study from catalyst activation to deactivation, Journal of Catalysis, 291 (2012) 138-148.

[25] P. Munnik, N.A. Krans, P.E. de Jongh, K.P. de Jong, Effects of Drying Conditions on the Synthesis of Co/SiO2 and Co/Al2O3 Fischer–Tropsch Catalysts, ACS Catalysis, 4 (2014) 3219-3226.

[26] E.S. Vasiliadou, T.M. Eggenhuisen, P. Munnik, P.E. de Jongh, K.P. de Jong, A.A. Lemonidou, Synthesis and performance of highly dispersed Cu/SiO2 catalysts for the hydrogenolysis of glycerol, Applied Catalysis B: Environmental, 145 (2014) 108-119.

[27] M. Wolters, P. Munnik, J.H. Bitter, P.E. de Jongh, K.P. de Jong, How NO Affects Nickel and Cobalt Nitrates at Low Temperatures To Arrive at Highly Dispersed Silica-Supported Nickel and Cobalt Catalysts, The Journal of Physical Chemistry C, 115 (2011) 3332-3339.

[28] J.R.A. Sietsma, J.D. Meeldijk, J.P. den Breejen, M. Versluijs-Helder, A.J. van Dillen, P.E. de Jongh, K.P. de Jong, The Preparation of Supported NiO and Co3O4 Nanoparticles by the Nitric Oxide Controlled Thermal Decomposition of Nitrates, Angewandte Chemie, 119 (2007) 4631-4633.

[29] P. Munnik, P.E. de Jongh, K.P. de Jong, Control and Impact of the Nanoscale Distribution of Supported Cobalt Particles Used in Fischer–Tropsch Catalysis, Journal of the American Chemical Society, 136 (2014) 7333-7340.

[30] P. Munnik, M. Wolters, A. Gabrielsson, S.D. Pollington, G. Headdock, J.H. Bitter, P.E. de Jongh, K.P. de Jong, Copper Nitrate Redispersion To Arrive at Highly Active Silica-Supported Copper Catalysts, The Journal of Physical Chemistry C, 115 (2011) 14698-14706.

[31] J.R.A. Sietsma, J.D. Meeldijk, M. Versluijs-Helder, A. Broersma, A.J.v. Dillen, P.E. de Jongh, K.P. de Jong, Ordered Mesoporous Silica to Study the Preparation of Ni/SiO2 ex Nitrate Catalysts: Impregnation, Drying, and Thermal Treatments, Chemistry of Materials, 20 (2008) 2921-2931.

[32] J.R.A. Sietsma, H. Friedrich, A. Broersma, M. Versluijs-Helder, A. Jos van Dillen, P.E. de Jongh, K.P. de Jong, How nitric oxide affects the decomposition of supported nickel nitrate to arrive at highly dispersed catalysts, Journal of Catalysis, 260 (2008) 227-235.

[33] D. Schanke, S. Vada, E.A. Blekkan, A.M. Hilmen, A. Hoff, A. Holmen, Study of Pt-Promoted Cobalt CO Hydrogenation Catalysts, Journal of Catalysis, 156 (1995) 85-95.

[34] S. Sartipi, H. Jansma, D. Bosma, B. Boshuizen, M. Makkee, J. Gascon, F. Kapteijn, Six-flow operations for catalyst development in Fischer-Tropsch synthesis: Bridging the gap between high-throughput experimentation and extensive product evaluation, Review of Scientific Instruments, 84 (2013) 124101.

[35] D.B.P.J. Van, M. Bracht, G.J.M. Gruter, R.R. de, B.H. Harji, Reactor assembly, in, Google Patents, 2014.

[36] R. Caicedo-Realpe, J. Pérez-Ramírez, Mesoporous ZSM-5 zeolites prepared by a two-step route comprising sodium aluminate and acid treatments, Microporous and Mesoporous Materials, 128 (2010) 91-100.

[37] J. Hong, W. Chu, P.A. Chernavskii, A.Y. Khodakov, Cobalt species and cobalt-support interaction in glow discharge plasma-assisted Fischer–Tropsch catalysts, Journal of Catalysis, 273 (2010) 9-17.

[38] P. Arnoldy, J.A. Moulijn, Temperature-programmed reduction of CoOAI2O3 catalysts, Journal of Catalysis, 93 (1985) 38-54.

[39] G. Prieto, P. Concepción, R. Murciano, A. Martínez, The impact of pre-reduction thermal history on the metal surface topology and site-catalytic activity of Fischer–Tropsch catalysts, Journal of Catalysis, 302 (2013) 37-48.

[40] Ø. Borg, S. Eri, E.A. Blekkan, S. Storsæter, H. Wigum, E. Rytter, A. Holmen, Fischer–Tropsch synthesis over γ-alumina-supported cobalt catalysts: Effect of support variables, Journal of Catalysis, 248 (2007) 89-100.

[41] G. Prieto, A. Martínez, P. Concepción, R. Moreno-Tost, Cobalt particle size effects in Fischer–Tropsch synthesis: structural and in situ spectroscopic characterisation on reverse micelle-synthesised Co/ITQ-2 model catalysts, Journal of Catalysis, 266 (2009) 129-144.

[42] S. Sun, N. Tsubaki, K. Fujimoto, The reaction performances and characterization of Fischer–Tropsch synthesis Co/SiO2 catalysts prepared from mixed cobalt salts, Applied Catalysis A: General, 202 (2000) 121-131.

[43] L.E.S. Rygh, C.J. Nielsen, Infrared Study of CO Adsorbed on a Co/Re/γAl2O3-Based Fischer–Tropsch Catalyst, Journal of Catalysis, 194 (2000) 401-409.

[44] L.E.S. Rygh, O.H. Ellestad, P. Klaeboe, C.J. Nielsen, Infrared study of CO adsorbed on Co/[gamma]-Al2O3 based Fischer-Tropsch catalysts; semi-empirical calculations as a tool for vibrational assignments, Physical Chemistry Chemical Physics, 2 (2000) 1835-1846.

[45] G. Kadinov, C. Bonev, S. Todorova, A. Palazov, IR spectroscopy study of CO adsorption and of the interaction between CO and hydrogen on alumina-supported cobalt, Journal of the Chemical Society, Faraday Transactions, 94 (1998) 3027-3031.

[46] A. Lapidus, A. Krylova, V. Kazanskii, V. Borovkov, A. Zaitsev, J. Rathousky, A. Zukal, M. Jancˇálková, Hydrocarbon synthesis from carbon monoxide and hydrogen on impregnated cobalt catalysts Part I. Physico-chemical properties of 10% cobalt/alumina and 10% cobalt/silica, Applied Catalysis, 73 (1991) 65-81.

[47] M.J. Heal, E.C. Leisegang, R.G. Torrington, Infrared studies of carbon monoxide and hydrogen adsorbed on silica-supported iron and cobalt catalysts, Journal of Catalysis, 51 (1978) 314-325.

[48] H. Xiong, Y. Zhang, K. Liew, J. Li, Fischer–Tropsch synthesis: The role of pore size for Co/SBA-15 catalysts, Journal of Molecular Catalysis A: Chemical, 295 (2008) 68-76.

[49] P. Concepción, C. López, A. Martínez, V.F. Puntes, Characterization and catalytic properties of cobalt supported on delaminated ITQ-6 and ITQ-2 zeolites for the Fischer–Tropsch synthesis reaction, Journal of Catalysis, 228 (2004) 321-332.

[50] S. Bessell, Support effects in cobalt-based fischer-tropsch catalysis, Applied Catalysis A: General, 96 (1993) 253-268.

[51] E. van Steen, M. Claeys, M.E. Dry, J. van de Loosdrecht, E.L. Viljoen, J.L. Visagie, Stability of Nanocrystals: Thermodynamic Analysis of Oxidation and Re-reduction of Cobalt in Water/Hydrogen Mixtures, The Journal of Physical Chemistry B, 109 (2005) 3575-3577.

[52] H. Xiong, M.A.M. Motchelaho, M. Moyo, L.L. Jewell, N.J. Coville, Correlating the preparation and performance of cobalt catalysts supported on carbon nanotubes and carbon spheres in the Fischer–Tropsch synthesis, Journal of Catalysis, 278 (2011) 26-40.

[53] C. Lancelot, V.V. Ordomsky, O. Stéphan, M. Sadeqzadeh, H. Karaca, M. Lacroix, D. Curulla-Ferré, F. Luck, P. Fongarland, A. Griboval-Constant, A.Y. Khodakov, Direct Evidence of Surface Oxidation of Cobalt Nanoparticles in Alumina-Supported Catalysts for Fischer–Tropsch Synthesis, ACS Catalysis, 4 (2014) 4510-4515.

[54] K. Azzam, G. Jacobs, W. Ma, B. Davis, Effect of Cobalt Particle Size on the Catalyst Intrinsic Activity for Fischer–Tropsch Synthesis, Catalysis Letters, 144 (2014) 389-394.

[55] W. Ma, G. Jacobs, Y. Ji, T. Bhatelia, D. Bukur, S. Khalid, B. Davis, Fischer–Tropsch Synthesis: Influence of CO Conversion on Selectivities, H2/CO Usage Ratios, and Catalyst Stability for a Ru Promoted Co/Al2O3 Catalyst Using a Slurry Phase Reactor, Top Catal, 54 (2011) 757-767.

[56] R.J. Gormley, V.U.S. Rao, R.R. Anderson, R.R. Schehl, R.D.H. Chi, Secondary reactions on metal-zeolite catalysts used in synthesis gas conversion, Journal of Catalysis, 113 (1988) 193-205.

[57] A.Y. Khodakov, W. Chu, P. Fongarland, Advances in the Development of Novel Cobalt Fischer−Tropsch Catalysts for Synthesis of Long-Chain Hydrocarbons and Clean Fuels, Chemical Reviews, 107 (2007) 1692-1744.

[58] R.J. Madon, E. Iglesia, The Importance of Olefin Readsorption and H2/CO Reactant Ratio for Hydrocarbon Chain Growth on Ruthenium Catalysts, Journal of Catalysis, 139 (1993) 576-590.

Appendix A

MOFs Mediated Cobalt/N-Doped Carbon Hybrids as Efficient and Chemoselective Catalysts for the Hydrogenation of Nitroarenes

Presentation of additional N_2 physisorption, elemental analysis, X-ray diffraction patterns, transmission electron microscopy, X-ray photoelectron spectroscopy and experimental data, associated with Chapter 2.
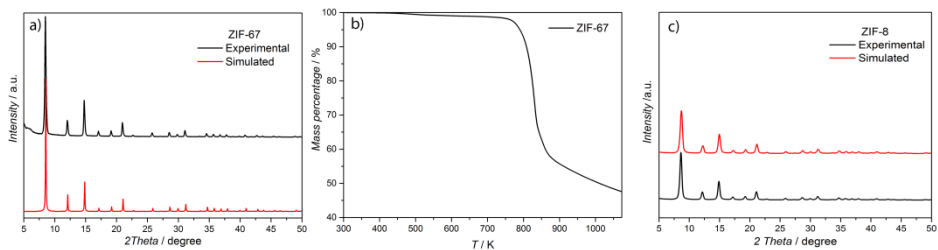
Figure A1. (a) XRD patterns of the synthesized ZIF-67, (b) TGA profile of ZIF-67 under N_2 flow (100 ml min^{-1} STP, heating rate 5 K min^{-1}). (c) XRD patterns of the synthesized ZIF-8.

The relative intensity and peak positions of the powder X-ray diffraction (PXRD) pattern confirm the formation of crystalline ZIF-67 (Fig. A1a) and ZIF-8 (Fig. A1c).
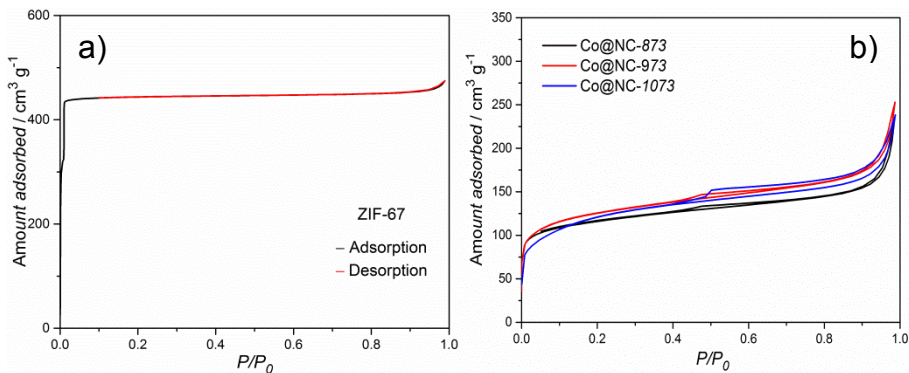
Figure A2. N_2 adsorption-desorption isotherms (77 K) of (a) ZIF-67, (b) Co@NC-*T* catalysts pyrolysed at different temperatures (*T* in K).

Table A1. Texture analysis by N_2-adsorption-desorption at 77 K of ZIF-67 and Co@NC-*T*.

Samples	S_{BET} / (m^2/g)			V_{pore} / (cm^3/g)		
	Total	Micro	Meso	Total	Micro	Meso
ZIF-67[a]	1930	1910	20	0.71	0.68	0.03
Co@NC-*873*[b]	400	280	120	0.36	0.13	0.23
Co@NC-*973*[b]	460	315	145	0.39	0.13	0.26
Co@NC-*1073*[b]	430	270	160	0.37	0.12	0.25

a: The given BET areas and pore volumes were calculated per gram of ZIF-67; b: The given BET areas and pore volumes were calculated per gram of support.

Table A2. Elemental Co and N content of Co@NC-*T* and Co@NC-*T(al)*.

Samples	Content (*wt.%*)	
	Co[a]	N[b]
Co@NC-*873*	31.0	7.8
Co@NC-*973*	32.9	3.7
Co@NC-*1073*	37.4	2.4
Co@NC-*873(al)*	27.1	9.4
Co@NC-*973(al)*	19.4	5.4
Co@NC-*1073(al)*	13.6	3.5
Co@NC-*1173(al)*	4.1	1.6

[a] Measured by atomic absorption spectroscopy (AAS); [b] measured by elemental analysis.

Table A2. The deconvolution analysis of the N*1s* XPS spectra of Co@NC-*T*.

Samples	Nitrogen content (*at.%*)			
	Pyridinic-N 399 eV	Graphitic-N 401 eV	Pyridinic-N$^+$-O$^-$ 402.3 eV	N_P/N_G [a]
Co@NC-*873*	75	23	2	3.3
Co@NC-*973*	66	27	7	2.4
Co@NC-*1073*	53	41	6	1.3
Co@NC-*1073(al)*				

[a] Ratio of Pyridinic-N/Graphitic-N

Table A3. Effect of reaction temperature on nitrobenzene conversion in the hydrogenation over Co@NC-*1073*.[a]

T (K)	X[b] (%)
303	<3
323	8
343	15
363	55
383	99

[a] Reaction conditions: 1 mmol nitrobenzene, substrate to cobalt molar ratio of 24, in 5 mL of ethanol, 3 MPa H$_2$, 3 h, aniline selectivity in all cases > 99%. [b] Determined by GC (internal standard: *n*-hexadecane).

Table A4. Effect of nitrobenzene (NB) concentration on its hydrogenation conversion over Co@NC-*1073*.[a]

C_{NB} (M)	Substrate to cobalt molar ratio	X (%)[b]	*TON* (mol NB/mol Co)
0.2	24	99	24
0.4	48	48	23
0.6	73	33	24

[a] Reaction conditions: 5 mL of ethanol, 383 K, 3 MPa H_2, reaction time 3 h, aniline selectivity in all cases > 99%. [b] Determined by GC (internal standard: *n*-hexadecane).

Table A5. Co particle size in Co@NC-*T* and Co@NC-*T(al)*.

Catalysts	d_{Co} (nm) [a]
Co@NC-*873*	8
Co@NC-*973*	14
Co@NC-*1073*	21
Co@NC-*873(al)*	8
Co@NC-*973(al)*	10
Co@NC-*1073(al)*	12

[a] Calculated from the 111 ($2\theta = 51.9°$) reflection of XRD.
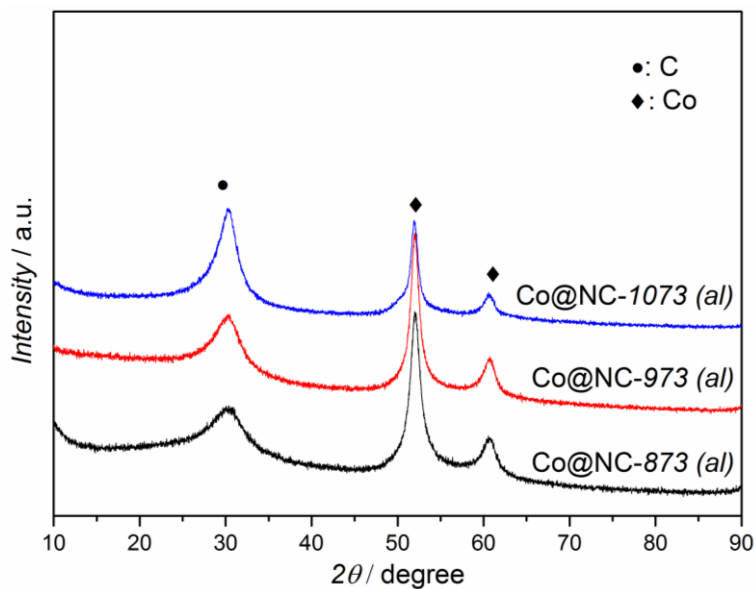
Figure A3. XRD patterns of Co@NC-*T(al)*.
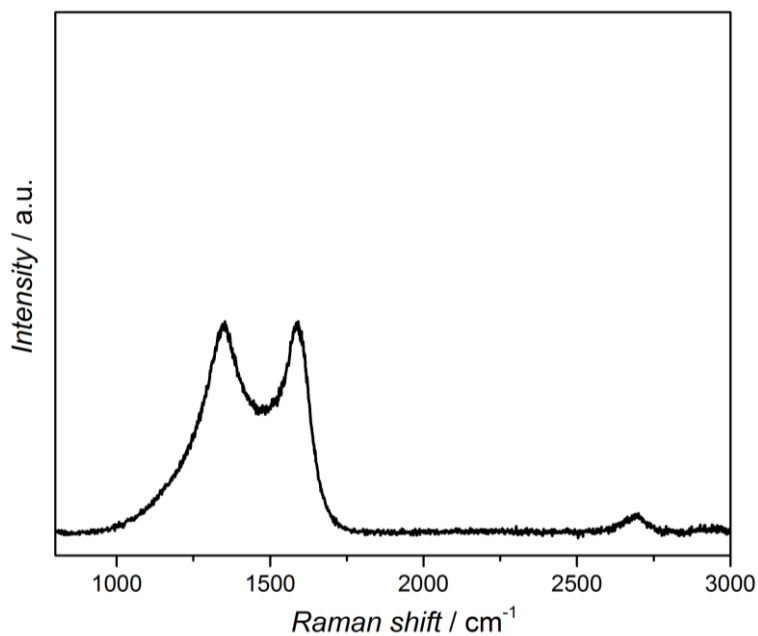
Figure A4. Raman spectrum of Co@NC-*1073(al)*.
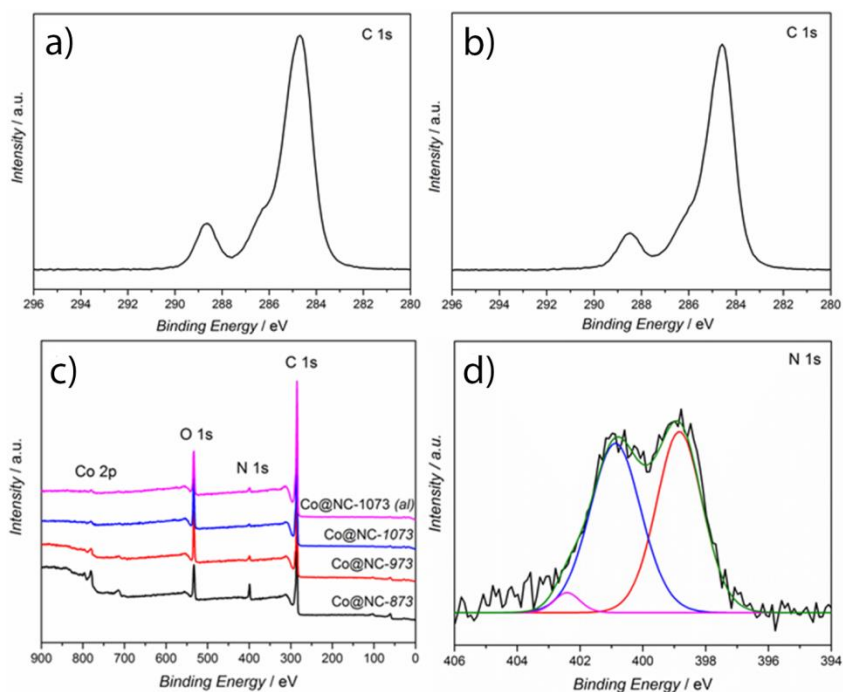
Figure A5. XPS spectra of C*1s* region of (a) Co@NC-*1073*, (b) Co@NC-*1073(al)*, (c) XPS survey of Co@NC-*T* and Co@NC-*1073(al)*, (d) XPS spectra of N*1s* region Co@NC-*1073(al)*. Colored lines represent the deconvolution of the N*1s* region.

The similar C *1s* XPS spectra in the Co@NC-*1073* and Co@NC-*1073(al)* samples demonstrate a well-preserved carbon structure after acid leaching. The survey indicates that all of the Co@NC samples contain C, N, O, and Co. A relatively higher graphitic-N content in Co@NC-*1073(al)* than in Co@NC-*1073* is also observed, presumably due to more detectable graphitic-N atoms after removal of some cobalt NPs.
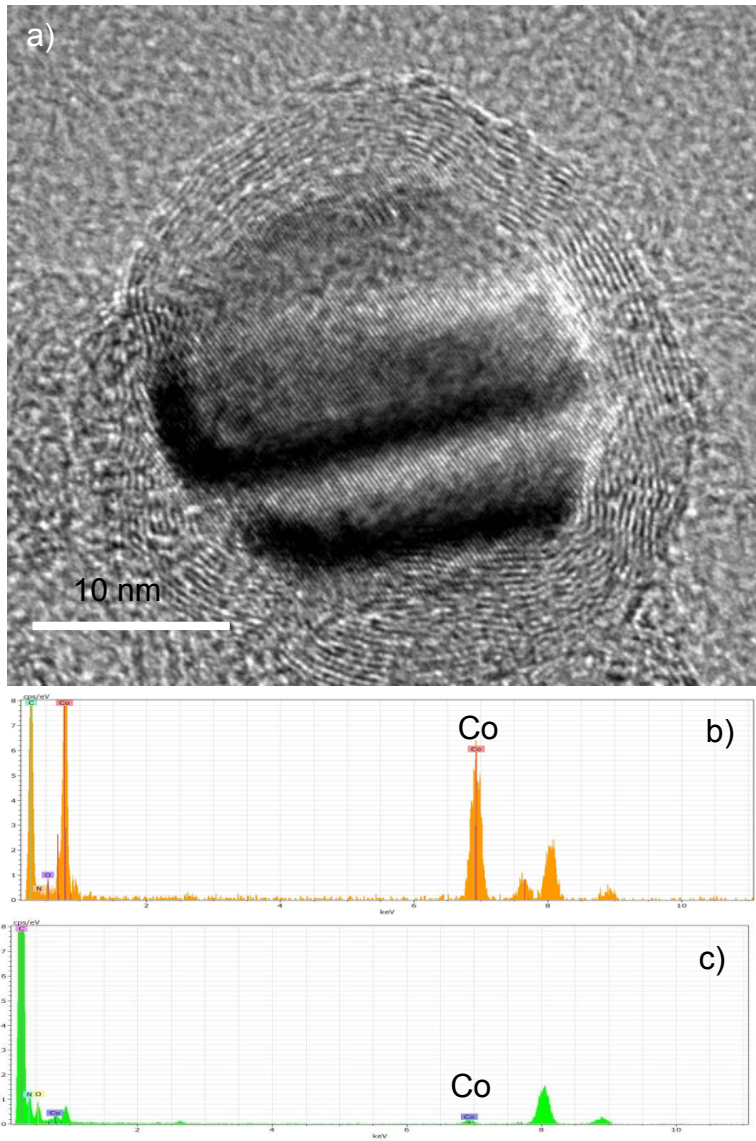
Figure A6. (a) HR-TEM of Co@NC-*1073(al)*, in which a Co crystallite encaged in a layered graphene shell can be clearly distinguished. EDXS analysis of Co@NC-*1073(al)* from (b) area 1 and (c) area 2 in Figure 4b.

Table A6. Cobalt content in the reaction solution after each run upon recycling Co@NC-*1073*

Run #	Cobalt content (ppm) [a]
1	< 3
2	<3
3	<3
4	< 3

[a] Obtained by ICP-AES analysis.

Table A7. Comparison of the nitrobenzene hydrogenation activity and number of turnovers *TON* (mol_{NB} converted/mol_{Co}) of the catalysts in this work and literature data.

Literature	Catalyst	Cobalt loading (*wt.%*)	Condition	*TON*	Activity (mol_{NB} $kg_{cat.}^{-1}$)
Nature Chemistry, 2013, **5**, 537.	1,10-phenanthroline, $Co(OAc)_2 \cdot 4H_2O$	3.05	383 K, 3 h, 50 bar	97	50
ACS Catal. 2015, **5**, 4783.	Co/N-doped carbon	27.2	383 K , 3 h, 30 bar	25	115
ChemCatChem 2016, 8, 1132.	$CoO_x@C$	29.15	393 K , 4 h, 30 bar	10	50
This work	Co@NC-*1073*	37.4	383 K , 3 h, 30 bar	24	150
This work	Co@NC-*1073* (*al*)	13.6	383 K , 3 h, 30 bar	53	120
This work[*]	Co@NC-*1073*	37.4	383 K , 4×3 h + 12 h, 30 bar	118[*]	735[*]
This work[a]	Co@NC-*1173* (*al*)	4.1	383 K , 2.5 h, 30 bar	88	61
This work[*a]	Co@NC-*1173* (*al*)	4.1	383 K , 5×2.5 h, 30 bar	393[*]	273[*]

[*]: Cumulated result of repeated runs with the same sample (see Figure 5 or Figure S10); [a]: 1 mmol nitrobenzene, substrate to cobalt molar ratio of 97, 5 mL ethanol, 383 K, 3 MPa H_2, 2.5 h for each run
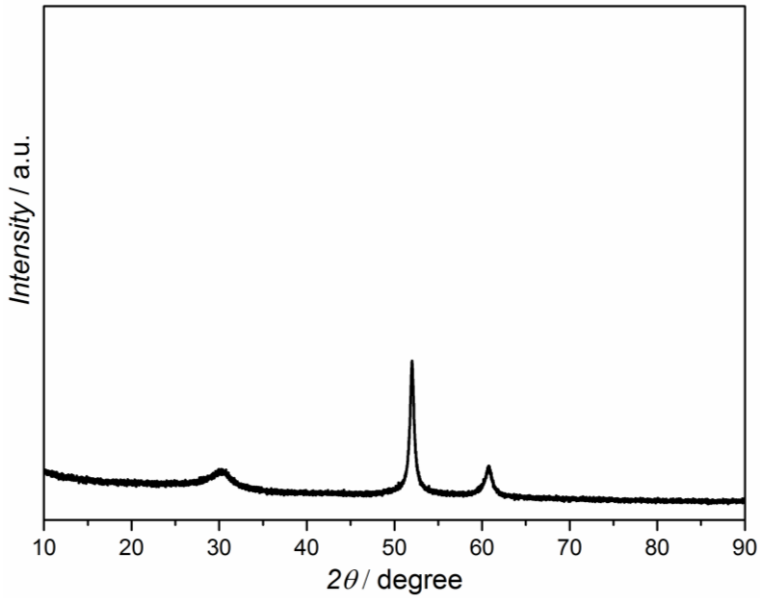
Figure A7. XRD pattern of spent Co@NC-*1073* after the 4th run.

The diffraction peak at 30.6° can be indexed to the (002) planes of graphitic carbon. In addition, the two peaks at 51.8° and 60.6° indicate the diffraction of (111) and (200) planes of metallic cobalt, respectively.
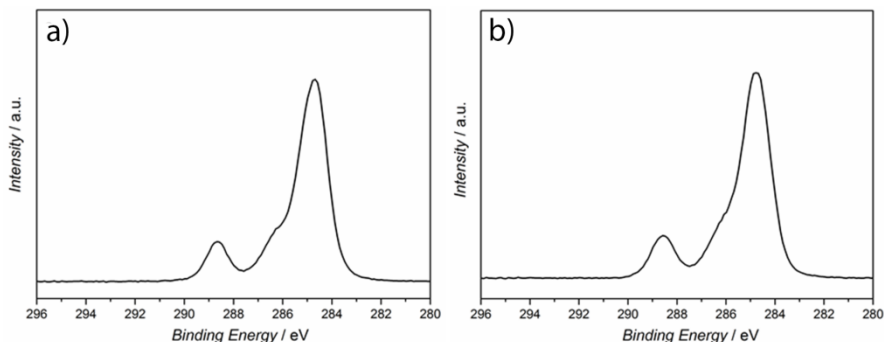
Figure A8. XPS spectra of C*1s* region of (a) fresh Co@NC-*1073*, (b) spent Co@NC-*1073* after the 4th run.

The similar C *1s* XPS spectra of the fresh and spent Co@NC-*1073* samples demonstrate a well-preserved carbon speciation after 4 times recycling.
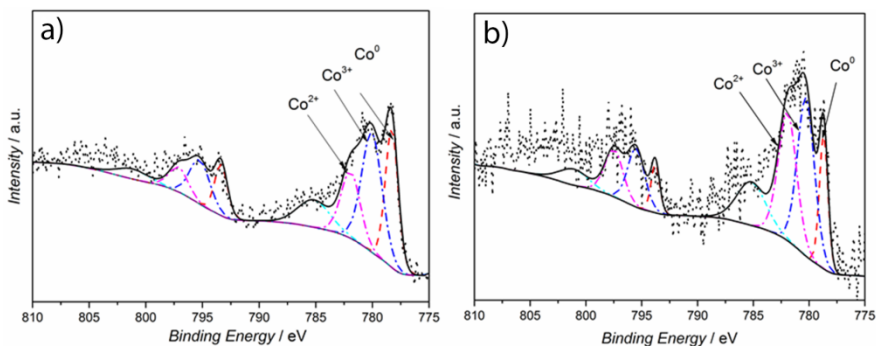
Figure A9. XPS spectra of Co*2p* region of (a) fresh Co@NC-*1073*, (b) spent Co@NC-*1073* after the 4th run. Deconvolution indicated by dashed curves.

Both the fresh and spent Co@NC-*1073* contain Co^0, Co^{2+} and Co^{3+}, as observed from Co *2p* XPS signal, and the spent Co@NC-*1073* has a higher fraction of cobalt oxide. Besides, a satellite peak at around 785 eV can also be observed, which is the characteristic peak for CoO, further confirming the presence of Co^{2+} in these samples.
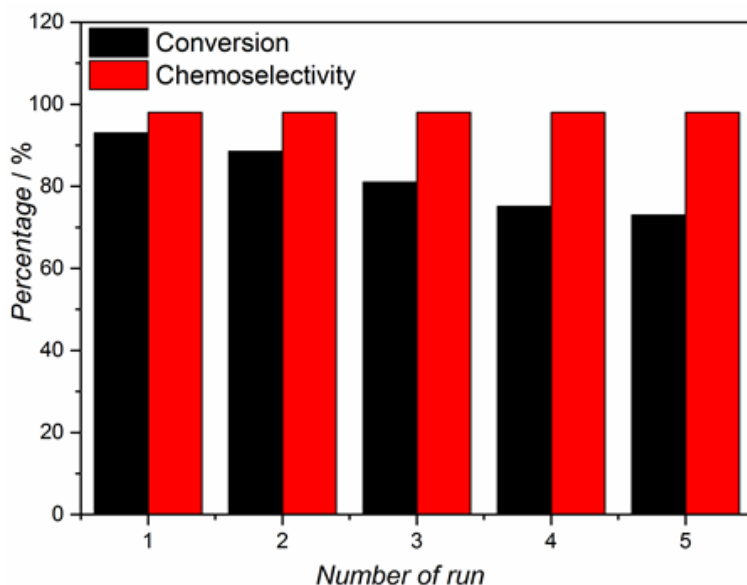
Figure A10. Nitrobenzene conversion and aniline selectivity upon reuse of Co@NC-*1173(al)*. Reaction conditions: 1 mmol nitrobenzene, substrate to cobalt molar ratio of 97, 5 mL ethanol, 383 K, 3 MPa H_2, 2.5 h for each run.

In an attempt to remove more cobalt nanoparticles completely encapsulated by graphitic carbon shells, ZIF-67 was pyrolyzed at 1173 K under the same conditions as the other Co@NC-*T* catalysts in this paper, followed by acid leaching. The cobalt loading in the Co@NC-*1173*(*al*) is 4 wt.% according to AAS analysis, indicating that more cobalt nanoparticles can be leached out with acid leaching after a pyrolysis treatment at a higher temperature. The hydrogenation performance clearly shows that the acid leached sample has a much better stability than the non-leached catalysts together with a much higher *TON* of 70 even only for the 5th run. Overall this catalyst reached 393 turnovers after 5 runs.

Atomically Dispersed Cobalt Sites in Mesoporous N-Doped Carbon Matrix for Selective Catalytic hydrogenation of Nitroarenes

Presentation of additional N_2 physisorption, X-ray diffraction patterns, transmission electron microscopy, Raman spectroscopy and experimental data, associated with Chapter 3.

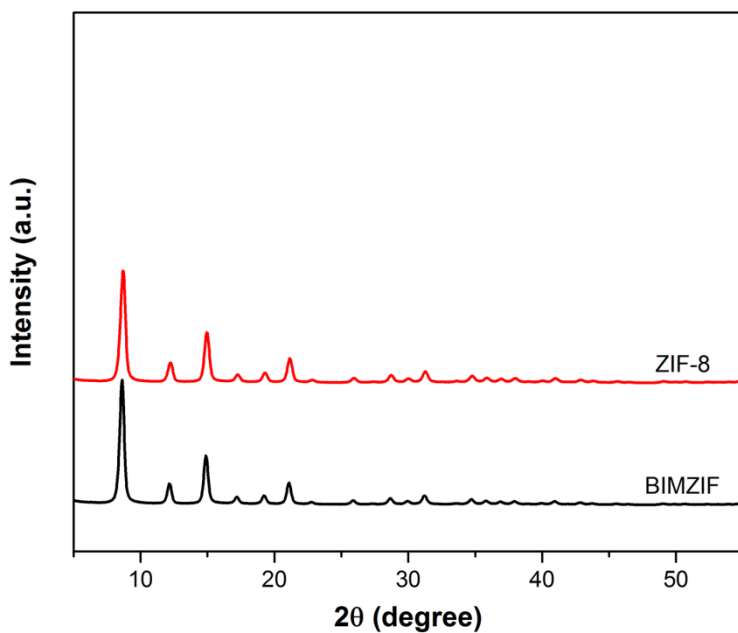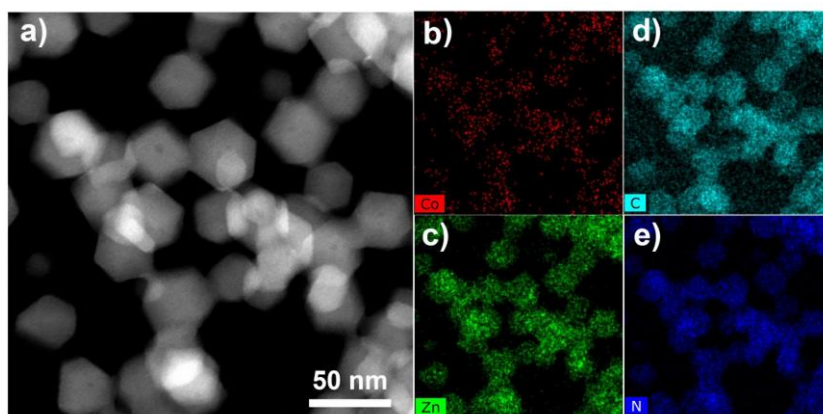**Figure B1**: X-ray diffraction (XRD) patterns of BIMZIF

Figure B2: Dark field TEM image of BIMZIF (a); and element mapping of Co (b), Zn (c), C (d), and N (e) in BIMZIF.

The crystals of BIMZIF(Co,Zn) exhibit a typical rhombic dodecahedral shape with homogeneously dispersed cobalt, zinc, carbon and nitrogen throughout the crystals.
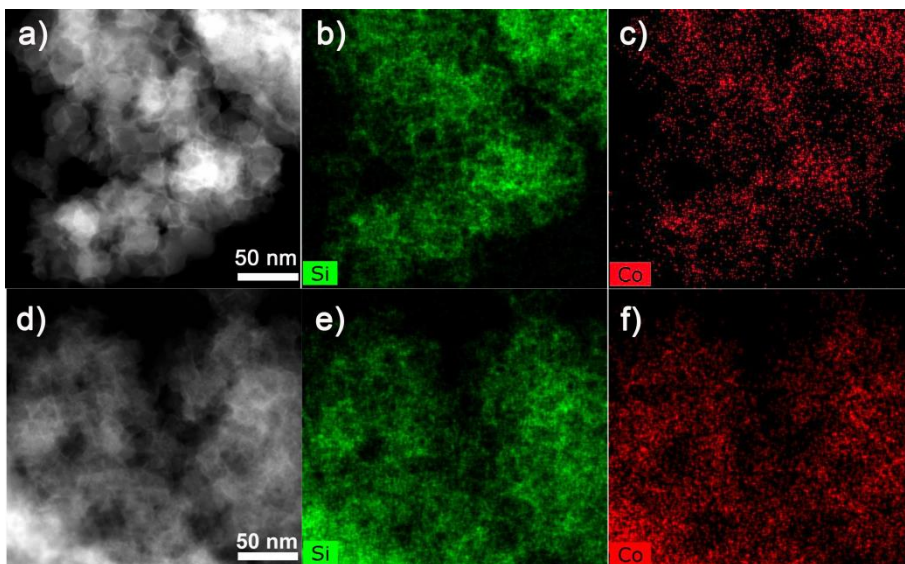
Figure B3: Dark field TEM image of BIMZIF@SiO$_2$ (a) and Co@NC-SiO$_2$ (d); and Si, Co mapping of BIMZIF@SiO$_2$ (b,c) and Co@NC-SiO$_2$ (e,f).

The EDX mapping confirms the homogeneous distribution of Si in the structure of both BIMZIF@SiO$_2$ and Co@NC-SiO$_2$. At the same time, no cobalt nanoparticles can be observed in Co@NC-SiO$_2$ sample.
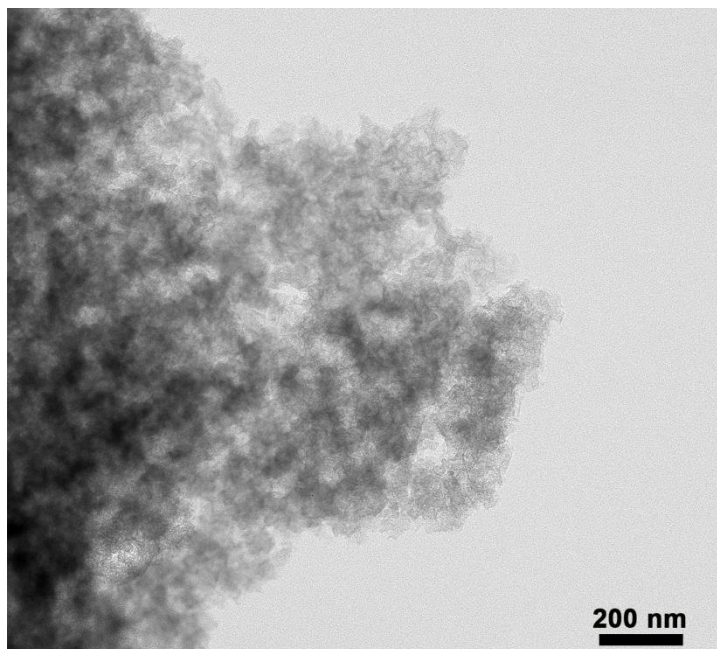
Figure B4: Bright field TEM image of Co@NC-SiO$_2$ catalyst

No cobalt nanoparticles can be observed in Co@NC-SiO$_2$ catalyst from the TEM image.
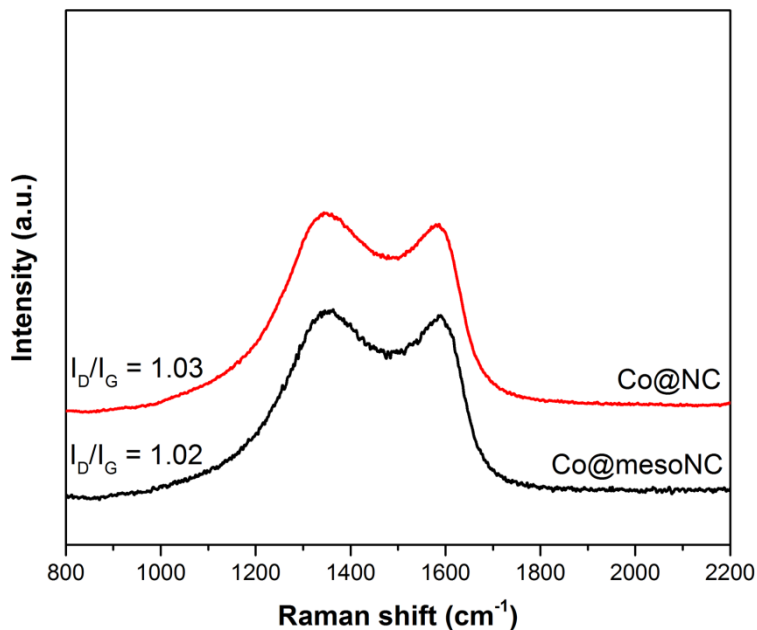
Figure B5: Raman spectra of Co@mesoNC and Co@NC.

The Raman spectra show a similar intensity ratio between D band and G band, indicative of a comparable graphitization degree of carbon in Co@mesoNC and Co@NC.
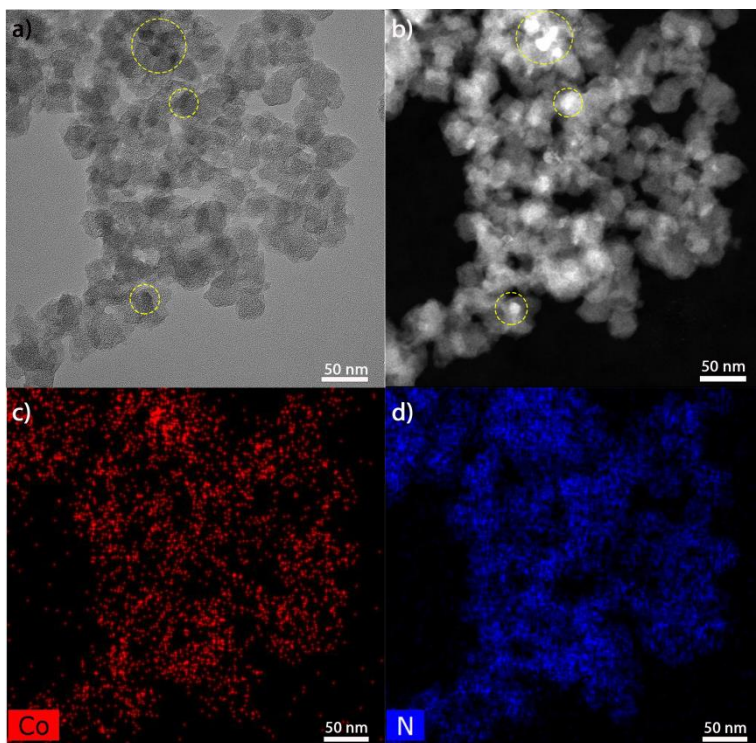
Figure B6: Bright field (a) and dark field (b) TEM image of Co@NC; and elemental mapping of Co (c) and N (d) in Co@NC catalyst.

TEM images claim that both highly dispersed cobalt species ($Co-N_x$) and cobalt nanoparticles can be observed in Co@NC sample.
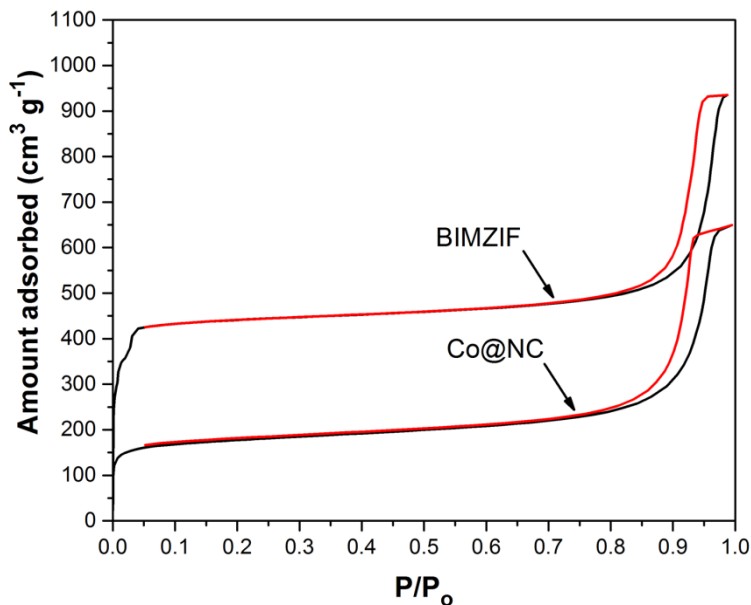
Figure B7: N$_2$ adsorption-desorption isotherms of BIMZIF and Co@NC.

Table B1: Texture analysis by N$_2$-adsorption-desorption (77 K) of BIMZIF, Co@mesoNC and Co@NC.[a]

Samples	S_{BET} / (m^2/g)			V_{pore} / (cm^3/g)		
	Total	Micro	Meso	Total	Micro	Meso
BIMZIF	1780	1640	140	1.44	0.62	0.82
Co@mesoNC	1230	710	520	1.54	0.30	1.24
Co@NC	680	520	160	0.98	0.20	0.78

a: The given BET areas and pore volumes were calculated per gram of catalyst.

Table B2: Comparison of the catalytic activity of Co@mesoNC to recent reported non-noble catalysts for nitrobenzene hydrogenation reaction to aniline.

Entry	Catalyst	T (°C)	P_{H2} (MPa)	S^a (%)	Catalyst productivity (mmol$_{NB}$ h^{-1} mg$_{Co}^{-1}$)	Reference
1	Co@mesoNC	110	3.0	>99	**0.72**[b]	This work
2	Co-Co₃O₄/NGr@C	110	5.0	>99	0.41	[1]
3	Co@N-doped carbon	110	5.0	>99	0.30	[2]
4	Co/mCN	120	1.0	>99	0.21	[3]
5	Co@NC	110	3.0	>99	0.14	[4]
6	CoOₓ@NCNTs	110	3.0	>99	0.14	[5]
7	Co-SiCN	110	5.0	>99	0.02	[6]
8	Ni-NiO/NGr@C	110	5.0	>98	0.04	[7]
9	Fe/N-C	120	4.0	>99	0.01	[8]
10	Fe₂O₃/NGr@C	120	5.0	98	0.03	[9]

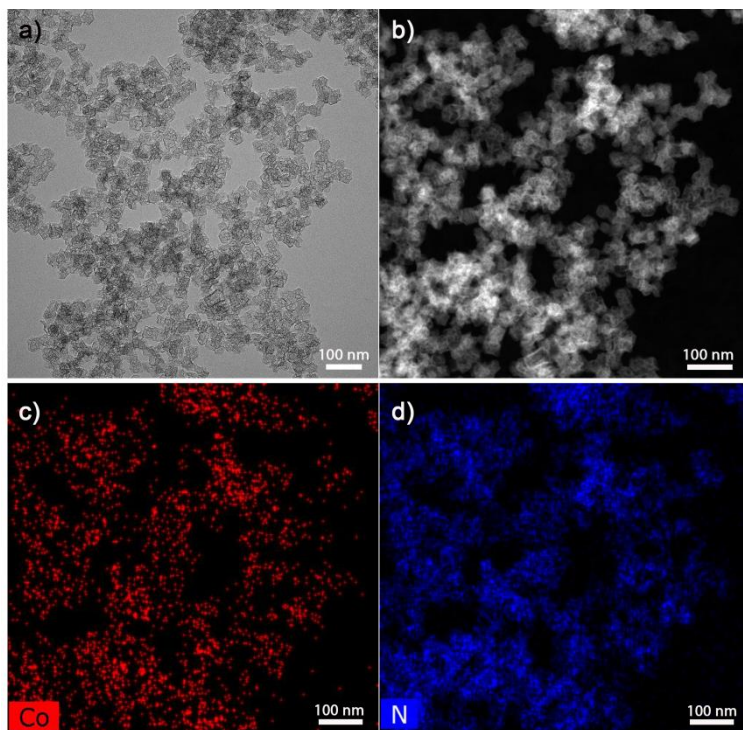[a]: aniline selectivity; [b]: calculated after 2 h reaction.

Figure B8: Bright field (a) and dark field (b) TEM image of Co@mesoNC (spent); and elemental mapping of Co (c) and N (d) in the spent Co@mesoNC catalyst.
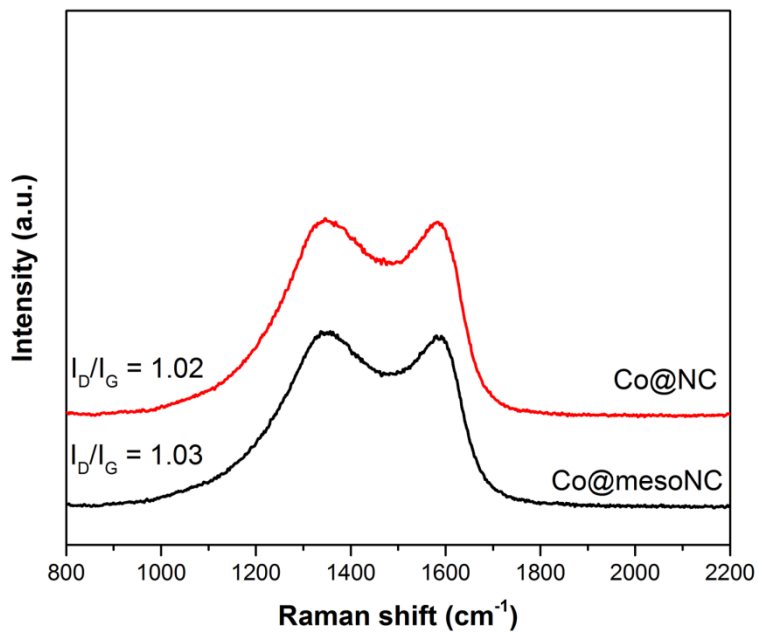
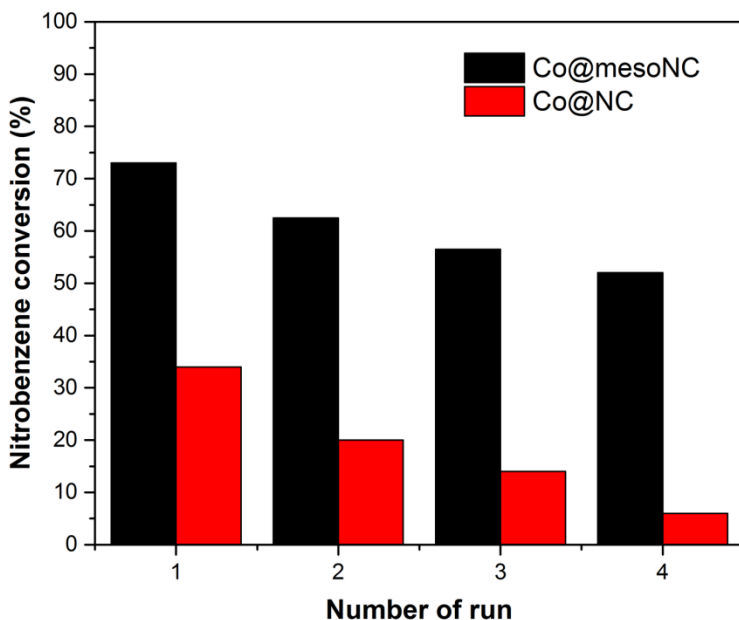**Figure B9**: Raman spectra of the spent Co@mesoNC and Co@NC.

Figure B10: Recycling experiments of hydrogenation of nitrobenzene with Co@mesoNC and Co@NC catalysts. Reaction conditions: 1 mmol nitrobenzene, substrate to cobalt molar ratio of 150, 0.65 mmol dodecane as internal standard, 5 mL ethanol, 383 K, 3 MPa H_2, 3 h for recycling experiments. Aniline selectivity >99%.

Table B3: Cobalt content in the reaction solution after each run upon recycling for Co@mesoNC[a]

Run #	Cobalt content (wppm) [a]
1	2.6
2	2.7
3	1.8

[a] Obtained by ICP-AES analysis.

Table B4: Comparison of the catalytic activity of Co@mesoNC to recent reported non-noble catalysts for 3-nitrostyrene hydrogenation reaction to 3-Vinylaniline.
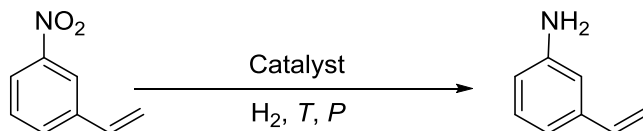
Entry	Catalyst (Substrate to cobalt molar ratio)	T (°C)	P_{H2} (MPa)	S^a (%)	Catalyst productivity (mmol$_{NB}$ h^{-1} mg$_{Co}^{-1}$)	Reference
1	Co@mesoNC	110	3.0	>97	**0.46**[b]	This work
2	Co-Co$_3$O$_4$/NGr@C	110	5.0	>92	0.27	[1]
4	CoO$_x$@NCNTs	110	3.0	98	0.04	[5]
3	Co-SiCN	110	5.0	82	0.02	[6]
5	Co/CoO@C	120	3.0	>95	0.04	[10]
6	Co@C	120	0.7	>97	0.02	[11]
7	Co/C-N	100	1.0	96	0.04	[12]
8	Ni@C	140	0.5	>95	0.21	[13]
9	Ni@SiCN	110	5.0	86	0.07	[14]

[a]: 3-Vinylaniline selectivity; [b]: calculated after 2 h reaction.

REFERENCES

[1] F. A. Westerhaus, R. V. Jagadeesh, G. Wienhöfer, M.-M. Pohl, J. Radnik, A.-E. Surkus, J. Rabeah, K. Junge, H. Junge, M. Nielsen, A. Brückner, M. Beller, Nat Chem 2013, 5, 537-543.

[2] D. Formenti, F. Ferretti, C. Topf, A.-E. Surkus, M.-M. Pohl, J. Radnik, M. Schneider, K. Junge, M. Beller, F. Ragaini, Journal of Catalysis 2017, 351, 79-89.

[3] X. Cui, K. Liang, M. Tian, Y. Zhu, J. Ma, Z. Dong, Journal of Colloid and Interface Science 2017, 501, 231-240.

[4] X. Sun, A. I. Olivos-Suarez, L. Oar-Arteta, E. Rozhko, D. Osadchii, A. Bavykina, F. Kapteijn, J. Gascon, ChemCatChem 2017, 9, 1854-1862.

[5] Z. Wei, J. Wang, S. Mao, D. Su, H. Jin, Y. Wang, F. Xu, H. Li, Y. Wang, ACS Catalysis 2015, 5, 4783-4789.

[6] T. Schwob, R. Kempe, Angewandte Chemie International Edition 2016, 55, 15175-15179.

[7] S. Pisiewicz, D. Formenti , A.-E. Surkus, M.-M. Pohl, J. Radnik, K. Junge, C. Topf, S. Bachmann, M. Scalone, M. Beller, ChemCatChem 2016, 8, 129-134.

[8] S. Xu, D. Yu, S. Liao, T. Ye, H. Sheng, RSC Advances 2016, 6, 96431-96435.

[9] R. V. Jagadeesh, A.-E. Surkus, H. Junge, M.-M. Pohl, J. Radnik, J. Rabeah, H. Huan, V. Schünemann, A. Brückner, M. Beller, Science 2013, 342, 1073-1076.

[10] B. Chen, F. Li, Z. Huang, G. Yuan, ChemCatChem 2016, 8, 1132-1138.

[11] L. Liu, P. Concepción, A. Corma, Journal of Catalysis 2016, 340, 1-9.

[12] X. Wang, Y. Li, Journal of Molecular Catalysis A: Chemical 2016, 420, 56-65.

[13] B. Tang, W.-C. Song, E.-C. Yang, X.-J. Zhao, RSC Advances 2017, 7, 1531-1539.

[14] G. Hahn, J.-K. Ewert, C. Denner, D. Tilgner, R. Kempe, ChemCatChem 2016, 8, 2461-2465.

Stepwise synthesis of highly loaded and active Silica supported Cobalt Fischer-Tropsch catalysts using Metal Organic Frameworks as sacrificial templates

Presentation of additional N_2 physisorption, X-ray diffraction patterns, transmission electron microscopy, Raman spectroscopy and experimental data, associated with Chapter 4.
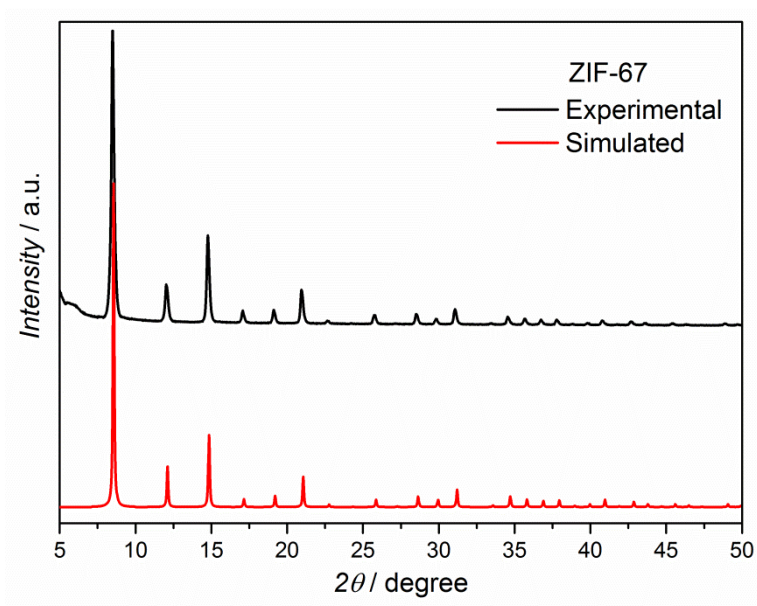
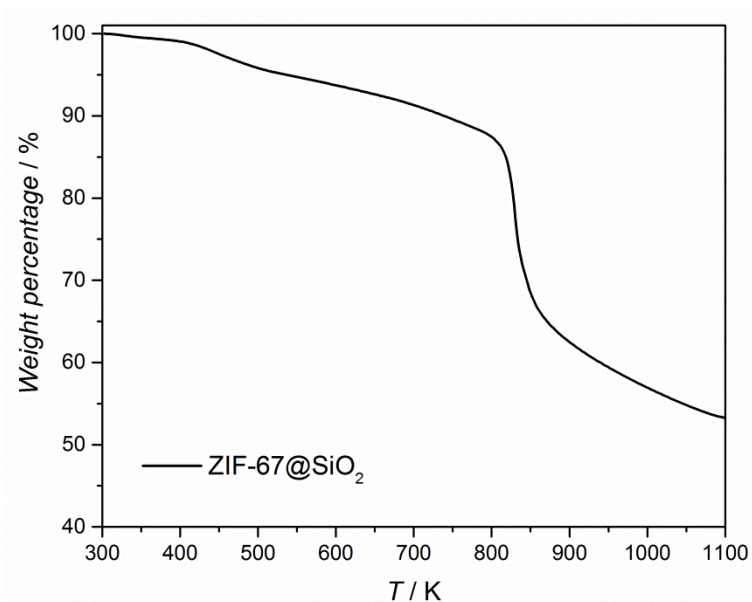**Figure C1**. X-ray diffraction patterns of the synthesized ZIF-67.

Figure C2. TGA profile of ZIF-67@SiO$_2$ heated in N$_2$ flow (100 ml min^{-1} STP) at a ramp of 5 K min^{-1}. The complete decomposition of the ZIF-67 structure occurs between 800 and 850 K.
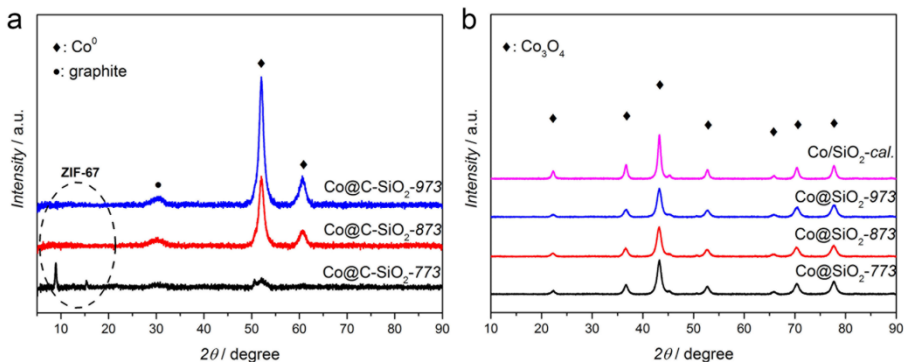
Figure C3. X-ray diffraction patterns of the different catalyst samples. (a) Co@C-SiO$_2$ catalysts after pyrolysis at different temperatures under N$_2$ atmosphere. (b) Co@SiO$_2$ catalysts after calcination at 673 K for 2 h in air.
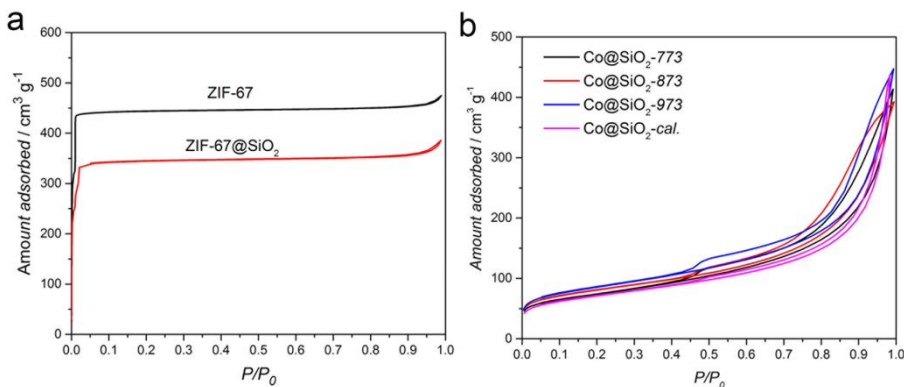

Figure C4. N$_2$ adsorption-desorption isotherms (77 K) of different samples. (a) ZIF-67 and ZIF-67@SiO$_2$ samples after hydrolysis treatment, (b) Co@SiO$_2$ samples after calcination at 673 K for 2 h in air.
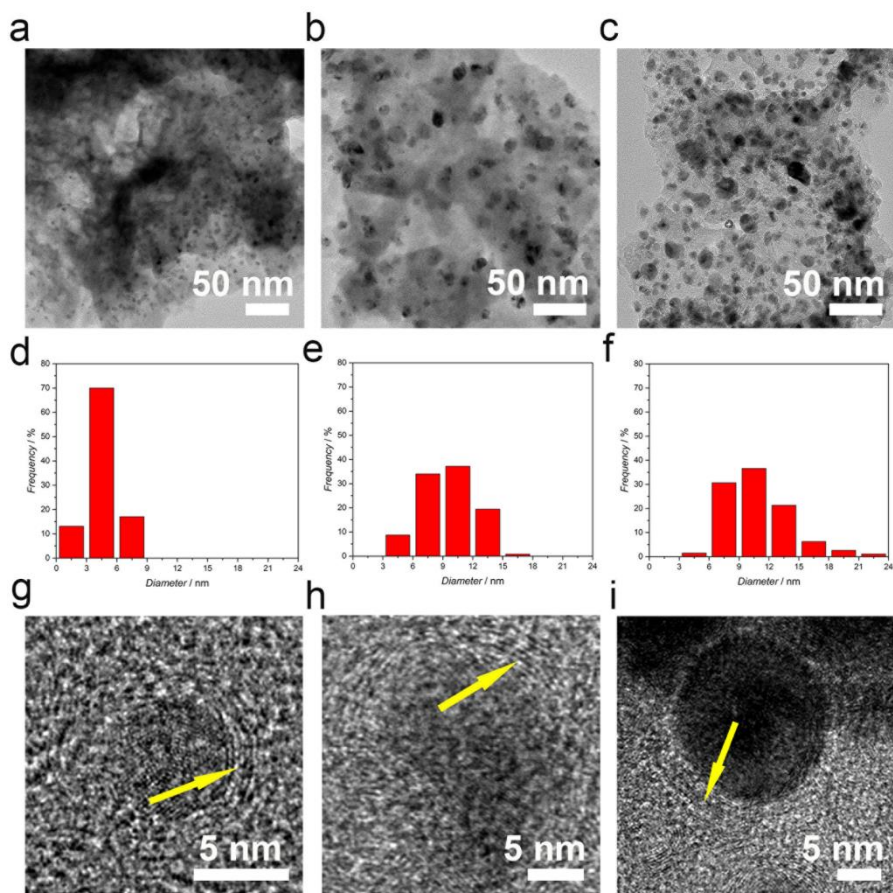
Figure C5. TEM micrographs and corresponding nanoparticle size distributions of Co@C-SiO$_2$-*T* catalysts. (a) TEM micrograph of Co@C-SiO$_2$-*773,* (b) Co@C-SiO$_2$-*873,* and (c) Co@C-SiO$_2$-*973*. (d) Particle size histograms obtained from TEM analysis for Co@C-SiO$_2$-*773*, (e) Co@C-SiO$_2$-*873*, and (f) Co@C-SiO$_2$-*973*. (g) High-resolution TEM (HR-TEM) micrograph of Co@C-SiO$_2$-*773,* (h) Co@C-SiO$_2$-*873,* and (i) Co@C-SiO$_2$-*973*.
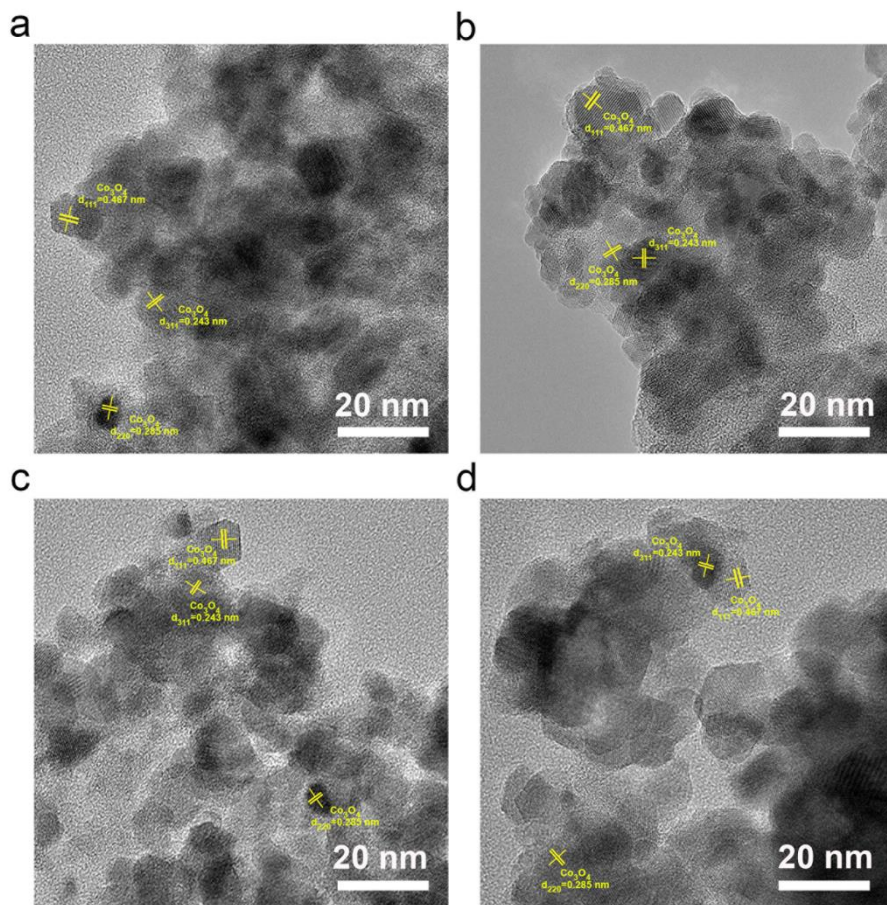
Figure C6. High-resolution TEM (HR-TEM) micrographs of Co@SiO₂-*T* catalysts. (a) Co@SiO₂-*cal.,* (b) Co@SiO₂-*773*, and (c) Co@SiO₂-*873*. (d) Co@SiO₂-*973*.
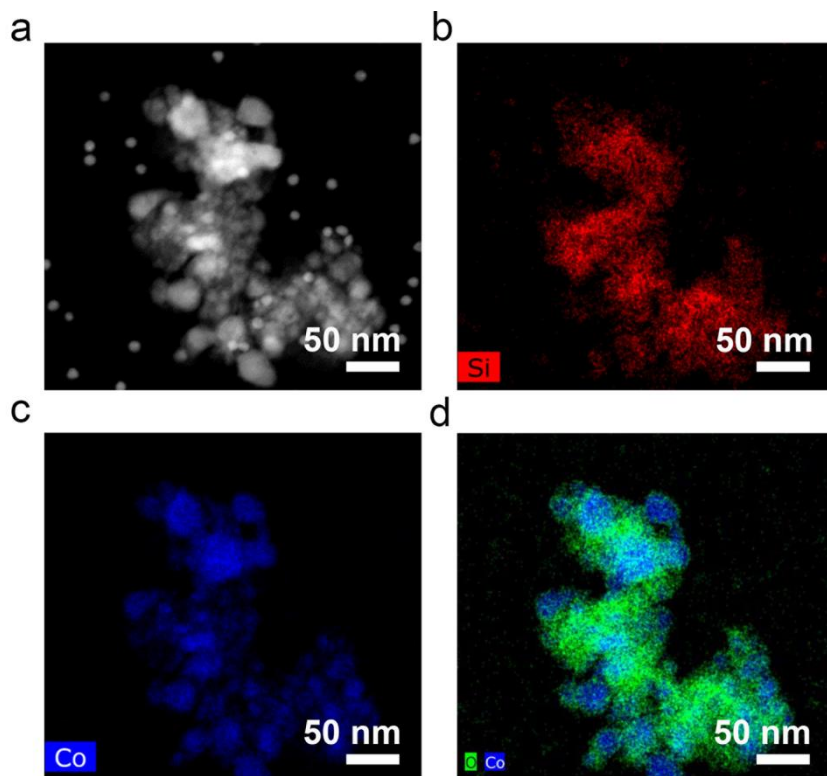
Figure C7. TEM analysis of Co@SiO$_2$-*873* after reduction in 10 vol.% H$_2$/Ar (30 ml min^{-1}, STP) at 673 K for 10 h at a heating rate of 2 K min^{-1}, followed by passivation in 6 vol.% O$_2$/Ar (50 ml min^{-1}, STP) at 303 K for 2 h. (a) HAADF-STEM micrograph, (b) Elemental mapping of Si, (c) of Co, and (d) of Co (*blue*) and O (*green*) in the reduced Co@SiO$_2$-*873* sample.
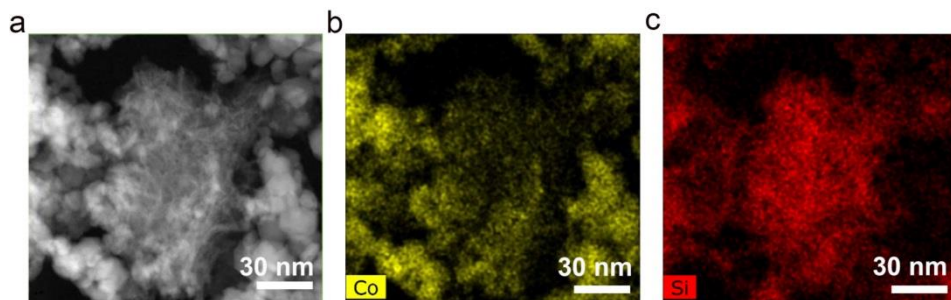
Figure C8. TEM analysis of Co@SiO₂-*cal*. catalyst. (a) Dark field TEM micrograph, (b) Elemental mapping of Co, and (c) of Si.
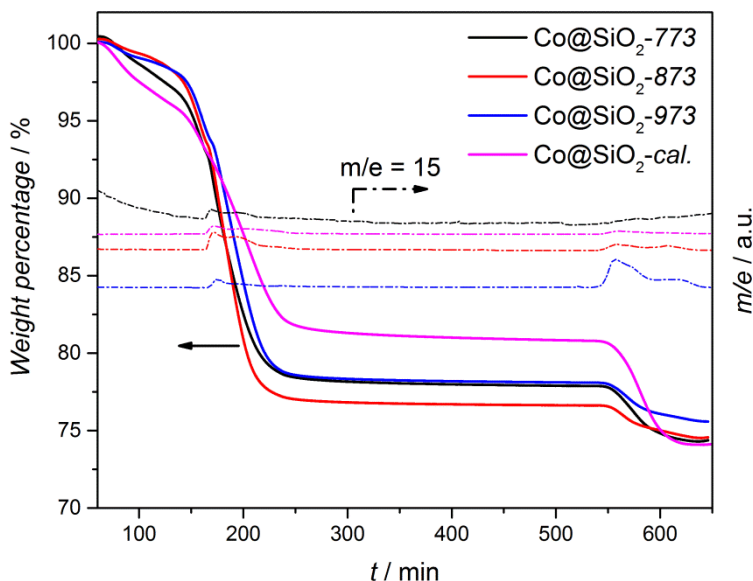
Figure C9. Thermogravimetric (TG) analysis (solid lines) of Co@SiO₂ catalysts in a flow of 10 vol.% H₂/Ar combined with mass spectroscopic (MS) gas phase analysis for $m/e = 15$ (CH₃⁺) corresponding to methane (dashed lines). Samples of ~10 mg Co@SiO₂ catalysts were used. The temperature was increased from room temperature to 673 K (5 K min⁻¹), held there for 5 h and then further increased to 1223 K (10 K min⁻¹).
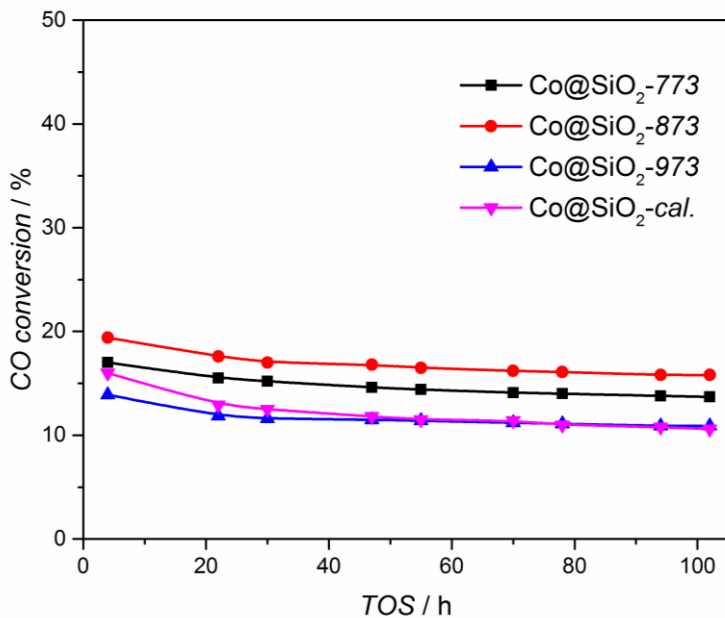
Figure C10. CO conversion as a function of time-on-stream (*TOS*) in the FTS over Co@SiO$_2$-*T* and Co@SiO$_2$-*cal*. Reaction conditions: 483 K, 20 bar, H$_2$/CO = 1, 100 mg catalysts and syngas flow of 40 ml min^{-1}.
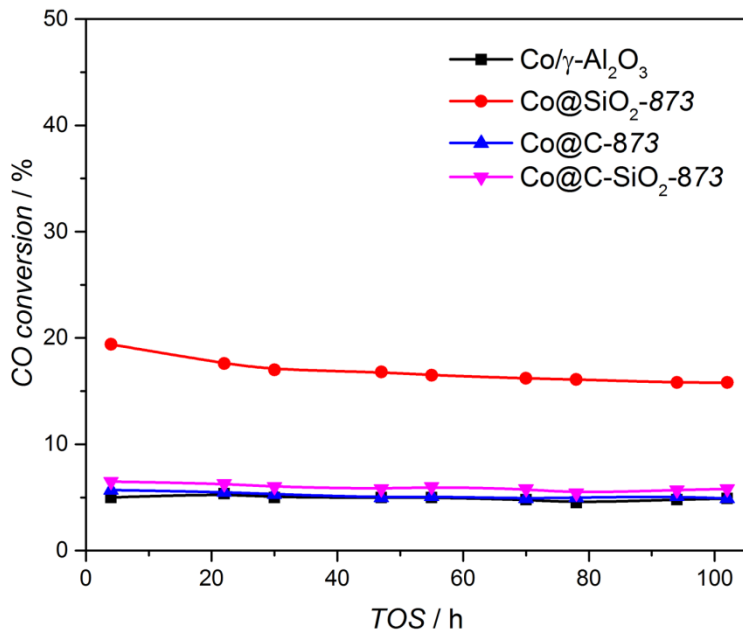
Figure C11. CO conversion as a function of time-on-stream (*TOS*) in the FTS over Co/γ-Al₂O₃, Co@SiO₂-*873*, Co@C-*873*, and Co@C-SiO₂-*873* catalysts. Reaction conditions: 483 K, 20 bar, $H_2/CO = 1$, and syngas flow of 40 ml min^{-1}.

Table C1. Catalytic performance of Co/γ-Al$_2$O$_3$, Co@SiO$_2$-*873*, Co@C-*873*, and Co@C-SiO$_2$-*873* catalysts after 102 h *TOS*.

Catalyst	Catalyst weight (mg)	Cobalt loadings (wt.%)	X_{CO} (%)	CTY (10^{-5} mol$_{CO}$g^{-1}$_{Co}$s^{-1})	S [%]		
					C1	C2-4	C5+
Co/γ-Al$_2$O$_3$[a]	250	17	4.9	1.7	6.8	7.8	85.4
Co@SiO$_2$-*873*	100	51	15.8	4.4	5.3	4.2	90.5
Co@C-*873*	150	32	4.9	1.5	13.1	7.5	79.4
Co@C-SiO$_2$-*873*	150	28	5.8	2.1	17.1	11.1	71.7

a: Co/γ-Al$_2$O$_3$ was prepared using incipient wetness impregnation with aqueous cobalt nitrate solution, followed by drying at 373 K under vacuum overnight and calcination under air flow (150 ml min^{-1}) for 2 h at a ramp rate of 1 K min^{-1}. Carbon conversion (X_{CO}, %), activity per gram of Co (*CTY*), hydrocarbon selectivity (*S*, %). FTS experiments were carried out at 483 K, 20 bar, and H$_2$/CO=1, and syngas flow of 40 ml min^{-1}.

Table C2. Cobalt loading in Co@C-*873* and Co@C-*873(al)* catalysts.

Catalyst	Co loadings (wt.%)
Co@C-*873*	32
Co@C-*873(al)*[a]	22

a: Co@C-*873(al)* was obtained by immersing 0.5 g Co@C-*873* in 500 ml of 0.5 M hydrochloric acid solution for 4 days at 303 K to dissolve the exposed cobalt nanoparticles, followed by washing with deionized water and drying at 323 K under vacuum.

Figure C12. TEM analysis of Co@C-*873(al)* catalyst.

Figure C13. TEM analysis of Co/SiO$_2$-*A-MI* catalyst. (a) Dark field TEM micrograph, (b) Elemental mapping of Co, and (c) of Si.
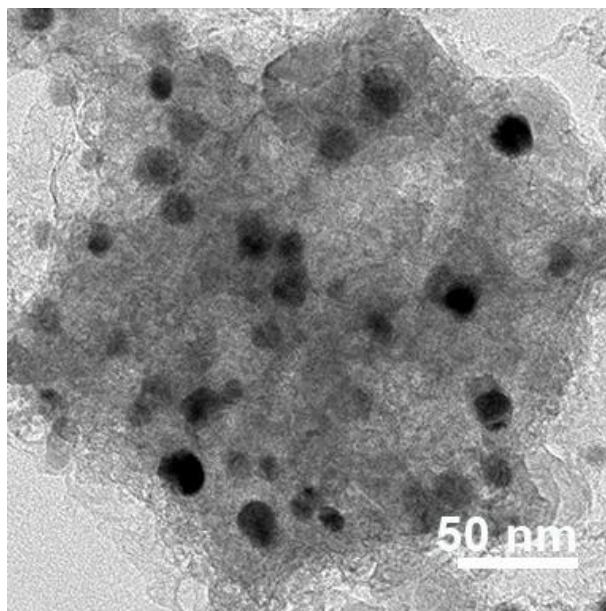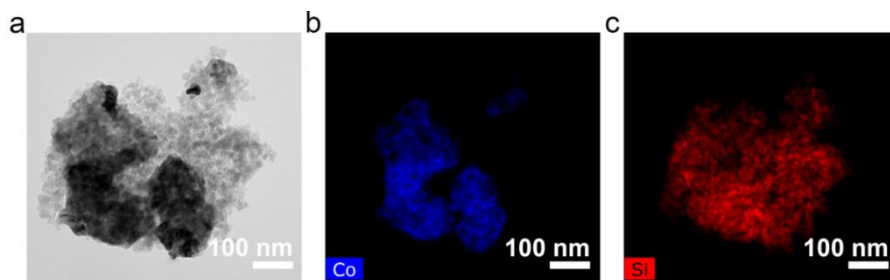
SUMMARY

The production of most industrially important chemicals involves catalysis. Depending on the difference in phases between the catalysts and reactants, one distinguishes homogenous catalysis and heterogeneous catalysis, with the latter being more attractive in real applications, due to the easy separation of products from catalysts and reusing the latter. In spite of the research and development of heterogeneous catalysts for decades, the exploration for catalysts system with outstanding activity, stability and selectivity remains a challenging task. In general, most of the chemical reactions occur on the surface atoms of supported metal (oxide) nanoparticles. Therefore, to address this challenge, current studies generally focus on understanding the relation between the catalytic performance and catalyst properties by controlling the particle size and distribution, and even the shape of supported nanoparticles, and the interaction between nanoparticles and support. In order to further contribute to this objective, in this thesis we applied metal-organic-frameworks (MOFs) as a sacrificial precursor to produce catalysts for catalytic hydrogenation reactions, important routes for the production of a variety of fine and bulk chemicals in industry. The recent application of MOFs as templates and precursors in material synthesis and catalysis has been thoroughly described in **Part I** (**Chapter 1**). The unique structure, atomic metal dispersion and textural properties of MOFs, together with the well controllable metal nanoparticle size and distribution in the carbon matrix after high-temperature pyrolysis ('MOF mediated synthesis', MOFMS) inspired us to design and develop new catalyst systems to go a step further to addressing the above-mentioned challenge in heterogeneous catalysis.

Part II includes Chapter 2 and 3. **Chapter 2** focuses on the selective hydrogenation of nitroarenes by using a highly loaded cobalt@N-doped carbon hybrid (Co@NC) prepared by high-temperature pyrolysis of a cobalt-containing ZIF (Co-ZIF) under N_2 atmosphere. The pyrolysis temperature was proven to influence the carbon structure (i.e. graphitization degree and N-content), cobalt composition (*i.e.* cobalt particle size, cobalt accessibility and distribution etc.) in the obtained Co@NC catalyst. During the high-temperature pyrolysis, cobalt cations in the parent ZIF are reduced to metallic cobalt, and the majority of cobalt atoms aggregate to cobalt nanoparticles, which further catalyze the formation of graphitic carbon shells on their surface. The unique structure of the Co@NC hybrid significantly avoids the agglomeration and leaching of active cobalt species during the hydrogenation process. With a subsequent acid leaching step, we found that only those partially encapsulated cobalt nanoparticles and the atomically dispersed CoN_x species catalyze the hydrogenation reaction, and the highly dispersed CoN_x species have a much higher activity contribution in this reaction. The unique structure of the Co@NC hybrid enables the chemoselective hydrogenation of aromatic '-NO_2' groups while other functional groups remain unaffected. The Co@NC catalyst inevitably deactivates after couple of runs, and the loss of activity can be ascribed to blockage of the active sites by strongly adsorbed product species.

The different activities between cobalt nanoparticles and atomically dispersed CoN_x species in the N-doped carbon matrix, together with the existence of 'dead' cobalt nanoparticles fully encapsulated by graphite shells triggered further investigation on the design and development of highly active single atom (CoN_x) catalysts for the nitroarene hydrogenation, as reported in **Chapter 3**. In view of the same coordination of Co^{2+} and

Zn^{2+} with 2-methylimidazole in ZIF-67 and ZIF-8, the Zn,Co-bimetallic zeolitic imidazolate framework (Co,Zn-BIMZIF) was first prepared as catalyst precursor. The further catalyst synthesis consists of hydrolysis of tetramethyl orthosilicate (TMOS) in the pores of Co,Zn-BIMZIF, high-temperature pyrolysis under N_2 atmosphere, and silica etching. On one hand, the zinc atoms in the framework act as a 'fence' to separate cobalt atoms, preventing the agglomeration of cobalt atoms to nanoparticles during high-temperature pyrolysis. On the other hand, the evaporation of zinc at high temperature generates liberates N-sites stabilizing single Co atoms as well. Furthermore, the presence of SiO_2 in the porosity of BIMZIF isolates to some extent the cobalt atoms, and thereby mitigates the sintering to nanoparticles. Besides, the SiO_2-templated strategy is also proven to increase the specific surface area of the carbon matrix and to create mesoporosity. This Co@mesoNC catalyst exhibits high hydrogenation activity, unique chemoselectivity towards the substituted anilines and a better catalytic stability than its counterpart that was synthesized by a direct pyrolysis of BIMZIF. The presence of mesoporosity largely improves the accessibility of the $Co-N_x$ sites that can otherwise easily be blocked by intermediates and/or products in the micropores.

Part III includes Chapter 4 and 5. When this Co@NC hybrid was directly used in Fischer-Tropsch Synthesis (FTS) process, low activity and C5+ selectivity, and high, undesired CH_4 selectivity were observed, as shown in **Chapter 4**. This can be attributed to the fact that the graphite shells on the surface of cobalt nanoparticles in the Co@NC material prevent the accessibility of cobalt cores from reactants (CO and H_2). Inspired by the uniform dispersion of cobalt nanoparticles in the Co@NC material and the successful synthesis of porous silica by replication of MOFs, we came up

with a new 'hydrolysis-pyrolysis-calcination' strategy to synthesize a highly loaded $Co@SiO_2$ catalyst with controllable cobalt particle size and distribution and high cobalt reducibility using a cobalt-ZIF (ZIF-67) and trimethyl orthosilicate (TMOS) as raw materials. The pyrolysis operated above the decomposition temperature of ZIF-67 prior to calcination is demonstrated to be essential to optimize the cobalt particle size distribution (>6 nm) and to avoid the formation of large cobalt clusters and irreducible cobalt silicate species. This novel high-loading (50 wt.% Co) $Co@SiO_2$ catalyst shows a cobalt-time-yield (*CTY*) almost twice as high as the conventional Co/SiO_2 and $Co/\gamma-Al_2O_3$ catalysts, together with an excellent stability and high C5+ selectivity under low-temperature FTS conditions.

Besides the above-mentioned route to control cobalt particle size distribution in supported-cobalt catalysts, another alternative way is to control the pretreatment conditions during catalysts preparation. In order to investigate the effect of pretreatment conditions on catalyst properties (i.e. cobalt particle size and distribution, cobalt reducibility), catalytic activity and product selectivity in FTS process, in **Chapter 5** we switched the emphasis from MOF-mediated synthesis strategy to zeolite-supported cobalt catalyst. Opposite to the Co/SiO_2 data reported in literature, the pretreatment under stagnant air conditions in our work results in the highest activity and the lowest CH_4 selectivity, despite that this catalyst displays a much broader cobalt particle size distribution compared to the catalysts prepared under N_2 and NO atmospheres. This difference can be attributed to the much stronger Co-zeolite interaction than that of Co-silica. The strong Co-zeolite interaction generates small cobalt nanoparticles and poor cobalt reducibility, resulting in non-optimal utilization of the active phase, especially when a better cobalt precursor distribution can be achieved during catalyst

preparation, such as pretreatment under N_2 and NO atmospheres. Thus, controlling catalytic activity and product selectivity by changing pretreatment conditions during catalyst preparation should be carefully taken into consideration from both metal-support interaction and the structure sensitivity of the reaction itself.

To conclude this research, the unique properties of MOFs, such as the atomic metal dispersion and well-developed porosity make them highly promising for catalyst manufacture. Supported catalysts with high cobalt loadings and controllable cobalt particle size can be synthesized with different approaches, which are largely dependent on the relation between active phases and structure of the catalyst in the target reactions, like liquid hydrogenation of nitroarenes and Fischer-Tropsch synthesis. In addition, the spatial segregation of metal atoms in the framework by other guest atoms can be another alternative to synthesize highly-, or even atomically-dispersed supported metal catalysts, maximizing the utilization of metal atoms. The flexible design of supported metal catalysts with nanoparticle size from Ångstrøm (single atom) to several nanometers (nanoparticle) undoubtedly makes MOFs a promising precursor in heterogeneous catalysis.

SAMENVATTING

Bij de productie van de meeste belangrijke chemicaliën in de industrie is katalyse essentieel. Afhankelijk van het verschil in fase tussen de katalysator en de reactanten, worden katalytische processen ingedeeld in homogene en heterogene katalytische processen, waarbij de laatstgenoemde bij toepassing op grote schaal de voorkeur heeft vanwege de eenvoudiger scheiding van de producten van de katalysator en hergebruik van de laatste. Ondanks tientallen jaren van onderzoek en ontwikkeling van heterogene katalysatoren blijft het een uitdaging om een katalysator te vinden met uitmuntende activiteit, stabiliteit en selectiviteit. Over het algemeen vinden de meeste chemische reacties plaats aan het oppervlak van de gedragen metaal (oxide) nanodeeltjes. Derhalve, om deze uitdaging aan te pakken, wordt in huidige studies de nadruk gelegd op het begrijpen van het verband tussen de katalytische prestaties en de katalysatoreigenschappen door synthetische beheersing van de deeltjesgrootte en -distributie en zelfs de vorm van de gedragen nanodeeltjes en de interactie tussen nanodeeltjes en drager. Om een verdere bijdrage leveren aan deze ontwikkeling, wordt in dit proefschrift ingegaan op het combineren van Metal-Organic-Frameworks (MOF's) als uitgangsmateriaal om heterogene katalysatoren te produceren voor hydrogeneringsreacties. Deze reacties worden in de industrie veel gebruikt voor de productie van diverse fijn- en bulkchemicaliën. De recente toepassing van MOF's als template en precursor in materiaalsynthese en katalyse wordt uitgebreid beschreven in **Deel I (Hoofdstuk I)**. De unieke structuur, atomaire metaaldispersie en textuureigenschappen van MOF's, samen met de goede beheersing van de metaal nanodeeltjesgrootte en -distributie in de koolstof matrix na pyrolyse op hoge temperatuur, waren de

inspiratie om nieuwe katalysatoren te ontwerpen en ontwikkelen, welke een stap dichter bij de bovengenoemde uitdaging in heterogene katalyse komt.

Deel II omvat hoofdstukken 2 en 3. **Hoofdstuk 2** richt zich op de selectieve hydrogenering van nitroarenen door gebruik te maken van een hoogbeladen kobalt@N-gedoteerde koolstofhybride (Co@NC) welke is bereid door pyrolyse van een kobalthoudende ZIF (ZIF-67) bij hoge temperatuur onder N_2-atmosfeer. De pyrolysetemperatuur bleek invloed te hebben op de koolstofstructuur (d.w.z. de grafitiseringsgraad en N-gehalte) en hoe het kobalt aanwezig is (d.w.z. kobaltdeeltjesgrootte, -toegankelijkheid en -verdeling etc.) in de verkregen Co@NC katalysator. Tijdens de pyrolyse bij hoge temperatuur worden kobaltkationen in het ZIF-uitgangsmateriaal gereduceerd tot metallische kobaltatomen, waarvan de meerderheid aggregeert tot kobaltnanodeeltjes die de vorming van grafeenlagen op hun oppervlak katalyseren. De unieke structuur van de Co@NC-hybride voorkomt de verdere agglomeratie en het verlies van actief kobalt tijdens het hydrogeneringsproces. Verder onderzoek wees uit dat alleen die gedeeltelijk ingekapselde kobaltnanodeeltjes en de atomair gedispergeerde CoN_x-complexen de hydrogeneringsreactie katalyseren waarbij de sterk gedispergeerde CoN_x-complexen het meest bijdragen aan de katalytische activiteit. De unieke structuur van de Co@NC hybride zorgt voor chemoselectieve hydrogenering van '-NO_2'-groepen tot '-NH_2' groepen waarbij de andere functionele groepen onaangetast blijven. De Co@NC-katalysator verliest activiteit na elk hergebruik, toegeschreven aan blokkering van de actieve plaatsen door sterk adsorberende, niet nader gespecificeerde componenten.

Het verschil in activiteit tussen kobalt nanodeeltjes en atomair gedispergeerde CoN_x-sites in N-gedoteerde koolstofmatrices, en ook het

bestaan van inactieve kobalt nanodeeltjes die volledig ingekapseld zijn door grafietschillen, was aanleiding voor verdere ontwikkeling van zeer actieve atomair gedispergeerde (CoN$_x$) katalysatoren voor het hydrogeneren van nitroarenen, beschreven in hoofdstuk 3. Omdat Co^{2+} en Zn^{2+} op dezelfde manier coördineren aan 2-methylimidazool in ZIF-67 en ZIF-8, zijn bimetallische Co en Zn bevattende ZIF's (Co,Zn-BIMZIF) gesynthetiseerd. De synthese van de katalysator omvat verder de hydrolyse van tetramethyl-orthosilicaat (TMOS) in de poriën van Co,Zn-BIMZIF, gevolgd door pyrolyse bij hoge temperatuur onder N$_2$ atmosfeer, en uitloging van silica. Enerzijds werken de zinkatomen in het framework als een 'hek' om kobaltatomen van elkaar gescheiden te houden, zodat de agglomeratie van kobaltatomen tot nanodeeltjes tijdens pyrolyse bij hoge temperatuur wordt voorkomen. Anderzijds zorgt de verdamping van zink bij hoge temperatuur ervoor dat vrije N-sites worden gevormd die ook atomair Co kunnen verankeren. Bovendien kan de aanwezigheid van SiO$_2$ in de poriën van BIMZIF er tot op zekere hoogte voor zorgen dat de kobaltatomen geïsoleerd worden, waardoor sintering tot nanodeeltjes ook wordt voorkomen. Verder is deze 'SiO$_2$-templated' strategie een beproefde methode om het specifieke oppervlak van de koolstofmatrix te verhogen en mesoporositeit in de drager te creëren. Deze Co@mesoNC katalysator heeft een hoge activiteit voor hydrogenering, unieke chemoselectiviteit voor gesubstitueerde anilines en een veel betere katalytische stabiliteit dan zijn tegenhanger gesynthetiseerd via een éénstapspyrolyse van BIMZIF. De aanwezigheid van mesoporositeit levert ook een betere toegankelijkheid van de Co-N$_x$ sites, die door tussenproducten en/of producten in de microporiën kunnen worden geblokkeerd.

Deel III omvat hoofdstuk 4 en 5. Directe toepassing van de Co@NC hybride in het Fischer-Tropsch Synthese (FTS) proces resulteerde in een lage activiteit, en lage C5+ selectiviteit en een onwenselijk hoge CH$_4$, zoals beschreven in **Hoofdtuk 4**. Dit kan worden toegeschreven aan het feit dat de grafeenschillen om de kobaltnanodeeltjes in het Co@NC materiaal de toegang tot het kobalt voor reactanten (CO en H$_2$) verhinderen. Geïnspireerd door de uniforme dispersie van kobaltnanodeeltjes in het Co@NC materiaal en de succesvolle synthese van poreus siliciumoxide via de pyrolyse van MOFs, is een nieuwe 'hydrolyse-pyrolyse-calcinatie' strategie ontwikkeld om daarmee een hoogbeladen Co@SiO$_2$ katalysator te produceren met gecontroleerde kobaltdeeltjesgrootte en -distributie en een hoge kobalt reduceerbaarheid. Kobalt-ZIF (ZIF-67) en trimethyl orthosilicaat (TMOS) werden gebruikt als ruwe grondstoffen. Het bleek cruciaal om de pyrolyse uit te voeren boven de ontledingstemperatuur van ZIF-67 vòòr de calcineringsstap teneinde de deeltjesgrootte-verdeling te optimaliseren (>6 nm) en om te voorkomen dat er grote kobalt clusters en/of onreduceerbaar kobalt silicaat ontstaan. Deze nieuwe Co@SiO$_2$ katalysator laat zonder twijfel zien dat de activiteit genormeerd op het aanwezige kobalt ('cobalt-time yield', CTY) bijna tweemaal hoger is dan van conventionele Co/SiO$_2$ en Co/γ-Al$_2$O$_3$ katalysatoren. Daarbij heeft dit systeem een uitstekende stabiliteit en een hoge C5+ selectiviteit onder lage temperatuur FTS reactiecondities.

Naast de bovengenoemde route om de kobaltdeeltjesgrootteverdeling in gedragen kobalt katalysatoren te beheersen, is een andere benadering mogelijk, namelijk via het beheersen van de omstandigheden van de voorbehandeling. Om te onderzoeken wat de effecten van verschillende synthesevoorbehandelingen zijn op de katalysator eigenschappen (zoals

kobalt deeltjesgrootteverdeling en kobalt reduceerbaarheid), de katalytische activiteit en de product selectiviteit in het FTS proces, is in **Hoofdstuk 5** de nadruk verlegd naar zeolietgedragen kobaltkatalysatoren. In tegenstelling tot de Co/SiO_2 literatuur, resulteert een voorbehandeling in stilstaande lucht in de hoogste activiteit en de laagste CH_4 selectiviteit, ondanks het feit dat deze katalysator een veel bredere kobalt deeltjesgrootte en -verdeling laat zien vergeleken met katalysatoren die bereid zijn in N_2 en NO bevattende atmosferen. Dit verschil is toegeschreven aan de veel sterkere kobalt-zeoliet interactie dan die van kobalt-siliciumdioxide.

We kunnen uiteindelijk concluderen dat MOFs door hun unieke eigenschappen, zoals de atomaire metaaldispersie en goed ontwikkelde porositeit, veelbelovende materialen zijn voor katalysator productie. Gedragen katalysatoren met hoge kobaltbelading en controleerbare deeltjesgrootte kunnen worden gesynthetiseerd op verschillende manieren, grotendeels afhankelijk van de relatie tussen actieve fase en structuur van de katalysator in de beoogde reactie, zoals de vloeistoffase hydrogenering van nitroarenen en de Fischer-Tropsch synthese. Bovendien is de ruimtelijke scheiding van metaalatomen in het framework door toevoeging van gastcomponenten een alternatief om een zeer hoge of zelfs atomaire dispersie te bereiken in gedragen metaalkatalysatoren, met een maximale benuttingsgraad. Het flexibele ontwerp van gedragen metaalkatalysatoren met nanodeeltjesgrootte variërend van Ångstrøm (enkele atomen) tot enkele nanometers (nanodeeltjes) maken MOFs een zeer veelbelovende precursor in de heterogene katalyse.

ACKNOWLEDGEMENTS

Looking back on my PhD study, I can say I improved myself a lot. The training in the past four years not only helped me to acquire enormous knowledge and skills in scientific field, but also enabled me to identify problems and come up with new ideas inspired on other people's work. More importantly, this period will be a meaningful experience in my whole life. Of course, this progress cannot be realized without the assistance of other people; thus I would like to thank them.

I would like to express my sincere thanks to my daily supervisor and promotor Prof. dr. Jorge Gascon to bring me to the world of metal-organic frameworks (MOFs). I was deeply attracted by your presentation in Aula and made my decision to work on MOFs, and I always believed that my decision was correct (Indeed, it is). In addition, your guidance helped me to know what a PhD should do with experimental data in hand, especially when the data is not as good as expected. I believe that this experience will be of high value in my future research. I also appreciate you to give me enough freedom to perform research, to discuss it together in time, and to encourage me all the time. I would like to express my gratitude to my promotor Prof. dr. Freek Kapteijn. Thank you so much for teaching me the rigorous analysis during scientific research. I always remember your questions related to catalyst preparation details and the experimental results during my first paper. These questions always reminded me to perform each step cautiously when I was doing experiments during my PhD. Now I believe that this is the first thing a PhD should learn prior to the experiment. Of course, I am also thankful to you for your kind discussion and suggestions. I further would like to appreciate the area supervisor, Prof. dr.

Michiel Makkee. Thank you so much to let me know 'Safety is always the priority.'

My PhD research could not be smoothly completed without the assistance of technicians. I would like to thank Harrie Jansma for the help to check and fix my six-flow reactor setup in time, so that the setup is always ready for use. Bart van der Linden for the kind and patient guidance for H_2-TPR, IR and Raman analysis. Willy Rook for the kind help for N_2-adsorption and H_2-chemisorption measurements and detailed data explanation. Kevin Mouthaan and Liliana Baron for the help in GC analysis. Bart Boshuizen for the help to solve the problems from the Labview in my setup and Duco Bosma for his help for SEM measurement and useful discussion about the six-flow setup. I also appreciate the gas team members Nico van der Knaap, Erwin Jansen and Alex Jonker. You are so kind and efficient to check the gas supply, so that I could always run successfully the long-time experiments.

I also would like to thank the secretaries in our group. Els Arkesteijn, thank you so much for the help to arrange meetings with my promotors and journeys for conferences, and for the administrative issues. Caroline Monna, thank you so much for help me for countless chemical delivery.

I always believe that a PhD student should also know how to collaborate with others, since it can help us to solve our problems with new ideas and broaden our knowledge as well. In this sense, I firstly would like to thank Sina Sartipi for the supervision on catalyst synthesis, setup operation and useful discussion during my first year PhD. Without your help, I could not easily start my project. I also appreciate Alma I. Olivos-Suarez to agree to join in my PhD project. Your chemistry background indeed broadened my knowledge a lot. Thanks Tim Wezendonk for the discussion on the Fischer-

Tropsch project, and our collaboration indeed produced very interesting results. Thanks Maria José Valero Romero, Dmitrii Osadchii, Lide Oar-Arteta and Elena Rozhko for the help in my project as well, your assistance made me managing my project easier.

Further I highly appreciate all the colleagues in the catalysis group providing me with a friendly environment for research and life. Xinlei, you behave like an old brother who encourage me and give me a lot of advices. Xuerui, you make me believe that a good chemist is also talented in cooking. Maxim, my best office mate, I feel very lucky having shared the office with you, and I hope for you it is the same. But do not kick the chair of your new office mate before you know his temper very well. Irina, you were the only Russian who could always be found in the old building during the weekend. This makes me think that my Chinese working style could only influence you and not the other Russians. Ina, although it took some time for me to realize, you confirmed that those German cliché qualities (i.e. punctual, well organized and diligent) were true. Robert, every time when I see your photo on our group website, I have to confirm further if you are really a PhD student or a young professor. Jara, you are the only Spanish who invited me for Croqueta once and continuously kept on telling me how delicious it is afterwards (It is not fair). Anahid, do not always spend 25 hours per day in the lab, otherwise you only have 29 days per month. Eduardo, we know that you are skillful in cooking cakes and fencing. Every time after cutting the cake into pieces with your sword, make sure it is clean, otherwise you cannot get scores even you stab your opponent. Last but not the least, Anastasiya, my best friend, what do you want me to say?

I also would like to express my gratitude to all the Chinese friends in this building. Guanna Li, Yixiao Wang, Meixia Shan, Riming Wang, Zhen

Liu, Liangyong Chu, Wuyuan Zhang, Anping Cao, Quan Pan, Jicheng Feng, Kai Zhang, Min Wang, Yujie Zhao, Yaya Liu, Yiming Wang, Ming Ma, and Kai Liu. We are like a big family, I really enjoyed the wonderful time with all of you during my PhD.

Finally, I would like to appreciate my parents for their endless love and unconditional support when I studied for my PhD. Also my young sister Qing, thank you so much to support and believe in me with everything. This made me feel confident to manage my project and complete my PhD study in four years.

LIST OF PUBLICATIONS AND PRESENTATIONS

Publication related to this thesis:

- *L. Oar‑Arteta, T. Wezendonk, <u>X. Sun</u>, F. Kapteijn, J. Gascon*, Metal Organic Frameworks as Precursors for the Manufacture of Advanced Catalytic Materials. Materials Chemistry Frontiers, **2017**, 1, 1709-1745.

- *<u>X. Sun</u>, A. I Olivos‑Suarez, L. Oar‑Arteta, E. Rozhko, D. Osadchii, A. Bavykina, F. Kapteijn, J. Gascon*, Metal-Organic Framework Mediated Cobalt/Nitrogen-Doped Carbon Hybrids as Efficient and Chemoselective Catalysts for the Hydrogenation of Nitroarenes, Chemcatchem, **2017**, 9 1854-1862.

- *<u>X. Sun</u>, A. I. Olivos-Suarez, D. Osadchii, M. J. Valero-Romero, F. Kapteijn, J. Gascon,* Atomically Dispersed Cobalt Sites in Mesoporous N-Doped Carbon Matrix for Selective Catalytic Hydrogenation of Nitroarenes. *Submitted, under revision.*

- *<u>X. Sun</u>, A. I. Olivos-Suarez, L. M. Meijerink, T. van Deelen, J. Zečević, K. P. de Jong, F. Kapteijn, J. Gascon,* Stepwise Synthesis of Highly Loaded and Active Silica Supported Cobalt Fischer-Tropsch Catalysts Using Metal-Organic Frameworks as Sacrificial Templates. *Submitted, under revision.*

- *<u>X. Sun</u>, S. Sartipi, F. Kapteijn, J. Gascon,* Effect of Pretreatment Atmosphere on the Activity and Selectivity of Co/*meso*HZSM-5 for Fischer-Tropsch Synthesis. New Journal of Chemistry, **2016**, 40, 4167-4177.

Other publications:

- *<u>X. Sun</u>, F. Kapteijn, J. Gascon,* Metal-Organic-Framework Mediated Synthesis of Highly Loaded and Active Co@SiO$_2$ Fischer-Tropsch Catalyst: Effect of Hydrolysis and Pyrolysis on Catalytic Performance. *In preparation.*

- *K. Holt, <u>X. Sun</u>, F. Kapteijn, J. Gascon etc.,* Designing New Catalysts for Synthetic Fuels: General Discussion, Faraday Discussions, **2017**, 197, 353-388.

- *J. L Eslava, <u>X. Sun</u>, J. Gascon, F. Kapteijn, I. Rodríguez-Ramos,* Ruthenium Particle Size and Cesium Promotion Effects in Fischer–Tropsch Synthesis over High-Surface-Area Graphite Supported Catalysts. Catalysis Science & Technology, **2017**, 7, 1235-1244.

- *M. J. Valero-Romero, S. Sartipi, <u>X. Sun</u>, J. Rodríguez-Mirasol, T. Cordero, F. Kapteijn, J. Gascon,* Carbon/H-ZSM-5 Composites as Supports for Bi-functional Fischer-Tropsch Synthesis Catalysts. Catalysis Science & Technology, **2016**, 6, 2633-2646.

- *V. P. Santos, T. A Wezendonk, J. J. Delgado Jaén, A. I. Dugulan, M. A Nasalevich, H. U. Islam, A. Chojecki, S. Sartipi, <u>X. Sun</u>, A. A Hakeem, A. CJ Koeken, M. Ruitenbeek, T. Davidian, G. R Meima, G. Sankar, F. Kapteijn, M. Makkee, J. Gascon,* Metal Organic Framework-Mediated Synthesis of Highly Active and Stable Fischer-Tropsch Catalysts, Nature communications, **2015**, 6, 6451.

- *W. Chen, D. Han, <u>X. Sun</u>, C. Li,* Studies on the Preliminary Cracking of Heavy Oils: Contributions of Various Factors, Fuel, **2013**, 106, 498-504.

Book Chapter:

- *L. Oar-Arteta, T. Wezendonk, <u>X. Sun</u>, F. Kapteijn, J. Gascon,* Metal-Organic Framework-Mediated Synthesis in Catalysis. Nanotechnology in Catalysis: Applications in the Chemical Industry, Energy Development, and Environment Protection, Wiley, **2017**, 225-250.

Presentations:

- *<u>X. Sun</u>, A. I Olivos-Suarez, L. Oar-Arteta, E. Rozhko, D. Osadchii, M. J. Valero-Romero, A. Bavykina, F. Kapteijn, J. Gascon,* Metal-Organic Framework Mediated Cobalt/Nitrogen-Doped Carbon Hybrids for the Hydrogenation of Nitroarenes, North American Catalysis Society Meeting, 4th June-9th June, **2017**. **(Oral)**

- *<u>X. Sun</u>, A. I. Olivos-Suarez, L. M. Meijerink, T. van Deelen, J. Zečević, K. P. de Jong, F. Kapteijn, J. Gascon,* Metal Organic Framework-Mediated Synthesis of Highly Laded and Active Co@SiO$_2$ Fischer-Tropsch Catalysts, The Netherlands' Catalysis and Chemistry Conference, 6th March-8th March, **2017**. **(Oral)**

- *<u>X. Sun</u>, A. I Olivos-Suarez, L. Oar-Arteta, E. Rozhko, D. Osadchii, A. Bavykina, F. Kapteijn, J. Gascon,* Metal-Organic Framework Mediated Cobalt/Nitrogen-Doped Carbon Hybrids for the Hydrogenation of Nitroarenes, Catalysis for Fuels Faraday Discussion, 24th January-26th January, **2017**. **(Poster) Best poster prize.**

- *<u>X. Sun</u>, A. I Olivos-Suarez, L. Oar-Arteta, E. Rozhko, D. Osadchii, A. Bavykina, F. Kapteijn, J. Gascon,* Metal-Organic Framework Mediated Cobalt/Nitrogen-Doped Carbon Hybrids for the Hydrogenation of Nitroarenes, The Netherlands' Catalysis and Chemistry Conference, 3rd March-9th March, **2016**. **(Poster)**

- ***X. Sun**, S. Sartipi, F. Kapteijn, J. Gascon,* Effect of Pretreatment Atmosphere on the Activity and Selectivity of Co/*meso*HZSM-5 for Fischer-Tropsch Synthesis, the 3rd ALP International Symposium, Hokkaido University, 18th November-19th November, 2015. **(Poster) Best poster prize.**
- ***X. Sun**, S. Sartipi, F. Kapteijn, J. Gascon,* Effect of Pretreatment Atmosphere on the Activity and Selectivity of Co/*meso*HZSM-5 for Fischer-Tropsch Synthesis, The Netherlands' Catalysis and Chemistry Conference, 2nd March-4th March, 2015. **(Poster)**

ABOUT THE AUTHOR

Xiaohui Sun was born on October the 11th, 1986 in Zibo, Shandong province, China. He received his bachelor's degree from the Department of Chemical Engineering at China University of Petroleum (Huadong) in 2010. Afterwards, he continued his masters study at the same university under the supervision of Prof. dr. Chaohe Yang. He obtained his MSc degree in 2013, with the thesis entitled: 'Studies on catalysts for NO_x removal from the regenerator in FCC plant'. In September 2013, he moved to the Netherlands and started his PhD project under the supervision of Prof. dr. Freek Kapteijn and Prof. dr. Jorge Gascon in the group of Catalysis Engineering at the Delft University of Technology (Faculty of Applied Sciences, Department of Chemical Engineering). This project was focused on the application of zeolite-based and metal organic framework (MOF) - mediated catalysts in heterogeneous hydrogenation reactions.

He has supervised two MSc students and contributed as teaching assistant to the Chemical Engineering undergraduate course 'Process Technology I' (coordinated by Prof. dr. Freek Kapteijn).

He has won two times the best poster prize during his PhD at the 3rd International Symposium of Ambitious Leaders Program 'Fostering Future Leaders to Open New Frontiers in Materials Science' in 2015, Hokkaido,

Japan and at the Faraday Discussions meeting 'Catalysis for Fuels' in 2017, Cape Town, South Africa**.**

Currently he is active at TUDelft as a post-doc on the production of bulk oxygenates from synthesis gas sponsored by Sekisui Chemical Co. Ltd (Japan) under supervision of prof.dr.ir. Michiel Makkee.